Experimental characterisation of evaporating and non-evaporating sprays using planar laser diagnostics and Lagrangian tracking

Hywel Davies

A dissertation submitted in partial fulfillment of the requirements for the degree of

Doctor of Philosophy

of

University College London.

Department of Mechanical Engineering
University College London

'I, Hywel Davies, confirm that the work presented in this thesis is my own. Where information has been derived from other sources, I confirm that this has been indicated in the thesis.'

Abstract

This thesis focusses on the measurement of parameters relevant to droplet evaporation in polydispersed sprays using planar optical techniques. A range of applications are addressed, from automotive to energy generation and epidemiology. These fields stand to benefit from improved understanding of droplet evaporation mechanisms within turbulent sprays.

Interferometric Droplet Sizing (IDS) is a planar method that provides spatially resolved measurements of droplet diameter and velocity over a large volume. To explore the suitability of the IDS method in performing measurements on turbulent sprays a series of experiments were performed using an automotive fuel injector to observe effects of ethanol content within ethanol-gasoline fuel blends. Results showed an increase in mean droplet diameter and homogeneity of droplet concentration distribution with increasing ethanol content. Several limiting factors were observed, restricting the ability of IDS to determine droplet volumetric concentrations. To improve performance a Lagrangian tracking processor was developed, using high-speed imaging and IDS principles. The Lagrangian tracking was shown to increase the number of droplet measurements and allowed the spatially resolved tracking of droplet position and diameter over time. The Lagrangian tracker was capable of directly measuring the evaporation of methanol droplets entrained within a heated air flow. Droplet evaporation rates were compared with a single droplet evaporation model, showing good agreement. The Lagrangian tracker was used to relate droplet diameter and droplet-gas slip velocity in an acoustic flow field. Close agreement was observed between data and modelled relations between stokes number and slip velocity. Evaporation rate enhancement of droplets from increasing

Abstract 5

acoustic amplitudes was observed to be considerable in comparison to enhancement with increasing ambient temperature.

During this work, the relevance of aerosol characterisation to the spread of infectious, diseases became apparent with the outbreak of COVID-19. Using high-speed imaging human expiration of droplets was monitored. The information recorded, such as typical droplet velocities, concentrations, inter-person variation and the impact of face coverings will help to improve research into the propagation of human produced aerosols and the impact this has on the spread of diseases.

Impact Statement

This thesis presents the use and development of planar laser diagnostic techniques to characterise multiphase flows. A particular focus is placed on the use of Interferometric Droplet Sizing (IDS) for the measurement of parameters relevant to droplet evaporation in turbulent sprays. The work describes the benefits limitations of existing IDS implementations and proposes novel developments. With the outbreak of COVID-19, work was refocussed onto the production of aerosols through human expiration.

The creation of an image and data post processing algorithm allows the Lagrangian tracking of multiple individual droplet position and diameter over time at droplet and flow scales relevant to industrial applications. This is used to directly measure methanol droplet evaporation within a spray and could be used to relate individual droplet evaporation rate to localised spatio-temporal parameters such as inter-droplet spacing and slip velocity, something which current measurement methods are unable to directly detect.

The proposed method improvement allows researchers to better develop improved analytical models for droplet evaporation within complex spray systems. Limitations in current measurement methods only allow simplified models to be produced. The proposed tracking technique also presents an opportunity to provide much needed validation methods for computational modelling. Current computational research is being limited in its applications by the inability to perform experimental measurements for validation.

Much of the work presented within the thesis relates closely to atomisation of renewable and alternative liquid fuels for the purposes of energy generation. The Abstract 7

results data contained such as effects of bio-ethanol content in gasoline fuel blends and the rate of methanol droplet evaporation within a spray can be directly used to better inform fuel injector and combustion system design. Beyond this, the use of a measurement technique capable of direct measurement of spray droplet evaporation can directly benefit other industrial applications including spray drying in food and pharmaceutical production, agricultural technologies and material coating.

Descriptions of novel methodologies and findings have been shared with the scientific community through the presentation and publishing of work at international conferences and well renowned journal publications as well as industrial partners.

The work presented relating to the production of aerosols through human expiration was especially relevant given the outbreak of COVID-19. The key purpose of this piece of work was to better understand factors effect human aerosol production such as variations between individuals, the impact of face coverings and type of vocal or non-vocal expiration. At the time of this research being performed public health and government policy was based on very little data, with one of the key purposes of the work was to publish information through both media and journal and help guide UK and international policy making. This work has provided a base from which further research into the spread of viral aerosols within clinical environments is being performed.

Acknowledgements

My sincerest gratitude to Prof. Ramanarayanan Balachandran, Dr. Midhat Talibi and Dr. Andrea Ducci for the significant guidance and help they have given me during the course of this research degree. The invaluable input given relating to technical understanding, experimental practices, data analysis and presentation, made the work put forward in this thesis possible. Perhaps more importantly, I would also like to thank these individuals, as well as my fellow students and researchers, for the genuine care and comfort shared within our group.

I would like to thank my fiancé Hongyi for her kindness and the much needed reminders that there is a world outside of work. I extend this thanks to the entire He family whom graciously shared their home with me. Finally, but by no means least, I would like to thank my parents and family for their continual love, support and advice, without which none of this would have been possible.

Contents

1	Intr	oductio	n	24
	1.1	Drople	et diameter	26
	1.2	Spray	breakup and droplet formation	26
	1.3	Drople	et evaporation	28
	1.4	Spray/	Droplet diagnostic techniques	35
		1.4.1	Phase Doppler Particle Anemometry	35
		1.4.2	Mie-scattering	37
		1.4.3	Particle Image/Tracking Velocimetry (PIV/PTV)	38
		1.4.4	Planar Laser Induced Fluorescence (PLIF) and Ratiometry	
			(LIF/Mie)	39
		1.4.5	Laser Diffraction	41
		1.4.6	Planar Interferometric Droplet Sizing	42
	1.5	Liquid	droplet evaporation	
		measu	rement methods	47
		1.5.1	Application of IDS to evaporating sprays	49
	1.6	Thesis	aims	53
		1.6.1	Chapter layout	54
2	App	lication	of an IDS technique to ethanol-gasoline fuel blends	56
	2.1	Chapte	er outline	57
	2.2	Introdu	action to droplet sizing in bio-fuel sprays	57
	2.3	Experi	mental Methodology	59
		2.3.1	Principle of interferometric techniques	59

10 Contents

		2.3.2	TSI Instruments GSV system	50
		2.3.3	Spray test facility	64
		2.3.4	Fuel blends	65
	2.4	Data re	eduction and analysis	66
	2.5	Valida	tion of GSV technique and measurement uncertainty	70
	2.6	Result	s and discussion	73
	2.7	Conclu	asions	80
3	Deve	elopmei	nt of a interferometric droplet tracking method	82
	3.1	Chapte	er outline	83
	3.2	Introdu	action to droplet tracking	83
	3.3	Curren	nt planar interferometric sizing and velocimetry methods 8	86
	3.4	Drople	et Tracking Expansion	87
		3.4.1	First pass processing with GSV	88
		3.4.2	PIT processor stage 1	90
		3.4.3	Processor stage 2	91
	3.5	Incorre	ectly-measured and unrecognised interference patterns 9	92
		3.5.1	Positioning droplets	93
		3.5.2	Application of focused interrogation	96
		3.5.3	Focused Interrogation Window	97
	3.6	Measu	rement uncertainty and performance)3
		3.6.1	Tracking diameter measurement uncertainty)3
		3.6.2	Tracking diameter uncertainty	10
		3.6.3	Tracking position uncertainty	12
		3.6.4	Tracking performance	13
	3.7	Summ	ary	14
4	Inte	rferome	etric droplet tracking to an evaporating spray	17
	4.1	Chapte	er Outline	18
	4.2	Introdu	action to methanol	18
	4.3	Experi	mental Setup	19

Contents	11	1

		4.3.1 PIT setup	
	4.4	Experimental conditions	
		4.4.1 Methanol evaporation model	
	4.5	Droplet tracking results	
	4.6	Conclusion and assessment of PIT performance	
5	Effe	ects of acoustic forcing on droplet evaporation 140	
	5.1	Chapter outline	
	5.2	Introduction to acoustic evaporation enhancement	
	5.3	Experimental Setup	
	5.4	Test Conditions	
	5.5	PIT performance	
	5.6	Droplet velocity response to acoustic forcing	
	5.7	Convection evaporation enhancement	
	5.8	Spray evaporation characterisation	
		5.8.1 Spray geometry and droplet concentration 165	
		5.8.2 Mass flux of droplets	
		5.8.3 Mean droplet diameter	
	5.9	Conclusion	
6	Cha	racterisation of droplet flows produced during expiration 175	
	6.1	Chapter outline	
	6.2	Introduction to Covid Studies	
	6.3	Methodology	
		6.3.1 Laser and Camera setup	
		6.3.2 Experimental Rig	
		6.3.3 Validation of droplet detection	
	6.4	Image Analysis	
	6.5	Data Analysis	
	6.6	Error and Uncertainty	
	6.7	Results and discussion	

12 Contents

		6.7.1	Time evolution	192
	6.8	Drople	t number	195
	6.9	Drople	t evaporation	198
	6.10	Conclu	ısion	200
7	Sum	mary o	f conclusions and future work	204
	7.1	Engine	eering impact	205
	7.2	Chapte	er conclusions	206
		7.2.1	IDS characterisation of ethanol-gasoline fuel sprays	206
		7.2.2	Development of Planar Interferometric Tracking (PIT) pro-	
			cessor	208
		7.2.3	PIT measurement of droplet diameter in evaporating spray	209
		7.2.4	Impact of droplet slip velocity of evaporation and charac-	
			terisation of slip velocity-diameter relation through the use	
			of PIT	211
		7.2.5	Optical characterisation of human produced droplet flows	214
	7.3	Future	Work	215
Bil	bliogr	aphy		219
Lis	st of p	ublicat	ions	236

List of Figures

1.1	Comparison between measured and modelled droplet entrainment	
	factor, η plotted against Stokes number, St , (Sujith et al., 1997)	31
1.2	Diagram showing basic IDS optical configuration (Glover et al.	
	(1995))	43
1.3	Images of droplets (a) without vertical compression (b) with vertical	
	compression (Kobayashi et al. Kobayashi et al. (2000))	44
1.4	Superimposed images of in-focus and out of focus IDS images. The	
	difference between glare point and oscillation pattern centre points	
	displaying centre discrepancy variation with droplet radial position	
	within image (Hardalupas et al., 2010)	46
1.5	IDS Lagrangian Tracking method produced by Kawaguchi et al. (a)	
	Droplet trajectories in heated flow (Kawaguchi, 2012), (b) individ-	
	ual ethanol droplet diameter reduction over timeKawaguchi et al.	
	(2010)	51
2.1	Diagram showing interferometric principles	59
2.2	(a) Glare points at focus, (b) Interference oscillation with slit aper-	
	ture at 8.55 mm defocus	60
2.3	Side view diagram of spray cross section with selected viewing win-	
	dow	61
2.4	Top view diagram of spray cone section, with (Camera position 1)	
	left side imaging and (Camera position 2) right side imaging	62
2.5	Vertical compression of interference pattern using slit aperture	63

2.6	Schematic of spray test facility (P-pressure gauge, PR-pressure	
	transducer, PFI-Port Fuel Injector)	65
2.7	(a)Low intensity indistinct oscillation patterns erroneously recog-	
	nised as small droplet (19.8 μ m), (b) Oscillation patterns show-	
	ing two frequencies, red outline showing the fringes from one fre-	
	quency, each containing 'sub-fringes' from a second frequency,	
	(c) Oscillation patterns containing multiple frequencies being er-	
	roneously measured as a large droplet diameter (207.6 $\mu\text{m}).$	67
2.8	Frequency distribution of droplet diameters with MPSPR variation	68
2.9	Superposed Probability distributions of droplet number (black) and	
	volume (red), expressed as a percentage of overall number and total	
	volume respectively, for E100	69
2.10	GSV measurements of droplets produced from FMAG set to pro-	
	duce droplets 65.6 μ m in diameter	71
2.12	D_{10} variation with sample number	72
2.11	Frequency distribution of FMAG droplets measured by GSV, corre-	
	sponding to table 2.2, page 72, where the FMAG set droplet diam-	
	eter is equal to (a) 71.3 μ m, (b) 65.6 μ m, (c) 62.0 μ m and (d) 52.0	
	μm	73
2.13	superposed Probability distributions of droplet number (black) and	
	volume (red) for a) E100, b) E80, c) E60, d) E50, e) E40, f) E30,	
	g) E20, h) E15, i) E10, j) E0, expressed as a percentage of overall	
	number and total volume respectively	74
2.14	Droplet radial (X) and axial (Y) position with size: $D_{10} < 30 \ \mu \text{m}$	
	(Red), 30 μ m < D_{10} < 150 μ m (Green), D_{10} > 150 μ m (Blue)	75
2.15	Droplet proportion with variation in radial position (X) for: D_{10} <	
	$30~\mu\mathrm{m}$ (Red), $30~\mu\mathrm{m}$ < D_{10} < $150~\mu\mathrm{m}$ (Green), D_{10} > $150~\mu\mathrm{m}$ (Blue).	75
2.16	Variation in (a) Frequency and (b) D_{10} , with axial and radial dis-	
	placement from the nozzle	77
2.17	Droplet radial distribution variation with ethanol content	78

2.18	D_{32} (Red-circle) and D_{10} (Blue-triangle) values with ethanol con-	
	tent (%)	78
2.19	Droplets identified per image (Red) and proportion of droplets be-	
	low 30 μ m (Blue) for fuel blends	79
3.1	(a) GSV setup top view, (b) GSV setup side view	87
3.2	Example GSV image (cropped) with sizing	88
3.3	Flow chart showing interferometric droplet tracking processor al-	
	gorithm. (Blue) Droplet tracking from GSV droplet data, (Pur-	
	ple) Re-analysis of interference patterns incorrectly measured or	
	unrecognised by GSV processor, (Yellow) Re-analysis of droplets	
	backwards in time	89
3.4	(a) Two frame composite GSV image, $Image_n$ (Green), $Image_{n+1}$	
	(Magenta), with inspection region (Red) located about $Drop_n(x,y)$.	
	(b) Inspection region dimensions	90
3.5	Example of incorrect measurement/detection of interference pat-	
	terns. $Image_n$ (Green), $Image_{n+1}$ (Magenta) and $Image_{n+2}$ (Cyan)	93
3.6	Diagram showing image defocus optical geometry for calculation	
	of image dewarp.	94
3.7	Focused inspection window for interference pattern re-analysis	98
3.8	Mean row pixel intensity for focused inspection region	99
3.9	Focused inspection region slice located about interference pattern	
	vertical centre	99
3.10	CWT Magnitude scalogram for single interference pattern, regions	
	labeled (a.) and (b.) showing response to interference pattern length	
	and interference pattern fringes respectively.	100
3.11	Focused inspection region slice located about interference pattern	
	vertical centre	101
3.12	(a) Focused inspection region slice normalised mean column pixel	
	intensity (NPI) with Hamming taper. (b) Spatial period (Fringe	
	Spacing)	101

3.13	Droplet camera orientation resulting in droplet defocus uncertainty.	
	Blue droplet representing the processor assumed defocus and grey	
	droplets representing potential extreme defocus positions	04
3.14	Final-to-initial droplet surface area ratio for non-evaporating spray,	
	markers showing experimental data. Dashed lines showing ex-	
	pected error due to defocus variation with laser thickness transit	
	for sheet of thickness: 2 mm (Blue), 1.5 mm (Red), 1.0 mm (Green). 1	06
3.15	(a) Diagram showing three droplets (Dark Blue, Light Blue and	
	Red) transiting laser sheet thickness due to their out of plane ve-	
	locity, W , (b) Proportion droplet surface area versus time for the	
	three droplets	07
3.16	Example of droplet diameter measurement variation due to mea-	
	surement for five droplets	08
3.17	Difference between GSV and Tracking diameter measurement with	
	respect to droplet (a) radial location (b) axial location	11
3.18	Difference between GSV and Tracking diameter measurement with	
	respect to droplet diameter	12
3.19	Difference between GSV and Tracking radial position measurement 1	13
3.20	Droplet volumetric concentration with time for GSV data only	
	(Red) and GSV and additional PIT data (Blue)	15
4.1	Sketch of the experimental setup. (a) Sonics Atomizer, (b) Cooling	
	air coupling, (c) Heated air coupling, (d) Heated air inlet thermo-	
	couple, (e) Cooling air thermocouple, (f) Laser Sheet, (g) LASER-	
	PULSE light arm head, (h) Laser sheet height (100 mm), (i) Phan-	
	tom VEO 710 camera, (j) Measurement Volume, (l) Downstream	20
	thermocouple, (k) 3-axis traverse	2 U

121
122
126
131
132
134
135
136
137

5.1	Diagram of optical rig with (a) upper and (b) lower dynamic trans-
	ducers installation positions and (c) speaker mounting point 145
5.2	Acoustic pressure amplitude at forcing frequency for, 0 Hz (Black),
	100 Hz (Blue), 257 Hz (Green) and 400 Hz (Orange). Amplitude
	measurement at lower transducer (\blacktriangle) and upper transducer (\blacktriangledown) 146
5.3	Diagram showing pressure variation for harmonic standing waves
	produced at 100 Hz (Blue), 257 Hz (Green) and 400 Hz (Orange)
	forcing frequencies
5.4	Example of position variations of PIT tracked droplets with an ap-
	plied acoustic forcing frequency of 257 Hz at an acoustic velocity
	amplitude of 2.96 m/s. (0,0) co-ordinate relates to image centre,
	positioned at the radial centre of the spray, 140 mm axially down-
	stream of the nozzle tip. Colourbar shows droplet instantaneous
	axial velocity, number label placed at the droplet staring position
	represents mean droplet diameter in microns
5.5	Mean subtracted instantaneous velocity $(u_d - \bar{u_d})$ for all droplets
	within the measurement volume against time for water with acous-
	tically forced at 257 Hz with an acoustic velocity amplitude of 2.96
	m/s, colourbar showing droplet diameter
5.6	Water droplet diameter against velocity amplitude at acoustic forc-
	ing frequency for (a) 257 Hz and (b) 400 Hz and air temperature of
	288 K, acoustic velocity amplitude shown by label. Note: Velocity
	Amplitude scale change
5.7	Droplet diameter against velocity amplitude at acoustic forcing fre-
	quency 100 Hz for Methanol at 338 K (Blue), 369 K (Green), 402
	K (Magenta), 486 K (Red) and Water at 288 K (Black)
5.8	Inverse droplet diameter squared versus entrainment factor (η) at a
	forcing frequency of 257 Hz at acoustic velocity amplitudes of 0.83
	m/s (Blue), 1.53 m/s (Red), 2.26 m/s (Yellow), 2.96 m/s (Purple)
	and 3.47 m/s (Green)

5.9	Droplet diameter versus entrainment factor (η) at forcing frequen-
	cies 100 Hz (Blue), 257 HZ (Green) and 400 Hz (Orange). Data
	points represent data from a range of forcing amplitudes at each
	forcing frequency as is shown in table 5.1
5.10	Stokes number (St) (equation 5.2) plotted against entrainment factor
	(η) at forcing frequencies 100 Hz (Blue), 257 HZ (Green) and 400
	Hz (Orange). Data points represent data from a range of forcing
	amplitudes at each forcing frequency as is shown in table 5.1 156
~ 1.1	
5.11	, , , , , , , , , , , , , , , , , , ,
	(η) at forcing frequencies 100 Hz , 257 HZ and 400 Hz. Colourbar
	showing forcing acoustic velocity amplitude
5.12	Droplet diameter versus entrainment factor (η) at 257 HZ forcing
	frequencies. Colours showing range of acoustic velocity amplitudes
	(u'_a)
5.13	Mean axial velocity variation with droplet size, bin size 15 μ m, and
	increasing forcing amplitude, 0 m/s (\times), 0.16 m/s (\ast), 0.33 m/s (\bigcirc),
	$0.48 \text{ m/s (+)}, 0.61 \text{ m/s (\triangle)}, 0.71 \text{ m/s (\square)}. \dots \dots$
F 1 4	
5.14	Methanol droplet mean evaporation rate κ versus diameter at start
	of measurement volume, D_M , with no acoustic forcing (—), and
	acoustically forced at 100 Hz, an amplitude of 0.48 m/s (), for
	air flow temperatures of 338 K (Blue) and 486 K (Red) 163
5.15	Modelled methanol droplet evaporation rate enhancement (%), due
	to the convection associated with a flow forced at 100 Hz, an ampli-
	tude of 0.48 m/s for air flow temperatures of 338 K (Blue) and 486
	K (Red)

5.16	(a) Methanol droplet sample size with acoustic forcing ampli-
	tude,(b) Mass flow rate, \dot{m} , of measured methanol droplets through
	measurement volume with acoustic forcing amplitude, (c) Mass
	flow rate reduction relative to 338 K conditions ($\Delta \dot{m} = \dot{m}_T - \dot{m}_{338K}$)
	at 100 Hz and temperature, 338 K (\bullet), 369 K (\blacksquare), 402 K (\blacklozenge), 486
	$K(\bigstar)$
5.17	Droplet diameter histogram for an unforced (Blue) and forced
	(Red), (100 Hz 0.48 m/s) conditions where air flow temperature is
	(a) 338 K, (b) 369 K, (c) 402 K, (d) 486 K
5.18	Mass contribution of droplets for an unforced (Blue) and forced
	(Red) (100 Hz 0.48 m/s) conditions where air flow temperature is
	338 K
5.19	Mean droplet diameter, D_{10} , with radial displacement, X, at air flow
	temperatures (a) 338 K, (b) 369 K, (c) 402 K and (d) 486 K at a
	forcing frequency of 100 Hz and acoustic velocity amplitudes of,
	0.0 m/s (×), 0.16 m/s (*), 0.33 m/s (\bigcirc) and 0.48 m/s (+) 170
5.20	Mean droplet diameter, D_{10} , with axial position, at air flow temper-
	atures (a) 338 K, (b) 369 K, (c) 402 K and (d) 486 K at a forcing
	frequency of 100 Hz and acoustic velocity amplitudes of, 0.0 m/s
	(×), 0.16 m/s (*), 0.33 m/s (\bigcirc) and 0.48 m/s (+) 171
6.1	a) Top view showing laser sheet and camera alignment, b) Side view
	of laser sheet alignment, with i.), high speed camera, ii. 50 mm lens
	with Scheimpflug adapter, iii. participant, iv. laser sheet, v. spray
	produced by participant and vi. laser direction
6.2	Laser safety booth and laser/camera traverse
6.3	Composite image for all frames captured during: a) exhalation, b)
	singing a note from two different participants
6.4	Histogram of individual droplet velocities determined through PTV
	for a participant singing a note

6.5	Variation in mean droplet velocity magnitude with distance from the
	mouth. Individual participant data displayed by markers, with over-
	all means shown by lines. Unmasked tasks shown as yellow/red,
	masked (where applicable) shown by blue/green 190
6.6	Droplet velocity magnitude inter-quartile range for tasks, markers
	showing individual participant ranges
6.7	Comparison of PIV and PTV mean velocity magnitudes with vari-
	ation in distance from the mouth, for the same participant exhaling
	(Red) and saying 'Hello' (Blue) with and without a mask 192
6.8	Variation in proportion of droplet number with distance from
	mouth, for unmasked and masked exhalation
6.9	Time with above noise level droplet densities for each task and par-
	ticipant
6.10	Example droplet density time evolution for: a) Exhale, b) 'Hello',
	c) 'Snake' and d) singing a note
6.11	Droplet density time evolution for a single participant performing:
	a) Exhale and b) Exhale with mask
6.12	a) Time averaged droplet density and b) Instantaneous maximum
	droplet density for all tasks and participant. Unfilled markers high-
	lighting data points where fewer than 200 frames contained above
	noise level droplet densities
6.13	Percentage reduction in (a) time averaged droplet density and (b)
	instantaneous maximum droplet density for all tasks with mask use. 198
6.14	Mean velocity magnitude for entire processing window against time
	averaged droplet density

List of Figures

6.15	(a) Axial velocity distributions for measurement volume located at	
	100 mm downstream of nozzle tip (Red) and 500 mm downstream	
	of nozzle tip (Blue). Droplet size distributions for measurement	
	volume located at (b) 100 mm downstream of nozzle tip, (c) 500	
	mm downstream of nozzle tip and (d) overlay of normalised distri-	
	butions for both measurement positions	.03

List of Tables

1.1	Popular bio-fuel component liquid properties at atmospheric pres-
	sure, Serras et al.Serras-Pereira et al. (2009)
2.1	Fuel blend properties at 20°C. ¹ Khuong et al. (2017), ² Wang et al.
	(2006)
2.2	Comparison of droplet diameters from Flow-Focusing Mono-
	disperse Aerosol Generator and GSV measurement
3.1	Calculated proportional droplet surface area change due to out of
	plane velocity at image centreline
4.1	Calculated proportional droplet surface area change due to out of
	plane velocity at image centreline
4.2	Expected error due to rate of defocus change for given droplet resi-
	dence times
4.3	Expected rate of proportion droplet surface area reduction for given
	initial droplet diameters
5.1	Two microphone method pressure (P) and axial velocity (U) ampli-
	tude estimations at the measurement volume axial centrepoint for
	all acoustic forcing conditions
5.2	Goodness of fit (R^2) for data recorded at 257 Hz forcing frequency. 154
5.3	Constants for equations 5.11 and 5.13 (Faghri and Zhang, 2006) 161
5.4	Mean droplet diameter increase (ΔD_{10}) with axial displacement
	from measurement volume top to bottom (≈20 mm) 172

Chapter 1

Introduction

The research of sprays and multi-phase flows stands to benefit numerous industries where sprays are fundamental in their function. These industries vary from agriculture, to pharmaceuticals, material production, health care, energy production and propulsion. It is in-fact hard to think of an industry that does not in some form involve the use of sprays, thus many research groups have dedicated their time to characterising the mechanisms involved. Despite the large amounts of work put into this field, the complexity of the subject and difficulty in performing observations means there is still much to be understood. As the application of sprays becomes evermore complex and improved efficiency and performance becomes increasingly valued, our understanding of the fundamental mechanisms is tested further. By breaking these problems down into their constituent elements and tackling the problem parametrically a foundation of understanding will develop.

Within experimental research, advancement is often dependant on the improvement and development of measurement methods. Each spray diagnostic technique has its benefits and compromises, as such having an understanding of the capabilities of these techniques allows industry and research scientists to know when and where to apply specific diagnostic methods. Within spray diagnostics optical techniques dominate due to their high fidelity, the wide range of techniques on offer and the vast amount of historical data and testing. With the development of higher resolution digital cameras, laser technologies and processing power, the number of techniques used in spray characterisation has grown significantly within recent decades.

Despite the advancements made, there are still a number of significant limitations in the current experimentalist's toolbox. With empirical data being the backbone of research, these restrictions not only limit experimental studies but also limit the capabilities of numerical modelling. The development and novel application of measurement methods is therefore paramount to a systemic improvement in our understanding of spray mechanisms.

The main focus of this work relates to the use and development of a planar optical measurement method and its specific application to the characterisation of

liquid fuel sprays. However, as a result of the COVID-19 epidemic, a significant amount of work was performed in the measurement and characterisation of human produced aerosols for the purposes of better understanding the spread of infectious respiratory diseases. This work is self-contained within a stand-alone chapter, having its own brief literature review.

1.1 Droplet diameter

In spray diagnostics there are an array of parameters that are consistently outlined as having key significance across various spray applications. These include spray geometry (e.g. cone angle, patternation and penetration length), mass flux, droplet velocity (axial, radial and tangential components) amongst many others. Perhaps the most fundamental metric of spray performance is the size distribution of droplets. In agriculture droplet diameter will dictate whether a crop-spray will deposit correctly or be entrained within local air currents, causing potential environmental damage (Maybank et al., 1978), in the food and pharmaceutical industry the size distribution of droplets produced in the spray drying process will dictate the final particle size (Thybo et al., 2008), and in the combustion of liquid fuels, droplet diameter directly influences fuel vaporisation rates, flame formation and propagation. Thus particular importance is placed on understanding the mechanisms dictating the evolution of droplet diameter.

1.2 Spray breakup and droplet formation

There are a number of mechanisms that result in the 'atomisation' of a liquid jet forming a spray, though for simplicity a liquid atomiser is a device which introduces disturbances to a liquid flow, leading to liquid breaking down into smaller droplets. Different atomisers make use of different methods to introduce the initial disturbances within the flow, some rely on turbulence within the flow, others using high frequency mechanical oscillations like those in ultrasonic atomisers, whilst others operate on entirely different principals such as electrostatic atomisers, where droplets form as a result of electrostatic repulsion. The breakup process often happens in multiple phases commonly referred to as primary and secondary,

where larger droplets, often non-spherical ligaments break down further to smaller droplets until reaching their final form. The final size of droplets in the atomisation process is determined by the point of equilibrium between forces promoting increased breakup, resulting from flow turbulence and aerodynamics shear, and forces resisting further division, primarily surface tension.

Thus liquid properties, in particular the surface tension and viscosity directly influence the atomisation process, understanding this being of fundamental importance in a number of spray applications, an example of which is that of fuel sprays given the increasing use of various fuel types and blends. Dorfner et al. (1995) observed that increases in both surface tension and viscosity increased droplet diameters. Ejim et al. (2007) stated that increases in viscosity had a more significant impact, accounting for approximately 90% of observed changes in diesel and biodiesel spray mean droplet diameter. As many bio-derived fuels used to reduce pollutant and greenhouse gas production have viscosity greater than those of traditional fossil fuels (Serras-Pereira et al., 2009), there is a need to properly characterise and define the interaction between liquid properties and the size of droplets produced in fuel sprays.

Fuel Properties	Ethnaol	Butanol	Gasoline	Iso-Octane
Desnity [kg/m ³] (20°C)	0.794	0.809	0.729	0.692
Viscosity [cP] (25°C)	1.08	3.64	0.4-0.8	0.51
Surface Tension [mN/m] (20°C)	22.4	25.4	25.8	14.7
Latent Heat [MJ/kg] (25°C)	0.902	0.430	0.364	0.305
Boiling Point [°C]	78.5	117.2	30-190	99.8
Reid Vapour Pressure [bar]	0.16	0.02	0.56	0.14

Table 1.1: Popular bio-fuel component liquid properties at atmospheric pressure, Serras et al. Serras-Pereira et al. (2009).

Beyond the point of initial breakup, droplet diameters can still change through a number of mechanisms. Should two or more droplets within a spray collide there is the potential for either the further breakdown to a greater number of smaller droplets or for them to coalesce forming fewer larger droplets. The likelihood of either these occurrences is dependent on a number of parameters, including droplet volumetric concentration and velocity, ambient gas pressure and density, liquid properties such as surface tension and viscosity as well as the relative quantity of surface contaminants (Orme, 1997). The complexity and 'random' nature by which the collision and interaction of droplets may occur means the assessment of droplet size change due to collision is more than often performed on a case by case basis, with little evidence for a general model being found in research.

1.3 Droplet evaporation

In all sprays the size of droplets will reduce with time due to evaporation, though the degree by which droplets will reduce in size over an applicable time scale often leads to a spray being assessed as either an evaporating or non-evaporating spray.

Droplet evaporation plays a key role in numerous industrial spray applications, such as fuel sprays in combustion and spray drying in pharmaceuticals, as well as being a critical factor in areas of research, such as the modelling of disease transport through human produced aerosols. In each of these example scenarios the relevant ambient conditions and evaporation timescales differ, however the fundamental principles and mechanisms dictating droplet evaporation remain the same. The classical model for the evaporation of a single droplet, described by Spalding (1950) shows droplet surface area to linearly reduce over time, with the rate of surface reduction being determined by the associated evaporation constant, κ , this relation being known as the D^2 law, Equation 1.1.

$$D_0^2 - D^2 = \kappa t \tag{1.1}$$

Where D is the droplet diameter at time, t and D_0 is the initial droplet diameter. The evaporation rate is controlled by the properties of both the liquid and ambient gas, this being apparent when evaluating κ for quasi-steady evaporation in a quiescent atmosphere.

$$\kappa = \frac{8k\ln\left(1+B\right)}{c_p\rho} \tag{1.2}$$

where k and c_p are the thermal conductivity and specific heat of the vapourgas 'cloud' surrounding the droplet respectively, ρ is the liquid density and B is a function of c_p , latent heat of liquid vaporisation, L, and the relative difference between ambient gas and vapour-gas cloud temperatures, T_{∞} and T respectively.

$$B = \frac{c_p \left(T_{\infty} - T \right)}{L} \tag{1.3}$$

Thus it can be seen that even for a simplified model of a single droplet in idealised conditions evaporation is dependent on a large number of variables. In more realistic scenarios better representing droplet evaporation in sprays a number of additional mechanisms dictating the rate of droplet evaporation must be considered. One such complication arrives when droplet volumetric concentrations are such that interactions between their respective vapour clouds must be considered. Studies such as those performed by Labowsky (1976) and Volkov et al. (2016) have shown that even at modest droplet concentrations evaporation rate is reduced, and further decreases as droplet concentrations are increased. In spray applications such as liquid fuel atomisation and combustion, where droplet concentrations are typically relatively high this phenomenon can have significant implications. Indeed Chiu and Liu (1977); Chiu et al. (1982) theorised that inter-droplet spacing is a key parameter in dictating combustion and flame characteristics, defining a non-dimensional group combustion value, G,

$$G = 3\left(1 + 0.276Re^{\frac{1}{2}}Sc^{\frac{1}{3}}\right)LeN^{\frac{2}{3}}\frac{\bar{D}}{2s}$$
 (1.4)

where Re, Sc, Le, N, \bar{D} and s are the flow Reynolds, Schmidt and Lewis numbers, number of droplets and inter droplet spacing respectively. At large values of G, droplet volumetric concentrations are such that combustion and vaporisation do not occur within the core of the spray, rather the flame envelopes the droplets, only oxidising fuel vapour located at the droplet cluster periphery. As the value of G decreases, combustion and evaporation within the droplet cluster can occur, and

at sufficiently low value of G all droplets will be seen to evaporate and combust individually. Given the intrinsic link between droplet oxidation and flame formation with emission production, evaporation models and experimental measurement methods used in the development of fuel sprays must consider the influence of spray characteristics relating to the spatial distribution of droplets. Thus, along with liquid properties directly controlling individual droplet evaporation, spray characteristics such as cone angle and droplet diameter (viscosity and surface tension) will influence droplet evaporation in realistic spray scenarios.

A further mechanism to consider in droplet evaporation under realistic conditions, relates to convective heat transfer due to the difference between droplet and gas velocities, commonly termed "slip-velocity". As the relative velocity between droplet and gas is increased, heat and vapour mass transfer to and from the droplets are enhanced, increasing the rate of evaporation. In most practical applications the droplet-gas slip velocity is not constant due to turbulent flow fields and/or acoustic pressure induced flow oscillations. In such conditions the droplet-gas slip velocity is dependant on the entrainment factor, η , of droplets within the gas flow, often defined as the ratio of droplet/particle velocity, u_D' and gas velocity, u_g' , Equation 1.5. A common tool in defining the level of entrainment of droplets within a flow field is through the definition of a non-dimensional number known as Stokes number, as was performed by Hjelmfelt and Mockros (1966), where the stokes number, St was defined as,

$$\eta = \frac{u_D'}{u_g'} \tag{1.5}$$

$$St = \sqrt{\frac{v}{\omega D^2}} \tag{1.6}$$

where v is fluid kinematic viscosity and ω is turbulence eddy/acoustic angular frequency. This measure of entrainment was shown to be in good agreement with experimental measurements of single droplet entrainment in an axially acoustically forced flow, Figure 1.1. Hjelmfelt and Mockros further described the phase difference between droplet/particle and fluid velocity oscillations, where by droplet-

gas phase difference increases with increasing droplet diameter and flow field frequency. These models and studies show that when within an oscillating flow-field, the instantaneous velocity differential between droplets and gas is a function of the ratio of fluid to particle density, flow field velocity frequency and amplitude and the particle diameter. These findings can be summarised by stating that smaller droplets display increased entrainment, thus reduced velocity differential. In further studies, Sujith et al. showed that single droplet evaporation was seen to be enhanced in the presence of an acoustically oscillating flow and Balachandran et al. (2008) observed that the presence of acoustic pressure fields increased droplet evaporation in water sprays.

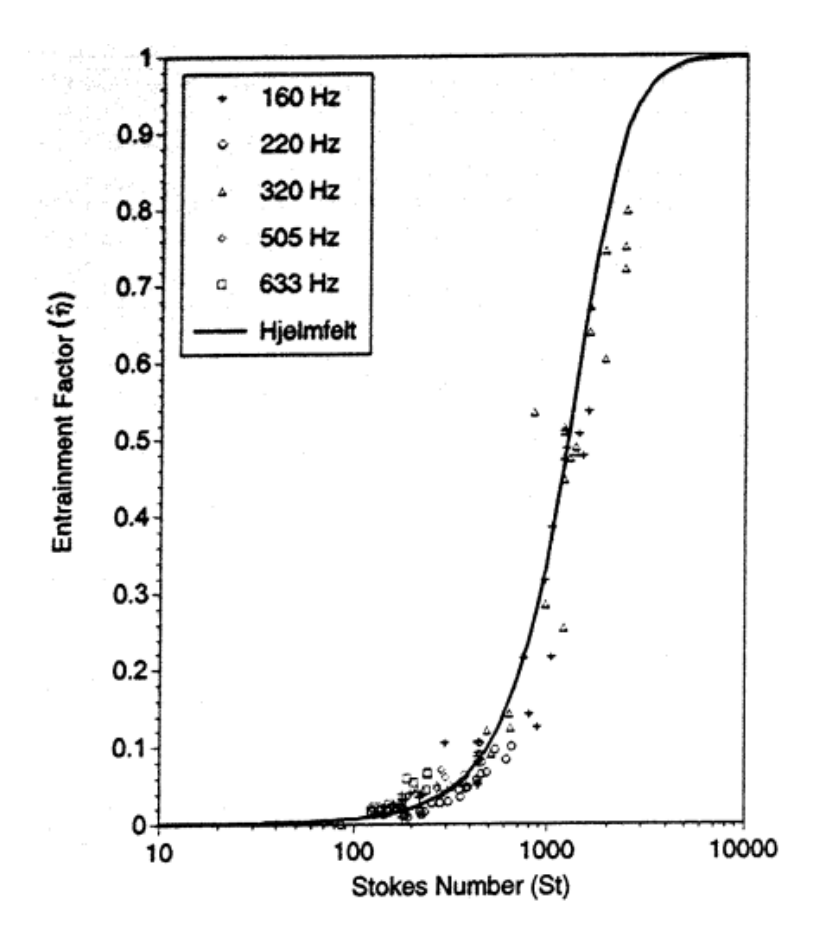


Figure 1.1: Comparison between measured and modelled droplet entrainment factor, η plotted against Stokes number, St, (Sujith et al., 1997).

In a number of industrial applications the use of acoustic fields in enhancing droplet evaporation has many potential benefits, one of which is the spray drying

process. Typically spray drying facilities either use a co-current or counter-current air flow, where heated air flows are in the same or opposite direction of droplet emission from the atomiser respectively. Due to higher relative velocities between droplet and heated gas flows, as well as an increased residence time within the drying chamber, counter-current systems have a higher thermal efficiency (Santos et al., 2018). However, in applications involving temperature sensitive materials, such as those commonly found in the pharmaceutical and food industries, the increased residence time can cause particles to be overheated, thus co-current systems are predominantly used in these applications despite the reduced thermal efficiency. Using an acoustic flow field to enhance droplet evaporation when drying could reduce air temperature requirements, improving thermal efficiency and reducing the potential damage to temperature sensitive materials (Bänsch and Götz, 2018). However, the presence of turbulence and/or acoustic oscillations has also been seen to cause droplets to accumulate into clusters, increasing the local droplet volumetric concentration. A number of studies attempted to characterise the interaction of parameters affecting the clustering of droplet in turbulent flows, and have shown that clustering is particularly affected by the mass fraction of liquid within a gas flow, the gas flow Reynolds number and the stokes number (St) of droplets. A number of these studies report that clustering occurs particularly in droplets for which $St_K \approx 1$, where St_K is defined as the stokes number of a droplet based on the Kolmogorov time scale, τ_K , equations 1.7, 1.8, 1.9 (Ferrante and Elghobashi, 2003; Fessler et al., 1994; Sahu et al., 2018b).

$$St_K = \frac{\tau_D}{\tau_K} \tag{1.7}$$

Where τ_D is the droplet aerodynamic response time and τ_K is

$$\tau_K = \sqrt{\frac{\nu}{\varepsilon}} \tag{1.8}$$

where ε , the rate of viscous dissipation of turbulent kinetic energy, is determined from the gas velocity fluctuation u'_g and l, the integral length scale as defined by Tennekes et al. (1972).

$$\varepsilon = \frac{u_g^{\prime 3}}{l} \tag{1.9}$$

As such though acoustic and/or turbulent flows will enhance the evaporation of droplets through convection, there is also the possibility that droplet evaporation rate will be reduced for droplets located within these clusters due to the interaction between droplet vapour clouds. Thus, to properly characterise the net effect of the presence of a turbulent and/or acoustic flow field on droplet evaporation both factors need to be measured simultaneously.

It is apparent that a large number of factors will affect the evaporation rate of a droplets within a spray, these include parameters directly and indirectly influencing droplet thermal conduction, heat and mass transfer through convection and localised vapour concentration. Certain influential parameters such as droplet slip velocity in a turbulent flow field or the effects of liquid properties on localised droplet volumetric concentration can be characterised in iso-thermal conditions where evaporation is not expected. Much of the work achieved has been focused on simplified conditions, such as single droplet studies, or have reduced observations to average spray properties, resulting from limitations in data processing and measurement methods. However, as the necessity to account for the true complexity grows, existing analysis methods must be improved and applied in novel manners and new techniques providing insight where other do not must be developed.

In these complex systems numerical analysis offers the precise control of relevant factors, allowing parametric analysis in conditions that would pose considerable issues to traditional experimental methods. Numerical studies play an important role in both the development of our understanding of fundamental interaction between droplet and gas in two-phase flows as well as offering a method by which empirically derived models can be applied to specific scenarios. Using Direct Numerical Simulation (DNS) research groups can effectively run virtual experiments to improve the fundamental understanding interactions within multi-phase flows. DNS studies have been used to form models relating droplet evaporation rate to the turbulence scale using a vaporisation Damköhler number, Da_{ν} for both single

droplet and multi-droplet systems by Wu et al. (2003) and Lupo et al. (2020) respectively. The vaporisation Damköhler number is a ratio of the turbulent eddy time scale, τ_{ed} and droplet vaporisation time scale, τ_{v} , equation 1.10 (Gökalp et al., 1992).

$$Da_{v} = \frac{\tau_{ed}}{\tau_{v}} \tag{1.10}$$

The two models put forward by both Wu et al. (equation 1.11) and Lupo et al. (equation 1.12) show a close agreement, in both cases as the Damköhler number increases, droplet evaporation (expressed as a ratio of evaporation rate of turbulent, κ and laminar conditions, κ_l) is decreased. These findings provide a measure of the increase in droplet evaporation rates through convection due to droplet-gas slip velocity resulting from a turbulent flow field. The reduction in evaporation with increasing turbulent eddy timescale (decreasing turbulent eddy frequency) follows the expected trend due to reduced droplet entrainment, as described and validated by Hjelmfelt and Mockros (1966) and Sujith et al. (1997) respectively, (Figure 1.1).

$$\frac{\kappa}{\kappa_l} = 0.771 Da_v^{-0.111} \tag{1.11}$$

$$\frac{\kappa}{\kappa_l} = 0.970 Da_v^{-0.1} \tag{1.12}$$

Numerical models are however dependant on our understanding of the mechanics involved in multi-phase flows and the knowledge of specific parameters for setting the correct boundary conditions. Additionally, in order for numerically derived theories to be implemented, results must be verified by experimental data and as is stated in an annual review of the DNS of droplet laden turbulent flows by Elghobashi (2019), *due to the complexity of turbulent flows laden with droplets or bubbles, the experimental data needed to validate the DNS results are virtually non-existent*. Thus, the use and development of experimental measurement techniques provide the basis for improved numerical modeling, through the development in fundamental knowledge and validation.

1.4 Spray/Droplet diagnostic techniques

In the characterisation of multiphase flows no single technique available is capable of measuring all features. As such researchers make use of a wide range of methods, differing in applications and principles. Knowing where and when particular techniques should be applied and the associated uncertainties and errors is a key skill required of experimentalists. This research degree focuses on the application and development of optical diagnostic techniques. To properly understand these methods, the wider context including other experimental techniques used in research relating to spray diagnostics must be considered.

1.4.1 Phase Doppler Particle Anemometry

Phase Doppler Anemometry (PDA) is one of the most popular droplets measuring techniques due to its ability to measure both droplet velocity and size. This technique was developed from an already existing laser diagnostic technique known as laser Doppler velocimetry (LDV) developed in the late 1960's and early 1970's. As its name suggests this technique was capable of measuring droplet velocities, but in the 1970's many researchers were beginning to also extract droplet size information from LDV setups with modifications (Farmer, 1972). Durst and Zaré (1976) released a paper outlining many of the principles of PDA for both droplet velocity and size measurements. However, is was not until the early 1980's that the PDA technique and hardware was created (Dan Hirleman, 1996). PDA makes use of two intersecting laser beams of the same intensity. The intersection of these two beams forms a volume in which the beams interfere forming an interference fringe pattern of regular light and dark zones. Knowing the wavelength of light being produced by the lasers and the angle at which the beams intersect the spacing between the interference fringes can be defined. When a droplet travels through this volume it scatters the light, and due to the presence of the interference patterns the scattered light varies in intensity as the particle travels through the measurement volume. The varying intensity of scattered light is detected by a photomultiplier tube converting the photon energy to a proportional voltage. The resultant output signal of the light intensity variation over time, as a droplet traverses the measurement volume, shows

a consistent frequency known as the Doppler frequency. The Doppler frequency is a function of the droplet velocity as shown by Equation 1.13, where f_d is the Doppler frequency, V_D is the particle or droplet velocity, λ is the wavelength of laser light and θ is the half angle of intersection for the two laser beams (Albrecht et al., 2013).

$$f_d = \frac{2V_D}{\lambda} \sin \theta \tag{1.13}$$

Using this method alone it is only possible to define the magnitude of the droplet velocity not its direction. To solve this, one of the laser beams has its frequency shifted by a known amount. Now the fringe patterns are no longer static but move continuously across the measurement volume. As such the velocity magnitude and direction of the droplet can be determined. In order to size droplets using PDA at least two PMT sensors are required. The sensors are located at different elevation angles from the scattering plane. The phase difference between the Doppler frequency signal is a function of the droplet diameter. This function varies depending on the predominant form of scatter. Usually, this scattering is from either the reflected beam, first refracted or second refracted beams. For a system set to detect scattered light from the first refraction, the formula to express the phase shift between signals is shown in Equation 1.14, where Φ is the phase shift between the two PMT detectors, D is the particle or droplet diameter, n is the refractive index of the fluid in use, θ is the half angle of intersection for the two lase beams, ε is the elevation angle of the two detectors from the scattering plane and ϕ is the scattering angle (Naqwi et al., 1991).

$$\Phi = \frac{-2\pi D n \sin \theta \sin \varepsilon}{\lambda \sqrt{2 \left(1 + \cos \theta \cos \varepsilon \cos \phi\right) \left(1 + n^2 - n\sqrt{2 \left(1 + \cos \theta \cos \varepsilon \cos \phi\right)}\right)}}$$
(1.14)

Should the phase shift between the signal be larger than 2π a 2-PMT PDA system is not able to distinguish between this particle and a particle smaller by an equivalent phase shift of 2π . As such systems predominately use three PMT sensors, removing the 2π shift source of uncertainty. The key advantage of PDA as a technique is that it is able to measure both the droplet size and velocity, in a single analysis technique. The technique does not require the use of other measurement methods to calibrate

or verify measurements as both velocity and droplet size measurements are absolute. Due to the small size of the measurement volume results are of high spatial resolution, enabling the user to detect small changes in droplet characteristics with varying position in the spray. As data acquisition is instantaneous the temporal resolution of PDA is very high, allowing the user to observe variations in the spray with time, such as those seen in transient conditions or in turbulent/acoustically forced sprays. The small measurement volume however, does have its disadvantages, making it difficult to create a global picture of a spray, thus requiring the integration of many measurement volumes, increasing the time taken to acquire data.

1.4.2 Mie-scattering

Mie scattering is one of the simplest forms of planar imaging, allowing the observation of spray structure, cone angle and in certain instances droplet volumetric concentration. The technique requires the use of a laser sheet and a camera typically orientated at a 90° scattering angle. The intensity of the light scattered from each droplet captured by the camera is approximately proportional to its surface area. When imaging droplets at relatively low volumetric concentrations it is possible to determine the position of individual droplets. To do so typically a blob detection method is employed. This image analysis technique uses an pixel intensity threshold to form a binary image and determines the position and area of pixels connected in groups (which are above the intensity threshold), commonly called blobs. In spray diagnostics these blobs represent individual droplets, the number of detected blobs over a given area within the image can be used to determine the spatially resolved droplet volumetric concentration. In conjunction with high speed imaging this method can be used to analyse the time evolution of droplet concentration as well as the velocity of droplets through the use of Particle Tracking Velocimetry (PTV), this being described in greater detail 1.4.3. When analysing denser sprays, such as fuel sprays, the spatial resolution of optics often does not allow the measurement of droplet volumetric concentration, though the spray characteristics such as cone angle can still be determined. It should be noted that though the intensity of light scattered is proportional to the droplet surface area, the Mie scattering method cannot be used as a single method to determine droplet diameter.

1.4.3 Particle Image/Tracking Velocimetry (PIV/PTV)

The basic concept behind both PIV and PTV is that by capturing two images of a particle flow or spray with a known time delay between image captures and then measuring the displacement of particles or droplets, the velocity can be calculated. In a flow were droplet volumetric concentrations are low enough such that the particle spacing displacement ratio, *p* Equation 1.15, is greater than unity individual droplet can reliably be identified allowing individual droplet to be tracked in a Lagrangian manner, this technique being PTV.

$$p = \frac{\sqrt{\frac{S}{N}}}{\bar{U} dt} \tag{1.15}$$

Where S is the image surface area, N is the number of droplets, \bar{U} is the mean droplet velocity magnitude and dt is the time between image capture (Qian et al., 1991).

In dense sprays (where p < 1) however, it is not possible to identify individual droplets across image captures, as such image analysis methods are used to interpret images and determine the most probable motion of small groups of droplets, these being the fundamental principles of PIV. To do this both images are broken down into smaller interrogation windows, typically ranging from 16×16 to 128×128 pixels. The interrogation windows are assumed sufficiently small that the motion of droplets within the window is uniform. The positions of particles within the interrogation window from the first image is then compared to the new positions within the second captured image. A cross-correlation process, then compares the droplet locations in the two interrogation windows, outputting the displacement of droplets located within the interrogation window. Knowing the displacement shift of droplet and the time between images it is possible to determine a velocity vector for the entire interrogation window (Dabiri, 2006; Keane and Adrian, 1992; Westerweel, 1993).

As a planar measurement methods a key advantage of both PIV and PTV over point measurement systems such as PDA is a large measurement volume. Depending on droplet sizes, spray geometry, droplet concentrations and optical setup, PIV and PTV have the potential to capture large portions of a spray within one image. This reduces data acquisition time and allows the observation of transient flow patterns (Husted et al. (2009)). As with other planar velocimetry techniques, out of plane motion is not accounted for, though stereoscopic PIV methods as put forward by Prasad (2000) can account for this, though add slightly to experimental complexity. Additionally PIV and PTV can be combined with high speed imaging to allowing the observation of droplet and flow velocity temporal evolution. Neither PIV or PTV provide any measure of droplet size, thus in conditions where droplet velocity is likely dependant on droplet size such as in turbulent and acoustic flow fields, PIV/PTV have limited use as a sole measurement method, though can be used effectively to determine flow field velocity variations at high spatial and temporal resolutions, through the observation of fully entrained seeding particles. A further limitation of PIV use in poly-dispersed sprays is that it has a potential bias towards larger droplet sizes due to the increased scattering intensity of larger droplets, as discussed by Gorman and Widmann (2004); Widmann et al. (2001).

1.4.4 Planar Laser Induced Fluorescence (PLIF) and Ratiometry (LIF/Mie)

The first experiments using Laser Induced Fluorescence (LIF) were reported by Tango et al. (1968). LIF takes place when a molecule absorbs light from a laser, increasing the energy state of orbital electrons, the excited electron then drops to its stable ground state and in the process releases a photon Lakowicz (2013). The photon released has a lower energy level to that which excited the molecule initially as such the wavelength of the emitted 'fluorescent' light is longer. In the case of PLIF analysis of sprays, the liquid in use is seeded with a fluorescent dye if no innate fluorescence is present. This liquid/dye is known to absorb the wavelength of light produced by the laser and then emits a known wavelength of light through fluorescence. This signal is first filtered by dichroic filter, eliminating any

wavelength of light not produced from fluorescence, and then detected by a camera. The images captured will show both fluorescence emitted from the liquid/dye contained within the liquid (droplet) and vapour phases. As such PLIF can be used to measure both droplet volume and vapour concentration within regions of a spray, through analysing the intensity of fluorescent light. In sprays with high volumetric concentrations, fluorescence emitted from vapour and liquid phases can become indistinguishable. The use of PLIF to determine the droplet vapour concentrations within a spray has obvious application to the measurement of droplet evaporation and is one of the only way to directly observe the presence and concentration of vapour.

LIF/Mie or Planar Droplet sizing is a technique that combines signals from laser induced fluorescence and Mie scattering of laser light by droplets and was developed by Yeh (1993). LIF/Mie droplet technique is based upon simultaneous use of both PLIF and Mie imaging methods where the intensity of dyed droplets is proportional to the volume and surface area for PLIF and Mie techniques respectively (Charalampous and Hardalupas, 2011). The ratio between both signals can be used to express the Sauter Mean Diameter (SMD), a measure of the average droplet size. Using two identical cameras analysing the same region of spray, this ratio, and thus SMD, can be calculated for each pixel Equation 1.16, where I_{LIF} is the intensity from fluorescence, I_{Mie} is the intensity from scattering and k is a factor determined by calibration (Zimmer and Ikeda, 2003).

$$SMD(x,y) = k \frac{I_{LIF}(x,y)}{I_{Mie}(x,y)}$$
(1.16)

The combination of LIF/Mie techniques allows the capture of a full image of the spray and instantaneously measure spatial droplet diameter distribution within the spray. Being able to characterise a spray from a single viewing window as compared to other techniques which require, in most cases, multiple measurement points, expediates the measurement process (Charalampous and Hardalupas, 2011). Key disadvantages of LIF/Mie is that it requires calibration from either a known spray, such as a droplet generator or by comparing diameter readings with another

technique, such as PDA. The technique is also sensitive to the concentration of fluorescent dye, liquid refractive index and scattering angle in use (Charalampous and Hardalupas, 2011; Zimmer and Ikeda, 2003). LIF/Mie does not measure individual droplets rather it shows a droplet size distribution across the spray and as such it may not be suitable to applications where the sizing of individual droplets and their relation to other parameters is necessary.

1.4.5 Laser Diffraction

Laser diffraction techniques measure the droplet diameter based on the angle at which light is scattered as it interacts with a droplet. A laser is used to illuminate droplets, the scattered light from this light-droplet interaction is then focused by a lens onto a detector consisting of a series of often concentric photosensitive rings. The angle of scatter when light interacts with the droplet is proportional to the droplet size, with smaller droplets producing larger angles of scatter. This measurement can then be interpreted using either the Fraunhofer or Mie scattering theories to calculate the droplet size distribution within a spray. The Fraunhofer theory is simplistic as it assumes that light only interacts with the surface of a droplet. As such the scattering of light is only affected by the surface radius of curvature. Mie scattering theory does not make these assumptions and accounts for other scattering mechanisms such as refraction and absorption. As such Mie theory gives a more complete analysis of droplet sizes when using laser diffraction techniques, however is also sensitive to the droplet optical properties (Merkus, 2009).

Laser diffraction key advantages are its simplicity and ease of use. As a line of site technique that requires the use of only one laser beam and a single detector, this technique is relatively easy to setup and run. Due to this simplicity laser diffraction techniques have been around and in use for a longer period of time, allowing for a well developed and understood measurement technique. The disadvantages of laser diffraction techniques are largely related to its lack of spatial resolution. The technique only outputs a size distribution of droplets within the measurement volume. As this measurement volume is relatively large it is not possible to detect information on the spray structure. Laser diffraction also suffers from significant

signal attenuation, particularly when analysing dense sprays. As explained the technique relies on the difference in scattering angle between large and small droplets, however as the light travels through the spray it does not interact with only one droplet, and as such the scattering angle is a result of several droplets between illuminated plane and sensor, leading to erroneous droplet size measurements (Cossali and Hardalupas, 1992).

1.4.6 Planar Interferometric Droplet Sizing

Interferometric droplet sizing (IDS) measures both the size and location of individual droplets within a spray. Fundamentally this technique revolves around the interference of superimposed reflected and refracted droplet images, produced when capturing images with optics deliberately out of focus. This produces an oscillation pattern for individual droplets, the spacing of which relates to droplet diameter. The principles of this technique were first put forward by König et al. (1986), where single droplet size measurements were obtained from oscillation patterns produced by the scattering of light from a single laser beam. Further investigations were performed by Ragucci et al. (1990) and Hesselbacher et al. (1991), where the equation relating the spacing of fringes within the oscillation pattern to the droplet diameter, D, was expressed, equation 1.17.

$$D = \frac{2\lambda N}{\alpha} \left[\cos\left(\frac{\theta}{2}\right) + \frac{n\sin\left(\frac{\theta}{2}\right)}{\sqrt{n^2 + 1 - 2n\cos\left(\frac{\theta}{2}\right)}} \right]^{-1}$$
 (1.17)

Where θ is the angle between the laser plane and focused lens plane, α is the aperture angle, λ is the laser wavelength, N is the number of fringes within an oscillation pattern and n is the refractive index of the fluid in use.

As is shown in Equation 1.17, the accuracy of droplet diameter measurement is reliant on correct evaluation of droplet refractive index. As is described by Calabria and Massoli (2000) this can limit the applicability of IDS techniques when monitoring droplets with internal variations in refractive index. As such, Calabria and Massoli determined that at a scattering angle of $(\theta =)$ 60°, droplet diameter mea-

surements are effected minimally by droplet refractive index (maximum variation from actual droplet size of 4%). This finding has particular importance in the measurement of droplet vaporisation at high temperature, where temperature gradients within the droplet cause internal variations in refractive index.

Further development of the technique was achieved by Glover et al. (1995), who made measurements in a sparse spray, determining both the position and diameter of droplets located on a laser illuminated plane, using an optical setup similar to that in use by most current IDS techniques, Figure 1.2. Glover et al. also suggested to combine this planar IDS technique with high speed imaging to additionally determine droplet two-component instantaneous velocity in a similar fashion to PIV and PTV techniques, this now being available in many commercial IDS methods.

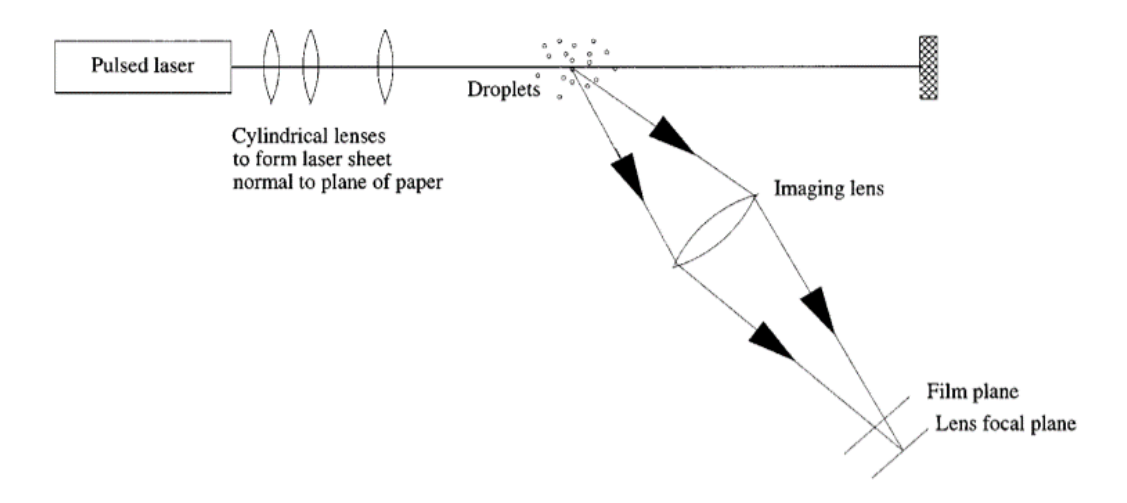


Figure 1.2: Diagram showing basic IDS optical configuration (Glover et al. (1995)).

The IDS technique has been applied to increasingly complex systems including in cylinder measurements of fuel spray evaporation during the intake and compression strokes of a reciprocating engine by Skippon and Tagaki (1996). Improvements in optical equipment, including the increased availability of higher resolution CCD and CMOS imaging sensors, and more powerful computing capabilities led to further improvements in IDS techniques. Kobayashi et al. (2000) used a slit aperture mounted in front of collecting optics to vertically compress oscillation patterns, reducing the occurrence of overlap increasing the upper limit of volumetric droplet concentration for reliable measurements (figure 1.3).

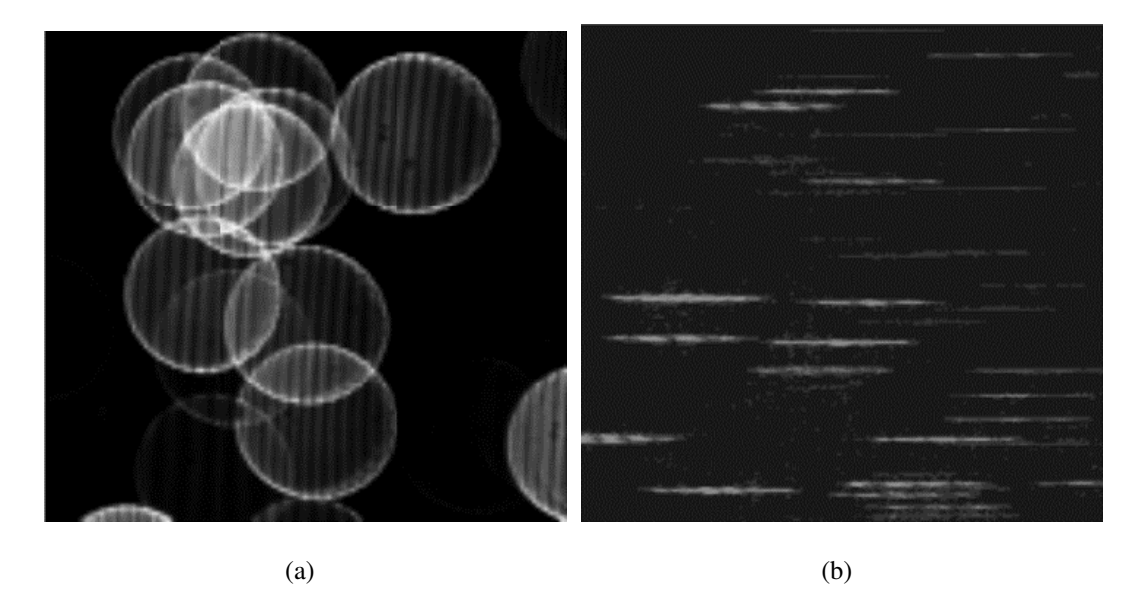


Figure 1.3: Images of droplets (a) without vertical compression (b) with vertical compression (Kobayashi et al. Kobayashi et al. (2000)).

In the same work Kobayashi et al. and in a further study, Kawaguchi et al. (2002), improved the detection and processing time of oscillation patterns present in images primarily through the use of FFT to determine the spacing of fringes within oscillation patterns. This method was seen to correctly detect 90% of droplets within captured images, analysing 300 oscillation patterns in 30 seconds, compared to the 72-95% detection ratio at a rate of eight oscillation patterns per minute using the Hough transform edge detection methods originally put forward by Glover et al. (1995).

As the a laser sheet in practice is not an ideal 2-dimensional plane, rather a 3-dimensional volume, with a defined thickness, t, usually 0.25-3.0 mm for IDS measurement methods, the precise defocus of a droplet can vary by as much as $\pm \frac{t}{2}$. Damaschke et al. (2002) related the precise defocus to the width of an imaged oscillation pattern, noting the importance of this relation when defining the upper limit of droplet volumetric concentrations for reliable IDS measurements. In a further study, Damaschke et al. (2005) proposed that when imaging at high speed the relative increase or decrease of oscillation pattern width can be used to define a third, out of plane, droplet velocity component. However, Sugimoto et al. (2006) found

that measuring the change in length of oscillation patterns "is not accurate enough to be applicable for measuring the three–component velocity of particles", this being primarily due to relatively small changes in oscillation pattern length due to out of plane motion over the short inter-capture time intervals, producing a poor spatial resolution. Instead Sugimoto et al. and in a further study Matsuura et al. (2006) showed that a stereoscopic IDS setup using two cameras to inspect the same region of space at opposing scattering angles, a similar setup to that used in stereoscopic PIV techniques, is a more effective method for determining droplet diameter and three-component velocity. These works all highlight the importance of considering the droplet out of plane motion and laser sheet thickness in properly defining potential sources of error in IDS droplet diameter measurements, when actual droplet defocus is not or cannot be feasibly accounted for.

When using IDS techniques to both observe droplet diameter and two-component velocity an image analysis technique capable of accurately resolving the droplet radial and axial position between image captures is needed. This is typically achieved by finding the axial and radial centre point of droplet oscillation pattern. By using the vertical optical compression finding the axial centre point of the oscillation pattern can be performed with relative ease. Finding the radial centre point however is a more complex task, due to the existence of a centre point discrepancy between the apparent radial centre of oscillation patterns and the actual droplet radial centre position, (Figure 1.4). In a work by Hardalupas et al. (2010), the centre discrepancy was seen to be dependant on the degree of defocus and radial position of a droplet within the image, noting the *centre discrepancy ... varies almost linearly [radially] across the image plane.* The authors describe an empirical method of characterising and subtracting the centre point discrepancy through linear fitting.

A key advantage of IDS over other planar droplet sizing techniques such as LIF/Mie are that it records individual droplet sizes rather than a local average. Additionally IDS offers the ability to measure droplet position and velocity, where LIF/mie does not. PDA is another technique that can measure droplet sizes with

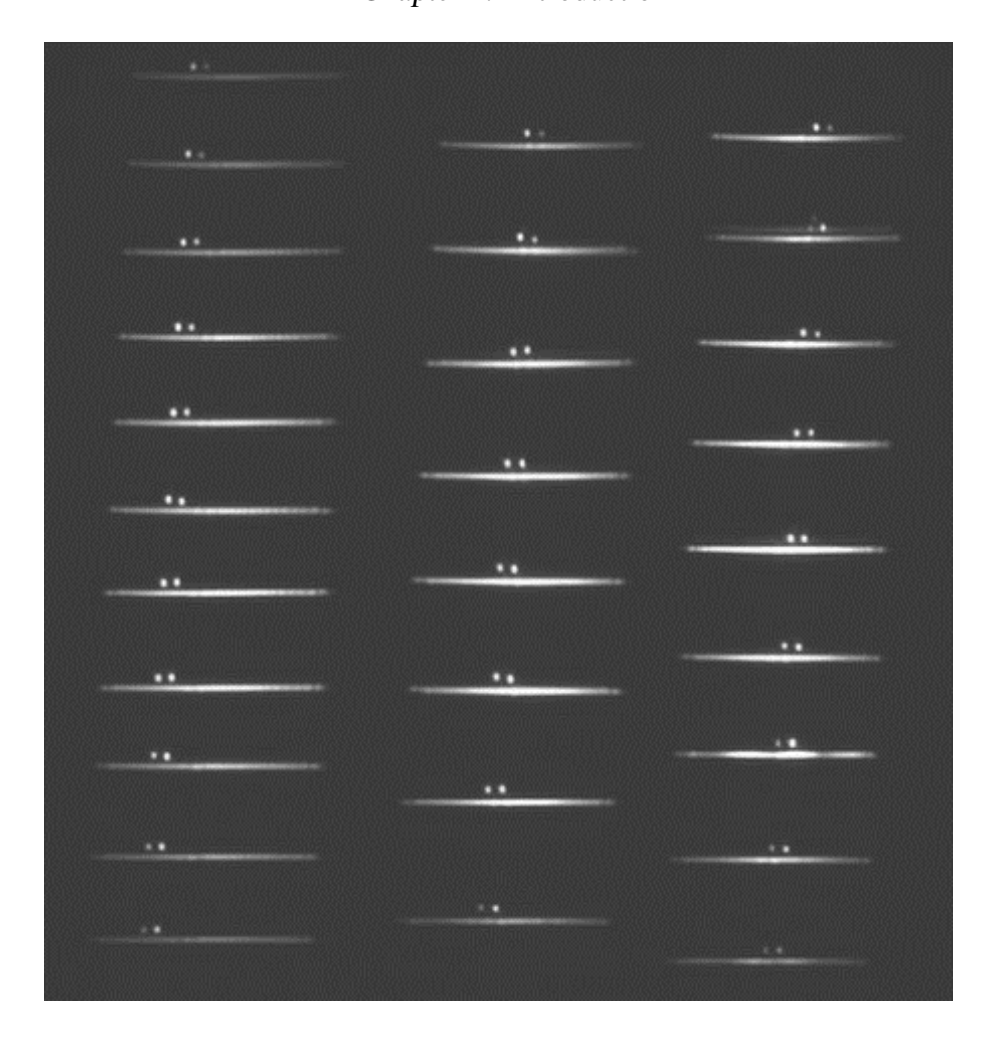


Figure 1.4: Superimposed images of in-focus and out of focus IDS images. The difference between glare point and oscillation pattern centre points displaying centre discrepancy variation with droplet radial position within image (Hardalupas et al., 2010).

high spatial resolution, giving the droplet location, however measurement volumes of IDS techniques are significantly larger than those of PDA, allowing a larger portion of a spray to be analysed in shorter period of time and providing assessment of temporal variations in inter-droplet spacing. Despite the previously highlighted developments, IDS is still somewhat limited to measurements in relatively sparse sprays, that is in contrast to PDA. Further the size range of droplet over which IDS can perform valid measurements is directly related to the spatial resolution of the imaging optics, thus a compromise is often made where by the measurement volume is reduced so as to be able to measure smaller droplets present within the spray. As such, depending on optical equipment in use, when sizing very small droplets,

typically less than 3 μ m, the relative benefit of the increased measurement volume as compared to PDA techniques is reduced. This becoming an even greater issue when attempting to measure both droplet diameter and velocities of fast moving smaller droplets, where by reducing measurement volume to increase spatial resolution, reduces the likelihood of droplets being reliably identified between image pairs.

1.5 Liquid droplet evaporation

measurement methods

Methods for the measurement of single droplet evaporation can be split into two groups, those measuring free droplets, and those measuring droplets suspended upon a wire or fibre. Techniques based around the latter method make up a large proportion of empirical data regarding droplet evaporation, this being due to the relative simplicity of the experimental setup. In such experiments a single droplet is formed on the end of a wire or fibre, fixing it's position in space, allowing the observation of droplet diameter variation overtime through microscopy (Chauveau et al. (2019)). Techniques of this form have been used to determine the effects of liquid properties on evaporation rates in quiescent and convective scenarios. One obvious limitation to such techniques is the potential for heat conduction through the supporting fibre to the droplet core, increasing observed droplet evaporation rates as detailed by Yang and Wong (2002). As such, techniques observing free droplets are likely more representative of actual droplet evaporation, though performing such tests is considerably more complex. One such method, as described by Deprédurand et al. (2010), involves the measurement of a droplet stream produced through a mono-dispersed droplet generator, where droplet spacing is such that droplet interaction is insignificant. Under these conditions it may be considered that all droplets are identical. Microscopy imaging regions are placed at two or more positions within the droplet stream for the purposes of droplet diameter measurement. Knowing the time taken for a droplet to traverse the distance between measurement location the rate of diameter reduction to be determined.

A technique similar in principle to that explained was used by Sujith et al. (1997, 2000) to measure droplet-gas velocity differential variations with respect to droplet diameter and the enhancement of droplet evaporation due to convection effects in the presence of an acoustically oscillating flow field. In this setup the measurement region and imaging frequency were large enough such that droplet position, velocity, velocity variation and diameter of droplets traveling at terminal velocities could be determined. Observing methanol droplet diameter differential at two points separated by 420 mm, evaporation rates were compared against single droplet evaporation models from a selection of sources, with the model of Burdukov and Nakoryakov (1965) showing the closest agreement. An important finding of the studies performed by Sujith et al. was the observation of two key elements leading to evaporation enhancement, these being the existence of an amplitude and phase difference between droplet and gas, as well as a reduction in the terminal velocities of droplets with the introduction of acoustic oscillations.

The use of acoustic levitation has been used to control the position of an individual droplet in space, allowing the measurement of droplet diameter reduction using microscopy. This experimental method is particularly useful when characterising the evaporation of droplets in conditions with extended evaporation timescales as has been performed by Maruyama and Hasegawa (2020) and Lieber et al. (2021) when monitoring the evaporation of saline and saliva droplets at room temperatures respectively. The use of an acoustic pressure fields to levitate a droplet will likely enhance the droplet evaporation rate, as was documented in numerical analysis by Bänsch and Götz (2018). This is due to the presence of a droplet-gas slip-velocity resulting in convective heat and mass transfer. As such models derived from data gathered using acoustic levitation methods must account for convective heat and mass transfer.

Using techniques such as those mentioned have provided good insight into the evaporation of single droplets. The use of microscopy as the method for droplet diameter measurement becomes implausible in flows containing multiple droplets and when tight control over droplet position is not maintained. PDA and laser diffrac-

tion are better suited to performing droplet size measurements within sprays, however there is no evident manner in which these methods individually can be used to record key factors relating to droplet evaporation such as inter-droplet spacing, relative droplet-gas velocities. As such often analysis is limited to general comments on global spray properties such as spatio-temporal changes in mean droplet size, as is shown in studies by Gong et al. (1992) when analysing the effects of ambient temperature and pressure on diesel spray evaporation using a laser diffraction method and McQuay and Dubey (1998), when determining the effects of acoustic oscillations on ethanol spray evaporation using a PDA system. In both cases theoretical predictions of evaporation enhancements were confirmed by changes in mean droplet diameter and variations in droplet size distributions measured at various positions with a spray, however the techniques used provide little provision to observe the causal mechanisms. For example, PDA can determine the diameter and velocity of droplets at high spatio-temporal resolutions, and through phase locking dropletgas velocity differential variations with respect to droplet size can be inferred, as shown by Kumara Gurubaran and Sujith (2008). However, as measurements cannot be preformed simultaneously at multiple positions within the spray, identifying instantaneous flow field variations is impossible. PDA is also incapable of determining the spacing of non-homogeneously distributed droplets as are present in many practical applications.

Planar measurement methods, such as PIV, LIF/Mie and IDS do allow for large regions of the spray to be simultaneously characterised, though only IDS can provide both simultaneous droplet size and velocity measurements. Indeed IDS provides the ability to measure most key parameters effecting the evaporation of droplets within sprays, resulting in its use across a number of studies.

1.5.1 Application of IDS to evaporating sprays

A relatively larger number of studies have used IDS techniques to observe droplet diameter reduction through the use of a mono-disperse droplet generator in a similar manner to the microscopy experiments described previously. König et al. (1986) monitored droplet diameter reductions in a mono-dispersed droplet stream with dis-

placement from the generator orifice. Using a similar setup Calabria and Massoli (2000) observed the effects of increasing ambient temperatures on the evaporation of iso-propyl alcohol droplets. Other studies have applied IDS methods to poly dispersed sprays such as Skippon and Tagaki (1996) observing the effects of fuel liquid properties on in-cylinder droplet evaporation during intake and compression strokes of a reciprocating engine using a planar IDS method. By combining the previously described IDS measurement methods with a high speed imaging setup, Thimothée et al. (2017) observed the reduction in mean diameter of aerosolised droplets contained within a high pressure chamber ahead of a propagating flame. Mean droplet surface area of droplets in the vicinity of the flame front was seen to linearly decrease with time, in agreement with the D^2 law.

In these studies focus is placed on the mean droplet diameter across the entire measurement volume, in a similar manner as to how PDA systems are typically used. Though the additional information provided by IDS measurements, including spatialy resolved droplet diameter, position and velocity have particular benefit to the study of droplet evaporation. These benefits being more thoroughly exploited by Sahu et al. (2014b, 2018a) when performing the simultaneous measurements of a poly-disperse spray using LIF and IDS measurement methods. Comparing the spatially resolved LIF and IDS measurements allowed the correlation of vapour cloud concentration to the size and velocity of droplets within a localised region of spray. Using the combination of techniques, the authors observed that generally vapour mass fraction was proportional to the volumetric concentration of droplets within the measurement region. A reasonable amount of variance is seen, this being shown to be a result of localised droplet clustering (non-uniform distribution of droplets within the measurement volume). At higher local droplet concentrations evaporation and vapour mass fraction was seen to reduce, this finding being in agreement with theoretical models and observations made in single droplet experimentation. Further Sahu et al. also observed a spatial disparity or lag between droplets and vapour cloud. This was related to instantaneous slip velocities as a result of flow turbulence, confirming the presence of convection effects on evaporation . Sahu et

al. did note though that the IDS measurement method did not detect and measure all interference patterns captured within an image, thus only relative measurements of localised droplet volumetric concentrations could be made.

By incorporating a Lagrangian tracking processor along with IDS and high speed imaging, Kawaguchi (2012); Kawaguchi et al. (2010) were able to track the size and position of multiple ethanol droplets entrained within a heated flow (570 K), transiting a measurement volume measuring $14 \times 14 \times 5$ mm, figure 1.5 (a). The Lagrangian tracking method enabled the authors to directly observe the droplet size reduction over periods of up to 14 ms at a sampling rate of 4000 Hz, figure 1.5 (b), allowing direct measurements of the evaporation rates and expected droplet lifetimes. Further, the rate of droplet evaporation was seen to be dependant on droplet positions within the measurement volume, this being likely due to a thermal gradient within the flow.

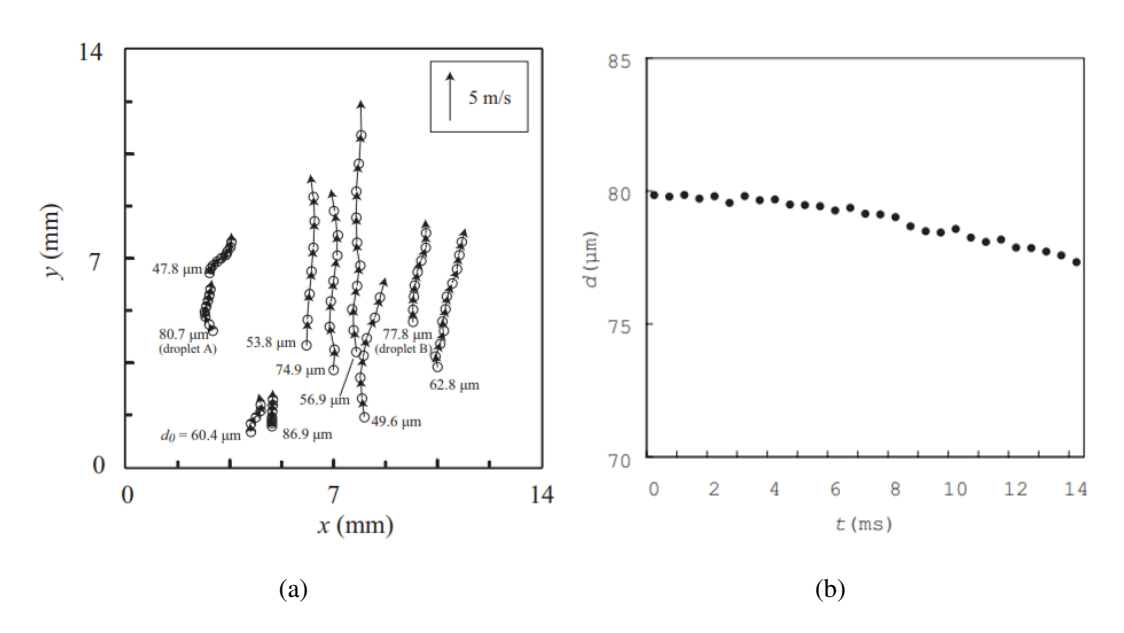


Figure 1.5: IDS Lagrangian Tracking method produced by Kawaguchi et al. (a) Droplet trajectories in heated flow (Kawaguchi, 2012), (b) individual ethanol droplet diameter reduction over timeKawaguchi et al. (2010).

Another study using IDS with Lagrangian tracking being that from Parant et al. (2021), measuring the onset of dodecane droplet evaporation in the presence of a flame. In this work the authors reported that it was not possible to observe droplet

diameter reduction as the high evaporation rates were seen to degrade and blur droplet oscillation patterns. Given this limitation, the IDS method was used to determine the onset of evaporation, observing the time taken before the droplet signal was extinguished, the evaporation rates were then estimated.

This Lagrangian tracking methodology has seen little further application despite the apparent advantages of a technique capable of directly measuring droplet trajectories, velocities and diameter reduction over extended periods of time. In addition to the observation of droplet evaporation the use of this technique could provide great insight into the individual spray droplet slip velocity as a function of droplet size in unstable flow fields. Thus with the added functionality of Lagrangian tracking, IDS techniques could be used to directly observe droplet evaporation and key parameters governing droplet evaporation, including droplet slip velocity and droplet volumetric concentrations.

However, there are a number of potential issues that may need to be addressed in order for this method to be more widely used. One of which, highlighted by Kawaguchi (2012), is the impact of the laser sheet thickness and droplet out of plane motion on droplet diameter measurements. To ensure droplets remain within the measurement volume for an extended period of time, the laser sheet thickness will have to be increased, with Kawaguchi et al. using a 5 mm thick laser sheet, considerably more than that used in standard IDS methods (\approx 0.5 mm). As a result the defocus distance of droplets with an out of plane velocity component will, in accordance with equation 1.17, vary during their transit of the measurement volume. To account for this Kawaguchi et al. made use of both the interference pattern total width and fringe spacing to determine the actual droplet diameter, however no specific details are given to how this was achieved. As previously mentioned, other researchers, such as Sugimoto et al. (2006), have attempted to relate the interference pattern width to out of plane position, however practical limitations relating to image noise and detection methods, created large amount of measurement error.

1.6 Thesis aims

The research presented within this thesis focuses on the characterisation of droplet parameters effecting both directly and indirectly droplet evaporation in complex, realistic spray systems. To characterise spatial variations of sprays and droplet properties, a number of traditional and novel planar laser illuminated optical analysis methods are used. Given the importance of droplet diameter measurement in studies relating to droplet evaporation particular focus is placed on the use and development of an Interferometric Droplet Sizing (IDS) technique. The experiments performed within this thesis cover both the use and development of an IDS measurement technique capable of droplet Lagrangian tracking. This allows the observation of droplet diameter variation in conditions conducive to evaporation, and in non-evaporating (isothermal) conditions the effect of specific parameter variations on spray characteristics known to influence the evaporation of droplets within a spray.

- 1. To asses the performance of an IDS technique in observing changes in droplet diameter and distribution within a spray where liquid properties (surface tension, viscosity and density) are varied. The diameter of droplets constituting a spray and their volumetric concentration are known to influence evaporation, with the IDS method being theoretically capable of simultaneously measuring both parameters. The potential benefits and drawbacks of using IDS techniques in this manner will be assessed and compared against that of other measurement methods.
- 2. To further develop the IDS technique by allowing the observation of individual droplet diameter and position history, through the addition of a Lagrangian droplet tracking processor. This additional data processing step aims to:
 - (a) Increase the number of correctly measured droplet interference patterns within captured images, improving the rate of data acquisition and provide better estimations of local droplet concentrations.
 - (b) Directly observe the rate of droplet size reduction resulting from droplet evaporation.

- (c) Asses the effect of individual droplet properties within a spray such as size, position, velocity, velocity variation on droplet evaporation.
- To investigate the potential limitations resulting from the application of Lagrangian tracking to the IDS measurement method. Sources of measurement error and uncertainty will be reported, and potential counteractions explored.
- 4. As a research group specialising in the analysis and characterisation of multiphase flows, our experimental facilities were converted to aid in the research relating to the spread of Covid-19 viral particles through human produced droplets and aerosols. The distribution and de-hydration rate of virus laden droplets produced by humans is one of the key parameters in determining virus transmission within enclosed spaces such as those present in houses, hospitals and schools. Given the urgent situation, the use Computational Fluid Dynamics (CFD) to provide information allowing effective guidance relating to social distancing, mask wearing and other methods of mitigation was an extremely valuable tool. For the models produced by CFD to be representative, certain parameters such as the amount, velocity and diameter of droplets produced by humans and the effectiveness of mitigating factors is required, much of which had seen little research prior to the outbreak of COVID-19. Thus, a series of experiments making use of laser illuminated planar high speed imaging were outlined, with the aims of improving our understanding of droplet characteristics as they exit the mouth and the effectiveness of face coverings in mitigating the spread of droplets.

1.6.1 Chapter layout

In the second chapter of this thesis a commercially available IDS technique is applied to an automotive spray to asses the performance of the measurement technique in determining the effect increasing ethanol content within gasoline on droplet diameter and spatial droplet diameter and concentration distribution at a fixed location. The third chapter describes the development of an IDS based tracking processor. Here the uncovered measurement errors inherent in Lagrangian tracking

through IDS will be fully characterised before the tracking processor is applied, in chapter four, to a methanol spray in a high temperature co-axial airflow, where individual droplets are observed to reduce in diameter due to evaporation. The observed droplet evaporation rates are then compared to those estimated by an evaporation model. In chapter five the tracking processor is the applied to observe the effects of acoustic forcing on the enhancement of droplet evaporation. In this case the IDS based tracking processor is used to determine the effects of droplet diameter on the relative velocity between gas and liquid phases. Chapter six covers work performed in characterising droplet flows produced by humans and the effectiveness of face coverings. With the assistance of medical professionals, epidemiologists and healthcare facility managers, our group began a study to determine the effectiveness of face coverings in reducing droplet emission from the mouth and nose, the concentration and velocities of droplets produced and the variation in droplet production depending on person and form of expiration.

Chapter 2

Application of an IDS technique to ethanol-gasoline fuel blends

2.1 Chapter outline

In this chapter an Inteferometric Droplet Sizing (IDS) technique is used to determine the effects of ethanol content within ethanol-gasoline fuel blends. The IDS measurement method is described and its performance assessed, including a detailed discussion into the sources of error and uncertainty. A brief introduction is provided, describing the current literature relevant to the optical characterisation of bio-fuel sprays.

2.2 Introduction to droplet sizing in bio-fuel sprays

In every application of liquid spray, be it spray drying in pharmaceutics, spray cooling in nuclear reactors or fuel injection in combustion engines, understanding spray characteristics enables a more informed nozzle design and allows optimisation of operating conditions. For example, a significant factor in the combustion of liquid fuel sprays is the degree of atomisation and the resulting size of fuel droplets. For a fixed volume of fuel, a dispersed distribution of smaller droplets creates a more homogenous air fuel mixture (which results in more uniform combustion), as compared to fewer larger droplets. Further the distribution of droplets within the combustion volume is seen to directly effect droplet evaporation and combustion, with increased inter-droplet spacing resulting in higher evaporation rates and more homogeneous flame propagation.

Techniques such as Phase Doppler Anemometry (PDA), ratiometry and interferometric droplet sizing (IDS) techniques have been shown to be effective for measurements of droplet diameters in industrial fuel sprays (Aleiferis et al., 2015; Ding et al., 2017; Kannaiyan and Sadr, 2014; Kim et al., 2012; Moriyoshi et al., 2009; Pierson et al., 2000). Pierson et al. (2000) used PDPA to characterise spray from a multi-hole gasoline port fuel injector, with the aim of using the findings as validation for computational spray modelling. Moriyoshi et al. (2009) successfully measured the influence of crossflow on droplet size, velocity and the droplet distribution in direct injection gasoline sprays using interferometric droplet sizing techniques. An advantage of planar sizing techniques, such as interferometric droplet sizing techniques

niques, over point measurement techniques, such as PDPA, is the increased field of view (typically 10×10 mm to 20×20 mm) (Pan et al., 2006), which allows for a better understanding of the global spray properties, and expedites the process of building a complete picture of droplet sizes across the entire spray. This function being of particular importance when observing the degree of distribution of droplets within a spray, enabling Sahu et al. (2014a,b, 2018a), to monitor inter-droplet spacing and relate this to the inhibition of acetone droplet evaporation.

Increasing concerns regarding the environmental impact of fossil fuel combustion has led to many governing bodies mandating the use of sustainable bio-derived fuels. Bio-ethanol is one of the most commonly used bio-fuels due to its miscibility in gasoline, its higher octane number and its well understood production from plant matter. Understanding spray formation and dynamics of such bio-fuels is fundamental for the development of more efficient combustion systems with reduced pollutant emissions. Park et al. (2009) investigated blends of bio-ethanol and gasoline using PDPA, and reported an increase in droplet diameters with increasing proportion of ethanol. Aleiferis et al. (2015) found the same trends in droplet diameter with ethanol addition in fossil gasoline, when analysing spray behaviour from spark-eroded and laser-drilled injectors using PDPA. The effect of ethanol content within gasoline fuels blends on the spatial distribution of droplets within the sprays is documented to a lesser degree. Gao et al. (2007), noted that spray cone angles of ethanol-gasoline blends produced by a multi-hole automotive fuel injector increased with increasing ethanol content, suggesting droplets maybe more dispersed. Using both Planar Laser Induced Fluorescence (PLIF) and Mie scattering techniques, Oh et al. (2010) observed localised fuel concentrations of ethanol to be lower than that of iso-octane.

It is evident from literature that the interferometric droplet sizing technique has excellent potential for detailed spray analysis, however, it has not previously been used for the study of ethanol fuel blends, particularly relevant for propulsion applications, with most researchers using point measurement techniques. This paper investigates the effect of ethanol content in fossil gasoline on droplet diameter

and spatial distribution using the commercial interferometric drop sizing system, Global Sizing Velocimetry (GSV), developed by TSI Instruments Ltd. The specific objectives of this study is to investigate i) the applicability of the GSV technique in measuring the droplet diameters of ethanol-gasoline fuel blends, ii) the capability of the technique to determine the spatial distribution of droplet number and size and iii) variations in droplet size for different blends of ethanol and gasoline.

2.3 Experimental Methodology

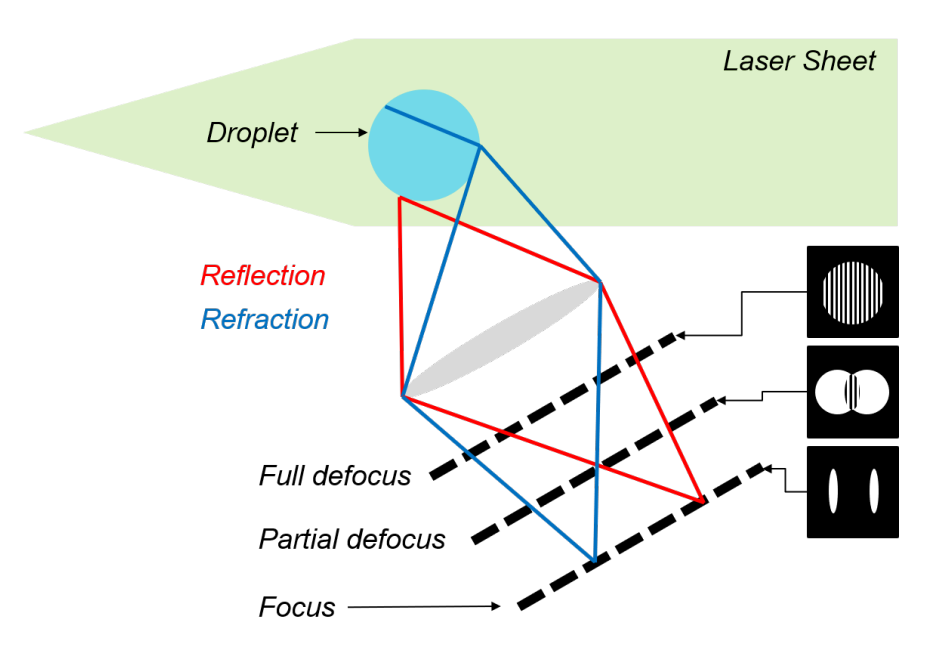


Figure 2.1: Diagram showing interferometric principles.

2.3.1 Principle of interferometric techniques

Interferometric droplet sizing techniques use both the reflected and refracted images from droplets to accurately determine their diameters, as can be seen in Fig. 2.1. The camera is set at a particular angle to the laser plane in order capture both reflected and refracted images. The camera is then deliberately defocused, so that the images superpose, creating an interference pattern. The number of oscillations and the fringe spacing of this pattern are used to determine the droplet size.

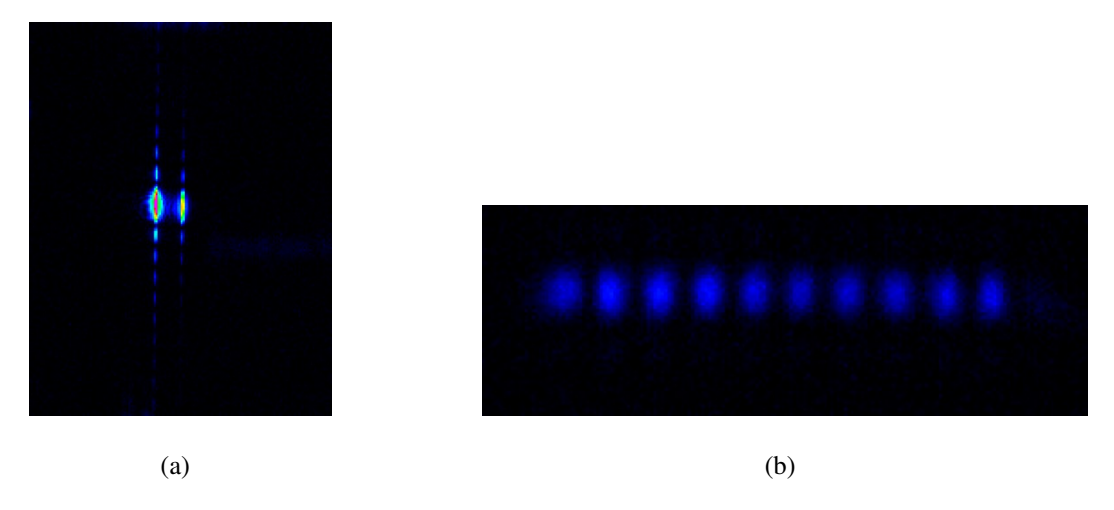


Figure 2.2: (a) Glare points at focus, (b) Interference oscillation with slit aperture at 8.55 mm defocus.

2.3.2 TSI Instruments GSV system

The TSI Instruments GSV setup uses the same basic principles of interferometric droplet sizing techniques described above. The imaging system for the GSV technique consists of a pulsed Nd:YAG laser (Quantel Evergreen 200) and a 4 MP (TSI PowerView, 12 bit, 2352 x 1768 pixels) camera. The laser sheet thickness was set to roughly 250 µm using variable focus optical lenses, with the laser energy being 185 mJ (pulse-width of 10 ns). A 100 mm focal length lens was used with the aperture set to F5.6 for the all the tests. The lens was focused at its minimum focal distance of 300 mm in order to produce a 1:1 magnification ratio, giving the best possible spatial resolution. The camera exposure time was set to 1 ms. The laser and camera were mounted such that their planes were at 60° to each other, for which the GSV software is optimised. As no Scheimpflug optics are in use, only the centre of the image was set in focus. Initially, the focus of the camera was adjusted so that the droplets along the vertical centreline of the viewing window appeared as double glare points. An example of this is shown in Fig. 2.2(a). The camera was then moved away from its focused position to create interference of the reflected and refracted images and form oscillation patterns, as can be seen in Fig. 2.2(b). Droplet diameters are determined from the spacing between the fringes within these patterns. The required amount of defocusing necessary is based on two

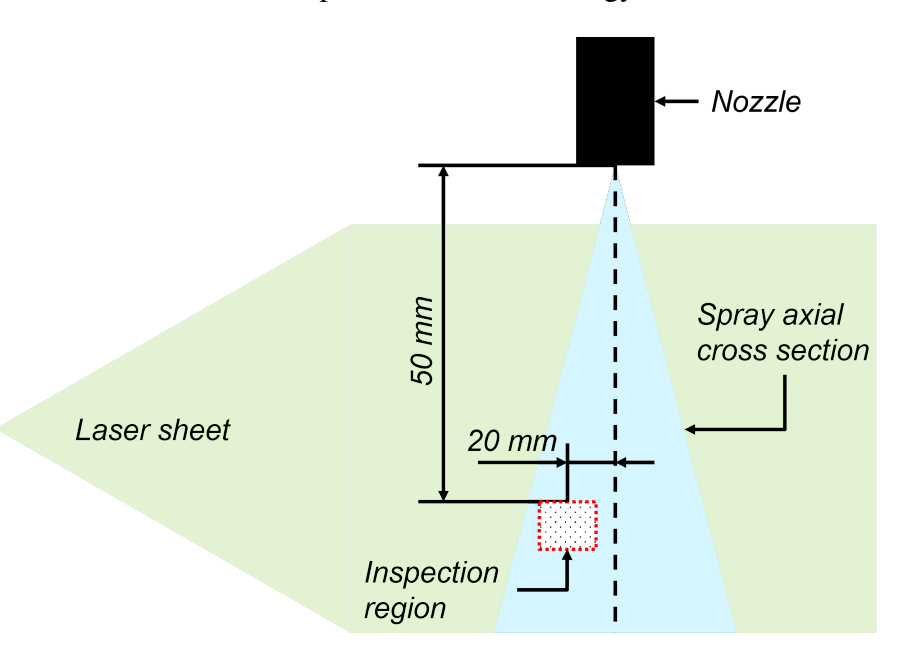


Figure 2.3: Side view diagram of spray cross section with selected viewing window.

main factors, the clarity of individual oscillation patterns and the degree of overlap between multiple oscillation patterns. If the image is not sufficiently defocused, oscillation patterns become too compact making the spacing between fringes difficult to measure accurately. This hampers the precision of the droplet diameters measured. Excessive defocusing results in drawn out, non-distinct and lower intensity oscillation patterns making it similarly difficult to determine the spacing between fringes. This also increases the degree of overlap between oscillation patterns due to their larger size.

As mentioned earlier, the camera and laser planes are offset by 60° , as such one side of the image is closer to the camera than the other and so is less defocused than the other. The TSI software corrects for this disparity when analysing the oscillation patterns, but it is important to ensure that the oscillation patterns in the more defocused portion of the image are not too drawn out and of very low intensity, and that the oscillations in the less defocused region are not too compact. It is recommended that the oscillation patterns in the less defocused region of the image should be at a minimum 96 pixels in length. In line with this recommendation, a minimum oscillation pattern length of 110 pixels was kept for all the experimental conditions. To get the required interference pattern, for these experiments, the

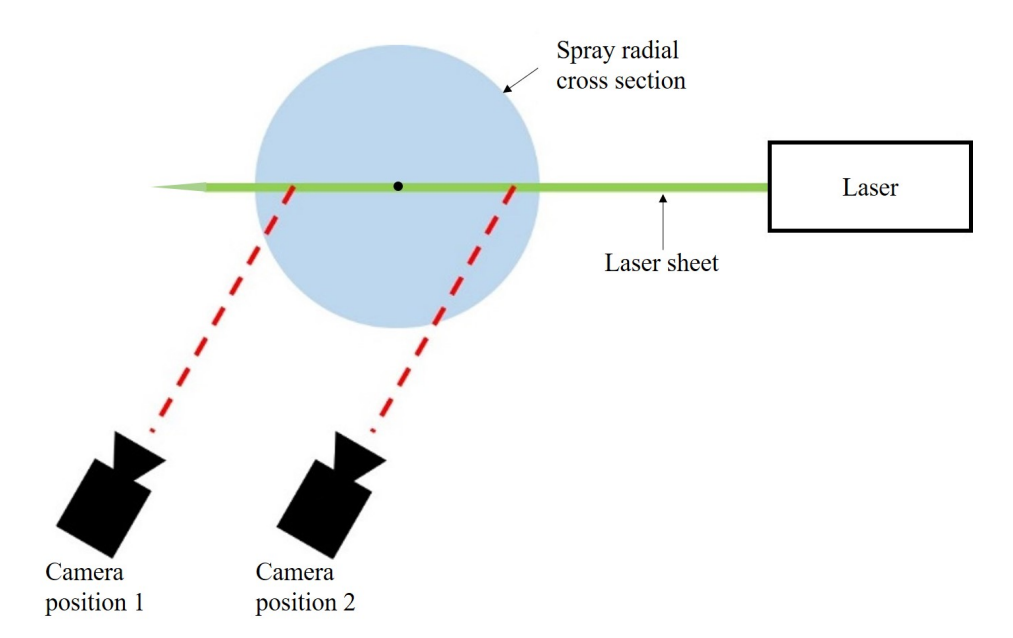


Figure 2.4: Top view diagram of spray cone section, with (Camera position 1) left side imaging and (Camera position 2) right side imaging.

camera was defocused by moving it 8.55 mm away from the laser plane, and was fixed for the entirety of experimentation. A micrometre-controlled traverse was used to get precise measurement of the defocus displacement. A slit aperture was mounted on the camera lens, which compressed the interference pattern from a full circle to thin single line of fringes, figure 2.5. This enables the GSV software to analyse denser sprays without having oscillation patterns overlapping and causing erroneous readings of droplet diameters.

The GSV image analyser software uses a windowed fast Fourier transform (FFT) technique to identify the frequency of the oscillation patterns. The basic principle of this technique is that strong oscillations show a single dominant frequency, whilst oscillation patterns created by invalid droplets, such as non-spherical droplets and background noise, exhibit multiple dominant frequencies. Once clear and valid oscillation patterns are identified, the spacing between fringes are analysed to determine the droplet size (Pan et al., 2006). The ability to measure droplets is dependent on the presence of at least two fringes in an oscillation pattern. Using the current setup, the minimum droplet size that can be measured is $10~\mu m$, any droplets smaller than this will not be detected.

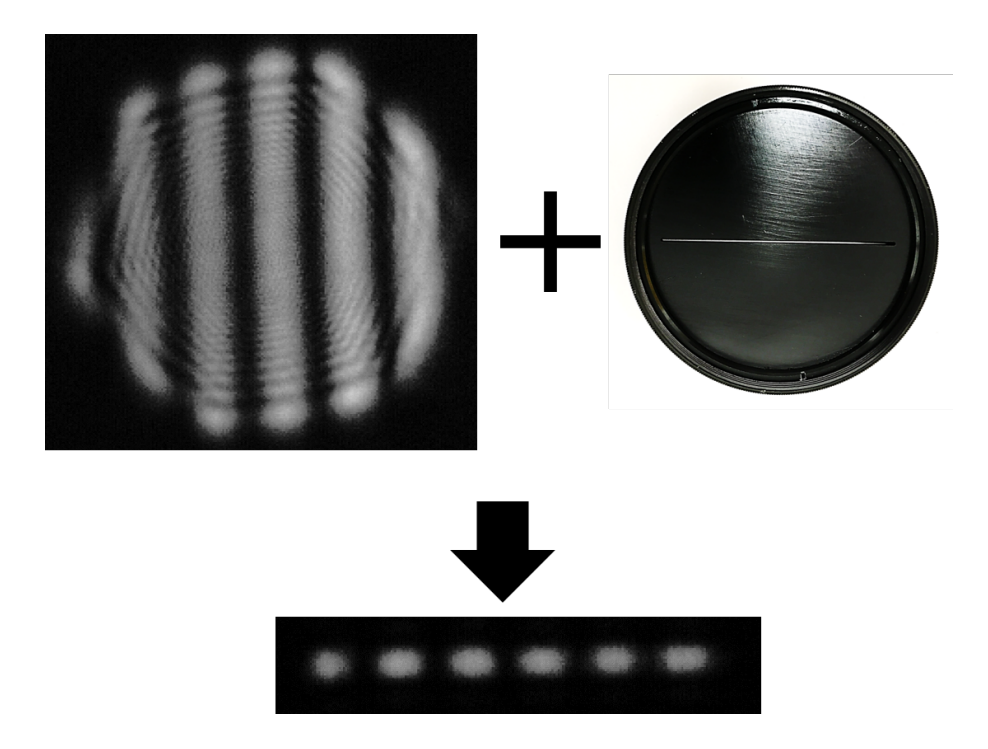


Figure 2.5: Vertical compression of interference pattern using slit aperture.

A potential limiting factor when using any interferometric technique is that, in regions of high droplet density, oscillations overlap creating blurred or high frequency oscillations. As such, TSI recommend that the maximum droplet count per cubic centimetre in the viewing region should be 3000. Preliminary tests were carried out by capturing different regions of the spray, in order to ensure that the droplet density within the selected viewing window was not above the recommended level. To measure the droplet density in the measurement volume, a sample of 20 images was taken. Based on visual examination, the most densely populated quarter of each image was selected and analysed, with the total number of droplets contained within the quarter averaged over the 20 sample images. Using this value, the laser sheet thickness and image geometry, the droplet density per cubic centimetre was calculated. In the denser regions of of the solid cone spray, such as along the spray centreline and close to the injector nozzle, the droplet concentration was considerably above 3000 droplets per cubic centimetre, leading to droplet overlaps and a reduction in the number of valid readings. Axially and radially displacing the measurement volume from the nozzle tip reduced the concentration of droplets,

64 Chapter 2. Application of an IDS technique to ethanol-gasoline fuel blends which is concurrent with findings reported in previous literature (Feng et al., 2016; Kannaiyan and Sadr, 2014; Li et al., 2011). In this study it was found that offsetting the viewing window 50 mm vertically from the nozzle and 20 mm radially from the spray centreline, shown in Fig. 2.3, meant the droplet concentration did not exceed the recommended limit.

The spray used in this study is symmetrical, which implies that either the left or right side of the spray cone can be imaged for analysis, as shown in Fig. 2.4. Viewing the right-side image was found to degrade the image quality and reduce the number of valid data readings as compared to the left side image. This is likely due to the increased volume of spray between the image and camera causing scattering of the light, known as off axis attenuation, resulting in a weaker signal reaching the camera sensor. As such the ROI selected for this study was located on the left-hand side of the spray centreline, shown in Fig. 2.3.

2.3.3 Spray test facility

Figure 2.6 shows the setup of test facility, including the fuel pressurisation and injection systems. An automotive, single hole, solid cone port fuel injector (PFI) was used to generate the spray. For all the tests, the fuel was injected at a pressure of 3.5 bar (flow rate of 0.73 litres per minute), which is within the PFI injector's specified operating range and demonstrated good atomisation during preliminary testing. The fuel was pressurised using a pressure vessel supplied with regulated pressurised air to achieve the desired fuel pressure. The fuel pressure was monitored by both an analogue gauge, and a digital pressure transducer which was monitored live on the LabVIEW interface using National Instruments data acquisition systems. The experiments were conducted in a test facility where the ambient temperature was maintained at a constant value for the duration of the tests. Spray timing and injection duration were controlled via LabVIEW, while the TSI Insight 4G software was used to time the camera and laser trigger signals. To contain the spray and to protect it from ambient effects, the injector was mounted in an optical vessel maintained at atmospheric pressure. Large viewing ports facilitated the required

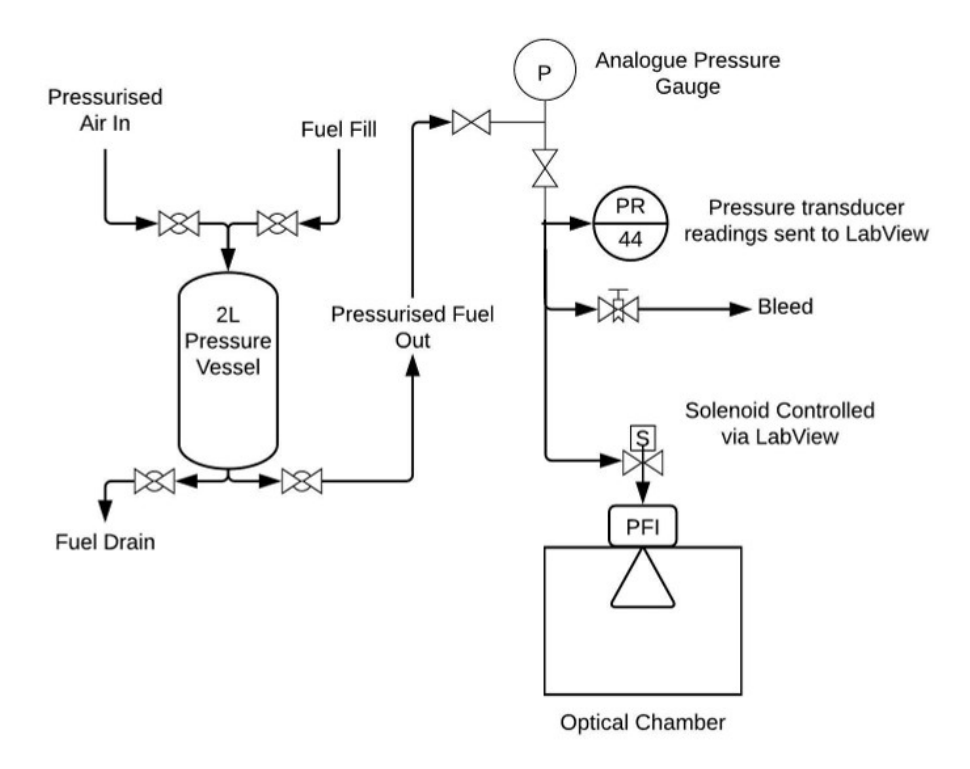


Figure 2.6: Schematic of spray test facility (P-pressure gauge, PR-pressure transducer, PFI-Port Fuel Injector).

60° angle between the camera and laser planes. To ensure the spray was fully developed when the camera was triggered, various time delays between the injector and camera trigger were tested. It was found that there was no change in the droplet distribution with delays of 30 ms and greater. Therefore, the delay between the start of the injector trigger and the start of the camera trigger for all experiments was set to 40 ms. The injector was opened for a total of 50 ms.

2.3.4 Fuel blends

To gain a comprehensive understanding of the effect of ethanol content on droplet diameters, a full range of fuel blends were tested, as can be seen in table 2.1. It should be noted that the pure gasoline used had no ethanol content prior to blending. Additionally, the blend properties of viscosity, surface tension and density are listed, the sources for data being noted beneath the table.

Increasing ethanol content is shown to significantly alter fuel blend viscosity and density, though surface tension is sees little variance, particularly so for blends

Table 2.1: Fuel blend properties at 20°C. ¹Khuong et al. (2017), ²Wang et al. (2006).

Fuel blend	Ethanol content (%)	Kinematic Viscosity ¹ (mm ² /s)	Surface Tension ² (mN/m)	Density ² (kg/m ³)
E100	100	1.478	22.12	790.6
E80	80	1.292	21.63	777.9
E60	60	-	21.55	765.2
E50	50	-	21.56	758.3
E40	40	-	21.58	752.4
E30	30	0.705	21.56	746.4
E20	20	0.614	21.59	739.8
E15	15	-	21.59	737.5
E10	10	0.546	21.58	734.3
E0	0	0.529	21.58	725.7

containing ethanol contents of 60% and less. No direct measurements of kinematic viscosity relating to ethanol-gasoline fuel blends at temperatures relevant to the conditions used in this study exist for blends E15, E40, E50 and E60, however Kheiralla et al. (2011) found blend viscosity to linearly increase with increasing ethanol content when observing viscosity at 30°C, thus it can be assumed that values lie linearly between those represented by Khuong et al. (2017) in table 2.1.

2.4 Data reduction and analysis

This section will discuss the selection of processor parameters on the TSI Insight 4G software, in order to optimise the analysis of droplet sizing and identify the single most dominant frequency using the windowed FFT technique. For this purpose, preliminary tests were carried out in which E100 spray images were captured, and in the first instance, analysed with the default processor settings. Visual inspection of the analysed images revealed that some droplets were being incorrectly detected by the processor. Generally, these manifested in one of two forms: (1) Due to low

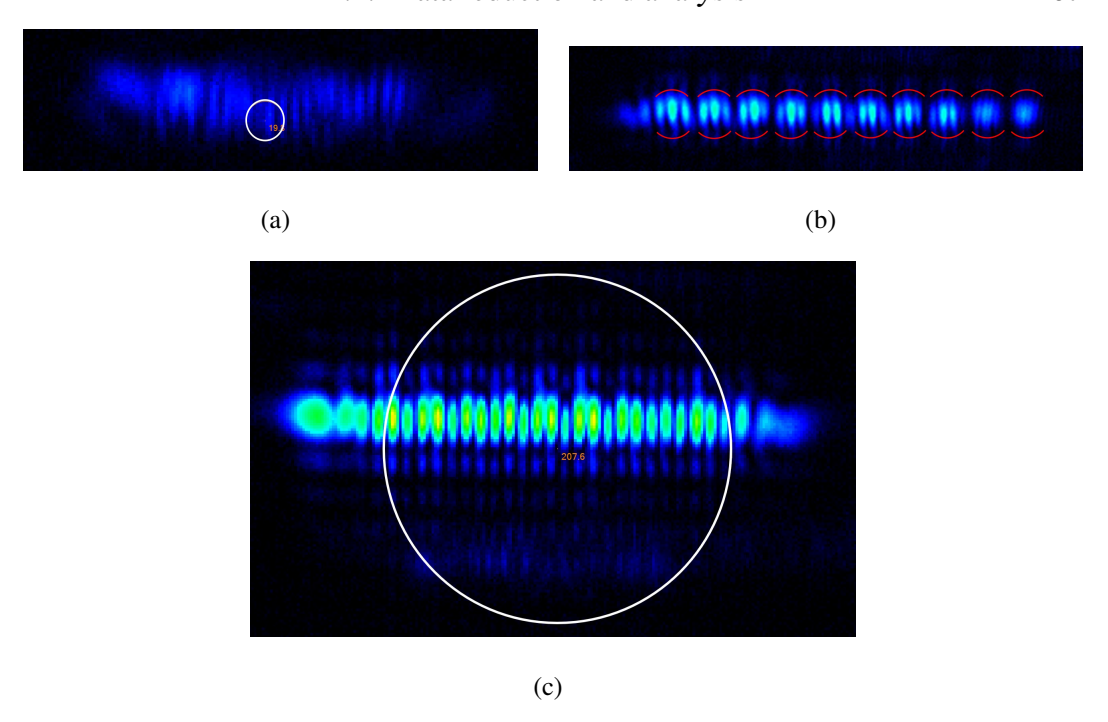


Figure 2.7: (a)Low intensity indistinct oscillation patterns erroneously recognised as small droplet (19.8 μ m), (b) Oscillation patterns showing two frequencies, red outline showing the fringes from one frequency, each containing 'sub-fringes' from a second frequency, (c) Oscillation patterns containing multiple frequencies being erroneously measured as a large droplet diameter (207.6 μ m).

intensity indistinct oscillation patterns, which typically lead to erroneous readings of low diameter droplets, as shown in Fig. 2.7(a). (2) Due to the additional interference in the oscillation pattern caused by multiple frequencies. Interferometric techniques ideally use the first refraction to create oscillation patterns. However, in practice higher order refractions are present, and in some circumstances these higher order refractions are refracted at such an angle that they are picked up by the camera, as found by Dehaeck and Van Beeck (2008). This results in the presence of multiple frequencies in the oscillation pattern, as is visible in Fig. 2.7(b). In some instances, oscillation patterns containing multiple frequencies are interpreted as a single higher frequency as shown in Fig. 2.7(c), resulting in the erroneous identification of large diameter droplets. These high frequency oscillation patterns were also of higher intensity due to the additional light from multiple signals, as observed by Dehaeck and Van Beeck (2008). As well as the errors described, it was

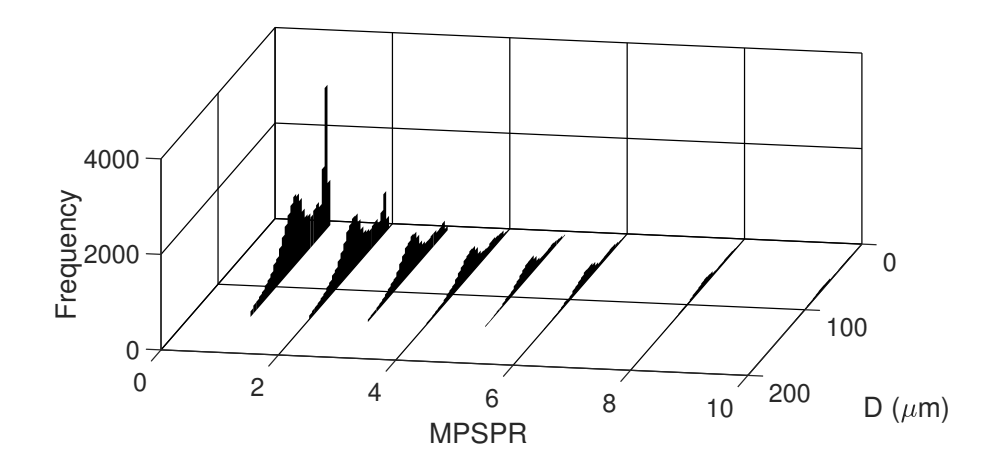


Figure 2.8: Frequency distribution of droplet diameters with MPSPR variation.

observed that not all clear oscillation patterns present in the image were being detected, through observation it is estimated that approximately 30-50% of coherent oscillation patterns were not being recognised, though this was not consistent across all images making a statistical correction outside the scope of this work. The selection of the processor parameters was therefore focused on reducing the occurrence of low diameter and large diameter erroneous readings, as well as maximising the overall number of droplets detected from each captured image to reduce the total number of images required to produce a valid data-set.

Three particular parameters were observed to have the largest impact, Vertical Scan Output (VSO), Horizontal Scan Interval (HSI) and Minimum Power Spectrum Peak Ratio (MPSPR). VSO allows the selection of the method used to define a general spacing (either mean, median or maximum) between fringes within an oscillation pattern. Whilst setting the VSO as maximum recorded the largest number of data points, it also produced a larger number of low diameter erroneous readings. The frequency of low diameter droplets was reduced (with no appreciable effect on the detection of large droplets) when using both the mean and median settings, with the mean setting showing the most reduction, hence this was chosen as the VSO setting for the current piece of work. The HSI parameter defines the minimum spacing, in pixels, between the fringes within an oscillation pattern. Increasing the HSI value beyond 20 significantly increased the number of low diameter readings,

as did values below 10. Similar to the VSO, the detection of large diameters did not vary significantly with this parameter. A HSI value of 15 was selected for this study. The MPSPR defines the minimum signal to noise ratio of the analyser. Changing the MPSPR value had the largest influence on the droplet detection and diameter measurement. The MPSPR at its lowest value of 1 gave the highest droplet count, however this had significant impact of increasing the low diameter peak, as can be seen on the histogram in Fig. 2.8. As the MPSPR value was increased above 1, the number of recorded droplets decreased, as did the frequency of low diameter droplets. The number of large droplet diameters also reduced when increasing the MPSPR value. As such, choosing the best value was a compromise between data count and the inclusion of potentially erroneous data. Based on the review of the data collected, a MPSPR value of 3 was set for the current set of experiments. The values of the three parameters were kept constant for the duration of the study.

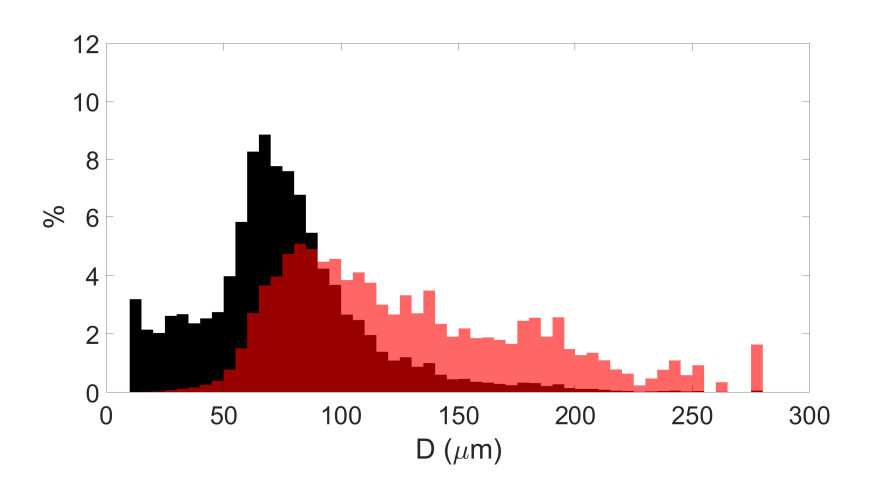


Figure 2.9: Superposed Probability distributions of droplet number (black) and volume (red), expressed as a percentage of overall number and total volume respectively, for E100

Figure 2.9 shows the frequency and volume probability distribution for E100, obtained using the above mentioned optimised parameter settings. It can be seen from the figure, that a small number of large droplets (above 200 μ m) contribute a considerable proportion to the overall volume of the spray. As stated previously, many of these large droplet diameters are due to oscillation patterns containing two dominant frequencies appearing as one higher frequency oscillation pattern (see

Fig. 2.7c). Whilst this phenomenon is infrequent (as evidenced by the low proportions of the larger droplets in Fig. 2.9), it could have an impact on the measurement of the average droplet diameters.

2.5 Validation of GSV technique and measurement uncertainty

A droplet generator was used to validate the droplet sizing measurements obtained from the GSV setup. The droplet generator used was a Flow-Focusing Monodisperse Aerosol Generator Model 1520 (FMAG), producing a focused column of droplets ranging between 15 and 90 μ m with a stated uncertainty of \pm 1.0%, figure 2.10.

Table 2.2 shows the comparison of the droplet sizes between the generator and GSV measurement. The four different diameters were chosen that represented the values around the peak diameters observed during this study. In all cases, the droplet size measured by GSV was in good agreement with the diameters produced by the droplet generator, the difference ranging between 0.3 and 1.6 μ m. The GSV results show a normal distribution of droplet diameter readings about the mean diameter value, figure 2.11. The average standard deviation of the four test cases was 1.5 μ m, which will be used to represent the measurement uncertainty in later analysis. In the work by Duan et al. (2016), the FMAG droplet sizes were measured using PDPA, and a standard deviation of 1.01 μ m was observed for droplet diameters above 40 μ m. This is in good agreement with the standard deviation determined in the current piece of work.

A further source of uncertainty results from the differences in refractive index between gasoline and ethanol. Ethanol is known to have a refractive index of 1.36 and gasoline 1.43, (Butcher et al., 2013). From Equation 1.17, it can be seen that at a scattering angle of $(\theta =)$ 60° the difference in measured droplet diameter for any interference pattern is approximately 1%. As the magnitude of this uncertainty is so low the refractive index has not been accounted for in this study, instead being



Figure 2.10: GSV measurements of droplets produced from FMAG set to produce droplets 65.6 μ m in diameter.

set to that of water (n=1.33).

The variation in the arithmetic mean of the droplet diameters, D_{10} , has been shown in Fig. 2.12 as a function of the number of droplets measured. The figure clearly shows that the variation in D_{10} reduced to a minimum beyond 2500 droplet measurements for E100. Hence, for all the fuel blends the minimum sample size of droplets measured was no less than 5000 to ensure a valid data set size.

Table 2.2: Comparison of droplet diameters from Flow-Focusing Mono-disperse Aerosol Generator and GSV measurement

FMAG Diameter (µm)	GSV D ₁₀ (μm)	Difference (µm)	Standard Deviation (µm)
71.3	72.4	1.1	1.5
65.6	65.9	0.3	1.6
62.0	63.5	1.5	1.5
52.0	53.6	1.6	1.2

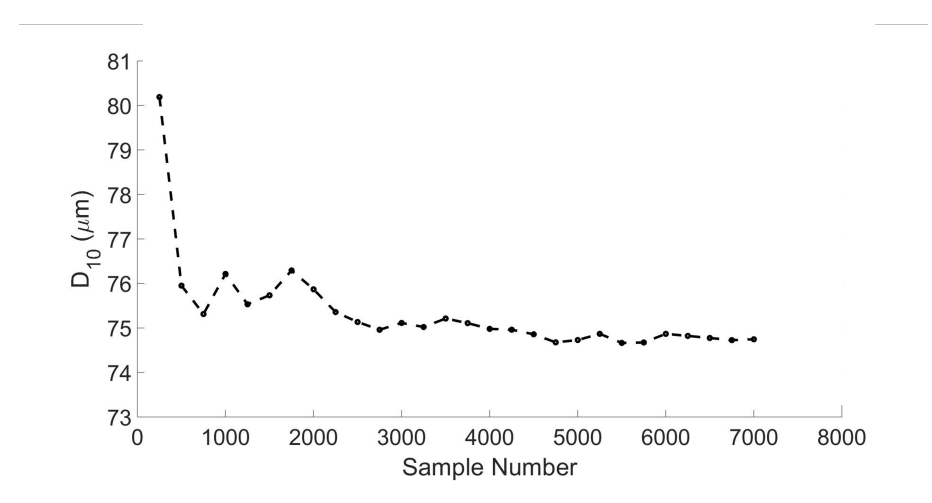


Figure 2.12: D_{10} variation with sample number

To ensure there were no significant changes in the laser or optical alignment during the experimentation period, the first two fuel blends tested (E100 and E0) were repeated at the end, the variation for E0 was $\approx 0.8 \,\mu\text{m}$ (63.94 - 64.72 mum) and E100 $\approx 0.4 \,\mu\text{m}$ (73.67 - 73.30 mum). Such variations can be considered negligible given the measurement uncertainty determined using the droplet generator. Due to the resolution of the graduations of the glassware used to prepare the ethanolgasoline blends, the average uncertainty in the ethanol content in gasoline is $\pm 2\%$ for all the fuel blends.

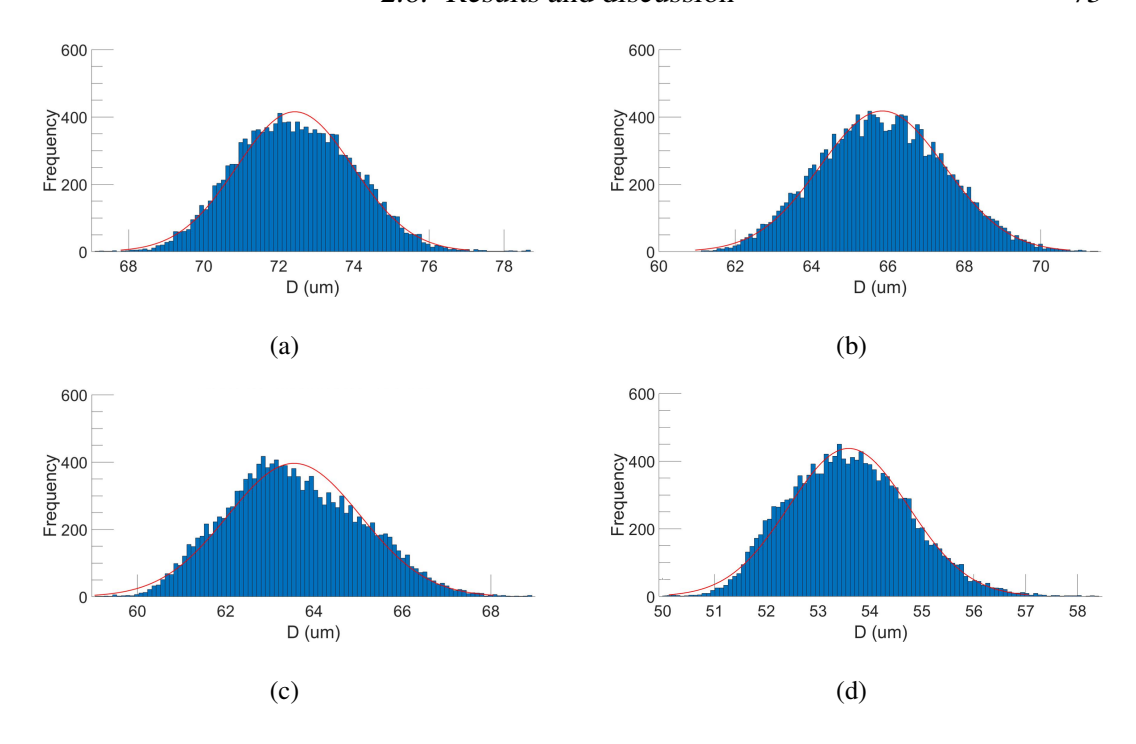


Figure 2.11: Frequency distribution of FMAG droplets measured by GSV, corresponding to table 2.2, page 72, where the FMAG set droplet diameter is equal to (a) 71.3 μ m, (b) 65.6 μ m, (c) 62.0 μ m and (d) 52.0 μ m.

2.6 Results and discussion

The number and contribution to total volume distribution of the droplet diameters for all the fuel blends is shown in Fig. 2.13. It can be seen from the figure that the number distribution for all the fuel blends are distinctly unimodal, with peak diameters of 60-70 μ m. Similar unimodal number distributions were found by Pan et al. (2006) when measuring direct injection gasoline spray with GSV. It can also be observed in the number distribution of all the fuel blends that there is a sharp peak of small droplets with diameters 10-15 μ m. This is more significant for fuel blends E20, E15 and E10. This observation will be discussed in more detail later. For the determination of the droplet volume, the droplets were assumed to be perfectly spherical. The volume distribution is also unimodal, showing a sharp increase for the diameters up to approximately 75 μ m, followed by a gradual reduction in the total volume proportion.

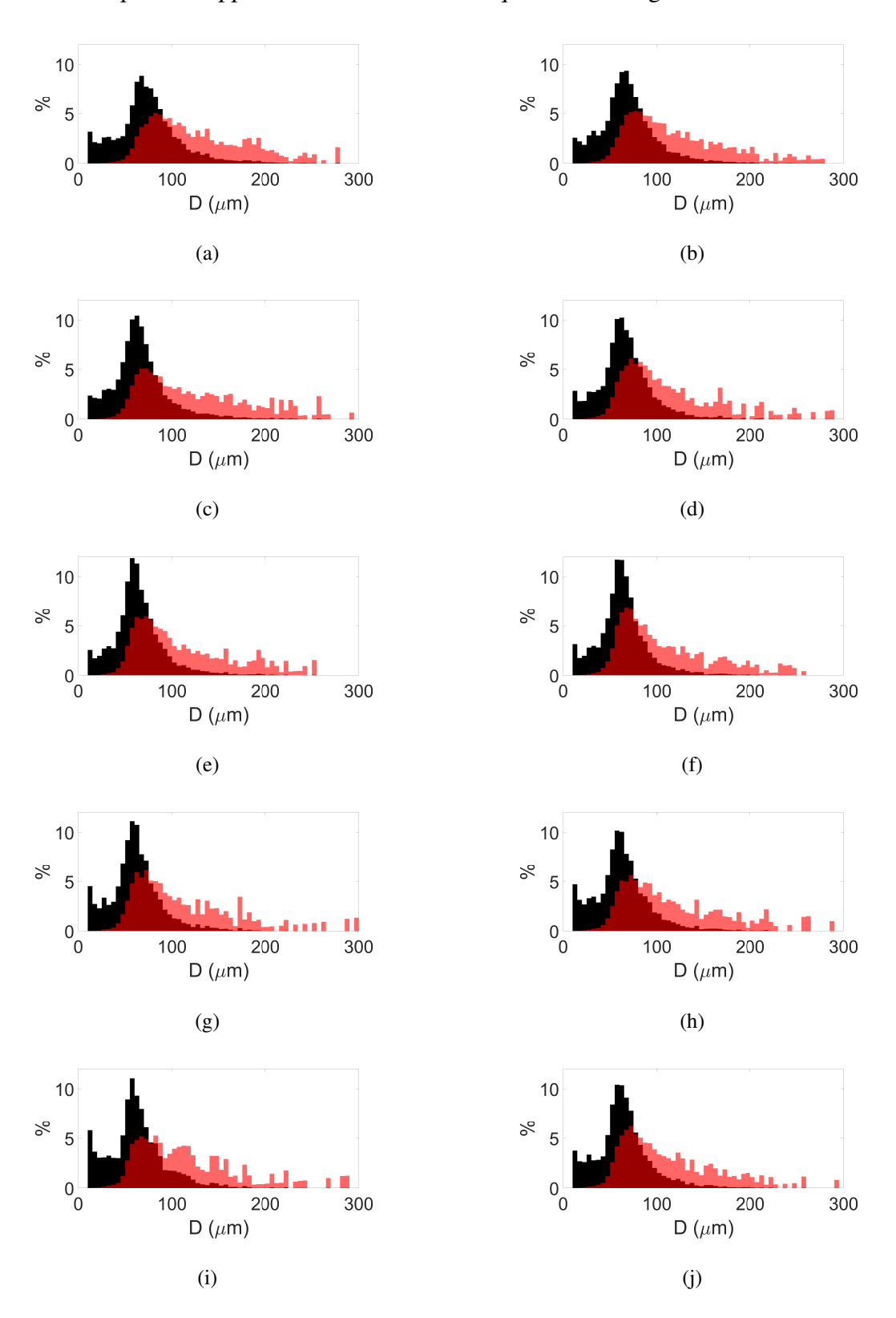


Figure 2.13: superposed Probability distributions of droplet number (black) and volume (red) for a) E100, b) E80, c) E60, d) E50, e) E40, f) E30, g) E20, h) E15, i) E10, j) E0, expressed as a percentage of overall number and total volume respectively.

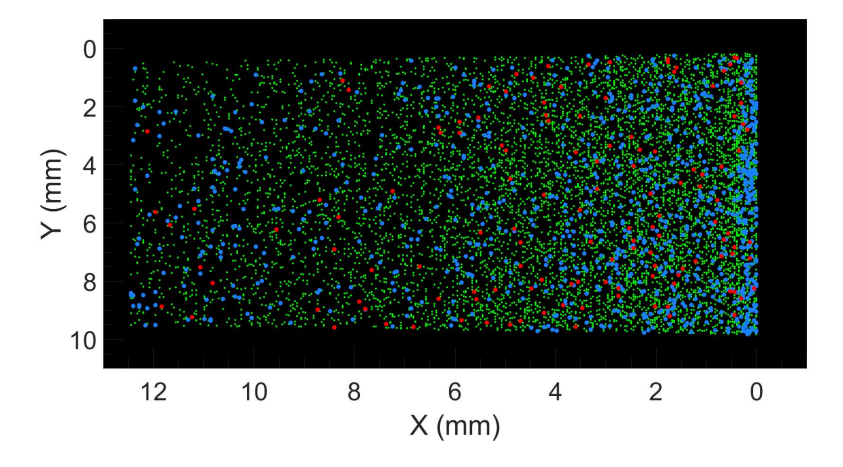


Figure 2.14: Droplet radial (X) and axial (Y) position with size: $D_{10} < 30 \ \mu \text{m}$ (Red), 30 $\mu \text{m} < D_{10} < 150 \ \mu \text{m}$ (Green), $D_{10} > 150 \ \mu \text{m}$ (Blue)

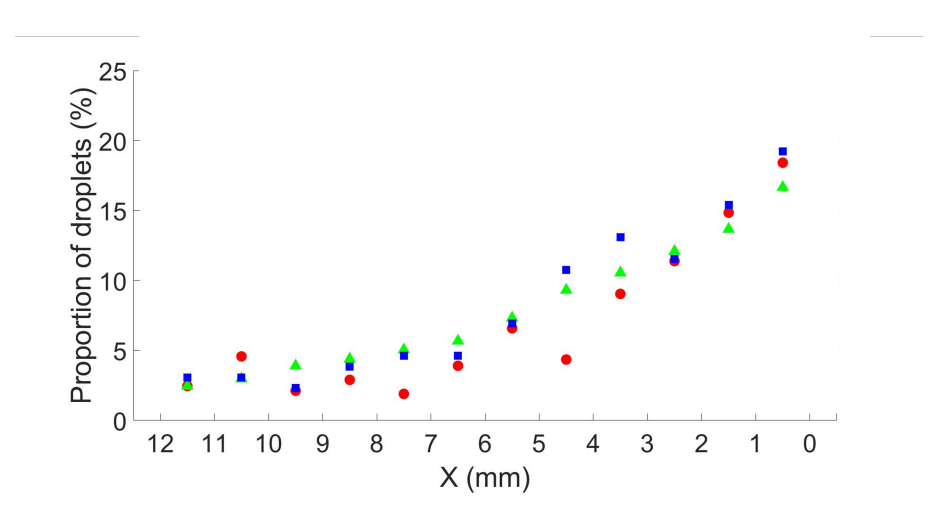


Figure 2.15: Droplet proportion with variation in radial position (X) for: $D_{10} < 30 \ \mu \text{m}$ (Red), $30 \ \mu \text{m} < D_{10} < 150 \ \mu \text{m}$ (Green), $D_{10} > 150 \ \mu \text{m}$ (Blue).

For all fuel blends a similar distribution of droplet concentration and sizes across the measurement volume was seen using the 100% ethanol content fuel blend as an example, figure 2.14 shows the spatial distribution of droplets, of three different droplet diameter ranges, within the measurement volume. Fig. 2.15 shows the change in droplet proportion with radial displacement. It can be seen that the three droplet size ranges are similarly distributed across the imaging window. The number distribution and the variation in droplet diameter are shown in Figs. 2.16(a) and (b) respectively. It can be clearly seen from the figures that no significant change

fringe of the spray.

The effect of ethanol content on the radial distribution of droplet concentration within the measurement volume was assessed, the importance of which with regards to droplet combustion, was theorised by Chiu et al. (1982). At high droplet concentration evaporation and combustion only occur at the group periphery, as inter-droplet spacing is increased a larger proportion of droplets can evaporate and the flame is able to propagate further into the droplet group. Using an IDS measurement method Sahu et al. (2018a) were able to observe inter-droplet spacing within a spray, however in the experiments performed here, as previously mentioned, a significant number of seemingly valid droplet oscillation patterns were unrecognised by the GSV processor meant reliable measurements of droplet spacing could not be performed. For such a measurement to be produced, either the processing method should be improved such that a larger proportion of valid droplets are properly recognised or a secondary analysis method be performed allowing for a statistical correction to be applied. In lieu of such methods these experiments are limited to expressing the variation in relative spatial distribution of droplets with respect to ethanol content. Figure 2.17 displays the variation in droplet distribution with radial displacement from the spray centreline for each fuel blend. It can be clearly seen that with increasing ethanol content the proportion of droplets located closer to the spray centreline decreases, whilst and increase is seen at locations for radially displaced. This would suggest that increasing ethanol content is increasing

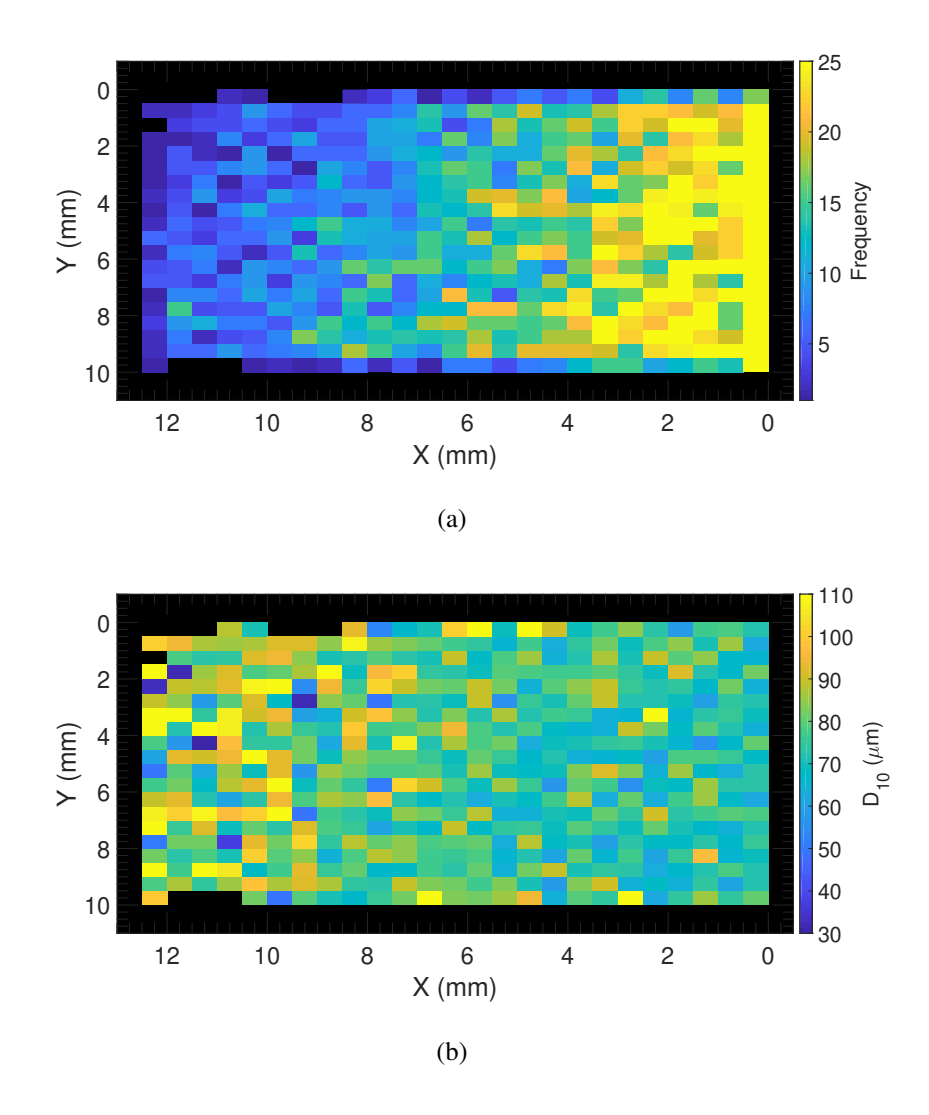


Figure 2.16: Variation in (a) Frequency and (b) D_{10} , with axial and radial displacement from the nozzle.

the cone angle and/or radial distribution of droplets, showing a general agreement with findings from studies by Gao et al. (2007) and Oh et al. (2010)

Fig. 2.18 shows the arithmetic mean diameter, D_{10} , and the SMD, D_{32} , with increasing ethanol content in gasoline. The results show that both D_{10} and D_{32} increased by $\approx 13\%$ between E0 and E100, with fluctuating trends observed below 40% ethanol content, and a stronger positive correlation noted beyond 50% ethanol content in gasoline. The observed increase in droplet diameter with increasing ethanol proportion in gasoline has been reported in previous studies investigating fully developed ethanol-gasoline sprays (Aleiferis et al., 2015; Fajgenbaum and dos

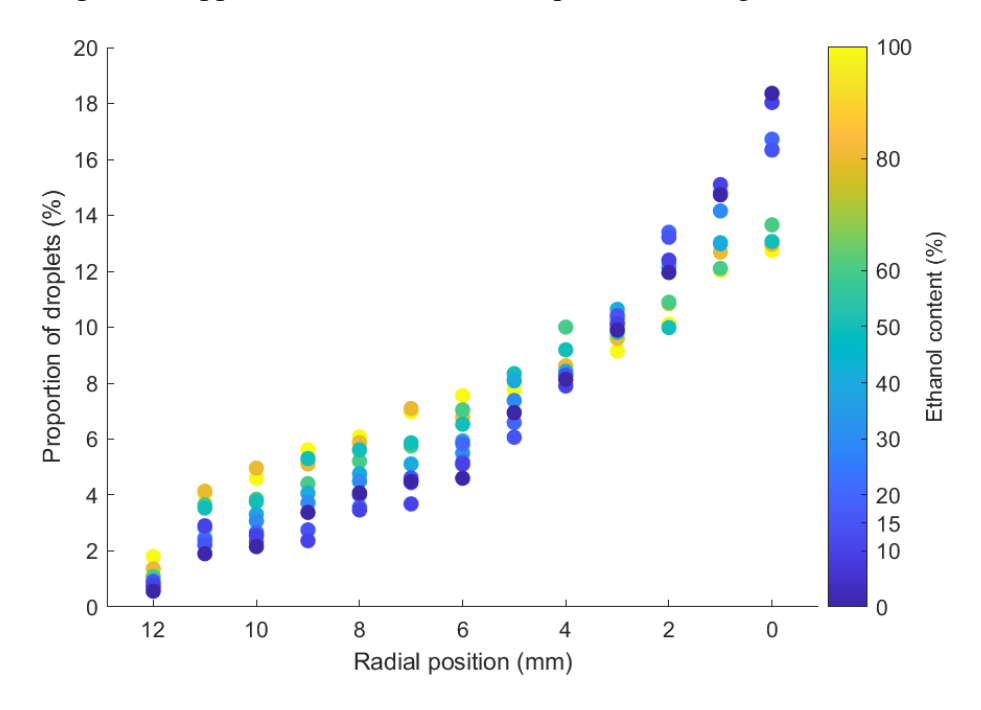


Figure 2.17: Droplet radial distribution variation with ethanol content.

Santos, 2016; Park et al., 2009). The E60 blend shows a higher D_{32} value than would be expected from the trend, this could be attributed to the presence of large diameter droplets (<200 μ m), as shown in Fig. 2.13(c). This effect is not apparent in the D_{10} as larger droplet diameters have a greater impact on SMD calculations.

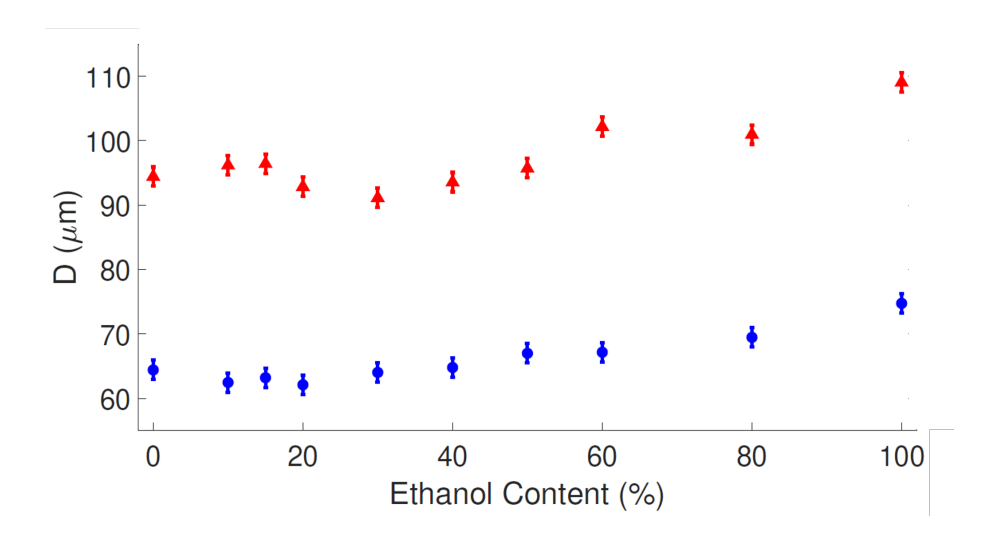


Figure 2.18: D_{32} (Red-circle) and D_{10} (Blue-triangle) values with ethanol content (%).

To further understand the observed trends for blends with less than 40% ethanol content, the analysed GSV oscillation pattern images were reviewed. A clear degra-

dation in image quality was seen with decreasing ethanol content, being most pronounced in blends E20, E15, E10 and E0. Oscillation patterns became blurred and distorted, along with an increase in the occurrence of high frequency patterns attributable to multiple frequencies. Whilst the overall number of droplets did not significantly change with ethanol percentage, and the droplet density remained below 3000 droplets per cubic centimetre in all cases, the clarity of the patterns decreased.

This visual degradation in the quality of the analysed oscillation patterns has a noticeable impact on the number of droplet measurements per image, as shown in Fig. 2.19, with a substantial reduction in the number of detected droplets for blends containing less than 40% ethanol. A possible explanation for the degradation in image quality is the change in the colouration and opacity of the droplets with varying composition of the fuel blend. As the proportion of gasoline is increased, the blend becomes increasingly opaque and coloured. This pronounces the effect of off-axis attenuation (see Section 2.2) thus resulting in weaker signals detected by the camera sensor, reducing the signal to noise ratio. Due to this, the software processor is more likely to discard oscillation patterns, hence reducing the number of droplets detected per image.

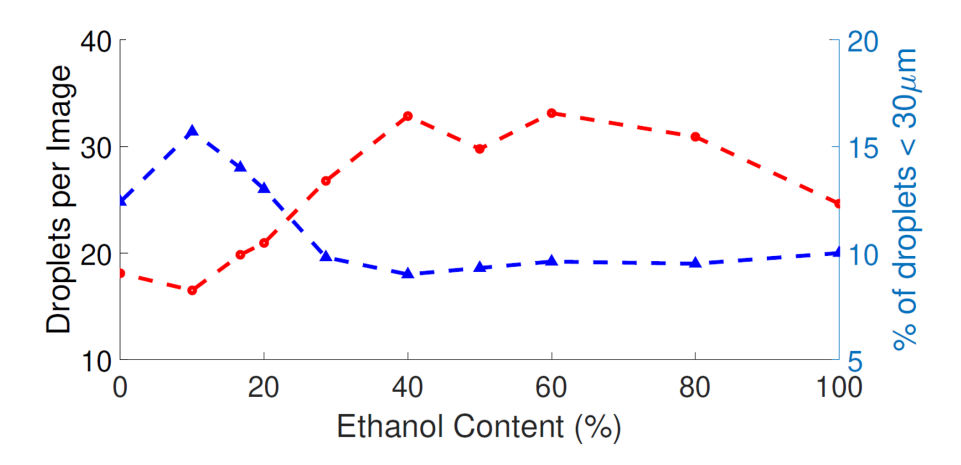


Figure 2.19: Droplets identified per image (Red) and proportion of droplets below 30 μ m (Blue) for fuel blends.

Figure 2.19 also shows the proportion of droplets below 30 μ m for the different fuel blends. It can be clearly observed from the figure that the proportion of

80 Chapter 2. Application of an IDS technique to ethanol-gasoline fuel blends droplets below 30 μ m increases as the ethanol content is reduced below 30%. This increase was also observed in Fig. 2.13, where, particularly for E10, E15 and E20, a sharp peak in droplet numbers was seen for diameters 10-15 μ m. The presence of low diameter droplets is potentially due to the erroneous detection and measurement of indistinct oscillation patterns, as described previously in Section 3. The reduction in image quality could further exacerbate the distortion of oscillation patterns, increasing the number of erroneous low diameter readings.

2.7 Conclusions

The TSI GSV system was used to acquire droplet measurements of sprays for a wide range of ethanol-gasoline blends, using a single hole PFI injector with an injection pressure of 3.5 bar. Measurements were taken in a $10 \text{ mm} \times 12 \text{ mm} \times 0.25 \text{ mm}$ measurement volume located 50 mm downstream from the injector nozzle tip and centred 20 mm radially from the spray centreline.

The GSV technique was found to be effective in measuring droplet diameters, with high repeatability, in liquid sprays with varying composition of ethanol and gasoline. The technique was able to provide a well-resolved spatial distribution of the number and size of droplets within the measurement volume, though it was noted that a significant number, approximately 30-50%, of seemingly coherent oscillation patterns were not recognised, thus preventing the direct measurement of the spatial distribution of droplet concentrations. The GSV drop sizing measurements were validated using a mono-disperse droplet generator (Flow-focusing Mono-disperse Aerosol Generator, FMAG), and an excellent agreement (within 2%) was observed.

For all ethanol-gasoline blends, distinct unimodal peaks between $\approx 60 \,\mu\text{m}$ and 75 μm were seen in all droplet size distributions. In blends with an ethanol content of 50% and more, increasing the proportion of ethanol in the fuel blend led to an increase in mean droplet diameter, as shown by both the D_{10} and D_{32} values. In fuel blends with less than 40% ethanol content there was a significant degradation in image quality, which reduced the number of droplets detected per image and increased erroneous identification of small diameter droplets. For all fuel blends,

the volumetric concentration of droplets reduced with increasing radial distance from the spray centreline, while the mean droplet diameter increased. Increasing ethanol content was seen to result in a more even radial distribution of droplets, potentially as a result of an increased cone angle.

Further investigations are required to understand reasons for the image quality degradation seen in low ethanol content blends. In addition, methods for mitigating the significant levels of incorrect measurements and apparently coherent oscillation patterns need forming in order for representative observations of the spatial distribution of droplet concentrations to be performed with GSV and potentially other IDS techniques.

Chapter 3

Development of a interferometric droplet tracking method

3.1 Chapter outline

This chapter describes the development of a Lagrangian droplet tracking algorithm, for the purposes of direct droplet evaporation measurements within sprays. The data and image processing methods used are outlined along with a detailed analysis of tracking performance and measurement uncertainty and error. To begin, a short description of current droplet evaporation measurement methods and the current status of planar droplet tracking techniques is provided.

3.2 Introduction to droplet tracking

Droplet evaporation plays a crucial role in numerous industries, from pharmaceuticals to energy generation, and reliable, accurate measurements of this physical process are essential to develop empirically derived evaporation models and inform infrastructure design and implementation. For example, such models often define the required temperatures in a spray drying facility (Cotabarren et al., 2018), or provide an estimate of the expected droplet size distribution at the point of ignition in combustion engines (Sazhin, 2006). Thus, the importance of having accurate and applicable evaporation models for industry is apparent.

Though much fundamental research has been performed in combustion and spray applications and several empirical evaporation models have been produced to address droplet evaporation in generalised cases (Hubbard et al., 1975), or for specific applications under relevant operating conditions for the vaporisation of fuel sprays (Abramzon and Sirignano, 1989), their reliability and applicability to a broader range of scenarios is hindered by the accuracy and limitations of the measurements methods to acquire the data used in the model fitting process and validation.

Typical experimental methods involve the suspension of a single liquid droplet along a fibre, thus creating a stationary droplet that can be repeatedly sized in time through optical measurements (Strizhak et al., 2018). This methodology comes with an obvious limitation as the fibre acts as a conduit for heat conduction to the centre of the liquid droplet, thus affecting the measured evaporation process.

To avoid the impact of droplet suspension fibres (Chauveau et al., 2019) acoustic levitation approaches have been developed to fix the position of a droplet in space (Yarin et al., 1999). However, this single-droplet approach to measure evaporation is still subject to several limitations, such as the difficulty to incorporate the effects of droplet volumetric concentration and multi-droplet interactions (Labowsky, 1976), and the effects of local and time dependent flow field variation, such as those present in oscillating flows (Sujith et al., 2000). With regards to fuel spray vaporisation Sahu et al. (2018a) observed that lower droplet evaporation rates are present at higher levels of droplet volumetric concentration. These observations are in agreement with theories developed for more realistic combustion conditions with multiple droplets as outlined by Chiu et al. (1982), while Balachandran et al. (2008) noted that the presence of acoustic oscillations enhanced droplet evaporation in a bluff body combustor.

Ideally measurements of the evaporation of free droplets should be carried out for spray conditions consistent with those encountered in industrial applications, thus providing a thorough characterisation of the evaporation process occurring in the actual infrastructure used within a given industry. However, given the complexity of the flow dynamics within "realistic" sprays evaporation processes, measurements in such conditions are often simplified to the comparison of time-averaged droplet diameter profiles at two or more locations within the spray. Such an approach does not allow to assess the impact of individual droplet characteristics, such as size and velocity, on the measured evaporation rates.

In order for a measurement method to directly determine evaporation rates of individual droplets the measurement technique must be able to detect, size and track each droplet in time and space. Current sizing and velocimetry techniques that allow for the direct measurement of individual droplet size can be narrowed to Phase Doppler Anemometry (PDA) and Interferometric Droplet Sizing (IDS). Whilst PDA can record the diameter of individual droplets, it is inherently a point measurement technique and there is no evident way in which it can be used to make multiple measurements of the same droplet over time to determine the rate of evaporation. IDS techniques however operate with a considerably larger measurement volume, where with the correct imaging frequency and imaging window dimensions for the given flow field velocities, a single droplet can remain in the measurement volume for multiple image captures.

A number of currently available IDS techniques such as Global Sizing Velocimetry (GSV) produced by TSI, use a double image system with short inter-capture interval to allow for measurements of droplet velocity along with droplet size. It stands to reason that this methodology could be expanded across more than two image captures, providing not only the "instantaneous" droplet diameter and velocity, but also the variation in time of droplet velocity (acceleration), droplet trajectory and, pertinent to this chapter, the rate of change of droplet diameter. Indeed, these aspects have been addressed in a previous study by Kawaguchi et al. (2010). In their work ethanol droplets were tracked over multiple frames from which the size reduction due to evaporation in a heated jet was measured. The authors then determined the evaporation rate constant and estimated evaporation times, over measurement duration of up to 14 ms, for a very small number of individual droplets. More recently a similar IDS tracking technique was proposed and implemented by Parant et al. (2021), where the time and position of dodecane droplets entering a methane flame and subject to rapid evaporation were estimated, though the presence of burnt gasses prevented direct measure of individual droplet size reduction over time. Despite the potential benefits of an interferometric tracking system, the literature describing its use, benefits and potential limitations is extremely limited.

In this chapter an in-house Lagrangian Planar Interferometric Tracking (PIT) processor, developed in MATLAB, in conjunction with an existing IDS technique, the Global Sizing Velocimetry (GSV) produced by TSI, is applied to a non-evaporating water spray to assess tracking performance and facilitate the observation of mea-

surement uncertainties. The subsequent chapter will asses the applicability PIT technique in measuring droplet evaporation of a methanol spray in a heated coaxial air flow.

3.3 Current planar interferometric sizing and velocimetry methods

To begin, it is important to understand the methodology of the current IDS velocimetry techniques, in particular TSI's GSV, this being one of the most successful IDS velocimetry techniques commercially available. Similar to Particle Imaging Velocimetry (PIV), IDS velocimetry starts with the capturing of image pairs. These being two images captured with a sufficiently small inter-capture time interval such that droplets move a measurable displacement within the measurement volume. In the case of IDS velocimetry, droplets appear as interference patterns as previously explained in Section 2.3, page 59. Typically IDS measurement techniques begin by defining the position and size of droplets from the first image of the image pair. The same analysis is then applied to the second image in the pair. Noting the position of a droplet in the first image, $D_1(x, y)$, an inspection region is created centred about this position in the second image. This is the region in which the droplet is expected to be found. Typically the dimensions of this inspection region are set based upon flow velocity, presence and scale of turbulent eddies and imaging frequency. Should one or more droplets be present within the inspection window then a series of validation steps are taken. These typically include a comparison with the global mean droplet velocity, comparison of interference pattern intensity and measured droplet diameter between the two frames. With the best matching droplet in the second frame identified, the displacement vector of the droplet between frames one and two can be determined, $D_2(x,y) - D_1(x,y)$, and with a known time interval between captures instantaneous droplet velocity can be measured. A benefit of IDS velocimetry over other particle tracking techniques is the cross correlation of the droplet size between captured images offering an additional degree of validation on particle identification.

This process is repeated for each droplet identified in the first of the image pairs, resulting in the provision of droplet diameters and two-component velocity vectors for droplets present in the image. The proposed PIT processor expands these principles to detect a droplet across more than two consecutive images.

3.4 Droplet Tracking Expansion

In order to develop the PIT technique a sequence of images with the necessary optical setup for IDS measurements was captured using a high imaging frequency. The spray used in this case was produced by an ultrasonic atomiser (SONICS ATOMIZER), this being a method of atomisation achieved through the breakup of a liquid ligament by high frequency oscillation. This spray was chosen due to its low flow rate and the ease of control of flow direction ensuring that droplets would remain within the imaging window for multiple captures. After preliminary testing a sequence of 100 images were captured at 7000 frames per second using a Phantom VEO 710 camera fitted with a Tokina 100 mm lens set to a magnification factor of 1:1. The camera and lens were moved to produce a defocus displacement of 20 mm. Illumination was provided by an EdgeWave IS-series high speed laser (532 nm), set to produce a scattering angle of 60° as shown in Figure. 3.1(a).

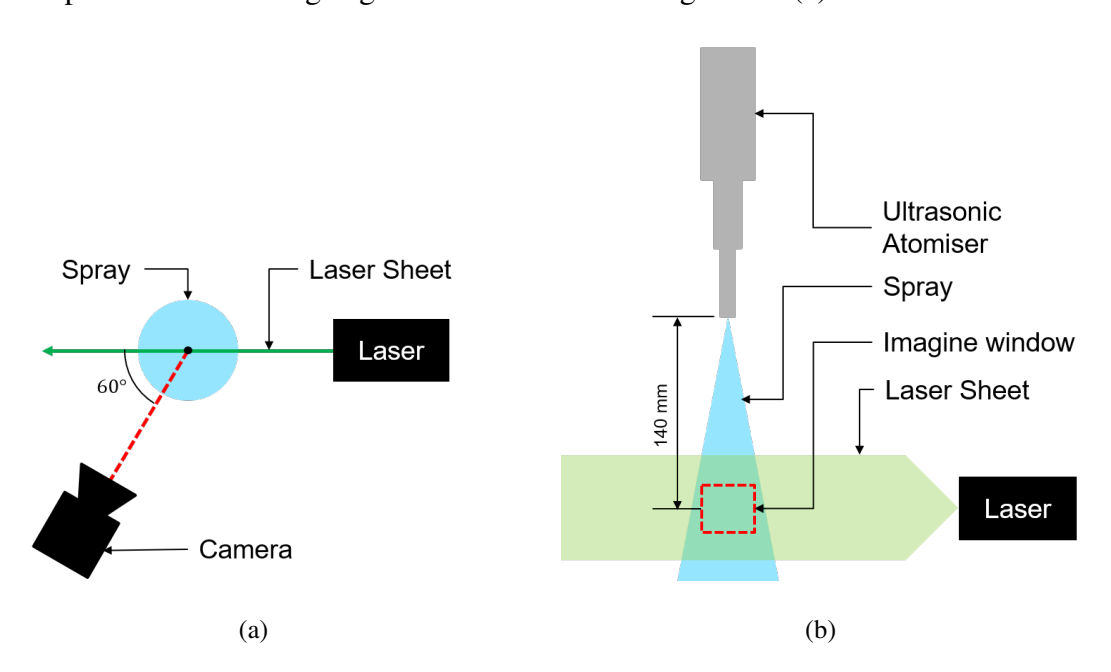


Figure 3.1: (a) GSV setup top view, (b) GSV setup side view.

88

The imaging window measured $\approx 12 \times 20$ mm, an example image is shown in Figure 3.2 (a). Initial observations showed multiple occurrences of droplets remaining within the imaging window for 5 or more consecutive images, thus providing a good starting point in the development of a multi-frame analyser.

First pass processing with GSV 3.4.1

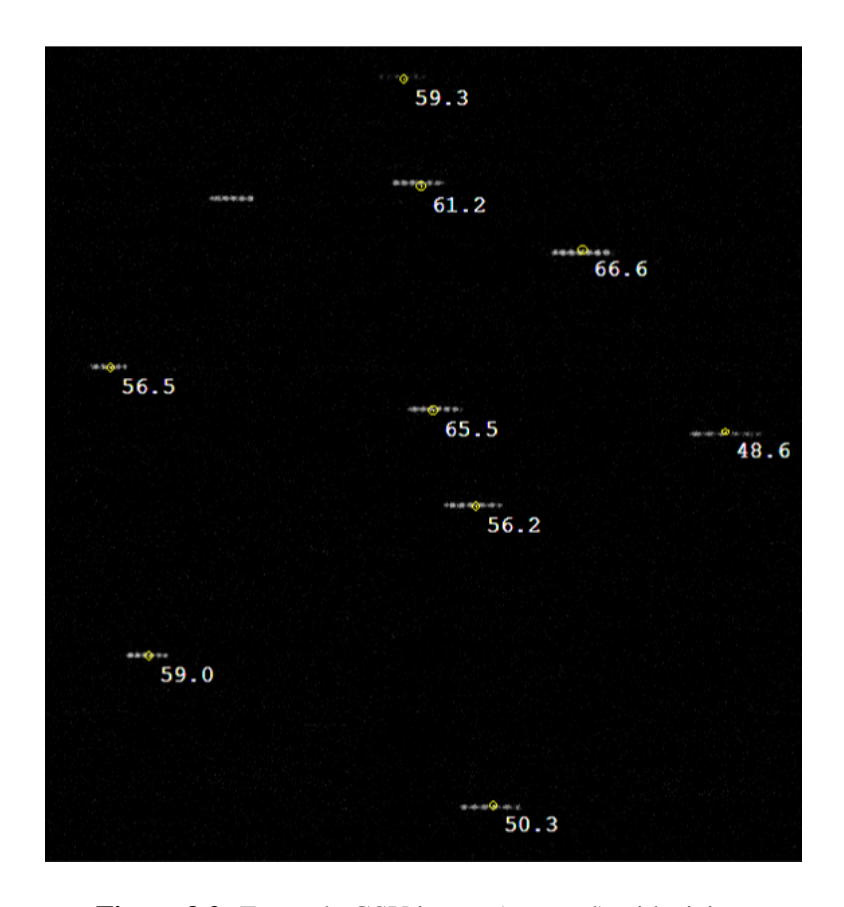


Figure 3.2: Example GSV image (cropped) with sizing.

The developed PIT processor makes use of the GSV produced by TSI, as a first pass processor (from raw images the GSV processor outputs the droplet size and 2-D position co-ordinates along with other parameters such as the intensity of interference patterns, but does not provide any tracking details). Figure 3.2 (b) shows an image analysed by GSV with droplet sizes and position markers. As shown in the block-diagram of Figure 3.3 the GSV data is given as an input to the PIT processor algorithm.

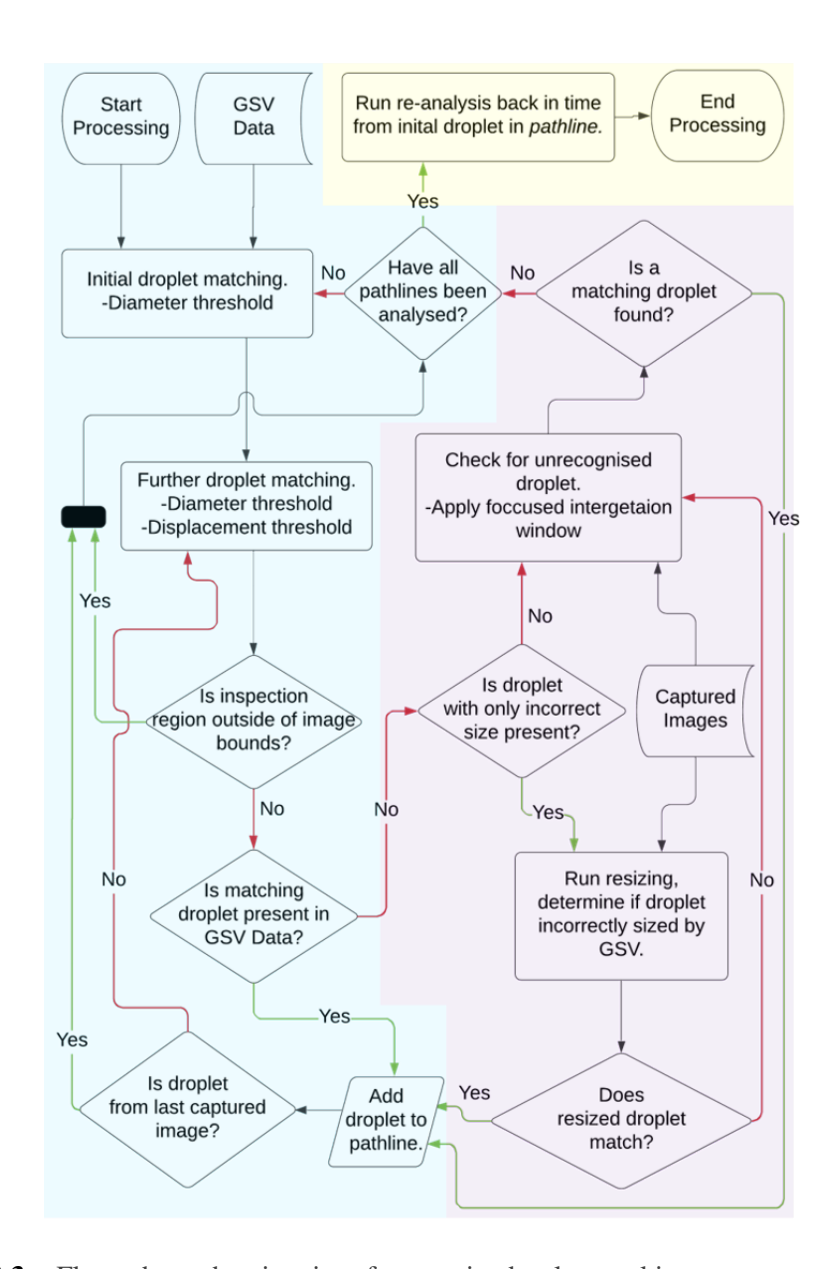


Figure 3.3: Flow chart showing interferometric droplet tracking processor algorithm. (Blue) Droplet tracking from GSV droplet data, (Purple) Re-analysis of interference patterns incorrectly measured or unrecognised by GSV processor, (Yellow) Re-analysis of droplets backwards in time.

3.4.2 Processor stage 1

The GSV data is first compiled into a single data file containing the information for all detected droplets. An additional data column is added labelling the specific image within the sequence that each individual droplet was detected. Starting with the first captured image, $Image_1$, the processor selects the first droplet, $Drop_1$, present within the compiled exported data from the GSV processor. An inspection region is then applied about the position of the droplet, $Drop_1(x,y)$, Figure 3.4 (a).

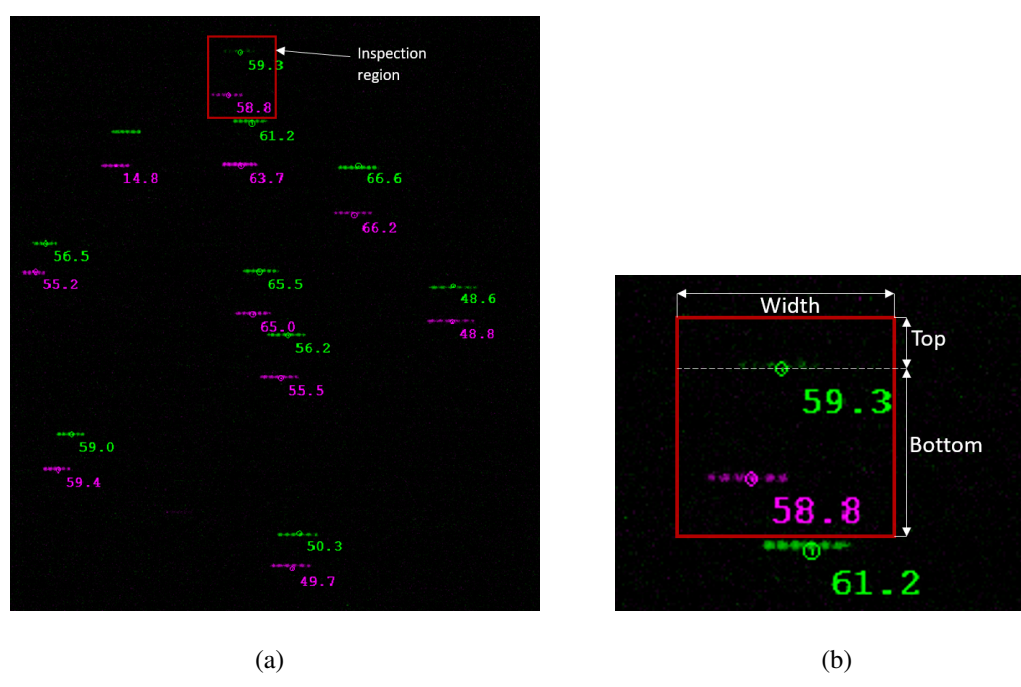


Figure 3.4: (a) Two frame composite GSV image, $Image_n$ (Green), $Image_{n+1}$ (Magenta), with inspection region (Red) located about $Drop_n(x,y)$. (b) Inspection region dimensions.

The exact dimensions of this inspection window are dependent on the local mean flow velocity and droplet expected velocity variations (resulting for example from turbulent or oscillating flow fields). The inspection region 'bottom' dimension is selected based on the realistic potential distance travelled axially between frames. The inspection region 'width' is based on the realistic potential radial movement of the droplet between frames and the 'top' dimension allows for the occurrence of reverse flow, Figure 3.4 (b). Droplet data from the second captured image, $Image_2$ is then analysed, with droplets present within the inspection region taken forward for further analysis. Matching between $Drop_1$ and the different droplets found in

the interrogation window of the second image is made by finding the $Drop_2$ whose diameter deviates the least from that of $Drop_1$. The level of allowable droplet diameter deviation is tuned with a threshold (e.g. within \pm 5% of $Drop_1$ diameter), this taking into account the measurement accuracy and potential evaporation over the time period between two consecutive images.

Having identified an individual droplet in two consecutive frames the droplet position and diameter for the droplet in both $Image_1$ and $Image_2$ is recorded, and a droplet pathline is created (this being a matrix containing the measured diameter, position, velocity and interference pattern intensity history of each droplet). In addition, a tag is added to the exported GSV data entries preventing this from being used in pathlines originating from other droplets. In case a suitable is not found in $Image_2$ the pathline is interrupted and closed.

3.4.3 Processor stage 2

The processor then moves to the third frame in the sequence, $Image_3$ and again looks for droplets within an inspection window of the same dimensions outline previously, though now positioned about the droplet's location within the second frame, $Drop_2(x,y)$. For the validation of droplet identity in $Image_3$, as well as the inter capture size difference, an additional velocity criterion is used. The position of droplets within the inspection window in the third frame is then checked against a projected 'likely' position based on a velocity vector, $Drop(v)_{1\rightarrow 2}$, created from the positions of the identified droplet in $Image_1$ and $Image_2$, (Equation 3.1).

$$Drop(v)_{1\to 2} = \frac{Drop(x,y)_2 - Drop(x,y)_1}{\Delta t}$$
(3.1)

An allowable deviation from the projected position is set, this accounting for potential non-linear droplet travel flow and the uncertainty in the position measurement. Should there be more than one droplet achieving the validation criteria, the one with the least size deviation from the previous droplet detected is selected. The processing procedure is then the same for subsequent frames, with the addition of an allowable droplet acceleration criteria, i.e. the difference in droplet velocity vector from the previous velocity vector. At this point, the number of criteria used for

droplet identification is sufficient to reliably select the seemingly correct droplet. As mentioned previously, in instances where multiple droplets meet the criteria, the one with least size deviation from the previously measured droplet is selected. In this instance should the 'incorrect' droplet be selected, it is unlikely to have significant impact on the progression of droplet tracking as the 'correct droplet' is still likely to be identified in the subsequent image, based on the projected position and velocity.

This process ends when no valid droplets are discovered or the inspection window reaches the limits of the image region. Identified droplets are added to the pathline previously created, producing a list of droplet positions, diameters, and intensities across sequential frames. Once the pathline for this first droplet is terminated, the processor begins the same procedure for the second droplet in the first frame captured. Once all pathlines for droplets present in the first captured image have been analysed the processor moves to analysing droplets which are not part of an existing pathline in the second frame. This procedure iterates itself for the entire image set.

3.5 Incorrectly-measured and unrecognised interference patterns

Though an effective measurement technique, GSV often can either incorrectly measure droplet sizes or not detect all interference patterns present in an image, Figure 3.5. Typically, only 50-75% of interference patterns are measured, with the remaining patterns not passing signal to noise ratio threshold, or not being detected at all. In addition a number of interference patterns are incorrectly analysed, typically significantly underestimated (Davies et al., 2019), preventing them from being included within a droplet *pathline*. These inconsistencies in droplet detection and sizing have an inevitable impact on the droplet tracking. To provide a more complete data set the PIT processor developed in this work re-analyses areas within an image where a droplet of a given size is expected to be according to its previous path. This extra analysis aims to correct mis-sized droplets by GSV, or measure

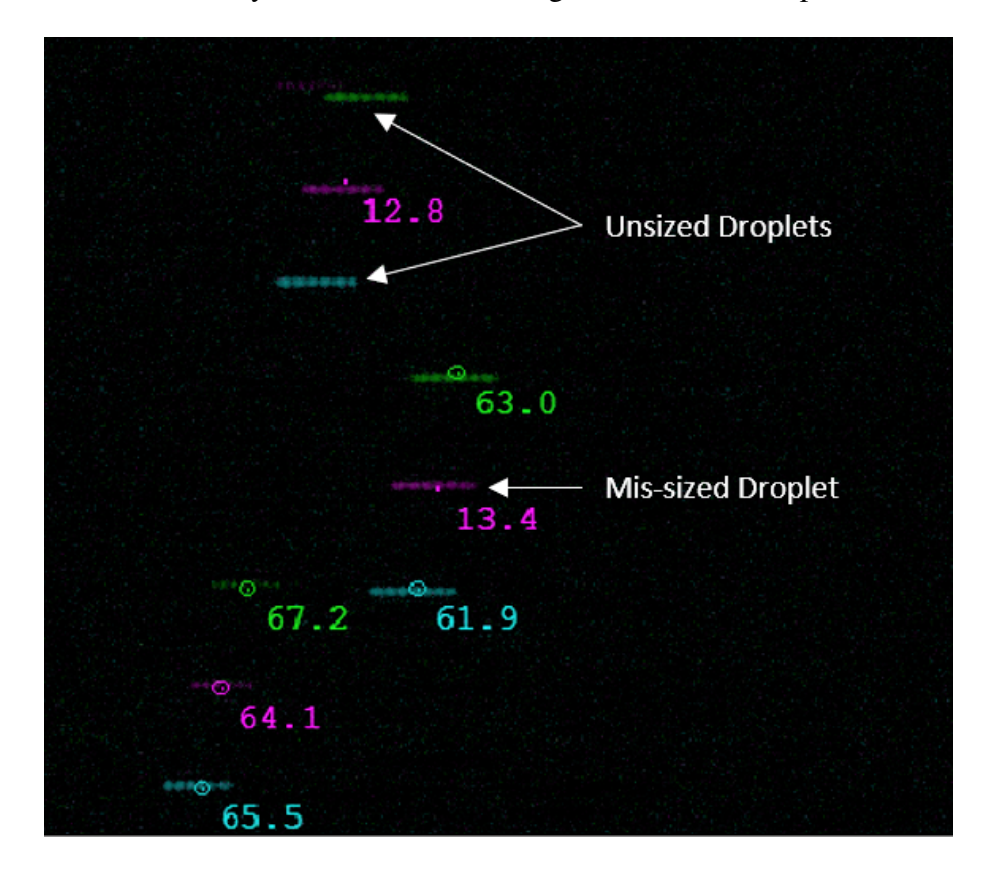


Figure 3.5: Example of incorrect measurement/detection of interference patterns. $Image_n$ (Green), $Image_{n+1}$ (Magenta) and $Image_{n+2}$ (Cyan).

interference patterns that had been originally discarded/undetected by GSV. Thus further image processing is required, which is highlighted in purple in the block diagram of Figure 3.3.

3.5.1 Positioning droplets

The method used for re-analysing interference patterns of mis-sized or unmeasured droplets revolves around the creation of a focused interrogation window centred on the expected position of the mis-sized or unmeasured interference pattern, within an image. The GSV technique makes use of a 60° scattering angle, as such pixels do not relate to a consistent dimension across the image. To relate the pixel position of droplets to their actual position in space, an image dewarp is applied during the initial GSV process. To correctly position the focused interrogation window the expected droplet position coordinates (in millimetres), need converting to

pixel coordinates, thus the image dewarp needs reversing. The dewarping methods employed by the GSV technique are shown in Equations 3.2 and 3.3, (Pan et al., 2006).

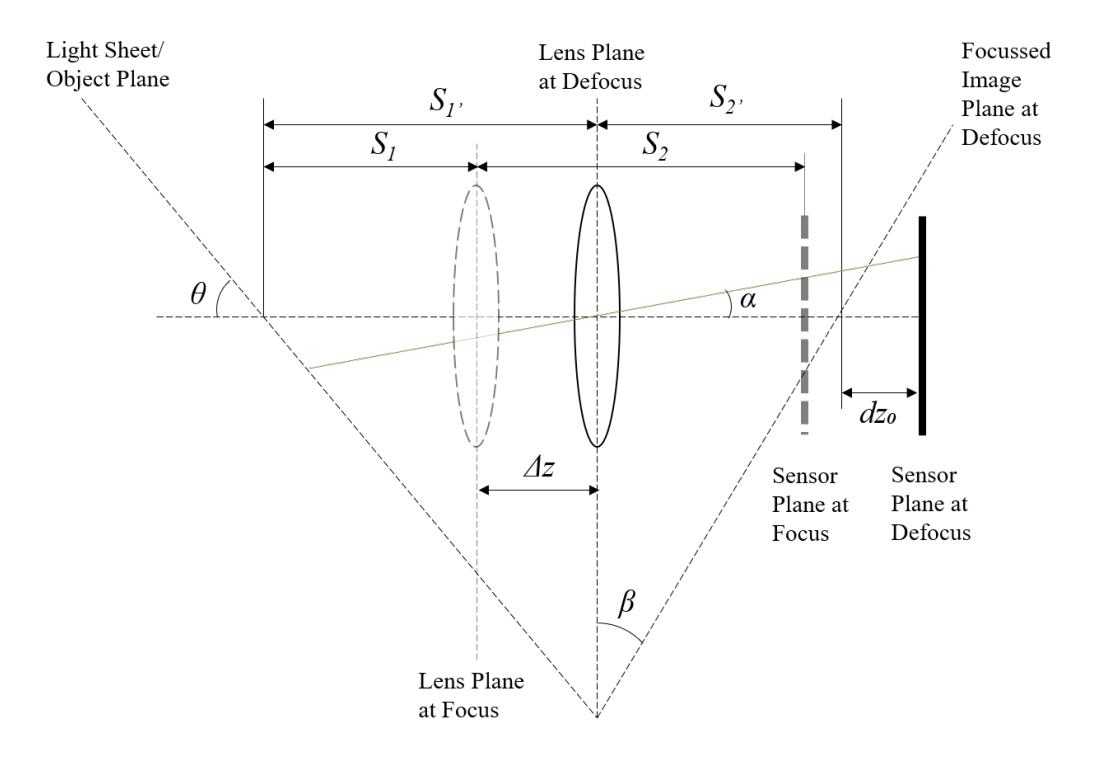


Figure 3.6: Diagram showing image defocus optical geometry for calculation of image dewarp.

$$dz = dz_0 + (1 + M_0) \cdot f \cdot sin(\alpha) \left[sin(\alpha) - cos(\alpha) \cdot tan(\alpha + \beta) \right]$$
 (3.2)

$$M = M_0 - (1 + M_0) \cdot \sin(\alpha) \left[\sin(\alpha) - \cos(\alpha) \cdot \tan(\alpha + \beta) \right]$$
 (3.3)

Where dz is the actual defocussing distance, dz_0 is the nominal defocus at the image centreline, M_0 is the nominal lens magnification after defocusing at the image centreline, f is the lens focal length at infinity focus, α is the horizontal angular position of the pixel relative to the lens axis and β is the Scheimpflug angle, as indicated in Figure. 3.6. The exact methods for calculation of the parameters listed above as used in the GSV processor are not openly available, though simple optical geometry and lens equations can be used to find them. Equations 3.4 and 3.5 show the relation between the optical magnification at focus, M_F , and when defocussed, M_0 , along the centreline of the image and the respective object to lens, S_1 and lens to image distances, S_2 , as shown in Figure 6.6.

$$M_F = \frac{S_2}{S_1} \tag{3.4}$$

$$M_0 = \frac{S_{2'}}{S_{1'}} \tag{3.5}$$

 S_2 is the lens to image distance and S_1 is the object to lens distance when at focus, with $S_{2'}$ and $S_{1'}$ corresponding to the equivalent distances after defocussing. At focus the lens to image distance, S_2 , must be equal to the effective focal length of the lens, this being dependant on the magnification and focal length at infinity, f, Equation 3.6.

$$S_2 = f \cdot (1 + M_{focus}) \tag{3.6}$$

After defocussing the lens by a distance Δz along the lens axis the object to lens distance, $S_{1'}$, can be given as:

$$S_{1'} = S_1 + \Delta z = \frac{S_2}{M_{focus}} + \Delta z$$
 (3.7)

The lens to image distance along the lens axis after defocus can be expressed as:

$$S_{2'} = f \cdot (1 + M_0) \tag{3.8}$$

Inputting Equations 3.7 and 3.8 into Equation 3.5, M_0 can be expressed as:

$$M_0 = \frac{f}{\frac{S_2}{M_{focus}} + \Delta z - f} \tag{3.9}$$

As the lens plane to image sensor distance does not change with defocussing, the nominal defocus can be determined using:

$$dz_0 = S_2 - S_{2'} \tag{3.10}$$

96

Finally the last unknown value, β , representing the Scheimpflug angle, can be determined using the equations given in Scheimpflugs's 1904 patent documents (Scheimpflug, 1904), (Steger, 2017).

$$\beta = \arctan\left(\frac{f}{S_{2'} - f} \cdot \cot \theta\right) \tag{3.11}$$

Through Equations 3.9, 3.10 and 3.11 the necessary equations 3.2 and 3.3 can be solved enabling the determination of pixel position from actual position.

3.5.2 Application of focused interrogation

Using this series of equations, a region within an image centred about the GSV coordinates of a potentially incorrectly sized droplet (case 1), or the expected position of a potentially unrecognised droplet determined through extrapolation (case 2) can be created.

- Case 1 Where a droplet has been found in two or more sequential frames and has its pathline terminated at $Image_n$ as no droplet is in the expected position or of correct size is present within $Image_{n+1}$. The processor checks the GSV data again and determines whether there are any droplets present at the expected location that have only failed the size criterion. The displacement of these potentially incorrectly sized droplets from $Image_n$ to $Image_{n+1}$ is determined and compared to the previous displacement vector, that being from $Image_{n-1}$ to $Image_n$. If the displacement vector magnitude difference is greater than a defined value (e.g. a 5% difference) that droplet will be excluded from further analysis. Should a droplet exist in $Image_{n+1}$ that fulfils the above criteria a focused interrogation region centred about its position is created within $Image_{n+1}$.
- Case 2 Should there be no GSV droplet data corresponding to $Image_{n+1}$ satisfying case 1, a focused interrogation region is centred about the expected interference pattern position determined via extrapolation of previous droplet displacement vectors as per equation 3.12. The processor checks for any interference patterns unrecognised in the initial pass present within this region.

$$Droplet(x,y)_{n-1} \rightarrow Droplet(x,y)_n \approx Droplet(x,y)_n \rightarrow Droplet(x,y)_{n+1}$$
 (3.12)

The purpose of this focused interrogation window is to re-analyse the interference pattern and determine whether the droplet is in fact that present in *Image_n* through the re-measurement of droplet diameter. Further should an interference pattern have been unrecognised its radial and axial position coordinates need defining. To ascertain whether a droplet has been either incorrectly measured or unrecognised the diameter of any interference pattern present within the focused interrogation window must be analysed, the method by which GSV achieves diameter measurements is described Pan et al. (2006), through equations 3.13 and 3.14.

$$D = X \cdot \frac{\lambda}{\Delta \zeta} \tag{3.13}$$

Where D is the droplet diameter λ is the laser wavelength in use and $\Delta\theta$ is the angular fringe spacing. The coefficient X is a constant based upon the scattering angle and liquid refractive index. As documented by Pan et al. (2006), the droplet diameter can then be determined through the use of Equations 3.13 and 3.14. At a 60° scattering angle the fringe spacing is very marginally affected by the refractive index of the liquid in use, and as such a generalised value of X = 1.129 has been used (Calabria and Massoli, 2000; Pan et al., 2006). The fringe angular spacing, $\Delta\zeta$, can be expressed in terms of the lens magnification after defocus (M), pixel size (δ) , defocusing distance (dz) and fringe spacing in pixels (n):

$$\Delta \zeta = \frac{M \cdot n \cdot \delta}{dz} \tag{3.14}$$

With M and dz, determined from equations 3.2 and 3.3 the only variable that needs to be directly measured is the spacing of fringes within the interference pattern, n.

3.5.3 Focused Interrogation Window

The process for analysing the focused window to determine droplet location and diameter is the same for both mis-measured and unrecognised droplet cases. Due

to the uncertainty in droplet position as determined by the GSV processor and the potential for non-linear movement of droplets within the flow, both the GSV coordinates of incorrectly measured droplets and the extrapolated expected position of an unrecognised droplet are unlikely to be exact. As such a region centred droplet position is analysed, Figure 3.7. The focused inspection region dimensions are selected such that the region is large enough to allow for deviation of the actual interference pattern position, whilst being targeted to the expected position of a potential interference pattern, reducing the potential of multiple interference patterns being present within the region.



Figure 3.7: Focused inspection window for interference pattern re-analysis

The pixel data contained within the focused interrogation window is then extracted from $Image_{n+1}$, producing a two-dimension pixel intensity matrix, **I**. To determine the presence of an interference pattern and, should one be present, the pixel intensity matrix is compressed to a vector by calculating the mean pixel intensity for each row within the 2-D pixel intensity matrix. Due to the vertical image compression through the use of a slit aperture, interference patterns take the form of high aspect ratio rectangles, which are aligned horizontally across the image, Figure 3.7. Thus, the presence of an interference pattern within the focused interrogation window will result in a significant peak in the mean pixel row intensity, Figure. 3.8. The position of the peak intensity value is used to determine the vertical position of the droplet centre point. To differentiate interference patterns from signal noise an intensity threshold value is set based upon the mean pixel intensity within the focused interrogation window.

Having identified the vertical positions of interference patterns contained within the focused window, a horizontal slice of the centred about the vertical po-

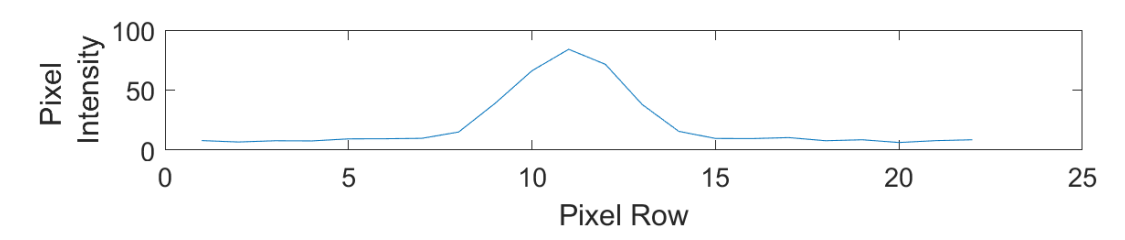


Figure 3.8: Mean row pixel intensity for focused inspection region

sition of each interference pattern is taken. The slice height is set to double the expected interference pattern height, which, due to the optical compression through the use of a slit aperture, is consistent across the entire image, Figure 3.9. The horizontal slice is then compressed vertically by taking the mean intensity of each column of the 2-D pixel intensity matrix, $\bar{\bf I}$.



Figure 3.9: Focused inspection region slice located about interference pattern vertical centre.

To define the horizontal centre point of the interference pattern a continuous wavelet transform (CWT) is used. This method was shown to be effective by Hardalupas et al. (2010, 2014) who used a Ricker wavelet as a mother wavelet. However, in this work a Morse wavelet was used as the mother wavelet, as Ricker wavelets are not supported within the MATLAB continuous wavelet transform function. The CWT analyses the input 1-D vector of interference pattern intensity which is zero padded, outputting a series of responses derived from the convolution of signal and scaled mother wavelet. Figure 3.10, displays a response at spatial periods relevant to both the total length of the interference pattern, approximately 180 pixels in this example, and that of interference pattern fringes, approximately 6 pixels, these labelled (a.) and (b.) in Figure 3.10 respectively.

Observing the highest magnitude at spatial periods relevant to the interference pattern length it can be seen that the peak magnitude very well approximates the horizontal centre point of the interference pattern, Figure 3.11. For verification, the CWT spatial period relating to interference pattern length was compared to the

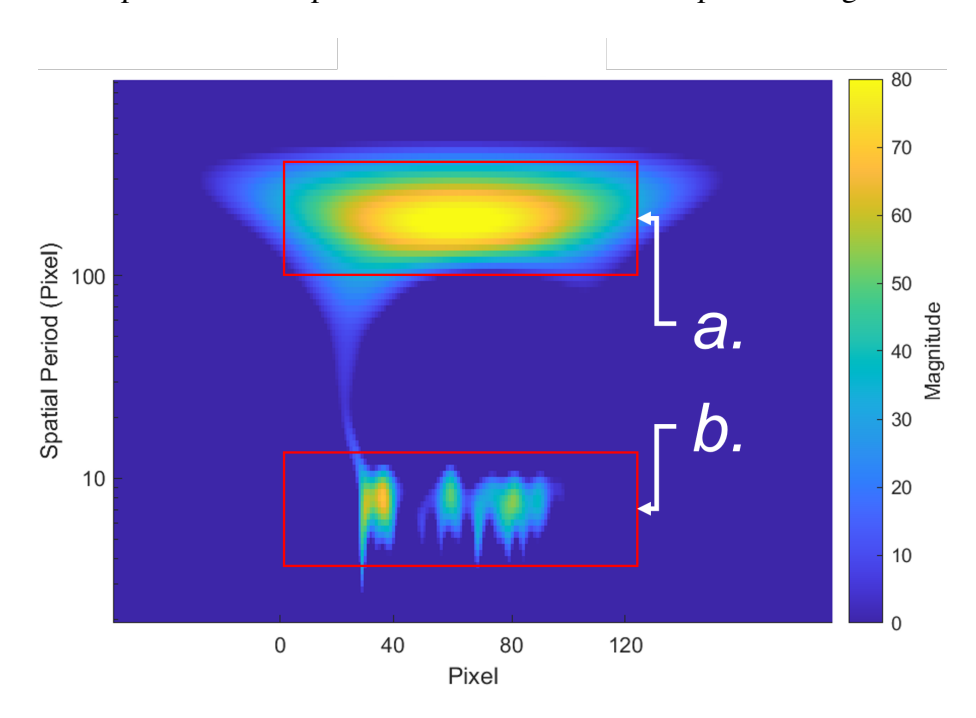


Figure 3.10: CWT Magnitude scalogram for single interference pattern, regions labeled (a.) and (b.) showing response to interference pattern length and interference pattern fringes respectively.

expected length of interference patterns. As in these experiments GSV was used as the first pass processor, the Scheimplfug condition was not in use, the length of interference patterns varies with the droplet horizontal (radial) position within the image, this being characterised through observation of a number of sample images.

Once the vertical and horizontal coordinates for interference pattern centre point within the inspection region is known, the interference pattern spatial periods are measured. A hamming taper is applied about the horizontal centre of the 1-D intensity vector of the interference pattern, $\bar{\mathbf{I}}$, Figure 3.12 (a). A fast Fourier transform (FFT) is applied to the tapered $\bar{\mathbf{I}}$ vector, the results of which are displayed in Figure 3.12 (b), in terms of spatial period. A measurement is disregarded if the ratio between the two highest peaks is less that the set signal to noise ratio. This process is repeated for all interference patterns present within the initial inspection region. That having the least difference in diameter being accepted as the droplet present in previous images.

Once the fringe spacing and centre point coordinates of the interference pattern

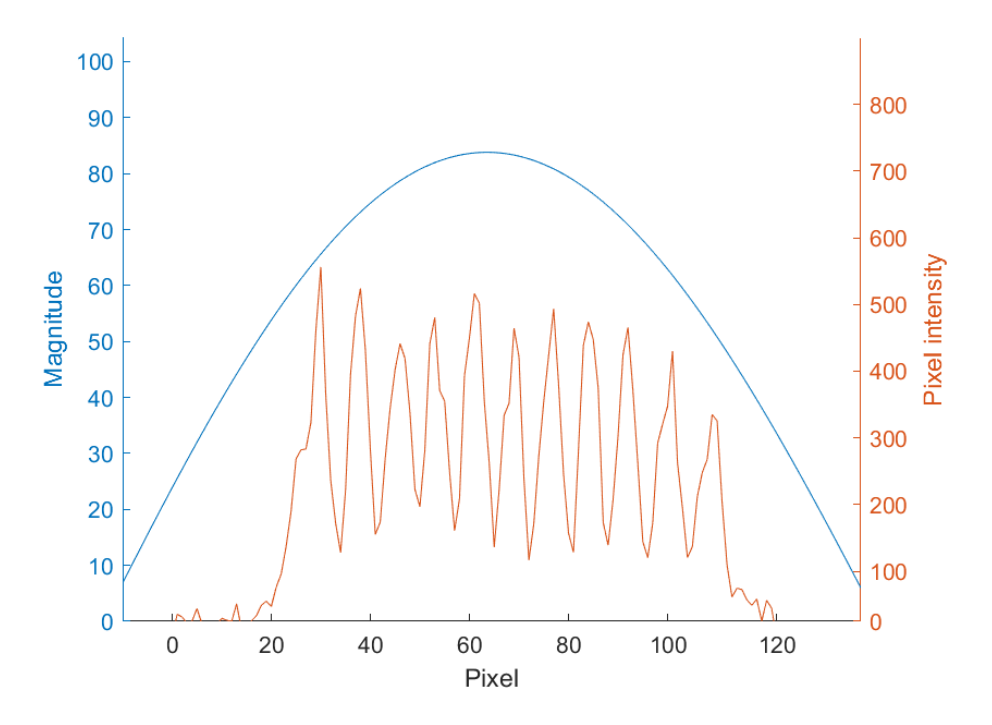


Figure 3.11: Focused inspection region slice located about interference pattern vertical centre.

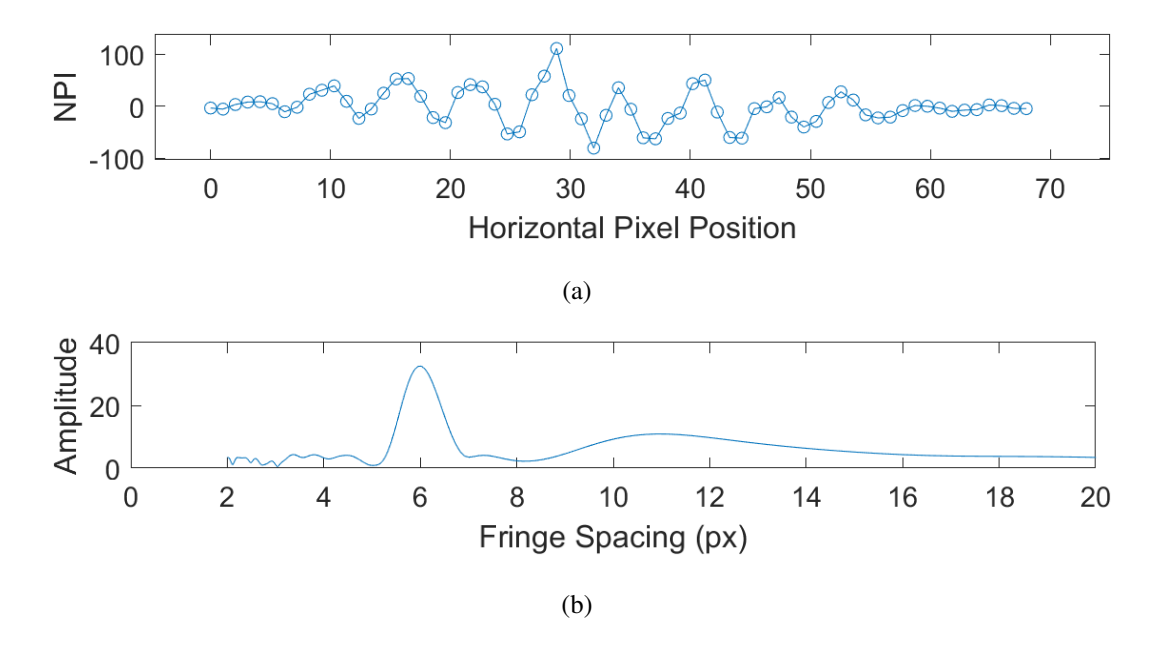


Figure 3.12: (a) Focused inspection region slice normalised mean column pixel intensity (NPI) with Hamming taper. (b) Spatial period (Fringe Spacing)

are determined the position and diameter of valid interference patterns within the focused interrogation window are known. These processing elements remove a substantial number of interruptions from droplet *pathlines*, increasing *pathline* length

102 Chapter 3. Development of a interferometric droplet tracking method were possible, providing more information on a droplets spatio-temporal evolution.

To further maximise the number of times a single droplet was measured over time, image data sets were also subject to a backward analysis, where the same process as described above was implemented starting from droplets present in the last image and extrapolating their previous position moving backward in time (yellow block in Figure 3.3).

3.6 Measurement uncertainty and performance

To asses the performance of the PIT processor and outline the potential errors present within the droplet history and position measurements a sequence of 771 images were captured at 7000 frames per second, with water being used as the atomising liquid, producing droplet concentrations at the measurement volume of up to approximately 300 drops/cm³. Experiments were carried out at atmospheric pressure and room temperature. Under these conditions droplet diameter reductions due to evaporation are likely negligible, thus any trends in temporal droplet size evolution identified in the dataset is likely due to measurement error. The specific experimental methodology will be covered in greater detail in Chapter 4.

3.6.1 Tracking diameter measurement uncertainty

The greatest source of uncertainty in the instantaneous measurement of droplet size is due to the thickness of the laser sheet and the transit time and path across the measurement volume taken by the droplet (i.e. out of plane velocity, W). All these variables directly affect the droplet defocus, which is assumed by the processor to be constant at a particular point in an image (i.e. perfect 2D plane with zero thickness). As shown in Equations 3.13 and 3.14 a droplet measured size is proportional to the actual defocus, and therefore any uncertainty in defocus directly affects the measured diameter. From geometrical considerations (see the sketch in Figure 3.13) the maximum defocus deviation, z', from the prescribed 2-D constant value, can be estimated from Equation 3.15,

$$z' = \pm \frac{L_t}{2} \cdot \sec \theta \tag{3.15}$$

where L_t is the laser sheet thickness ($\theta = 60^{\circ}$ for GSV).

In time-resolved droplet sizing the droplet defocus uncertainty can result in a non-evaporating droplet apparently increasing or decreasing in size, depending on the droplet out of plane direction. In the case of a droplet moving towards the camera, +W, the actual defocus will decrease as it travels through the laser sheet. Conversely when moving away from the camera (-W) the actual defocus increases. The effect of the droplet out of plane motion and defocus impact on droplet size can



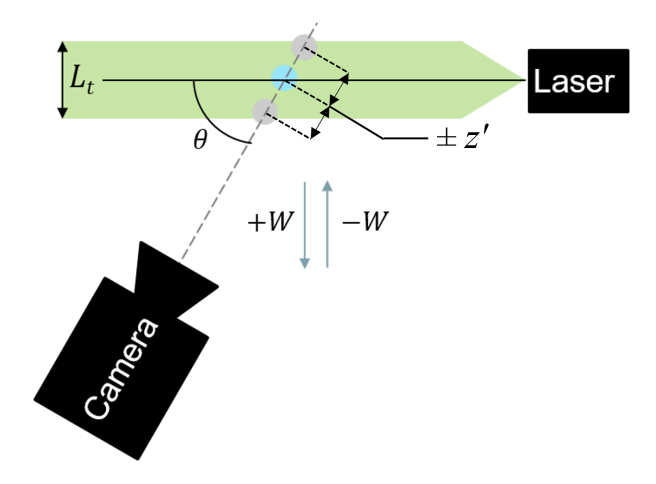


Figure 3.13: Droplet camera orientation resulting in droplet defocus uncertainty. Blue droplet representing the processor assumed defocus and grey droplets representing potential extreme defocus positions.

be determined using Equations 3.2 and 3.3, where it is apparent the error in proportional droplet surface change from initial droplet diameter (D_0) to final droplet diameter (D_f) due to change in actual defocus, E, Equation 3.16. E is only a function of the radial position of the droplet within the image, droplet out of plane direction $(\pm W)$ and the laser sheet thickness, and independent of droplet diameter. Table 3.1 shows the estimated error in final-to-initial droplet surface area ratio at the image centreline for relevant laser sheet thicknesses. (Note: these values may change for different optical setups).

$$E = \frac{D_f^2}{D_0^2} \tag{3.16}$$

Figure 3.14 shows the variation of the measured final-to-initial droplet external surface area ratio, against their corresponding mean radial positions for water droplets at a temperature of 300 K. The dashed lines indicate the theoretical maximum potential error magnitude, E, due to defocus for three possible laser thicknesses, L_t =1, 1.5 and 2 mm. The experiments were run with water and taking into account the temperature, the size of the interrogation window and measurement timescale, no significant evaporation is expected for these conditions (i.e. no variation of D_f/D_0). However, according to Figure 3.14 the variation of measured

Effective Laser Sheet Thickness (mm)	E[+W] (%)	E [-W] (%)
0.25	-2.47	2.53
0.50	-4.88	5.13
1.00	-9.52	10.52
2.00	-18.14	22.16

Table 3.1: Calculated proportional droplet surface area change due to out of plane velocity at image centreline.

droplet surface from its initial value can vary between 5 to 20%. It is clear that the apparent increase or decrease in final-to-initial external surface area ratio closely follows the variation in the theoretical error due to droplet defocus with radial distance. Deviations from the expected error being due to the processor prematurely ending the tracking of a droplet. Not following the droplet for the entirety of its measurement volume transit, results in proportional diameter changes less than expected. In addition, the processor may incorrectly track multiple droplets of similar size as a single droplet, potentially resulting in larger increases in droplet diameter.

Figure 3.15 (a, b) illustrates how the out of plane velocity, W, magnitude and direction affect the droplet measurement as droplets transit through the laser sheet. In the case of the two droplets with a decreasing defocus, +W, dark blue and light blue dots in Figure 3.15 (a), they will both experience the same level of defocus, resulting in an erroneous proportional droplet diameter change. However, the dark blue droplet will go through this process in a shorter time and therefore exhibits an erroneous higher rate of droplet surface area variation, which is captured in Figure 3.15 (b) by the gradient of the dotted lines .

It is possible to correct for the measurement error due to the variation of the droplet defocus across the measurement volume when the out of plane droplet direction is known. In non-evaporating conditions, droplet out of plane direction can be

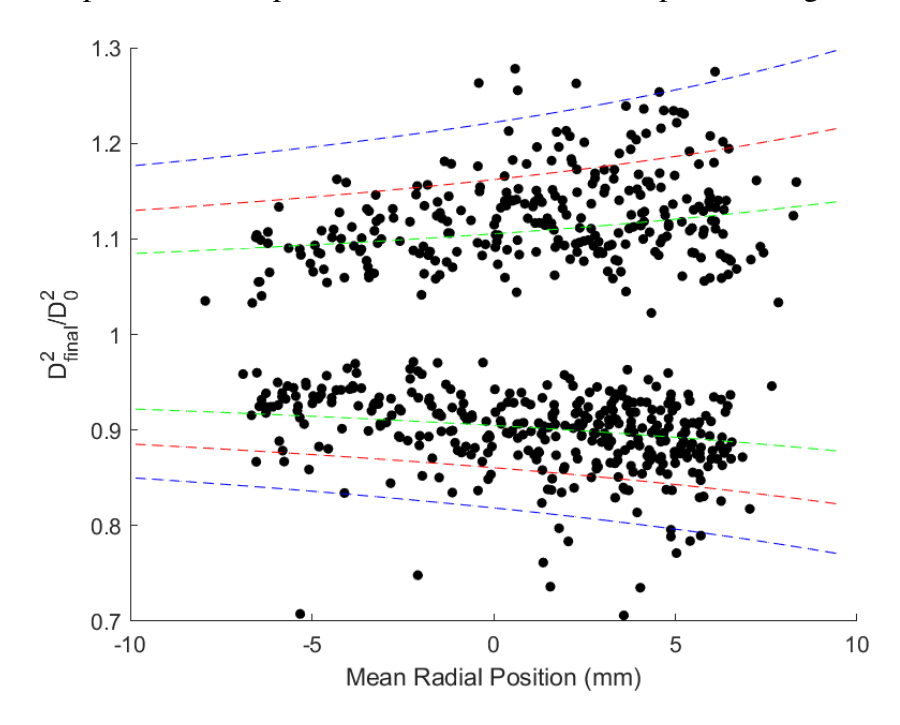


Figure 3.14: Final-to-initial droplet surface area ratio for non-evaporating spray, markers showing experimental data. Dashed lines showing expected error due to defocus variation with laser thickness transit for sheet of thickness: 2 mm (Blue), 1.5 mm (Red), 1.0 mm (Green).

determined by observing whether measured droplet diameter increases or decreases with time¹. This is well elucidated in equations 3.17 - 3.19.

$$\frac{D'^2}{D_0'^2} = \frac{D^2}{D_0^2} \pm \frac{E}{t_{total}} \cdot t \tag{3.17}$$

Where D_0' is the measured droplet diameter at t = 0, D' is the measured droplet size at t = t, D_0 is the actual initial droplet diameter at t = 0, D' is the actual droplet size at t, where $0 < t < t_{total}$, t_{total} being the time taken for the droplet to completely transit the laser sheet thickness. As no appreciable droplet diameter change is likely in the experimental conditions the actual droplet surface area should not vary overtime.

¹In evaporating conditions, it is not sufficient to determine the out of plane direction through observing the droplet diameter change

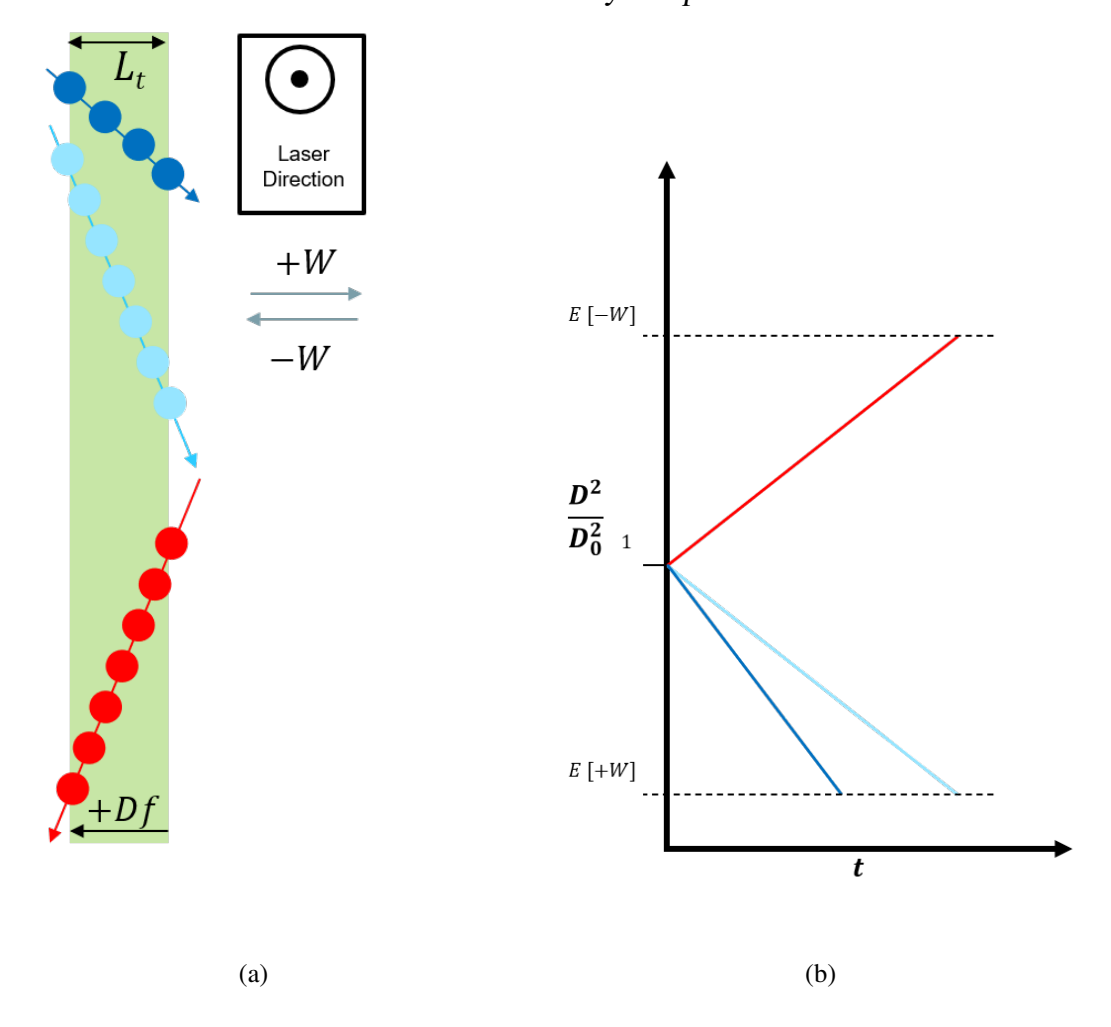


Figure 3.15: (a) Diagram showing three droplets (Dark Blue, Light Blue and Red) transiting laser sheet thickness due to their out of plane velocity, W, (b) Proportion droplet surface area versus time for the three droplets.

$$\frac{D^{\prime 2}}{D_0^{\prime 2}} = \frac{D_0^{\prime 2}}{D_0^{\prime 2}} \pm \frac{E}{t_{total}} \cdot t \tag{3.18}$$

Reorganising equation 3.18 it is clear the error associated with defocus variation due to out of plane motion will manifest as a linear increase or decrease in droplet diameter with time.

$$D^{\prime 2} \mp \frac{E \cdot D_0^{\prime 2}}{t_{total}} \cdot t = D_0^{\prime 2} \tag{3.19}$$

As E, D'_0 , t_{total} and t are known values it is possible to remove this error through subtraction. It should be noted that this error subtraction is applicable only

to droplets, which could be tracked across the entire control volume thickness (i.e. between the front and back faces of the laser sheet). This process can be monitored by checking the intensity of the light scattered signal of the same droplet at different instances, as this will display an increase (decrease) as the droplet moves towards (away from) the mid-section of the laser sheet thickness (i.e. the laser sheet intensity has a gaussian-like distribution across its thickness).

$$D^{\prime 2} \mp \frac{E \cdot D_0^{\prime 2}}{t_{total}} \cdot t = D_0^{\prime 2}$$
 (3.20)

Figure 3.16 shows the corrected droplet diameter variation with time for five water droplets in an unheated air flow (air flow temperature of 255 K). In this case droplets were determined to fully transit the laser sheet thickness via observation. From the figure it is apparent that after correction droplets diameter does not change appreciably with time.

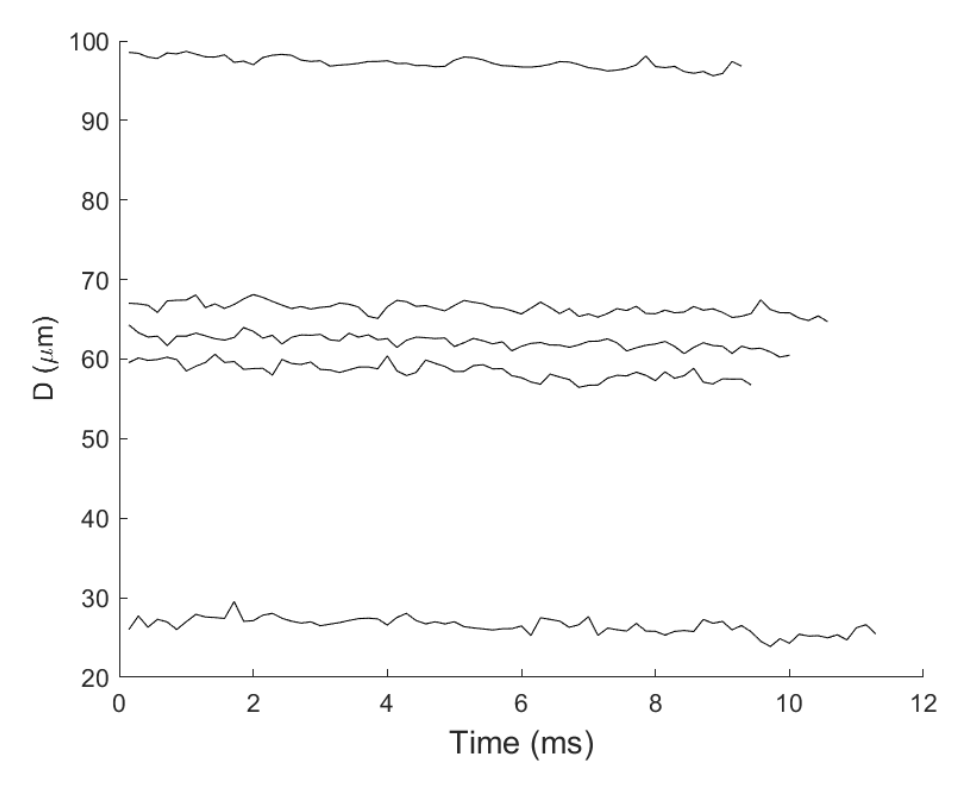


Figure 3.16: Example of droplet diameter measurement variation due to measurement for five droplets

Another method to determine the direction of droplet out of plane motion is

to observe the change in interference pattern width as the droplet transits the laser sheet (see Damaschke et al. (2002, 2005) and Kawaguchi et al. (2010)). As the interference pattern width is independent of droplet diameter, this method can be used to determine the out of plane direction of droplets in evaporating conditions. Knowing whether droplet interference pattern width is increasing or decreasing with time can be used to determine whether the droplet is traveling away from or towards the camera.

Using the data gathered in these experiments for non-evaporating droplets, the effectiveness of an interference pattern width measurement method at determining droplet out of plane direction was compared against the likely out of plane direction determined through observing the erroneous increase or decrease in droplet diameter.

Blob analysis was used to determine the width of interference patterns within the focused inspection window, figure 3.9. Interference pattern widths were typically seen to increase or decrease by 10 to 12 pixels depending on the radial position of the droplet within the measurement volume. Interference pattern width measurements showed a significant level of random error as droplets entered and exited the laser sheet, with the width measurements fluctuating by 3-5 pixels from measurement to measurement. On further analysis it became evident that at lower interference pattern intensities, seen with smaller droplets and those entering and exiting the laser plane, the image processor struggled to distinguish the peripheral fringes from signal noise. As such only larger droplets, with longer residence times provided interference patterns with sufficient intensities such that multiple measurements of interference pattern width could be made. In the situation where D>70 μ m and residence times (t>10 ms) the interference pattern width measurement method was in agreement with the expected out of plane direction based on apparent droplet size change of approximately 85% of the time.

The relatively low reliability in determining out of plane direction using this measurement method meant it was not further used, instead the impact of the error due to out of plane motion on droplet diameter measurement in evaporating conditions would be assessed. The issues in measuring interference pattern width are likely made worse by the relatively large pixel size in use (20 μ m), limiting the imaging resolution, though the noted problems were similarly experienced by Sugimoto et al. (2006) when trying to determine the out-of-plane velocity from the rate of change of interference pattern width. Potential improvements to this method are further discussed in Chapter 7.

3.6.2 Tracking diameter uncertainty

As discussed in the Section 2.4 all IDS measurement techniques, including GSV are susceptible to a degree of droplet diameter measurement uncertainty originating from signal noise, aliasing, attenuation and the multiple scattering of light. Indeed the tracking software offers an opportunity to observe and define the measurement repeatably as the same droplet is measured multiple times during its transit of the measurement region. From Figure 3.16, it can be seen that for all five droplets the measured diameter varies randomly by as much as $\pm 2\mu m$. This degree of variation is consistent across the full data set 2 .

To ensure the difference between the GSV and PIT droplet sizing methods are not beyond the expected measurement uncertainty, a large sample of individual droplets (>15,000) were measured by both GSV and PIT. Figures 3.17 (a) and (b) show the difference in droplet diameter measurement between the GSV and tracking methods relative to droplet radial and axial positions respectively. It can be seen that the tracking software measurement is typically slightly larger than that measured by GSV, though the mean differences are within 0.5 μ m for all regions of the image. The variation in differences between GSV and tracking software is also relatively small with an average standard deviation across all regions of the image being 0.75 μ m.

Figure 3.18 shows the difference in measurement methods with respect to droplet diameter, it can be seen that the mean difference is relatively consistent across the spectrum of droplet diameters. The standard deviation however is seen to

²Correction applied per equations 3.17 - 3.19 does not affect the measurement uncertainty, demonstrated in figure 3.16.

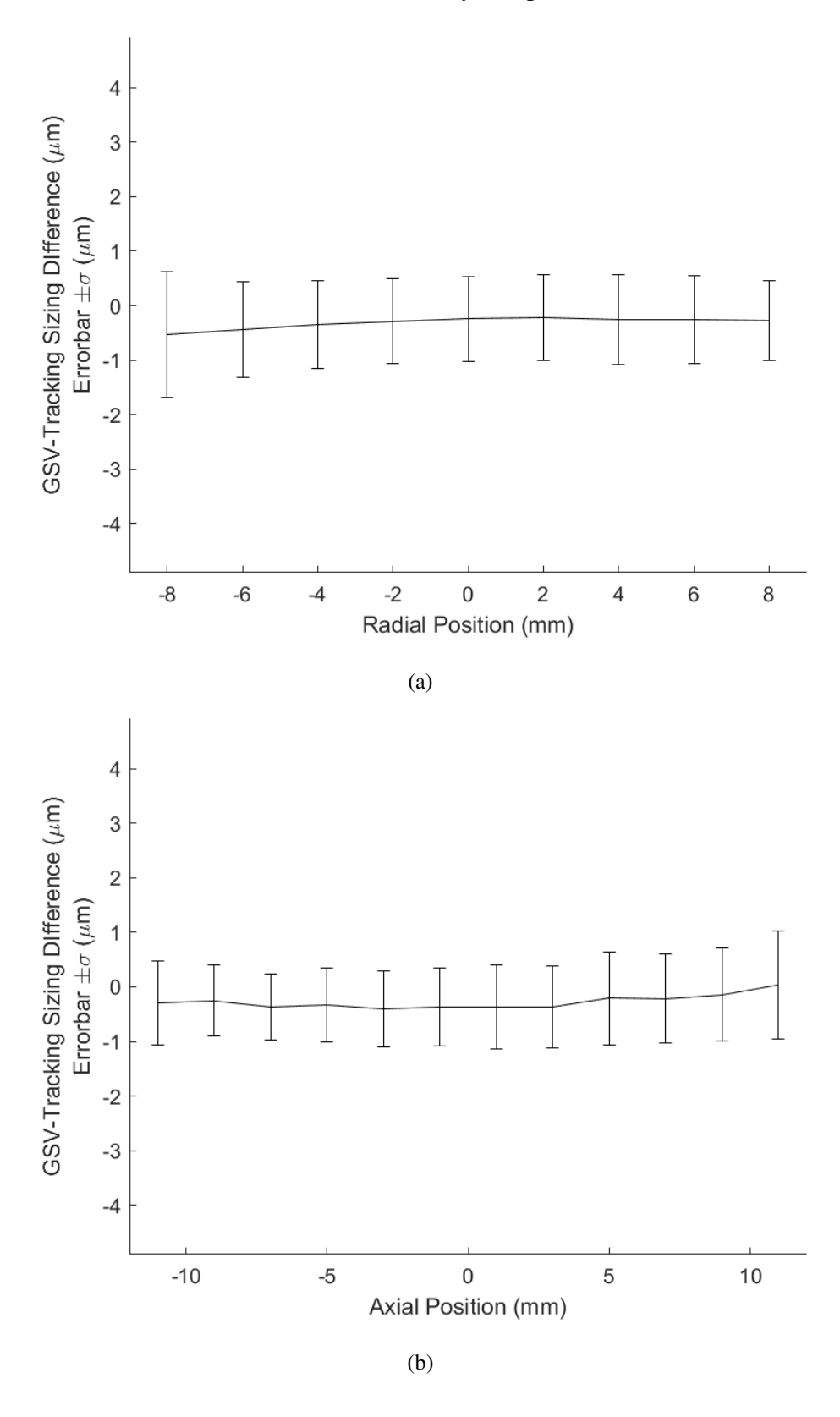


Figure 3.17: Difference between GSV and Tracking diameter measurement with respect to droplet (a) radial location (b) axial location

decrease with increasing droplet diameter, with the standard deviation for droplets from 30-50 μ m having a standard deviation of $\approx 1.00~\mu$ m. This almost halving for droplets from 80-85 μ m, $\approx 0.6~\mu$ m. The measured differences between standard GSV and tracking processors compare well to the general uncertainty in standard GSV measurements, described in section 2.5, suggesting there is no considerable addition of uncertainty with the use of the PIT processor.

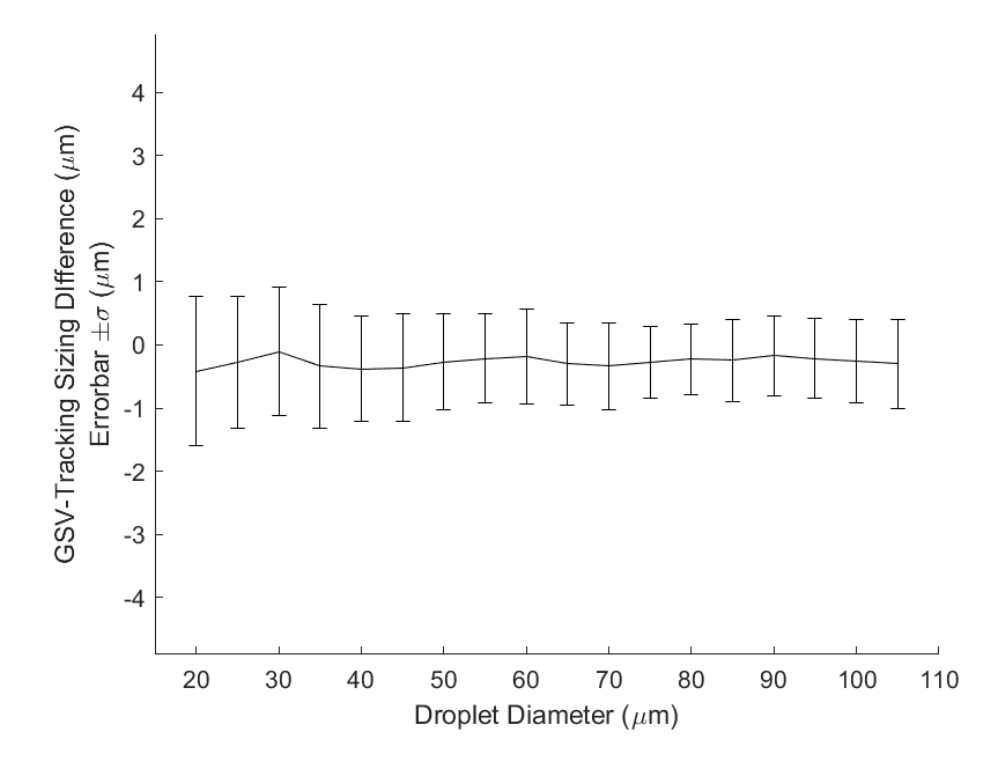


Figure 3.18: Difference between GSV and Tracking diameter measurement with respect to droplet diameter

3.6.3 Tracking position uncertainty

In addition to the droplet diameter the tracking processor must also be able to reliably determine the position of the droplet, this being particularly important when analysing the variation in droplet velocity with time. A comparison of the GSV and tracking processor droplet position, for the same droplet, is used to determine the relative uncertainty of droplet positioning within the tracking processor. The mean droplet axial position difference between tracking and GSV was approximately 0.05 mm with a standard deviation of approximately 0.1 mm, this difference being con-

sistent with variation in droplet position within the image. It is apparent that the radial position of the droplet within the image affects the difference between GSV and tracking positioning, Figure 3.19. A likely cause for this is the tracking processor not accounting for the centre discrepancy. The centre discrepancy, as outlined in Hardalupas et al. (2010), is the difference between interference pattern centre and the actual droplet centre point. Given the research intentions for this current iteration of tracking processor, in which the radial velocity variation is not the main focus, The radial droplet positions determined by the tracking processor are corrected based upon the difference between GSV and tracking positions.

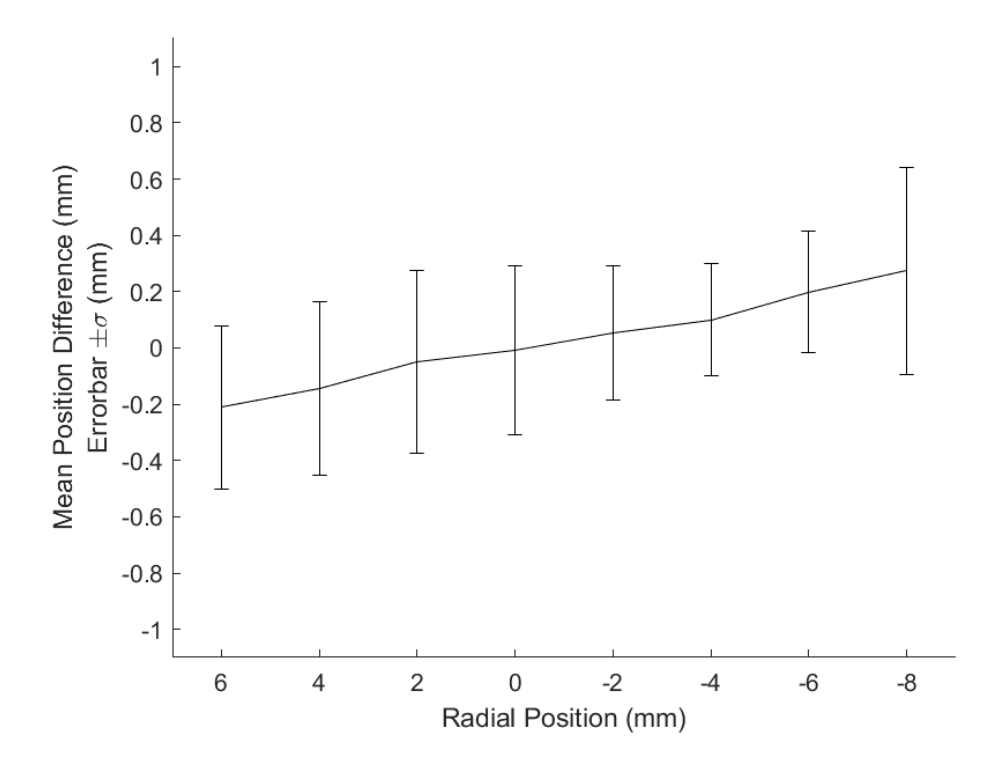


Figure 3.19: Difference between GSV and Tracking radial position measurement

3.6.4 Tracking performance

Along with the measurement uncertainty, the relative performance of the tracking software in comparison to standard GSV must also be considered when gauging the tracking processor performance. In the event of the standard GSV image processor either miss-sizing or not measuring seemingly valid droplet interference patterns, the tracking processor must use position interpolation and extrapolation to

determine the location of missing droplets. In doing so the tracking software can better measure the droplet characteristics for a greater proportion of its residence time within the measurement volume. From the 771 captured images the standard GSV image processor detected and measured 31,510 interference patterns of which 23,541 passed the validation criteria set and were used in the tracking of droplets. An additional 11,100 interference patterns were detected by the tracking processor that had been either miss-sized or unmeasured by the standard GSV image processor. These 11,100 interference patterns had their diameter and position determined and then included into a droplet path as part of the tracking data. This equates to a 47.3% increase in valid interference patterns being included in droplet tracking through the use of the tracking processor.

From this set of images a particular droplet was tracked over a sequence of 182 images (26 ms) with 118 of the 182 interference pattern measurements being made by the tracking processor. The performance of the tracking processor in this example highlights in particular the importance of the extrapolation of droplet positions, enabling otherwise unrecognised or incorrectly sized droplets to be measured and recorded. Not only does this benefit the primary measurements of droplet position and diameter history, but also greatly reduces the errors previously present within measurements of droplet concentration spatial distribution. Figure 3.20 shows an example of the temporal evolution of measurement volume droplet concentration measured using GSV only and GSV and PIT. Though the trends shown closely match between measurement methods, the data collected using only GSV is consistently ≈33% lower than the combined GSV and PIT measurements across the recorded duration. The increase is the number of measured droplets, not only improves data rate, but also enables IDS methods to better approximate localised droplet concentrations.

3.7 Summary

To summarise a new Lagrangian Planar Interferometric Tracking (PIT) processor has been developed. From an initial processing pass performed by the TSI Global

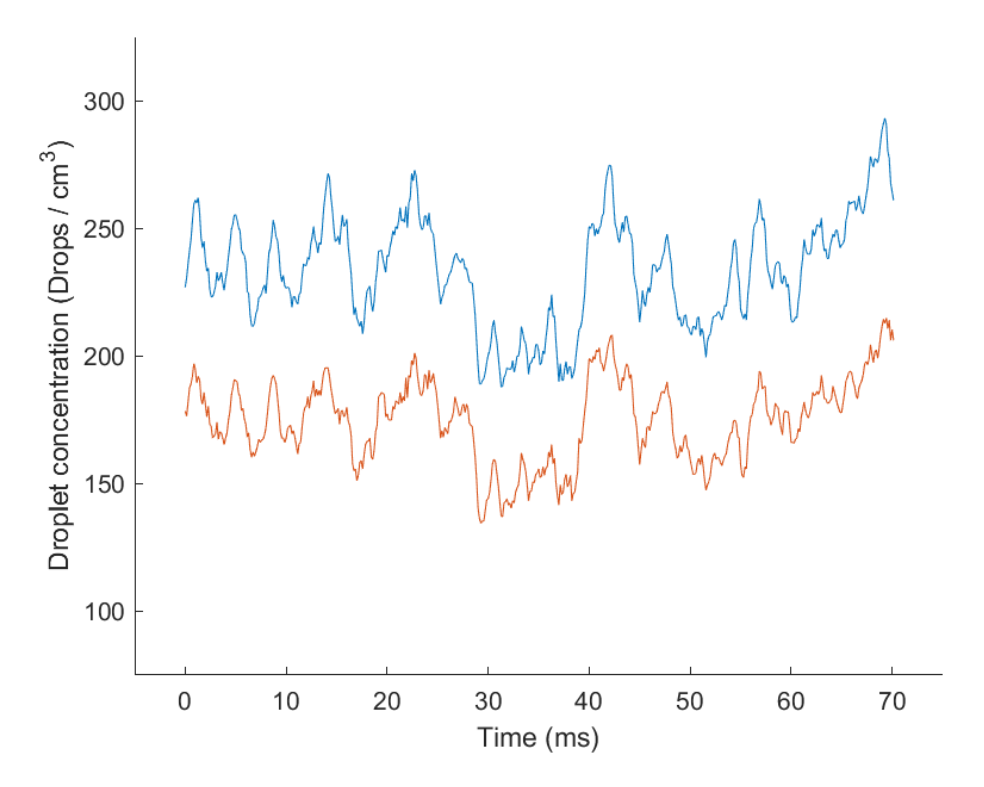


Figure 3.20: Droplet volumetric concentration with time for GSV data only (Red) and GSV and additional PIT data (Blue).

Sizing Velocimetry, GSV, droplet diameters and positions within the image window are determined. From this initial data individual droplets are identified and tracked over multiple frames through a combination of validation factors. In the event that the GSV processor incorrectly analyses an interference pattern the PIT processor uses a targeted Fast Fourier Transform to re-analyse image regions, thus allowing to further track individual droplets. The use of re-measurement increased the number of valid droplet measurements used in tracking by 47.3% as compared to those identified by the GSV processor.

Analysis of the PIT re-measurement showed diameter measurement uncertainty to be of similar a magnitude as that seen in conventional GSV measurements. The ability of the PIT processor to accurately determine the droplet position within the imaging window was successful. Direct comparisons between droplet position as measured by GSV and PIT showed a mean difference in axial droplet position of 0.05 mm and a standard deviation of 0.1 mm, radial position differences where higher due to the PIT processor not accounting for a centre discrepancy, though

116 Chapter 3. Development of a interferometric droplet tracking method after statistical correction mean difference between measurements was reduced to 0.08 mm with a standard deviation of 0.23 mm.

From observing droplet diameter change over time, an inherent measurement uncertainty within all planar interferometric droplet sizing (IDS) techniques became apparent. Uncertainty in the actual droplet defocus, dependant on droplet out-of-plane velocity and laser sheet thickness, resulted in considerable diameter measurement uncertainty. This uncertainty increases with laser sheet thickness, though even for relatively thin sheets the effects are noticeable, and for instance the estimated diameter measurement uncertainty when using a 0.5 mm thick laser sheet is $\pm 5\%$. With the use of PIT this measurement uncertainty is seen to manifest as an erroneous increase or decrease in droplet diameter over time. This aspect was tested on experimental data obtained in non-evaporating conditions and it was found that the measured droplet diameter showed a variation in time in agreement with that predicted by the defocus error source identified in this work.

Chapter 4

Interferometric droplet tracking to an evaporating spray

4.1 Chapter Outline

In this chapter the Lagrangian tracking algorithm described in Chapter 3 is used to observe the evaporation of methanol droplets in a heated air flow. The performance of the tracking algorithm in determining droplet evaporation rate is assessed, including comparison with a methanol droplet evaporation model. Before this a brief introduction is provided explaining the specific importance of methanol and its relevance in this Chapter.

4.2 Introduction to methanol

The reduction of greenhouse gas production and fossil fuel extraction is one of the defining socio-scientific issues of our time. Whilst the long term goal of energy production lies with new renewable technologies such as solar and wind and nongreenhouse gas emitting nuclear technologies, in the short and medium term the use of internal combustion will likely continue. In such cases replacing fossil fuels with those derived from renewable resources such as plant matter will help in the further reduction in the effects of climate change. In the second chapter of this thesis, Global Sizing Velocimetry (GSV), a commercial Interferometric Droplet Sizing (IDS) technique was used to characterise droplet sizes of various ethanol fuel blends. Ethanol along with other bio-derived alcohols are some of the best researched and implemented renewable fuels. Though currently less prevalent in comparison to other renewable liquid fuels, there is an increasing interest in the use of methanol as a bio-fuel. One potential benefit of methanol over other bioalcohol fuels is it's production from waste biomass through anaerobic digestion. Unlike the fermentation of ethanol from grain, the forming methanol from biomass waste could remove potential conflict between food and fuel production. In addition, the formation of methanol in controlled anaerobic digestion, reduces the emissions of methane into the atmosphere, with methane being considerably more potent as a greenhouse gas than CO₂ (Yvon-Durocher et al., 2014) and being responsible for approximately 20% of global temperature increase since the pre-industrial age (Kirschke et al., 2013).

In order for the potential benefits of methanol fuels to be seen, combustion processes must be adapted for methanol use. The difference in liquid properties will have noticeable effects on the spray characteristics of methanol in comparison to traditional gasoline, aviation and diesel fuels. One key characteristic when comparing methanol to more traditional fuels such as gasoline, is its volatility. Though methanol has a relatively low boiling point, its latent heat of vaporisation is relatively high, approximately three times that of gasoline. Indeed in a work by Danis et al. (1988) a reduction in fuel pre-vaporisation when comparing methanol to n-heptane was noted, resulting in methanol requiring 3-5 times higher ignition energies. As such forming a detailed understanding of the vaporisation of methanol sprays in heated conditions is of fundamental importance in the development and implementation of methanol as a fuel source.

In this chapter the newly developed Planar Interferometric Tracking (PIT) processor is used to observe the evaporation of methanol droplets in a heated air flow. The measured diameter reduction of droplets will be compared with that predicted by a single droplet evaporation model.

4.3 Experimental Setup

A custom-made optical rig was designed and employed to measure droplet evaporation rates using planar interferometric droplet tracking under heated flow conditions (See Figures 4.1 and 4.2).

The optical rig has a squared cross-section with side length of 150 mm, and a height of approximately 900 mm. Four 150 mm by 120 mm fused quartz windows allowed optical access whilst retaining heat within the test rig. An ultrasonic atomiser (Sonics Atomizer) was used to produce droplets ranging from approximately 20 - 150 μ m in diameter, while a Harvard Apparatus PHD Ultra 70-3006 syringe pump was used to feed liquid methanol to the atomiser at a rate of 200 ml/hour. The spray was injected into a coaxial annular heated air flow (Figure 4.2 and 4.3), which was provided by a process heater connected with a PID controller. Fitted in line, an Alicat-M gas flow meter, allowed for precise control of air flow rates (75 - 200

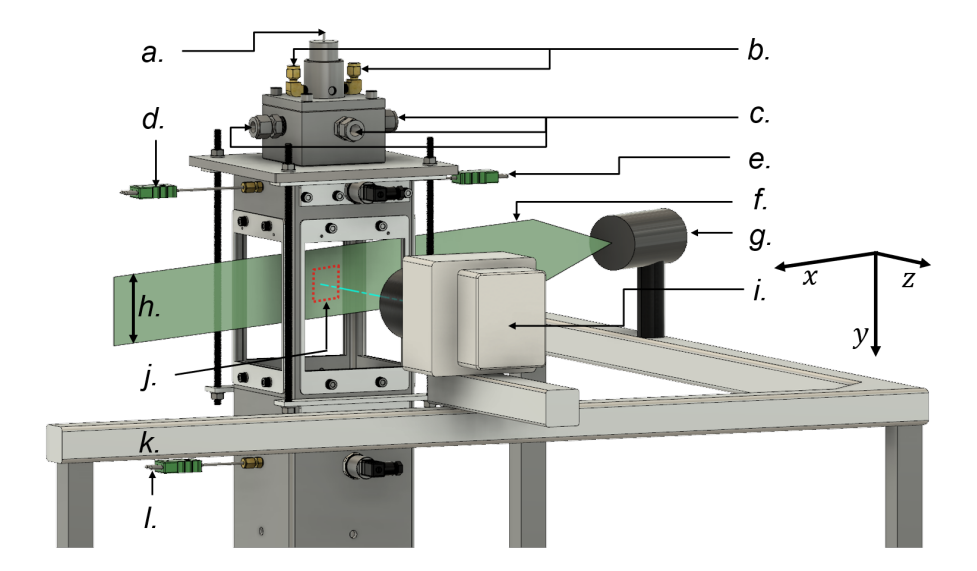


Figure 4.1: Sketch of the experimental setup. (a) Sonics Atomizer, (b) Cooling air coupling, (c) Heated air coupling, (d) Heated air inlet thermocouple, (e) Cooling air thermocouple, (f) Laser Sheet, (g) LASERPULSE light arm head, (h) Laser sheet height (100 mm), (i) Phantom VEO 710 camera, (j) Measurement Volume, (l) Downstream thermocouple, (k) 3-axis traverse.

slpm) and output temperatures (288 - 550 K). To prevent overheating and damaging of the injection system, the atomizer was cooled down in between tests by an air flow (see Figure 4.2). The temperature of both the cooling and heated air flows were monitored using two thermocouples at the corresponding inlets of the spray chamber (see Figure 4.2). In addition the temperature 300 mm beneath the atomizer nozzle tip was recorded by a thermocouple. For all tests the heated air flow rate was 100 slpm, and for heated conditions the air temperature at spray chamber inlet was measured at 515 K, whilst the thermocouple located 300 mm downstream measured 475 K. The temperature at the measurement volume (140 mm downstream of the atomizer) was estimated to be 495 K by linear interpolation.

Laser illumination was provided by an EdgeWave IS-series high speed laser (532 nm) with a TSI Laserpulse light arm and sheet optic redirecting and focussing the laser beam into a sheet with a thickness of approximately 1.5 mm in the measurement region. A Phantom VEO 710 high speed camera fitted with a Tokina 100 mm lens and slit aperture mounted at a scattering angle of 60° was used for imaging.

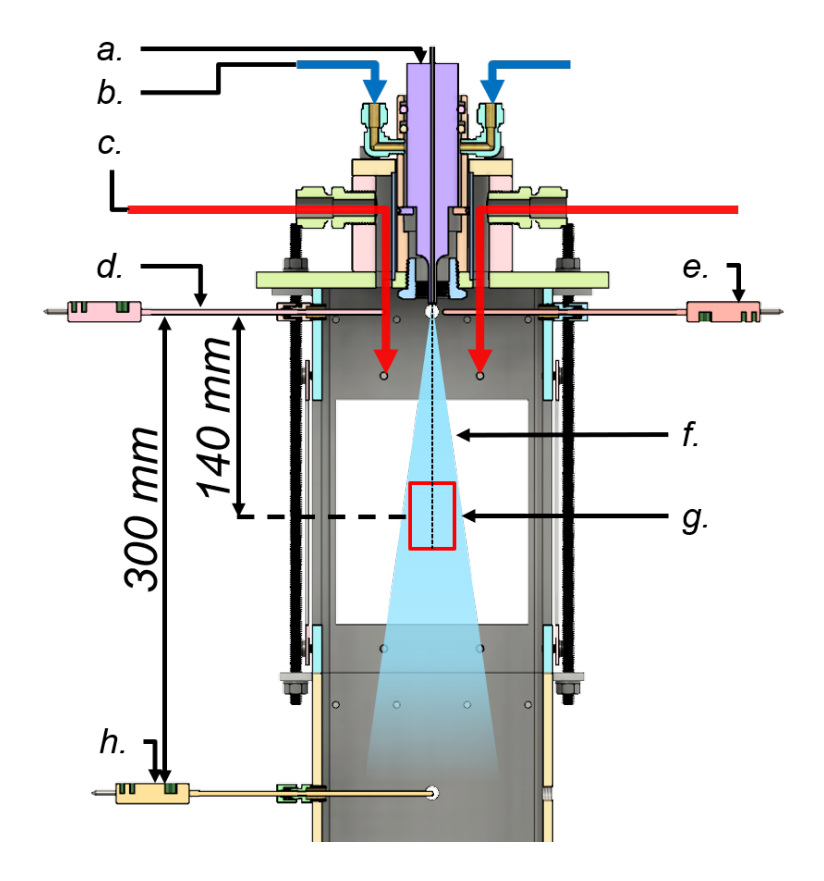


Figure 4.2: Sketch of the system used to heat the air and control its temperature through thermocouples. (a) SONICS Atomizer, (b) Cooling air coupling, (c) Heated air flow, (d) Heated air inlet thermocouple, (e) Cooling air thermocouple, (f) Liquid spray, (g) Measurement volume region, (h) Downstream thermocouple.

For all tests presented in this study the lens aperture was set to f/5.6 and a 1:1 magnification factor was used at a resolution of 800×1024 pixels, resulting in a field of view measuring ≈ 16 mm in width and 20 mm in height. The laser pulse frequency and camera framerate were set to 7 kHz synchronised using a TSI Laserpulse Synchronizer 610036 and TSI Insight 4G.

To control the positioning of the measurement volume an in-house software-controlled three-axes traverse was developed, allowing for the adjustment along the axial, y, and radial, x, directions of the measurement volume location and camera defocus, $z \csc \theta$ with a displacement resolution (Δz) of 2.5 μ m. This allowed the identification and optimal control measurement location, which is informed by local droplet concentration. On one hand a large droplet concentration is desired to in-

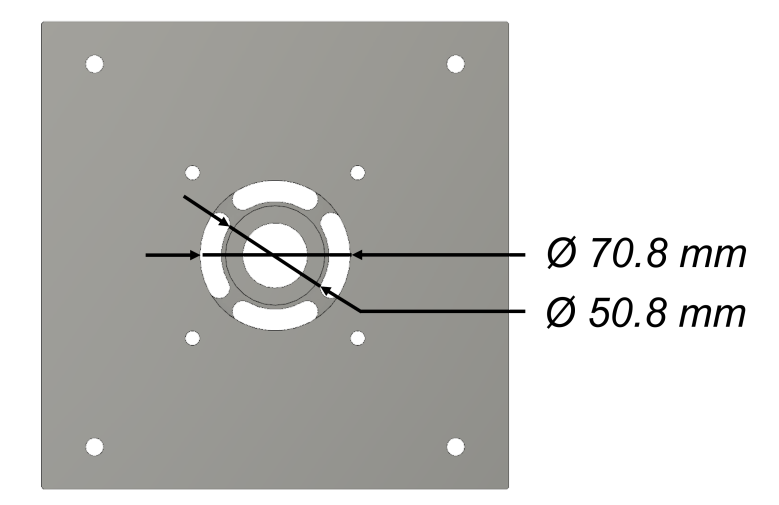


Figure 4.3: Top view of rig top plate, showing the dimensions and layout of the partial annulus which air was fed into the rig.

crease data-set size and build statistics. On the other hand it can result in the overlap of multiple droplet interference patterns, with a reduced accuracy of the TSI Insight software to detect and size them. The data included in this work was obtained along the spray axis, 140 mm downstream of the nozzle tip, where the average droplet diameter and concentration were 41.4 μ m and approximately 300 droplets per cm³ respectively. This droplet concentration level reduced the likelihood of oscillation pattern overlap. It should be noted that GSV measurements have been shown to be reliable up to concentrations of 3,000 droplets per cm^3 (Pan et al., 2006). The defocus displacement was optimised and set to 20 mm.

4.3.1 PIT setup

As previously outlined the analysis of captured images is performed in two steps. The first processing pass is completed by TSI's Global Sizing Velocimetry (GSV), with processing parameters being input to the GSV user interface in INSIGHT 4G. The key parameter is the Minimum Power Spectrum Peak Ratio (MPSPR), this assesses the prominence of a single frequency in detected interference patterns. For all tests this was set to 1.25. From the initial pass by GSV the location and diameter of detected droplets is imported into the Planar Interferometric Tracking (PIT) processor. The key parameters set in the PIT processor are as follows:

- The initial inspection region measured 1.6 mm in width and 1.0 mm in height (0.2 mm top, 0.8 mm bottom), centred about the droplet position.
- The focused interrogation window used for the determination of droplet diameter in cases of droplets being incorrectly sized or unrecognised by the GSV processor measured 50 pixels in height and had a width of 1.5× the expected width of interference patterns at the given radial position within the image.
- The sizing signal to noise ratio was set to 1.25, this being determined in a similar manner to the GSV MPSPR.
- Inter-image droplet diameter variation limit was set to 10%.

The allowable diameter change between two consecutive images was set to 10%. This value is far greater than any expected droplet diameter change over the interframe time interval. The main function of the allowable diameter change is to account for variations in measured droplet diameter resulting from signal noise and other sources of measurement error. The value of 10% was selected to ensure droplet pathlines were not prematurely terminated due to measurement uncertainty or error. As mentioned along with droplet diameter other criteria are used to ensure the correct droplet is identified in tracking, including droplet position, velocity and velocity variation. The actual change in droplet diameter would be observed over multiple droplet diameter measurements.

The minimum measurable droplet size of the system was deemed to be 20 μ m. This being equivalent to an interference pattern containing 4 fringes. The main cause of this lower limit is the ability of the FFT to reliably identify droplets with less than 4 fringes. Whilst seemingly 'good' measurements were performed on droplets with diameters less than 20 μ m in diameter, many 'droplets' in this size range were observed to result from noise, overlapping interference patterns, or partially obscured interference patterns. For the purposes of this study, all droplets of 20 μ m or less are ignored in analysis.

4.4 Experimental conditions

To determine the ideal test conditions a series of preliminary tests were carried out. These tests aimed to determine the best methanol flow rate for stable atomisation, the ideal heated air bulk velocity, the range of ambient air temperature achievable with the equipment in use and the ideal measurement position within the spray.

When using methanol with the SONICS ATOMIZER it was found that spray stability was heavily dependent on the selected liquid flow rate. At lower flow rates, the spray would intermittently stop, at higher flow rates atomisation would not properly occur with liquid simply 'dripping' in ligaments from the nozzle tip. At a methanol flow rate of 200 ml/hour the spray was at its most stable, thus this flow rate was selected.

Using the Alicat M gas flow meter the bulk air flow rate was varied from 75 to 200 slpm. From the images captured it was evident that increasing bulk flow rate increased droplet concentration within the measurement window. From visual inspection this is likely due to a reduction in spray cone angle with increasing air flow rate, reducing the radial dispersion of droplets from the spray centreline. With increasing air flow rate the droplet axial velocities increased, reducing the residence time within the measurement volume. To detect large droplet diameter change due to evaporation, a longer residence time within the control volume is ideal, therefore a low air flow rate would be sought. However, at the lowest flow rate of 75 slpm, the droplet concentration along the spray centreline was deemed too low to allow for a large enough data set to be produced in a timely manner. A bulk air flow rate of 100 slpm was selected as an ideal compromise.

For the selected air flow-rate, the maximum recommended outlet temperature for the TUTCO-SureHeat Serpentine II heater is over 900 K. However to safely operate within the laboratory setting this was limited to 750 K. With the heater output set to 750 K on the PID controller interface the heated air outlet thermocouple, Figure 4.2, recorded a stable temperature of 550 K. The downstream thermocouple, Figure 4.2, located 300 mm axially beneath the atomizer nozzle tip, registered a stable temperature measurement of 505 K. At this maximum temperature setting, the

droplet concentration within appropriate measurement regions was very low, likely due to a high level of droplet evaporation. By reducing the temperature at the heated air inlet temperature to 520 K (with the downstream thermocouple measuring 475 K), the droplet concentrations increased to a level where a significant dataset could be produced. For these conditions it was found that at 140 mm downstream from the nozzle tip, the image quality was ideal for droplet interference pattern measurement. Observations showed a number of droplets remaining within the measurement volume for durations over 15 ms.

The measurement window position is approximately $y_m = 155$ mm from the heated air inlet (see Figure 4.2) and as such should be located within the hydrodynamic entrance region ($\frac{y_m}{R_H} \approx 1$, where R_H is the hydraulic radius). A hot wire anemometer, RS PRO DT-8880 was used to determine the local air velocity magnitude in proximity of the measurement region. The recorded mean air velocity at the measurement position was 0.63 m/s, resulting in a Reynolds number of approximately Re = 3000. The droplet velocity measurement agreed closely with the droplet axial velocities obtained using PIT, which are normally distributed about a mean of 0.66 m/s with a standard deviation for the entire volume of 0.25 m/s, Figure 4.4. These levels of local velocity fluctuations and turbulence are consistent with the unsteady nature of the flow present within the inner mixing region of the expanded annular coaxial flow (Ko and Chan, 1978, 1979).

4.4.1 Methanol evaporation model

To test the performance of the PIT system in tracking droplet diameter reduction over time, a droplet evaporation model was adapted for use with methanol, to allow a comparison. The chosen model put forward by Lefebvre and McDonell (2017), is an iterative model, with each term defining the change in droplet diameter, D, and droplet surface temperature, T_s , over a short time period, dt. In addition to calculating the steady state evaporation, commonly described by the D^2law , Equation 4.1, this model also accounts for initial 'heating up period', where droplet surface temperature increases when droplets are introduced in a high ambient temperature.

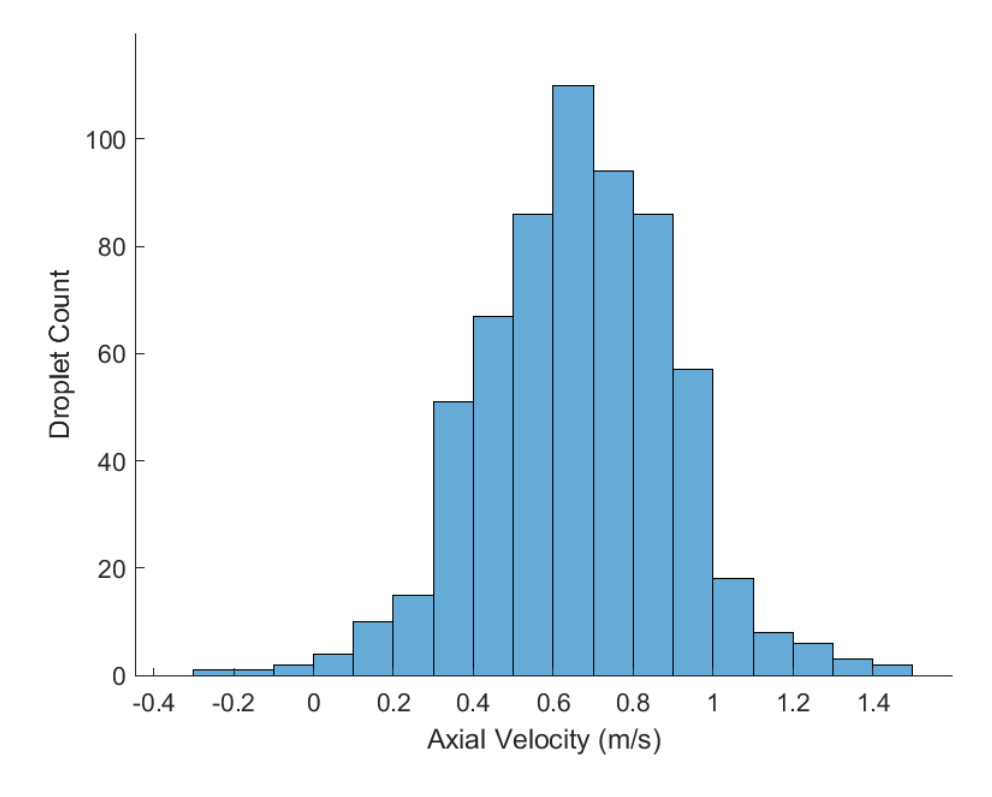


Figure 4.4: Histogram of preliminary droplet data showing droplet axial velocity distribution, measured using PIT.

$$D_0^2 - D^2 = \kappa t \tag{4.1}$$

Where κ is the evaporation constant.

The equations used in each iteration of the model are described below. Further references are shown for empirical models of methanol liquid and vapour properties.

The model assumes the average properties can be evaluated at a reference temperature, T_r and a mass fraction of methanol vapour, γ_{F_r} , where the reference temperature, the vapour mass fraction and the air mass fraction, γ_{A_r} , are defined in Equations 4.2, 4.3 and 4.4 respectively.

$$T_r = T_s + \frac{T_\infty - T_s}{3} \tag{4.2}$$

Where T_s is the droplet surface temperature and T_{∞} is the ambient air temperature.

$$\gamma_{F_r} = \frac{2}{3}\gamma_{F_s} \tag{4.3}$$

$$\gamma_{A_r} = 1 - \gamma_{F_r} \tag{4.4}$$

The vapour pressure, P_{F_s} of methanol has been empirically modelled with an Antoine equation as shown in Equation 4.5 where a = 7.205, b = 1581.993 and c = -33.289 (Arce et al., 1997).

$$P_{F_s} = 10^{a - \frac{b}{T_s + c}} \tag{4.5}$$

From the vapour pressure of methanol at the droplet surface the mass fraction of methanol vapour, γ_{F_s} , at the droplet surface can be calculated, Equation 4.6, where P is the ambient pressure and M_A and M_F are the molecular weights of air and methanol respectively.

$$\gamma_{F_s} = \left[1 + \left(\frac{P}{P_{F_s}} - 1\right) \frac{M_A}{M_F}\right]^{-1} \tag{4.6}$$

Having defined the droplet surface vapour fraction, the mass fractions of air and methanol vapour can be determined from Equations 4.5 and 4.6 respectively.

The reference value for thermal conductivity, k_g , can be expressed as

$$k_g = \gamma_{A_r}(k_A \text{ at } T_r) + \gamma_{F_r}(k_v \text{ at } T_r)$$
(4.7)

Where k_A is the thermal conductivity of air

$$k_A = T_r \cdot 6 \times 10^{-5} - 0.0078 \tag{4.8}$$

And k_v is the thermal conductivity of methanol vapour (Touloukian et al., 1970)

$$k_v = 4.184 \times 10^{-3} \left(2.57489 - 1.21163 \times 10^{-2} T_r + 5.22159 \times 10^{-5} T_r^2 \right)$$
 (4.9)

Similarly the reference specific heat at constant pressure, c_{p_s} , is

$$c_{p_s} = \gamma_{A_r}(c_{p_A} \text{ at } T_r) + \gamma_{F_r}(c_{p_v} \text{ at } T_r)$$
 (4.10)

where c_{p_A} is the specific heat of air modelled as

$$c_{p_A} = 2.520 \times 10^{-10} T_r^4 - 1.018 \times 10^{-6} T_r^3 + 1.400 \times 10^{-3} T_r^2$$

$$-0.568 T_r + 1075.790$$
(4.11)

and c_{p_V} is the specific heat capacity of methanol vapour (Strömsöe et al., 1970).

$$c_{p_V} = \left[2.444(1.73 + 8.2 \times 10^{-3} T_r) + 1.774 \times 10^{-13} e^{\frac{10977}{T_r}}\right] \frac{4184}{M_f}$$
(4.12)

The latent heat of vaporisation for methanol, *L*, can be modelled by the formula of (Majer and Svoboda, 1986),

$$L = 45.3e^{0.31\frac{T_s}{T_{Cr}}} \left(1 - \frac{T_s}{T_{Cr}}\right)^{0.4241} \frac{1 \times 10^6}{M_F}$$
 (4.13)

 T_{Cr} being the critical temperature for methanol.

For a droplet of diameter D, its mass can be expressed as

$$m_D = \frac{\pi}{6} \rho_{F_T} D^3 \tag{4.14}$$

The change in liquid methanol density, ρ_{F_T} , with temperature can be determined using the model of Vogel and Weiss (1982)

$$\rho_{F_T} = -0.946(T_s - 273) + 810 \tag{4.15}$$

Defining B_m and B_t as

$$B_m = \frac{\gamma_{F_s}}{1 - \gamma_E} \tag{4.16}$$

$$B_t = c_{p_s} \frac{T_{\infty} - T_s}{I_s} \tag{4.17}$$

The rate of change of droplet mass, m_F can be expressed as

$$m_F = 2\pi D \frac{k_g}{c_{p_s}} ln(B_m + 1)$$
(4.18)

The rate of change of droplet surface temperature, \dot{T}_s , is

$$\dot{T}_s = m_F \frac{L}{c_{p_F} m_D} \frac{B_t}{B_m - 1} \tag{4.19}$$

Where c_{p_F} is the specific heat capacity of liquid methanol, Equation 4.20. This can be found from the model of Khasanshin and Zykova (1989).

$$c_{p_F} = \left(2.786 - 5.1901T_s \times 10^{-3} + 5.7482 \left(T_s \times 10^{-3}\right)^2\right) \times 10^3$$

$$+29.47 \left(T_s \times 10^{-3}\right)^3 \times 10^3$$
(4.20)

Finally, the rate of change of droplet diameter, \dot{D} , can be obtained as

$$\dot{D} = \frac{4k_g ln(1 + B_M)}{\rho_{F_T} c_{D_S} D} \tag{4.21}$$

Knowing the rate of change of droplet diameter and surface temperature, the droplet size and temperature after a time interval, dt, can be input in the same series of equations in an iterative process to model the change in droplet size over time.

For the experimental conditions represented in this study, the specific values and parameters used within the model are shown in Table 4.1.

Parameter	Value / unit				
T_{∞}	495 / (K)				
T_{Cr}	513 / (K)				
T_{s_0}	288 / (K)				
M_A	28.97 / (g/mol)				
M_F	32.04 / (g/mol)				
dt	1 / (ms)				

Table 4.1: Calculated proportional droplet surface area change due to out of plane velocity at image centreline.

Figure 4.5 shows the droplet diameter change over time for droplets with initial surface temperatures, T_{so} , of 288 K (15°C), for a flow with an ambient air temperature of 485±10 K (212°C). The ambient temperature is estimated through linear interpolation between the temperature measurements at the heated air outlet and downstream thermocouples. To check if the PIT algorithm would be capable of measuring the droplet evaporation rates of droplets, the model was used to estimate the expected evaporation rates of droplets of representative diameter at the measurement volume. Assuming a constant droplet velocity of ≈ 0.6 m/s and measurement volume location, 140 mm downstream of the nozzle tip, droplets would be measured at approximately 230 ms after being introduced to the heated air flow. From the model, a droplet with an initial diameter of 110 μ m would reduce in diameter to $\approx 63 \ \mu \text{m}$ in 230 ms. This droplet would reduce in diameter by a further 12 μm if it remained within the measurement volume for 20 ms. This degree of diameter reduction due to evaporation over these realistic timescales should be detectable by the PIT system. In addition the model also predicts that all droplets of applicable diameters, $\leq 250 \mu \text{m}$, would have reached a stable surface temperature, with the heating up time for a 250 μ m diameter droplet being 85 ms. As such, according to the model, the rate of surface area reduction, κ , should be constant for all droplets within the measurement volume. For the given test conditions the model predicts a steady state evaporation constant of $43.3\pm2.5 \,\mu\text{m}^2/\text{ms}$.

4.5 Droplet tracking results

For this study a total of 28 repeat tests were performed with 770 images captured in each test, meaning a total of 21,560 images. From these images a total of 24,343 individual droplets were identified and tracked. The droplet diameter distribution for all the recorded data is shown in Figure 4.6 (a), with the mean diameter, D_{10} , being 62.36 μ m. Figure 4.6 (b) shows the distribution of droplet residence times within the measurement volume for all data captured. The mean residence time was 1.3 ms.

To properly assess the decrease in droplet diameter in evaporating conditions,

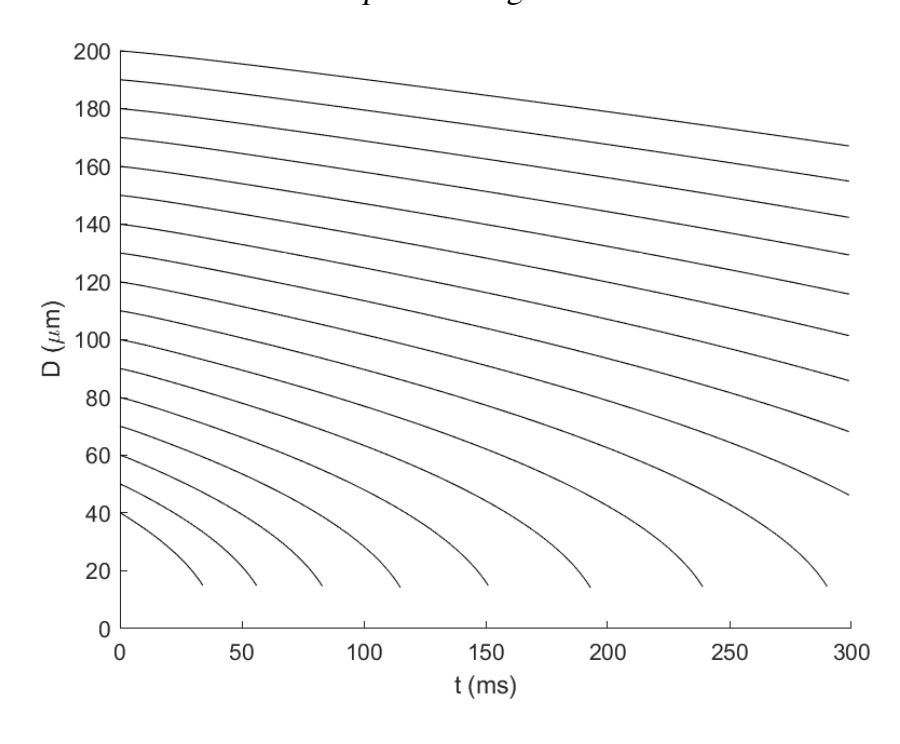


Figure 4.5: Model droplet diameter change overtime for various starting diameters.

the rate of proportional droplet diameter reduction should be much greater than the error due to rate of defocus variation, Equation 4.22. The ability of the PIT technique, in its current state, to observe droplet diameter reduction due to evaporation is limited by the actual evaporation rate of droplets and the duration for which they reside within the measurement volume. Thus, either the actual rate of proportional droplet diameter reduction must be much larger than the error due to rate of defocus change, or the total residence time of the droplet within the measurement volume, t_{total} , must be large.

To accurately assess the change in droplet diameter in evaporating conditions, the contribution of the error due to droplet defocus on the rate of reduction of the final to initial surface ratio must be considered. According to Equation 4.22 the accuracy of the measurement for a given laser sheet thickness increases when the actual rate of droplet evaporation, κ , is significantly larger than the error due to the rate of change of measured droplet diameter due to defocus, $\frac{E}{t_{total}}$. This condition can be achieved when the total residence time of a droplet within the measurement volume, t_{total} , is large. In essence the capability of the PIT technique to accurately determine the droplet diameter reduction due to evaporation is limited by the ac-

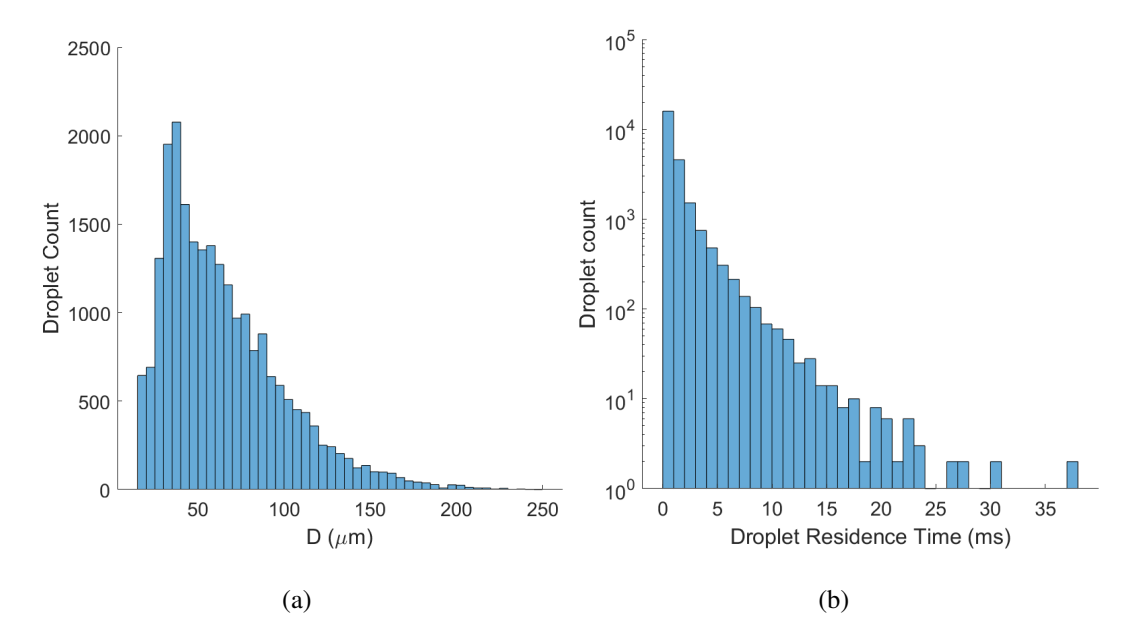


Figure 4.6: Histograms showing droplet (a) diameter and (b) residence time distributions for all tests.

tual evaporation rate of the droplets in comparison to the defocus error, E, and the residence time.

$$\frac{d}{dt} \left(\frac{D^{'2}}{D_0^{'2}} \right) = \frac{d}{dt} \left(\frac{D^2}{D_0^2} \right) \pm \frac{E}{t_{total}}$$

$$\frac{d}{dt} \left(\frac{D^2}{D_0^2} \right) = \frac{-\kappa}{D_0^2} \gg \frac{E}{t_{total}}$$

$$\frac{T_{total} / (ms)}{E/T_{total} / (\%/ms)} = \frac{5}{2.4} = \frac{1.2}{1.2} = \frac{0.8}{0.6} = \frac{0.48}{0.4} = \frac{0.4}{0.4}$$

Table 4.2: Expected error due to rate of defocus change for given droplet residence times.

D_0 / (μ m)	30	50	70	90	110	130
$\frac{d}{dt} \left(\frac{D^2}{D_0^2} \right) / \left(\%/\text{ms} \right)$	4.6	1.6	0.8	0.5	0.3	0.2

Table 4.3: Expected rate of proportion droplet surface area reduction for given initial droplet diameters.

From tables 4.2 and 4.3, it is evident that for larger droplets, >90 μ m, there is no realistic droplet residence time for which the diameter measurement error due to the rate of change of defocus from droplet out of plane motion does not exceed the modelled reduction rate in proportional droplet surface area. This is also seen for droplets entering the measurement volume with diameters greater than 40 μ m and having residence times of 5 ms or less. In this study the ratio, ψ , Equation 4.23 between the measured rate of change of proportional droplet surface area and the rate of change of measured droplet diameter due to the defocus error, is considered to assess the measurement accuracy.

$$\psi = \frac{\frac{d}{dt} \left(\frac{D^2}{D_0^2}\right)}{\frac{E}{T_{total}}}$$
(4.23)

A comparison between the model predicted droplet surface area reduction rate and that measured by PIT is shown in Figure 4.7. The data points are colour coded based on the value of ψ , which takes into account their residence time in the laser sheet. As mentioned above larger values of ψ corresponds to a lower impact of the defocus error. These data points (green and blue, $\psi > 1$) are scattered around the 45° line indicating a reasonably good agreement between the experiments and the model. However, when $\psi < 1$, many data points disagree considerably with the model estimation. In particular points with negative reduction rates are indicative of an increase in droplet diameter which is completely nonphysical and are mainly due to the direction of droplet out of plane motion resulting in a change in defocus as they cross the control volume. It is worth mentioning that none of the droplets associated to a lower percentage error, $\psi > 1$, are characterised by a negative and nonphysical surface reduction rates. The sample size of droplets with values of $\psi > 1$ is very low. From the 24,343 individual droplets tracked by PIT only 166 have measurement to error ratios greater than one, 0.68% of the total data set.

For the 166 droplets with $\psi > 1$, the mean and standard deviation of the evaporation rate constant, κ , were 41.74 μ m²/ms and 15.28 μ m²/ms, respectively, with data points following the normal distribution of Figure 4.8. Despite the large standard deviation due to the errors outlined previously, the mean evaporation con-

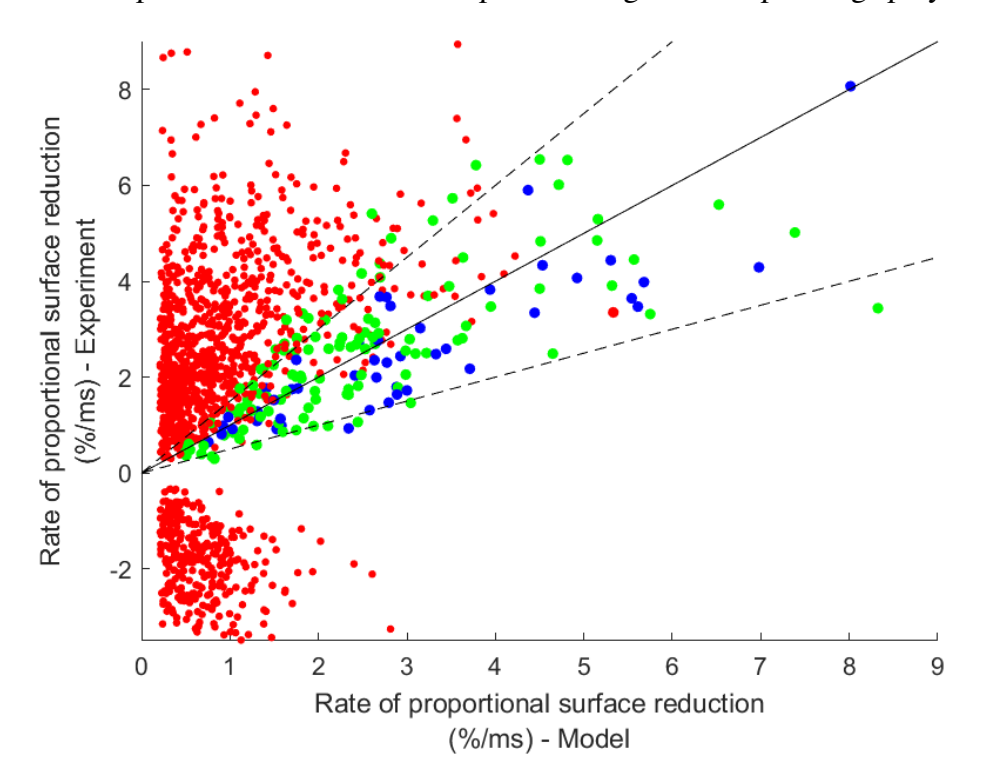


Figure 4.7: Model-experiment comparison of proportional droplet surface area reduction rate, $\frac{d}{dt} \left(\frac{D^2}{D_0^2} \right)$. Marker colour showing ratio of proportional droplet surface area reduction rate to expected due to rate of change of defocus, ψ , (Blue-Square) $\psi \ge 2$, (Green-Diamond) $1 \le \psi < 2$, (Red-Circle) $\psi < 1$. Solid central line showing perfect agreement between model and experiment, dashed lines showing a deviation from the model prediction by ± 50%.

stant as measured by PIT compared relatively well with the value predicted by the model, $43.3 \pm 2.5 \,\mu\text{m}^2/\text{ms}$.

The data was further analysed to identify those droplets with small out of plane velocity component. These droplets did not fully traverse the laser sheet thickness, but entered at the top of the measurement volume, traversed the full vertical height of the image (\approx 20 mm), and then left at the bottom of the measurement volume. As the magnitude of out of plane velocity for these droplets is small, their measured droplet diameter is subject to minimal diameter measurement error due to change in defocus. As would be expected, droplets having small out of plane velocities, were seen to predominantly be droplets with higher axial momentum. The combination of larger droplet diameters, most of which were in excess of 150 μ m, and low

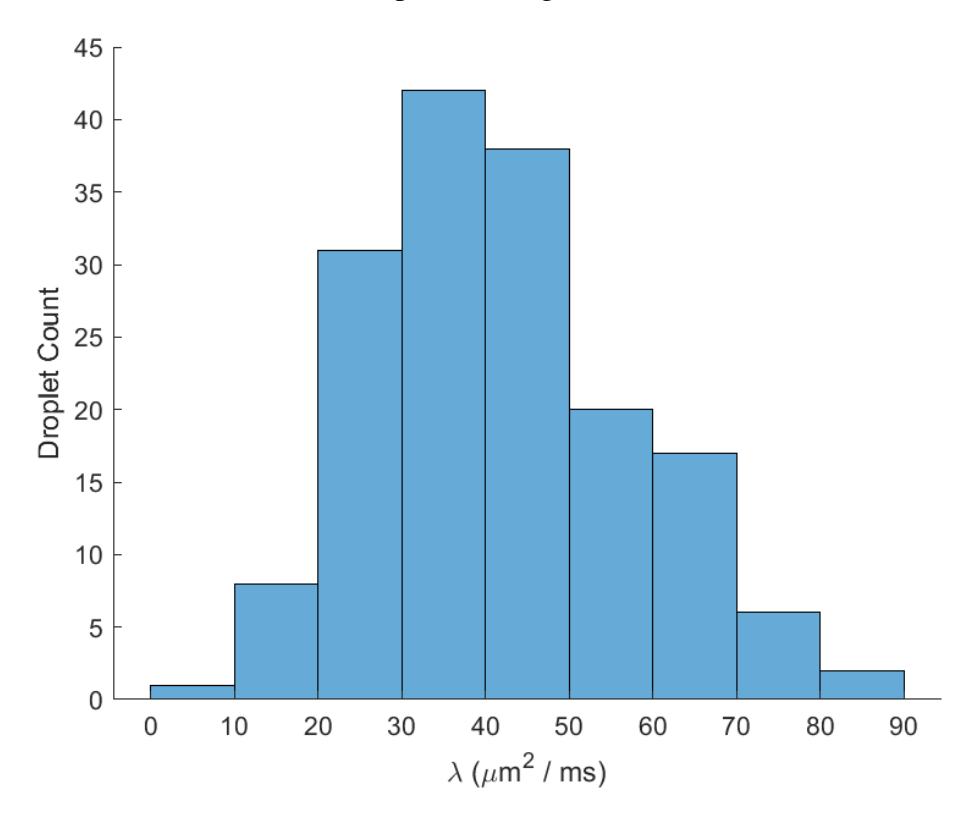


Figure 4.8: Histogram of measured evaporation constants, κ , from experimental data, determined through linear regression.

measurement volume residence times, meant many of the droplets fully transiting the measurement volume height did not show any significant size variation. From the current experiments only six droplets fitting the criteria mentioned above were observed. The diameter time evolution of these droplet is shown in Figure 4.9. For all of them a clear decay in droplet diameter with time is seen, much greater in magnitude than the apparent random variation due to noise.

Figure 4.10 shows the change between the initial and instantaneous droplet surface area over time. Assuming the droplets are in steady state evaporation the rate of change in droplet surface area should be constant, in accordance with the D^2 law. The data shown in Figure 4.10 are in reasonable agreement with this model, as the rate of droplet surface decrease is characterised by a nearly linear variation with time. The evaporation rate constant of these droplets was found to agree within a $\pm 25\%$ margin with that derived from the prediction model, a considerable reduction from the $\pm 50\%$ deviation of the results shown in Figure 4.7. This clearly indicates

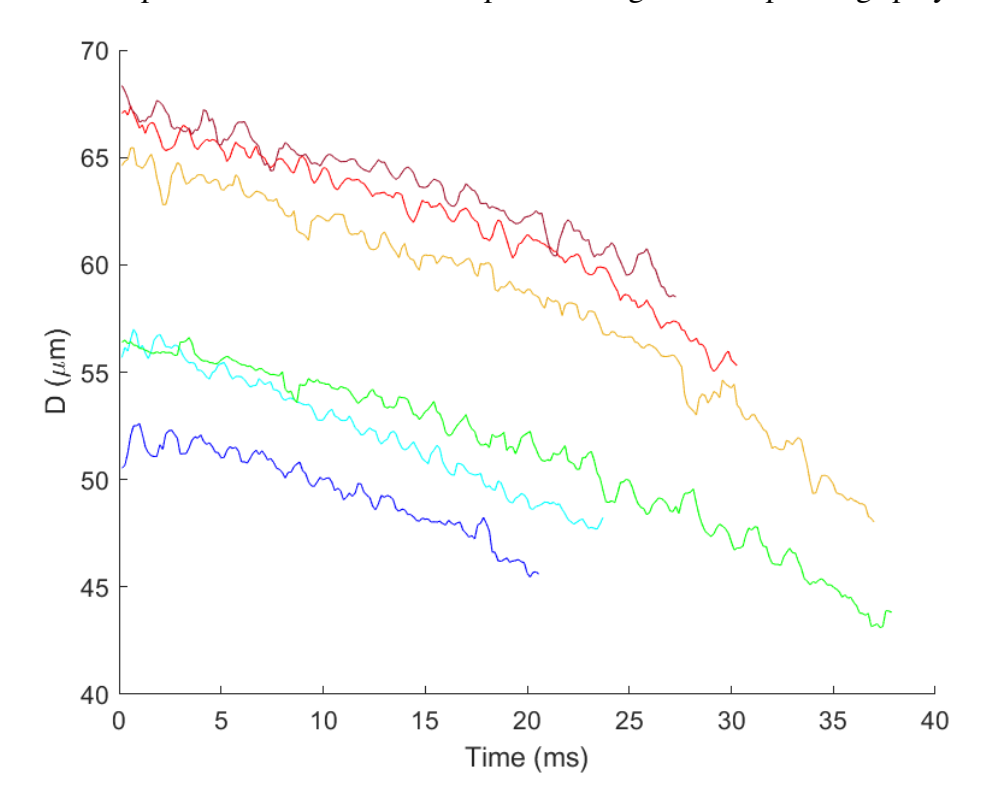


Figure 4.9: Droplet diameter change with time for six droplets transiting the measurement volume height.

that as the expected error due to the droplet defocus is reduced, the agreement between measurements and model improves.

The variation in evaporation rates displayed in Figure 4.10, may not be a result of the described measurement error in entirety. A proportion of the variation might be related to air flow temperature fluctuations and the presence of convection (not accounted for in the simple model). As previously described, a turbulent flow region is expected within the measurement volume, and has been confirmed by the variation of droplet velocities observed through PIT measurements. Indeed, the recorded velocities of the six tracked droplet reported in Figure 4.11 show a considerable difference from the mean flow velocity (0.6 m/s). In such a flow regime, the slip velocity between the gas and liquid phases could fluctuate, and therefore have an impact on the convection coefficient. To estimate the extent to which slip velocity and convection effect the evaporation rate, an additional factor based on droplet Reynolds and Prandtl numbers (Lefebvre and McDonell, 2017) was incor-

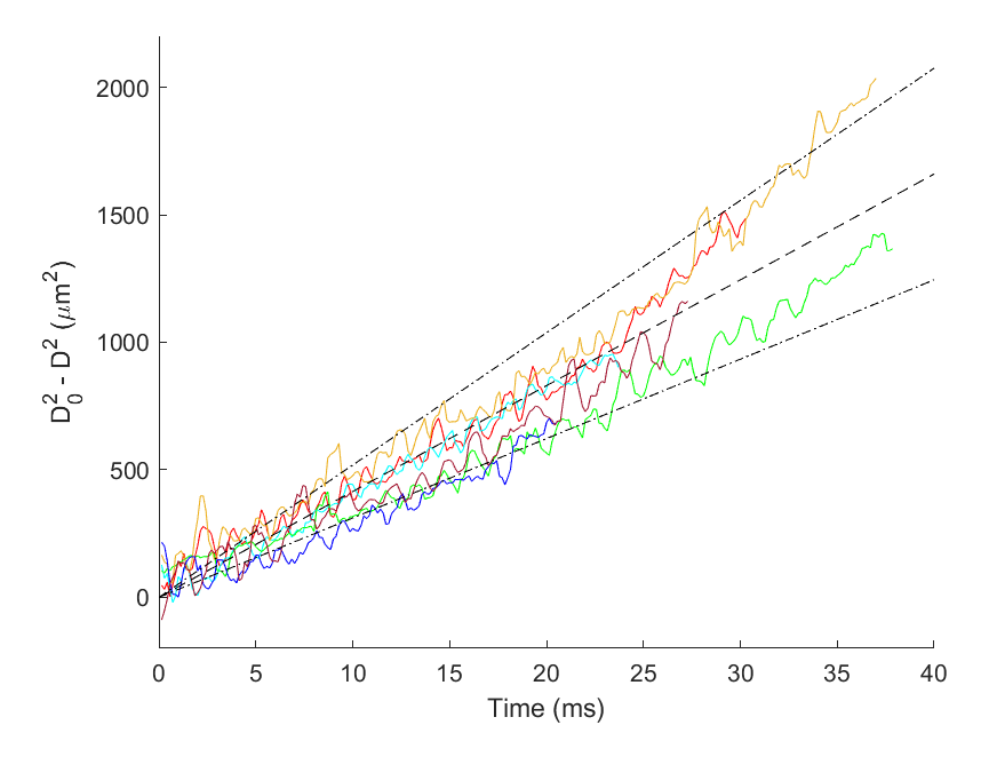


Figure 4.10: Droplet surface change with time due to droplet evaporation for droplets with residence time greater than 20 ms. Reference lines in (b) representing $\kappa_{Model}t - - - \pm 25\%$

perated into the evaporation model. For a range of slip velocities, 0.01-0.3 m/s, the increase in predicted evaporation rate was observed to be between 5 and 30%, respectively. This increase is consistent to the variation in evaporation rates observed in Figure 4.10. The air flow temperature fluctuation observed in this study could therefore introduce an additional uncertainty in evaporation rate (6%). In order to fully understand the influence of flow parameters on droplet evaporation rate, detailed measurements of individual droplet velocity and temperature histories would be required, which is beyond the scope of this work.

4.6 Conclusion and assessment of PIT performance

PIT was seen to be capable of tracking methanol droplet position, and diameter variations when transiting a $16 \times 20 \times 1.2$ mm measurement volume, in ambient air temperatures of 485 K. Observing the temporal evolution of droplet diameter, direct measurements of individual droplet size change due to evaporation could be

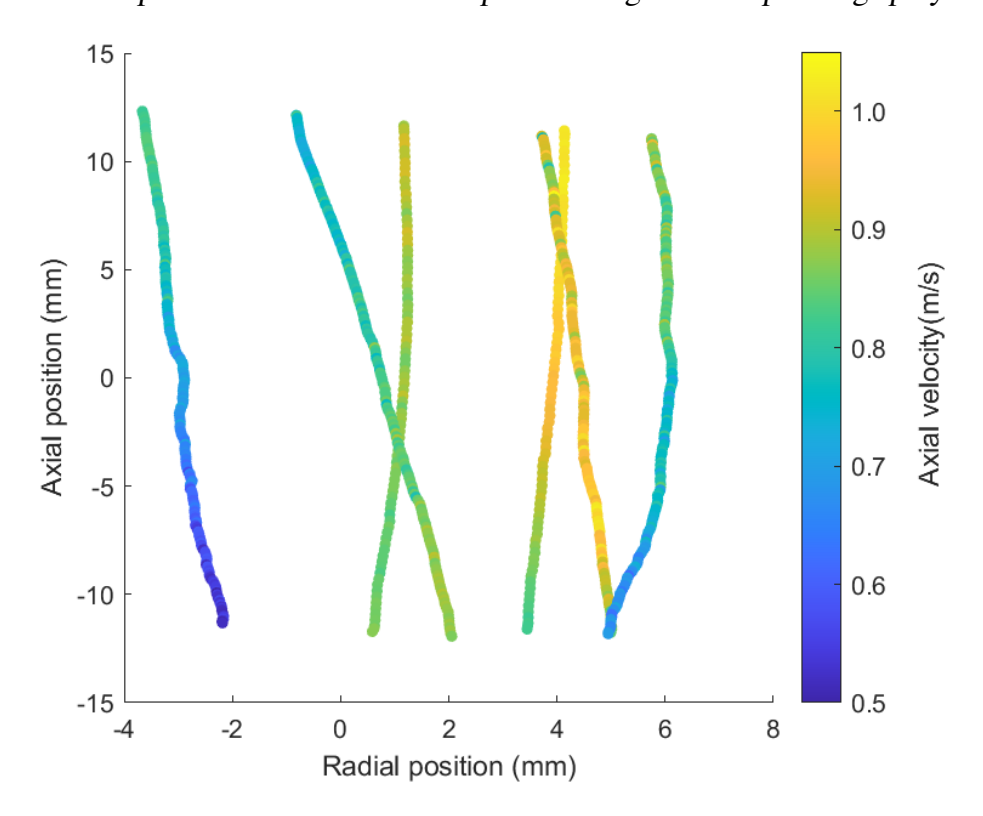


Figure 4.11: Visualisation of the pathlines for the six tracked droplets with colour indicating the instantaneous axial velocity.

performed.

Considerable variations in droplet evaporation rate were noted between PIT measurements and estimations from a single droplet evaporation model. Further, in some instances non-physical droplet diameter increase was measured by the PIT algorithm. The cause of the disagreement between model and measurement is likely due to an uncertainty in the actual droplet defocus distance resulting from out of plane droplet motion. The droplet defocus distance is a required parameter in the calculation of droplet diameter from interference pattern spatial frequency, used in all planar interferometric sizing systems (see Chapter 3). When tracking a droplet using the PIT system this uncertainty manifests as an artificial rate of change of droplet diameter, relating to the droplet out of plane velocity. The effects of this error are particularly apparent in droplets with low expected proportional surface reduction rates, $\frac{d}{dt} \left(\frac{D^2}{D_0^2} \right)$, and those with short residence times within the measurement volume. These droplets make up the vast majority of the data captured in this

study.

Analysing only droplets confirmed to have lower out of plane velocity magnitudes and longer residence times, thus affected to a lesser degree by the outlined error, the PIT system was seen to detect the evaporation rates of heated methanol droplets with good agreement to the single droplet evaporation model. The mean measured evaporation constant of $41.74~\mu\text{m}^2/\text{ms}$ being within 4% of that predicted, though the variation in measured data is considerable, with the evaporation constant coefficient of variation being 36.6%. A small number of droplets measured (166 of the 24,343 droplets measured) were seen to have sufficiently low out of plane velocities such that they traversed the complete height of the measurement volume, thus had reduced error in droplet diameter measurement. All of these droplets were seen to have evaporation constants within $\pm 25\%$ of the model prediction. A significant proportion of observed difference in measurement and model outcomes could be attributed to complex droplet—flow interactions not accounted for by the basic model, thus complete agreement between measurement and model would not be expected.

For PIT to be used for the measurement of droplet evaporation in realistic scenarios further developments need to be made. A key area of improvement would be the removal or reduction in error associated with the change in defocus distance due to droplet out of plane velocity (these being outlined in Chapter 3).

Chapter 5

Effects of acoustic forcing on droplet evaporation

5.1 Chapter outline

In this chapter the Lagrangian droplet tracking algorithm is applied to droplets within an acoustically oscillated air flow. The relation between droplet size and entrainment within the oscillating flow are analysed and compared with analytical models. The impact of air flow oscillation on methanol droplet evaporation is observed. Before this a brief introduction on the influence of oscillating flows on droplet evaporation is provided.

5.2 Introduction to acoustic evaporation enhancement

In Chapter 4, droplet evaporation was observed in conditions where the primary mode of heat transfer occurs due thermal conduction. In most spray applications, such as those present in liquid fuel combustion and spray drying, flow turbulence and/or the presence of an acoustic field, result in relative difference between the droplet and gas phases, this being often termed 'slip'. The velocity differential between droplet and gas has been monitored to enhance droplet evaporation rates, through the introduction of an additional mechanism of heat transfer, convection (Sujith et al., 2000).

As is mentioned by Lefebvre and McDonell (2017), in most practical applications of liquid sprays, droplet sizes are such that a free droplet will quickly assume the velocity of the surrounding gas, thus removing droplet slip velocities and convection enhancement. However, in the presence of turbulent or acoustic flow field slip velocities are likely to exist. The amount by which a droplet's velocity will differ to that of the gas velocity is dependant on the degree of entrainment. As Hjelmfelt and Mockros (1966) discussed the level of entrainment is a factor of droplet size, relative density between particle and fluid, and the intensity and timescale of velocity variations. As such understanding the relations between factors impacting slip velocities is of key importance to the functioning of sprays in industry.

The physical relevance of acoustic flow fields in spray applications is also of key importance. In the case of liquid fuelled engines thermo-acoustics resulting from the combustion process have been shown in multiple studies to effect the fuel spray characteristics, leading to changes in combustion emissions and general flame dynamics Balachandran et al. (2008). In addition to the enhancement of heat and mass transfer through convection, a number of studies have reported a reduction in mean droplet velocities with the introduction of an acoustic field Baird et al. (1967); Chishty et al. (2005); Houghton (1966); Kumara Gurubaran and Sujith (2008); Sujith (2005); Sujith et al. (1997, 2000), thus increasing droplet mass reduction over a given displacement due to an increased residence time, though others have found no significant link between acoustic forcing and mean droplet velocities Dubey et al. (1998).

Experimentally determining the relative velocity difference between free droplets and gas in realistic conditions is a difficult task, meaning much of the research has focused on single droplet/particle scenarios (Sujith et al., 1997, 2000). These 'simplified' conditions have allowed for the development of an understanding of the mechanisms involved within acoustic evaporation enhancement, however our understanding of how these mechanisms manifest in more realistic scenarios is lacking. Studies which have observed more realistic conditions have done so through the use of multiple measurement techniques to provide the droplet size, velocity and gas velocity variations over time, such as those performed by Sujith (2005) and Kumara Gurubaran and Sujith (2008). In these studies a combination of Particle Imaging Velocimetry (PIV), Phase Doppler Anemometry (PDA) and Laser Doppler Velocimetry (LDV) were used to determine the acoustic velocity field, spray droplet velocity and mean droplet diameter variation with acoustic forcing amplitude through a process of phase locking. The difficulty and equipment requirement of such research projects, along with the complexity of interactions involved with the acoustic forcing of realistic sprays may well hinder research within this field, despite the apparent importance.

The PIT processor developed in Chapter 3 could be an ideal tool for the assessment of droplet velocity amplitude response to an oscillating flow. The PIT processor allows for the tracking individual droplet position and size across a mea-

surement volume of $16 \times 20 \times 2$ mm, for droplet concentrations upwards of 500 droplets per cm³. This enabling the direct measurement of droplet-gas relative velocity with respect to droplet diameter across large regions within the flow. As the equipment required for this measurement method is the same as that used for high speed PIV, many research institutes could potentially make use of this measurement method, accelerating research.

In this chapter the performance of PIT processor, in measuring both size and velocity variations of droplets produced in a realistic acoustically forced spray in the presence of a coaxial air flow is assessed. The recorded data is then compared to existing theoretical models relating flow conditions and droplet diameter to the relative entrainment of droplets. Additionally, through the use of PIT, the effects of coaxial air flow temperature on droplet velocity variation are to be observed, and using a standard IDS technique, the effects of increasing forcing amplitude and coaxial air flow temperatures on droplet evaporation are monitored.

5.3 Experimental Setup

The same experimental and optical setup was used as that previously outlined in section 4.3, page 119, with a few exceptions. The air bulk flow rate was increased to 120 slpm from 100 slpm, as this was seen to increase droplet concentration within the measurement volume. Though droplet residence time is decreased with the increased bulk flow rate, for these experiments, increased droplet concentration was seen as a priority over droplet residence time within the measurement volume. At the volume flow rate of 120 slpm, air velocity at the annulus exit is approximately 1.0 m/s, using an RS PRO DT-8880, hot wire anemometer a mean air velocity of 0.9 m/s at the measurement position. A further measure taken to increase the number of droplets measured in each image was to increase the laser sheet thickness from 1.5 mm to 2 mm. In doing so the uncertainty in droplet diameter measurement due to defocus variation was estimated to be approximately $\pm 20\%$ (see Figure 3.14). As the purpose of the PIT technique, in this study, is to measure droplet velocity variation due to acoustic forcing with respect to droplet diameter, rather than droplet

diameter variation over time, the increased diameter measurement uncertainty is an acceptable compromise for the given increase in potential droplet residence time. Increasing the laser sheet thickness also allows a greater potential for droplets to remain in the measurement volume for a longer period of time.

The position of the measurement volume remaining centred along the atomiser axis, 140 mm downstream of the nozzle tip. The liquid flow rate (200 ml/hr) also remained the same.

To produce the required acoustic excitation, two speakers were added to the rig, the mounting positions are shown in Figure 5.1. The frequency and amplitude of acoustic signal from the speakers was controlled via a signal (frequency) generator and amplifier. The distance from the speakers to the nozzle tip was 865 mm from the nozzle tip (725 mm from the measurement volume). To record the acoustic pressure within the test rig, two dynamic pressure transducers (10 kHz sampling rate) were used, one of which was located inline with the nozzle tip, the other 300 mm downstream of the nozzle tip. The total length of the 150×150 mm tubing including the speaker mount measured 920 mm. With all component interfaces and ports tightly secured and making use gasket seals, no significant air leaks were present, thus the rig could be assumed a closed tube.

5.4 Test Conditions

To determine the ideal forcing frequencies a preliminary tests was performed. From a frequency sweep three frequencies were seen to produce higher pressure amplitude measurements, these being 100 Hz, 257 Hz and 400 Hz. Figure 5.2 shows the recorded pressure amplitude for these three forcing frequencies for given steps in pre-amplification voltage amplitude. Cross referencing the pressure amplitudes measured with the expected standing wave pressure profiles, figure 5.3, confirms that the chosen frequencies most likely relate to the 1st, 3rd and 5th harmonics of the 920 mm long, closed square section pipe used in these experiments. The dynamic pressure transducers in use were not capable of operating in heated conditions, as such the pressure amplitude measurements were taken in un-heated condi-

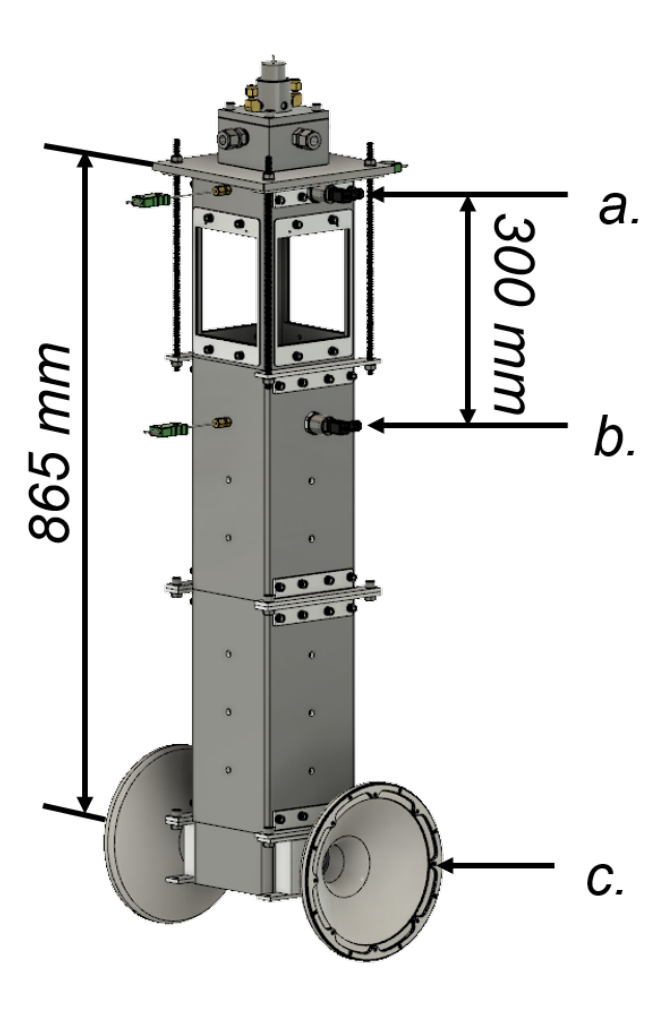


Figure 5.1: Diagram of optical rig with (a) upper and (b) lower dynamic transducers installation positions and (c) speaker mounting point.

tions, pressure amplitudes were assumed not to change significantly with increasing air temperature.

From the data captured by the dynamic pressure transducers, located 300 mm apart, approximately straddling the measurement volume location, acoustic pressure, P, and velocity, u'_a , amplitudes at the measurement volume axial centrepoint were estimated using a two-microphone method as used by Balachandran et al. (2005), the results of which are shown in table 5.1.

The two-microphone method results show acoustic velocity amplitudes to increase linearly with speaker pre-amplification voltage amplitude. The pressure amplitude estimations are inline with expectations based on the amplitudes observed

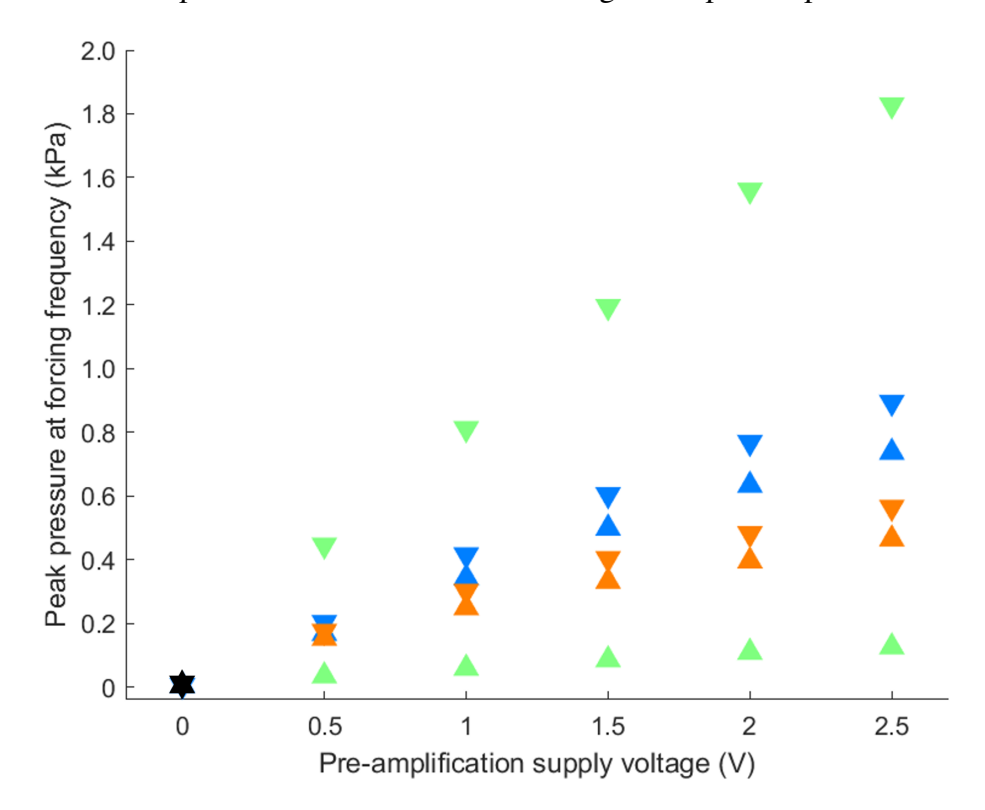


Figure 5.2: Acoustic pressure amplitude at forcing frequency for, 0 Hz (Black), 100 Hz (Blue), 257 Hz (Green) and 400 Hz (Orange). Amplitude measurement at lower transducer (▲) and upper transducer (▼).

from upper and lower dynamic pressure transducers, figure 5.2 and standing wave pressure profiles, figure 5.3. The highest acoustic velocity amplitudes are seen at the 257 Hz forcing frequency, with the lowest being seen at 100 Hz. The chosen test conditions will allow for the effects of both frequency and acoustic velocity amplitude on droplet velocity variation amplitude to be observed.

To assess the droplet velocity response to acoustic forcing the PIT processor would be used to identify and measure droplet size and axial velocity variation over time for individual droplets present within the spray. The images were captured at a frame-rate of 7000 frames per second. For the three outlined forcing frequencies (100 Hz, 257 Hz and 400 Hz) the droplet diameter response to acoustic forcing for water droplets in unheated conditions was measured at six forcing amplitudes. The forcing amplitudes correspond to pre-amplification forcing amplitudes shown in table 5.1. Further tests using methanol in heated conditions at a forcing frequency of

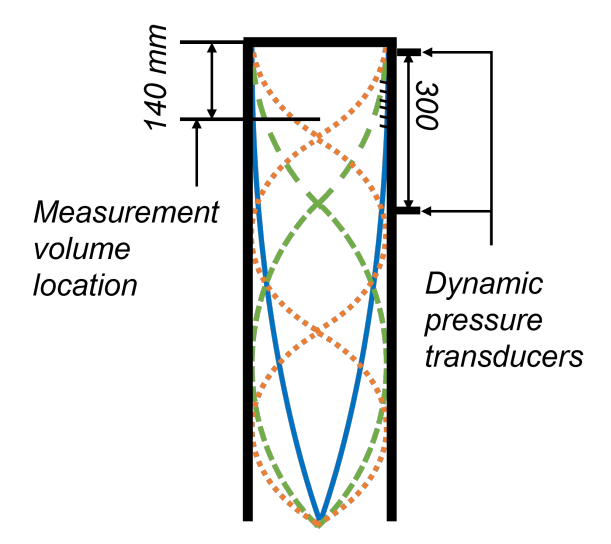


Figure 5.3: Diagram showing pressure variation for harmonic standing waves produced at 100 Hz (Blue), 257 Hz (Green) and 400 Hz (Orange) forcing frequencies.

100 Hz were conducted to observe the effects of liquid properties and air temperature on the droplet velocity response to forcing.

Using the same optical setup, the standard, slow speed, GSV processor was used to observe the change in mass flow rate of methanol droplets through the measurements volume with increasing temperature and forcing amplitude at 100 Hz forcing frequency. In these tests the frame-rate was reduced to 100 frames per second to ensure no individual droplet was measured more than once. Three forcing acoustic velocity amplitudes, 0.16, 0.33 and 0.48 m/s were compared with an unforced case at air temperatures 338 K, 369 K, 402 K and 486 K. The chosen temperatures relating to approximately 1×, 1.5×, 2× and 3.2× the boiling point of methanol.

5.5 PIT performance

For the purposes of testing PIT performance, droplet concentrations were kept low such that the tracking of individual droplets could be more easily manually assessed. Tests were also performed at low mean droplet velocities (no co-axial air flow) to ensure maximum droplet displacement amplitude. The results show the PIT to be capable of measuring droplets over multiple frames (100+) with droplet vertical

Forcing	Amplitude	Pre-amplification forcing amplitude (V)				
Frequency (Hz)	Estimate	0.5	1	1.5	2	2.5
100	P (Pa)	193.77	396.52	577.14	733.42	853.64
	u_a' (m/s)	0.16	0.33	0.48	0.61	0.71
257	P (Pa)	308.69	554.51	812.56	1061.48	1242.57
	u_a' (m/s)	0.83	1.53	2.26	2.96	3.47
400	P (Pa)	40.39	86.85	116.79	139.27	161.43
	u_a' (m/s)	0.45	0.75	1.00	1.19	1.40

Table 5.1: Two microphone method pressure (P) and axial velocity (U) amplitude estimations at the measurement volume axial centrepoint for all acoustic forcing conditions.

displacements of over ± 2 mm. Figure 5.4 shows a compilation of example droplets displaying a response to the acoustic forcing, clear sinusoidal trajectories can be observed. As droplet concentrations increased, and the coaxial air flow introduced, the PIT processor was still able to correctly identify and track droplets, successfully tracking multiple droplets in concentrations of up to 500 drops/cm³. The results of preliminary testing provide evidence for the performance of the PIT processor giving the necessary confidence in results to continue experimentation.

Droplet velocity response to acoustic forcing 5.6

For all of the chosen forcing frequencies droplet axial velocities were seen to respond. Figure 5.5 shows the mean subtracted instantaneous axial velocities for all droplets transiting the measurement volume for an example case at 257 Hz with an acoustic velocity amplitude estimated to be 2.96 m/s, droplet velocity variations are clearly seen to be following a sinusoidal profile for the full duration of measurement. The amplitude of axial velocity variation is seen to vary with droplet diameter, suggesting the rate of change of velocity for larger droplets is being reduced due to inertia and/or viscous drag forces. The amplitude of axial velocity variation is seen to vary from approximately 0.1 m/s for droplets greater than 80 μ m in diameter, increasing to approximately 0.9 m/s for droplets less than 40 μ m

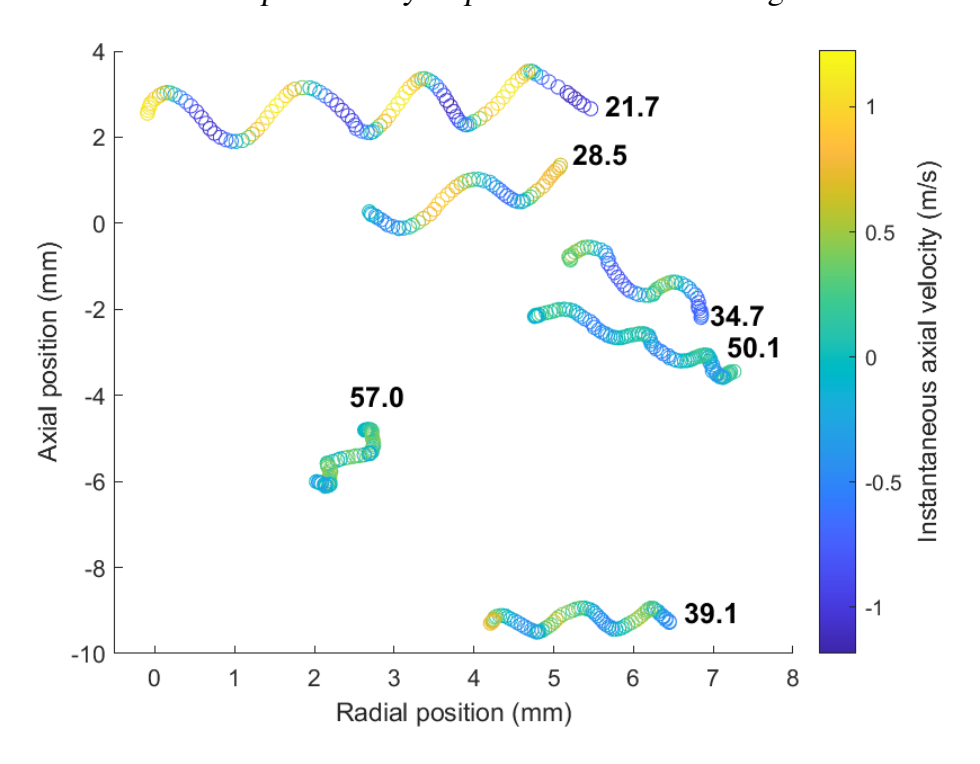


Figure 5.4: Example of position variations of PIT tracked droplets with an applied acoustic forcing frequency of 257 Hz at an acoustic velocity amplitude of 2.96 m/s. (0,0) co-ordinate relates to image centre, positioned at the radial centre of the spray, 140 mm axially downstream of the nozzle tip. Colourbar shows droplet instantaneous axial velocity, number label placed at the droplet staring position represents mean droplet diameter in microns.

in diameter. Given the mean air flow axial velocity of approximately 0.9 m/s at the measurement position these velocity variation amplitudes are significant, with smaller droplets (D<20 μ m) at this forcing frequency and amplitude, observed to become momentarily stationary. For all measured droplet diameters, droplet velocity amplitudes (u_d') are seen to be considerably less than that of the estimated acoustic velocity amplitude u_a' , thus velocity slip is likely occurring for all droplets at the given condition. The data presented in figure 5.5 shows no significant phase delay increase with droplet diameter.

A windowed FFT was used to determine the axial velocity variation amplitude at the forcing frequency for each droplet present within the measurement region for at least one period of acoustic oscillation. Figures 5.6 and 5.7 showing velocity variation amplitude with respect to droplet diameter for all test cases. It should be

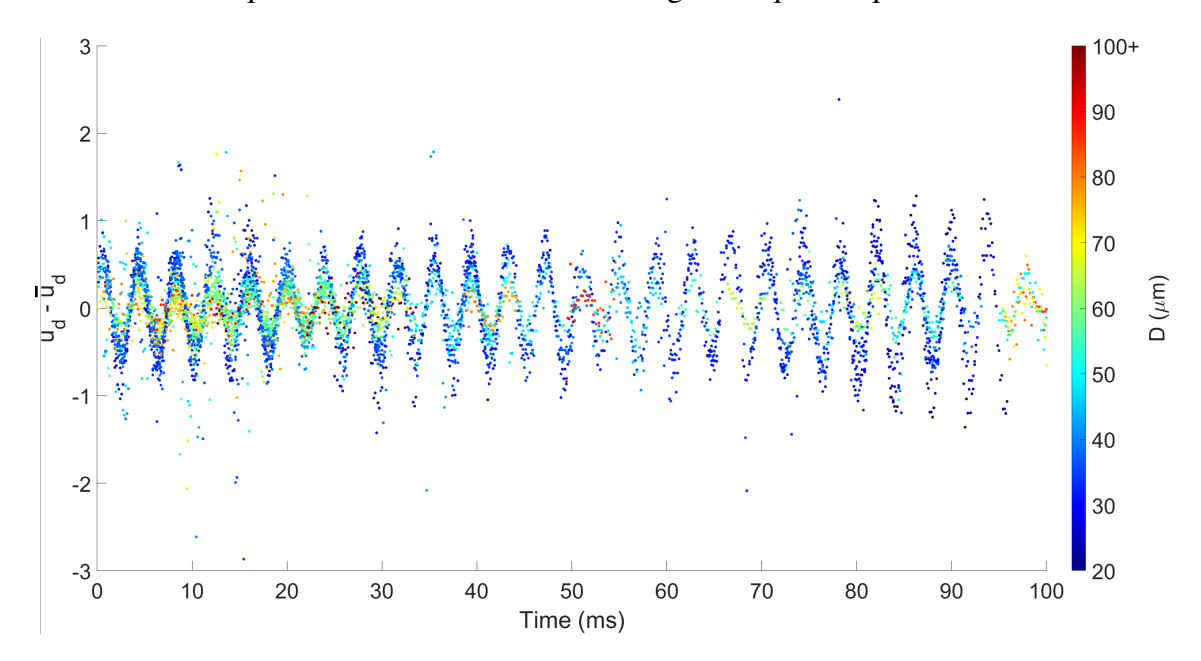


Figure 5.5: Mean subtracted instantaneous velocity $(u_d - \bar{u_d})$ for all droplets within the measurement volume against time for water with acoustically forced at 257 Hz with an acoustic velocity amplitude of 2.96 m/s, colourbar showing droplet diameter.

noted that as forcing frequency is increased the number of droplets that fulfil the criteria of having residence times of at least one acoustic oscillation period increases, hence the increase in sample number with increasing forcing frequency.

For all three forcing frequencies a clear droplet velocity amplitude response to acoustic velocity amplitude is evident. For smaller droplets, axial velocity variation amplitudes are seen to increase with forcing amplitude. The size range of droplets showing a response to forcing is also seen to increase with increasing forcing amplitude. The data acquired shows that trends in droplet velocity amplitudes across the test forcing frequencies are in good agreement with the predicted trends of acoustic velocity amplitudes. The 257 Hz condition is seen to display the highest droplet velocity amplitudes, with 100 Hz showing the lowest. Figures 5.6 and 5.7 confirm that droplets are not becoming fully entrained within the air flow. Full entrainment would be apparent as a plateau in the velocity amplitude of lower diameter droplets as droplet and air velocity reached equivalence. Observing the PIT results showing the droplet diameters versus velocity amplitude no plateauing is evident for any of the forcing conditions, suggesting droplets are not fully entrained within the flow

and a relative velocity fluctuation between droplet and air exists for all droplets measured.

Increasing air flow temperature and using methanol in place of water was seen to have no significant effect on droplet velocity response to acoustic forcing and seen in figure 5.7.

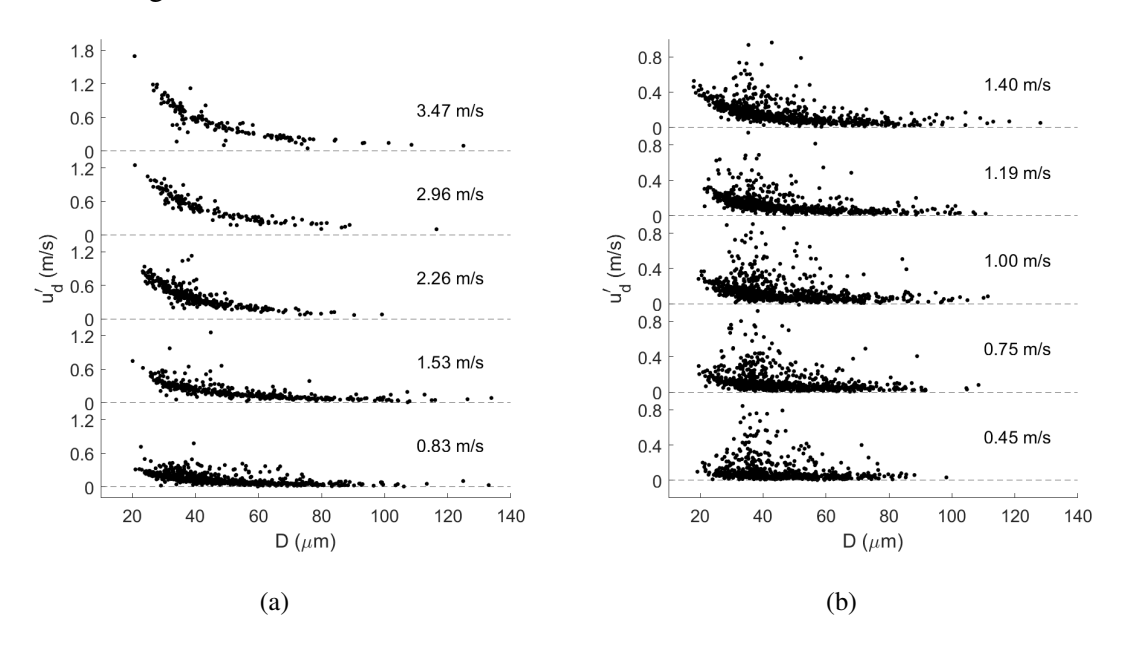


Figure 5.6: Water droplet diameter against velocity amplitude at acoustic forcing frequency for (a) 257 Hz and (b) 400 Hz and air temperature of 288 K, acoustic velocity amplitude shown by label. Note: Velocity Amplitude scale change.

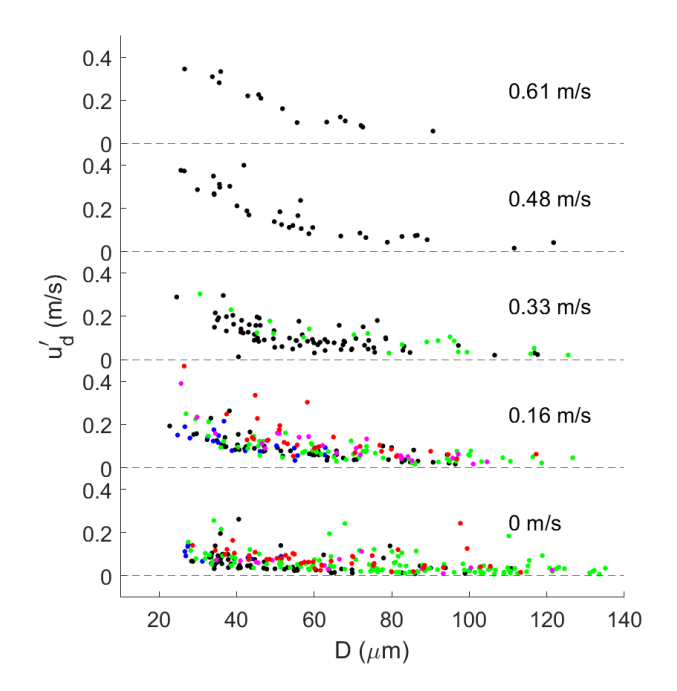


Figure 5.7: Droplet diameter against velocity amplitude at acoustic forcing frequency 100 Hz for Methanol at 338 K (Blue), 369 K (Green), 402 K (Magenta), 486 K (Red) and Water at 288 K (Black).

Using a similar approach as that shown by Sujith et al. (1997), the acoustic forcing amplitude can be normalised by using an entrainment factor, equation 5.1. From further analysis it is evident that the droplet entrainment is linearly proportional to the inverse of the droplet surface area, $\eta \propto \frac{1}{D^2}$, figure 5.8. As can be seen in figure 5.8 the relation between entrainment factor and inverse droplet diameter squared is negligibly influenced by acoustic amplitude. A greater number of droplets recorded in test conditions at lower acoustic velocity amplitudes are seen to display significant deviations from the general linear relation between the inverse of the droplet surface area and entrainment factor, Table 5.2. At lower acoustic velocity amplitudes, the impact of droplet velocity amplitude measurement error will be greater.

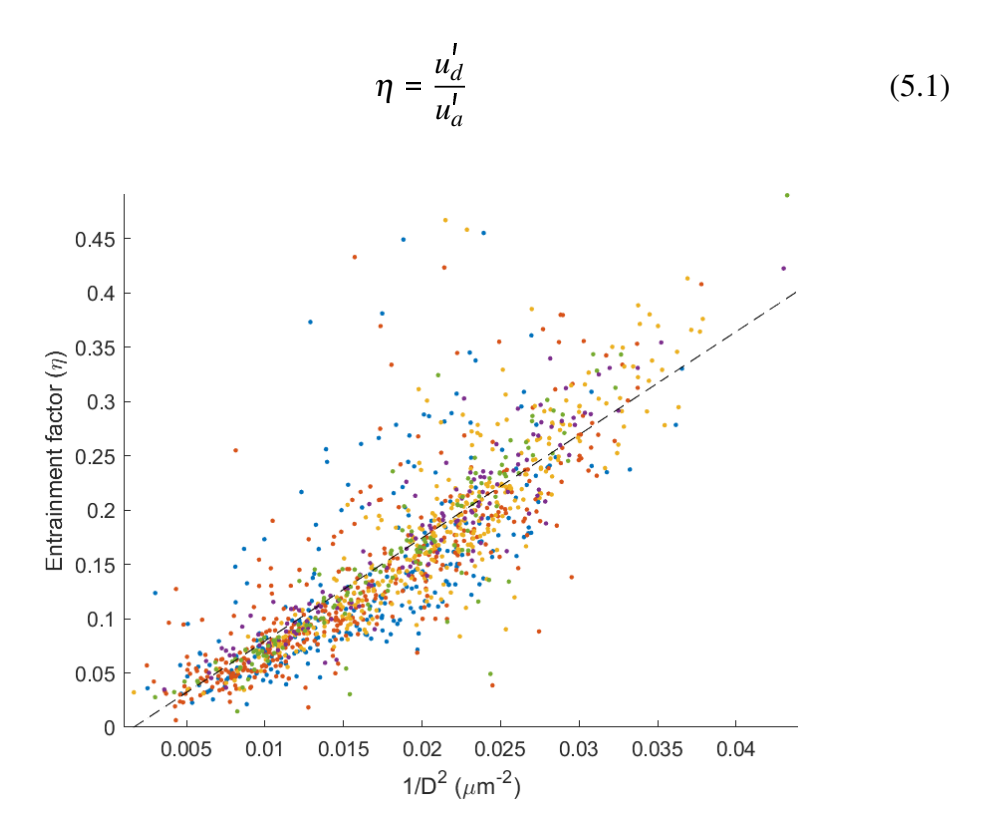


Figure 5.8: Inverse droplet diameter squared versus entrainment factor (η) at a forcing frequency of 257 Hz at acoustic velocity amplitudes of 0.83 m/s (Blue), 1.53 m/s (Red), 2.26 m/s (Yellow), 2.96 m/s (Purple) and 3.47 m/s (Green).

Figure 5.9 shows the change in entrainment factor with change in droplet diameter and forcing frequency. It is apparent that increasing forcing frequency reduces

Acoustics Velocity Amplitude (m/s)	R^2
0.83	0.42
1.53	0.79
2.26	0.86
2.96	0.90
3.47	0.95

Table 5.2: Goodness of fit (R^2) for data recorded at 257 Hz forcing frequency.

the entrainment of droplets within the flow, with the entrainment factor of a $20~\mu m$ reducing by approximately a third when comparing the 100~Hz and 400~Hz conditions. Though the trend in droplet diameter and entrainment factor is consistant, as can be seen in figure 5.9~for a given droplet diameter at a given forcing frequency there is a spread of entrainment factors. It is likely that this variation is due to measurement uncertainty in droplet diameter and droplet velocity measurement. However, beyond measurement uncertainty, other physical factors are likely to have an effect on the droplet entrainment within the acoustic flow field. The 'history' of the droplet before entering the inspection region is unknown, variations in axial velocity, trajectory, interfering turbulent frequencies and droplet inertia will affect the droplet entrainment within the measurement region. To account for the droplet history would be incredibly difficult, likely impossible. Through processes such as phase locking of image capture and acoustic forcing frequencies, as well as observing the change in individual droplet entrainment during its transit of the imaging window could give insight into the transient nature of the droplet motion.

The occurrence of increasing forcing amplitude reducing droplet entrainment is predicted for in the Stokes number, St, as defined by Hjelmfelt and Mockros (1966), equation 5.2, where increasing Stokes number indicates increased entrainment of droplets within the flow. Using equations 5.3-5.5, Hjelmfelt and Mockros (1966) related the Stokes number to the droplet entrainment factor, η , analytically.

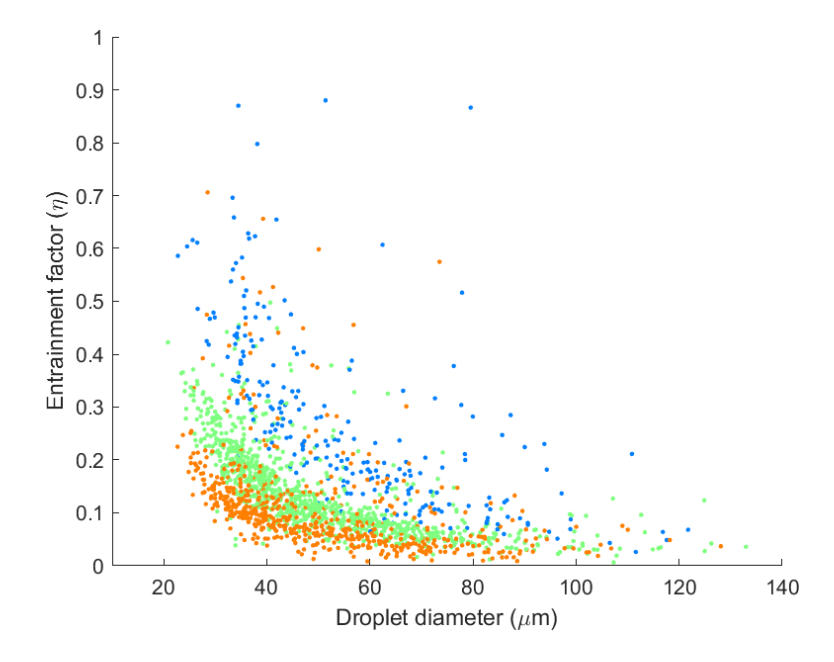


Figure 5.9: Droplet diameter versus entrainment factor (η) at forcing frequencies 100 Hz (Blue), 257 HZ (Green) and 400 Hz (Orange). Data points represent data from a range of forcing amplitudes at each forcing frequency as is shown in table 5.1.

$$St = \sqrt{\frac{v}{\omega D^2}} \tag{5.2}$$

$$f_{1} = \frac{\left[1 + \frac{9St}{\sqrt{2}\left(s + \frac{1}{2}\right)}\right] \left[\frac{1 - s}{s - \frac{1}{2}}\right]}{\frac{81}{\left(s + \frac{1}{2}\right)^{2}} \left[2St^{2} + \frac{St}{\sqrt{2}}\right]^{2} + \left[1 + \frac{9St}{\sqrt{2}\left(s + \frac{1}{2}\right)}\right]^{2}}$$
(5.3)

$$f_{2} = \frac{\left[1 + \frac{9(1-s)}{\left(s + \frac{1}{2}\right)^{2}}\right] \left[2St^{2} + \frac{St}{\sqrt{2}}\right]}{\frac{81}{\left(s + \frac{1}{2}\right)^{2}} \left[2St^{2} + \frac{St}{\sqrt{2}}\right]^{2} + \left[1 + \frac{9St}{\sqrt{2}\left(s + \frac{1}{2}\right)}\right]^{2}}$$
(5.4)

$$\eta = \sqrt{(1+f_1)^2 + f_2^2} = \frac{u_d'}{u_d'} \tag{5.5}$$

Where v is the kinematic viscosity of air, ω is the angular frequency and s is the ratio of droplet and air densities, $\frac{\rho_d}{\rho_a}$.

Comparing the relation between Stokes number and entrainment factor (shown in Figure 5.10) it can be seen that the experiment measurements closely follow the

predicted trend from equations 5.2-5.5. From further analysis those droplet data points showing significant deviations from the predicted trends are found to be from low acoustic velocity amplitude test conditions, 5.11, this being expected for the reasons mentioned previously.

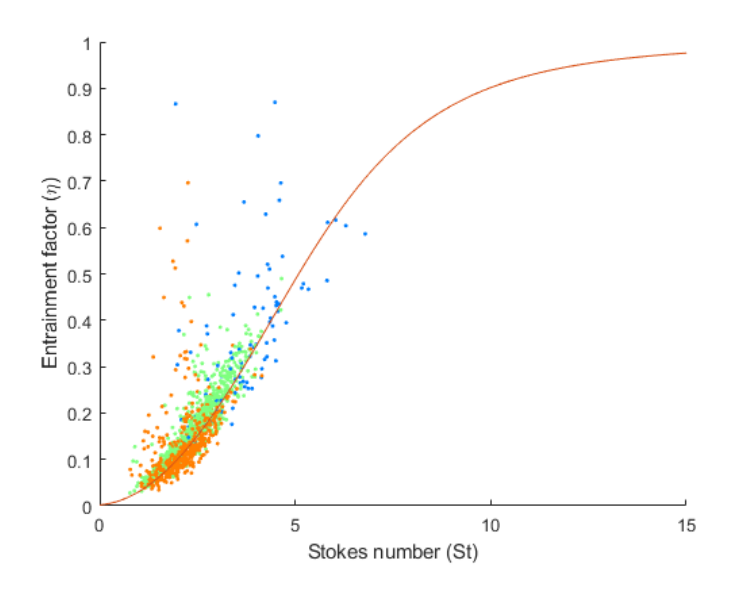


Figure 5.10: Stokes number (St) (equation 5.2) plotted against entrainment factor (η) at forcing frequencies 100 Hz (Blue), 257 HZ (Green) and 400 Hz (Orange). Data points represent data from a range of forcing amplitudes at each forcing frequency as is shown in table 5.1.

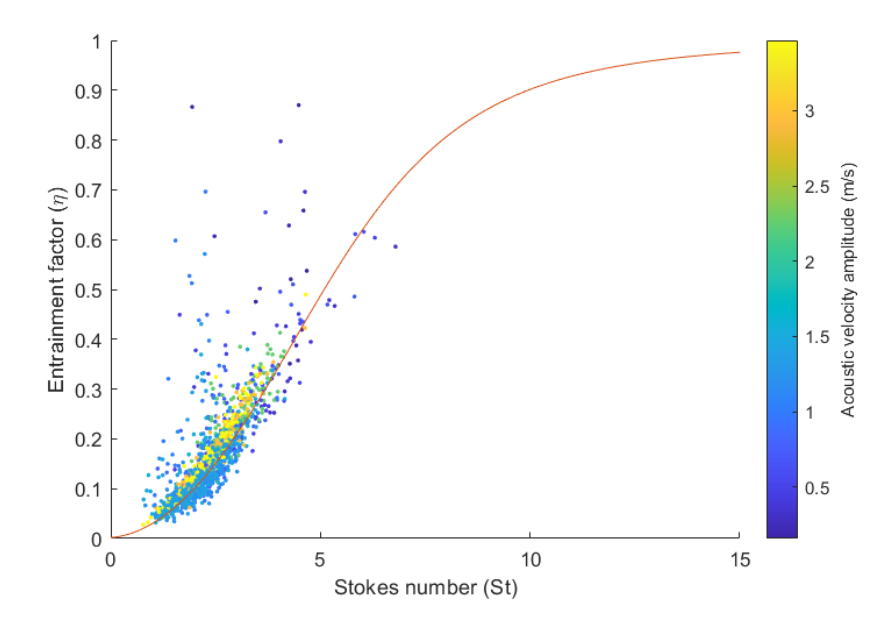


Figure 5.11: Stokes number (St) (equation 5.2) plotted against entrainment factor (η) at forcing frequencies 100 Hz , 257 HZ and 400 Hz. Colourbar showing forcing acoustic velocity amplitude.

According to the predictions made by Hjelmfelt and Mockros (1966) and observations made of single droplet responses to acoustic forcing by Sujith et al. (1997), in addition to a decrease in amplitude response with increasing droplet diameter the phase difference between acoustic and droplet velocity variance is also seen to increase, that is larger droplets experience an increased phase delay. However, no significant relation between droplet diameter and phase differential was noted in the experiments carried out in this study. The introduction of acoustic forcing was seen to have no effect on either radial velocity variations or mean radial velocity magnitude for any of the test conditions.

It must be noted that the analytical model produced by Hjelmfelt and Mockros (1966), shown in figure 5.10 assumes small acoustic Reynolds numbers (creeping flow) such that entrainment factor is independent of acoustic velocity amplitude. Thus, entrainment factor is a solely a function of droplet stokes number, as per equations 5.2 - 5.5. For systems with higher acoustic Reynolds numbers, droplet drag has a nonlinear dependence on acoustic velocity amplitude. Despite the good agreement displayed between measured data and model in figure 5.10, at the acous-

tic Reynolds numbers for the test conditions exceed the stated assumptions, a degree of error is expected when applying this model at the given test conditions. As is shown by Sujith et al. (1999), droplet entrainment would be expected to increase as acoustic velocity amplitude increases. Figure 5.12 shows the effect acoustic velocity amplitude on the relation between droplet diameter and entrainment factor. The measurement do not show any clear variation in droplet diameter-entrainment factor relation with increasing acoustic velocity amplitude.

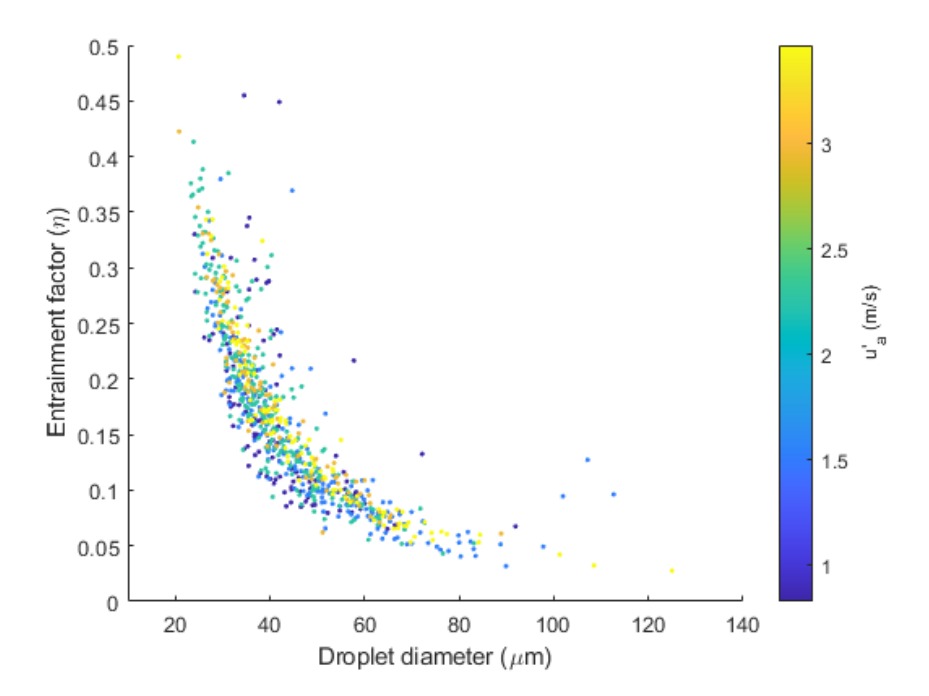


Figure 5.12: Droplet diameter versus entrainment factor (η) at 257 HZ forcing frequencies. Colours showing range of acoustic velocity amplitudes (u_a^l) .

At the relatively low acoustic velocity amplitudes achieved in this study, the difference in entrainment factor due to assuming a linearised solution is relatively insignificant (<5% (Sujith et al., 1999)). Considering the error in droplet diameter measurement due to defocus variation (approximately $\pm 20\%$), the PIT measurement method in its current state is not capable of discerning the relatively small changes in droplet entrainment due to acoustic velocity amplitude. Given the limitation in measurement certainty, further work in comparing more complex solutions of droplet motion, such as those described by Sujith et al. (1999) and Clift et al.

(2005), to the data gathered was not seen to be applicable.

Along with acoustic forcing amplitude having an effect on the droplet fluctuating velocity component amplitude, a clear reduction in mean droplet axial velocity with increasing forcing amplitude was observed. Figure 5.13 shows the mean axial velocity decrease with increasing forcing amplitude for the 100 Hz forcing frequency, an approximate 50% reduction in droplet mean axial velocity on increasing forcing amplitude from 0.0 to 0.71 m/s. For the unforced condition mean axial droplet velocities are approximately equal to that of the air flow velocity as measured by a hot wire anemometer. The non-linear dependence of droplet drag on the relative velocity between the droplet and gas phase is known to result in a decrease in droplet mean terminal velocity with increasing velocity amplitude, as noted by Sujith et al. (1999).

As can be seen in Figure 5.13, in all conditions mean axial velocity is seen to increase with increasing droplet diameter. These findings regarding the reduction in droplet terminal velocities with the introduction of axially oscillating fluids are in agreement with other studies, both numerical and empirical (Baird et al., 1967; Chishty et al., 2005; Houghton, 1966; Kumara Gurubaran and Sujith, 2008; Sujith, 2005; Sujith et al., 1997, 2000).

5.7 Convection evaporation enhancement

To determine the significance of evaporation enhancement due to convection effects, the single droplet evaporation model defined in the previous chapter 4.4.1, page 125, was implemented with an additional factor accounting for the relative difference in velocities between the air flow and droplet. As described by Lefebvre and McDonell (2017), a correction factor, a function of Reynolds and Prandtl numbers, shown in equation 5.6, is multiplied against the rate of droplet mass reduction from conductive evaporation put forward previously in equation 4.18.

$$1 + 0.3Re_d^{0.5}Pr_g^{0.33} (5.6)$$

The Reynolds and Prandtl numbers for the correction factor are calculated us-

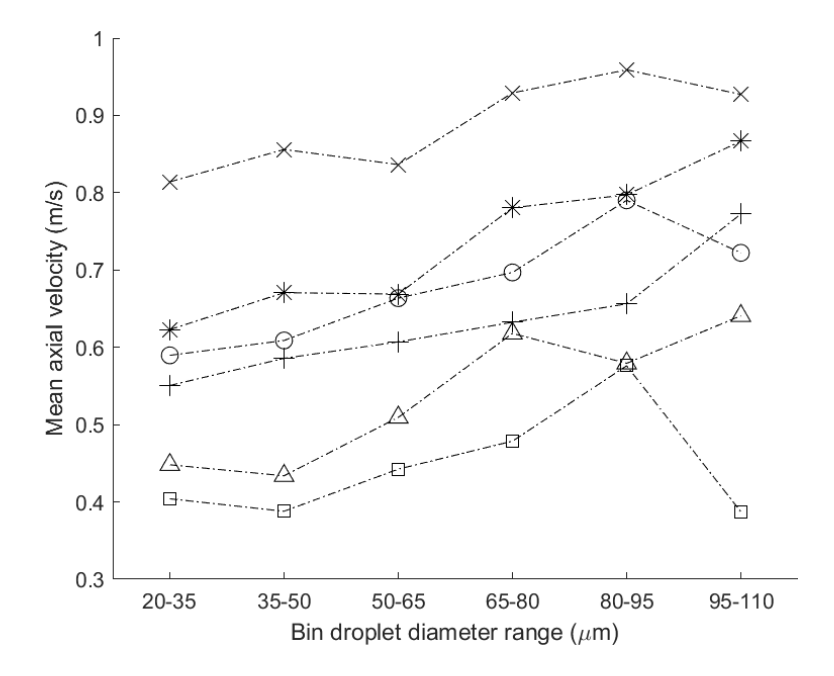


Figure 5.13: Mean axial velocity variation with droplet size, bin size 15 μ m, and increasing forcing amplitude, 0 m/s (×), 0.16 m/s (*), 0.33 m/s (\bigcirc), 0.48 m/s (+), 0.61 m/s (\triangle), 0.71 m/s (\square).

ing equations 5.7 and 5.8.

$$Re_d = \frac{u_{rel}D\rho_g}{\mu_g} \tag{5.7}$$

$$Pr_g = \frac{c_{p_s} \mu_g}{k_g} \tag{5.8}$$

Where k_g and c_{p_s} have been determined in equations 4.7 and 4.10. u_{rel} , is the relative velocity between air and droplet. The variables ρ_g and μ_g are the methanol vapour-air mixture at the reference temperature (T_r) and reference air and methanol mass fractions $(\gamma_{A_r}$ and $\gamma_{F_r})$ described in equations 4.2, 4.3 and 4.4. These values being calculated using the following equations 5.9 and 5.10.

$$\rho_g = \left(\frac{\gamma_{A_r}}{\rho_{A_r}} + \frac{\gamma_{F_r}}{\rho_{V_r}}\right)^{-1} \tag{5.9}$$

$$\mu_g = \gamma_{A_r} \left(\mu_A \ at \ T_r \right) + \gamma_{F_r} \left(\mu_V \ at \ T_r \right) \tag{5.10}$$

Assuming air to be an ideal gas, ρ_{A_r} can be determined. Equation 5.11 describes the relation between methanol vapour density and temperature Faghri and Zhang (2006).

$$\rho_{v} = exp\left(a_{1} + b_{1}T_{r} + c_{1}T_{r}^{2} + d_{1}T_{r}^{3} + e_{1}T_{r}^{4} + f_{1}T_{r}^{5}\right) \times 10^{3}$$
(5.11)

Where constants a_1 to f_1 can be found in table 5.3. Similarly equations 5.12 and 5.13 describe the relation between the dynamic viscosity's of air White and Majdalani (2006) and methanol vapour Faghri and Zhang (2006) with temperature respectively. Constants a_2 to f_2 can also be found in table 5.3.

$$\mu_A = 1.716 \times 10^{-5} \frac{273 + 111}{T_r + 111} \left(\frac{T_r}{273}\right)^{3/2}$$
 (5.12)

$$\mu_{\nu} = exp\left(a_2 + b_2T_r + c_2T_r^2 + d_2T_r^3 + e_2T_r^4 + f_2T_r^5\right) \times 10^{-7}$$
 (5.13)

Constant	Methanol vapour	Methanol vapour		
Constant	density 1	viscosity 2		
a	-67.3	4.4794		
b	2.1944	3.93e-03		
c	-3.09e-02	4.02e-06		
d	2.14e-04	-7.34e-08		
e	-7.20e-07	2.46e-10		
f	9.47e-10	-2.10e-13		

Table 5.3: Constants for equations 5.11 and 5.13 (Faghri and Zhang, 2006).

As has been observed, the relative velocity, u_{rel} , between droplet and air will be dependent on droplet diameter, figure 5.9. Using the model relating droplet entrainment and stokes number as defined by Hjelmfelt and Mockros (1966), the relation between droplet stokes number (a function of droplet diameter, equation 5.2) and entrainment factor can be used to define the specific slip velocities for a

methanol droplet of given diameter. Thus the relative velocity between droplet and air flow, u_{rel} , as a function of time can be expressed as an equation with form:

$$u_{rel}(t) = u_a'(1-\eta)\sin(\omega t)$$
 (5.14)

where u_a^{\prime} is the axial acoustic (air) velocity amplitudes determined through the two microphone method, η is the droplet entrainment factor, calculated from equations 5.2-5.5, with the densities of liquid methanol and air with respect to temperature being expressed in equations x and x.

Combining equations 5.6, 5.7 and 5.14, it is evident that when acoustic forcing is present, modelled droplet evaporation rate will vary sinusoidally with time. The mean droplet evaporation rate, \bar{k} , over a period of 20 ms (equivalent two full oscillation cycles), can be used to display the effects of an acoustic flow field (100 Hz at an acoustic amplitude of 0.48 m/s) on modelled evaporation rate, figure 5.14. The model shows that at air flow temperatures of 338 K and 486 K, considerable evaporation enhancement should be expected especially for droplets of larger diameter figure 5.15.

As defined by Gökalp et al. (1992), vaporisation Damköhelr number, Da_v , the ratio of timescales relating to turbulence (in this case acoustic oscillations), τ_e and vaporisation, τ_v , equation 5.15, can be used to examine the relative influence of velocity variations on the evaporation of droplets. Numerical works have shown a strong correlation between the vaporisation Damköhelr number and evaporation enhancement of droplets in turbulent flows (Lupo et al., 2020; Wu et al., 2003), where the lower the value of Da_v the higher the evaporation enhancement. For both air flow temperatures 338 K and 486 K forced at 100 Hz at an amplitude of 0.48 m/s the timescales relating to oscillations, τ_e will be similar, as temperature was seen to have no noticeable effect on droplet velocity response, figure 5.7. As temperature increases, the evaporation time scale, τ_v , will reduce, increasing the value Da_v , and reducing the influence of flow oscillation induced convection on droplet evaporation.

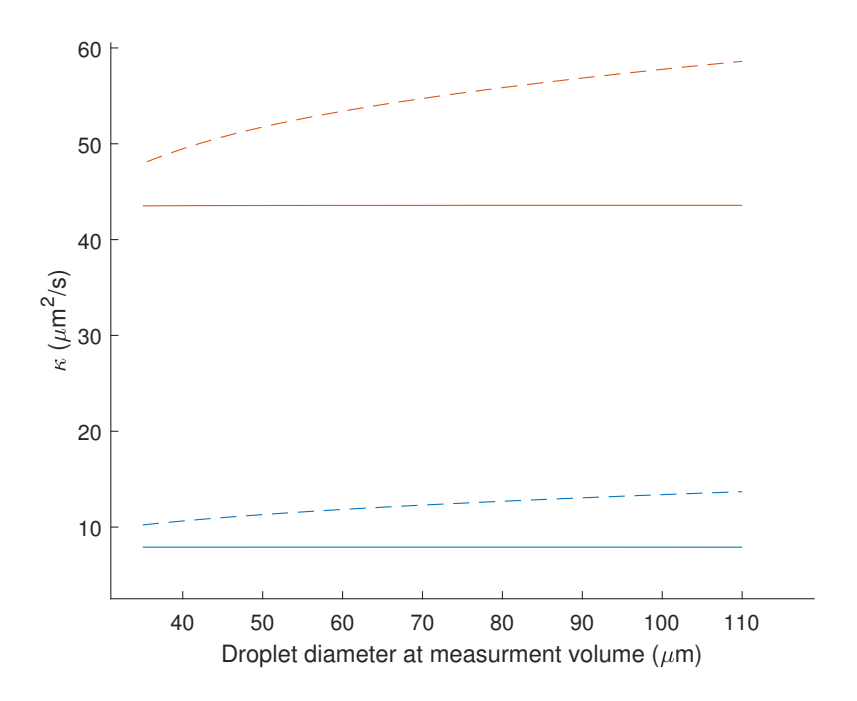


Figure 5.14: Methanol droplet mean evaporation rate κ versus diameter at start of measurement volume, D_M , with no acoustic forcing (—), and acoustically forced at 100 Hz, an amplitude of 0.48 m/s (- - -), for air flow temperatures of 338 K (Blue) and 486 K (Red).

$$Da_v = \frac{\tau_e}{\tau_v} \tag{5.15}$$

The model estimate as displayed in 5.15 is in agreement with these expectations. At air flow temperatures of 338 K droplet evaporation enhancement increases from 30% to 75% as droplet diameter increases from 35 μ m to 110 μ m, at air flow temperatures of 486 K evaporation rate enhancement reduces to 10-35% across the same droplet diameter range.

5.8 Spray evaporation characterisation

A series of tests were performed to asses whether the predicted relations between temperature, acoustic velocity amplitude and droplet evaporation are seen within the methanol spray.

Though the direct measurement of droplet evaporation rate through Lagrangian tracking using PIT, as shown in chapter 4, would be an ideal method for determining

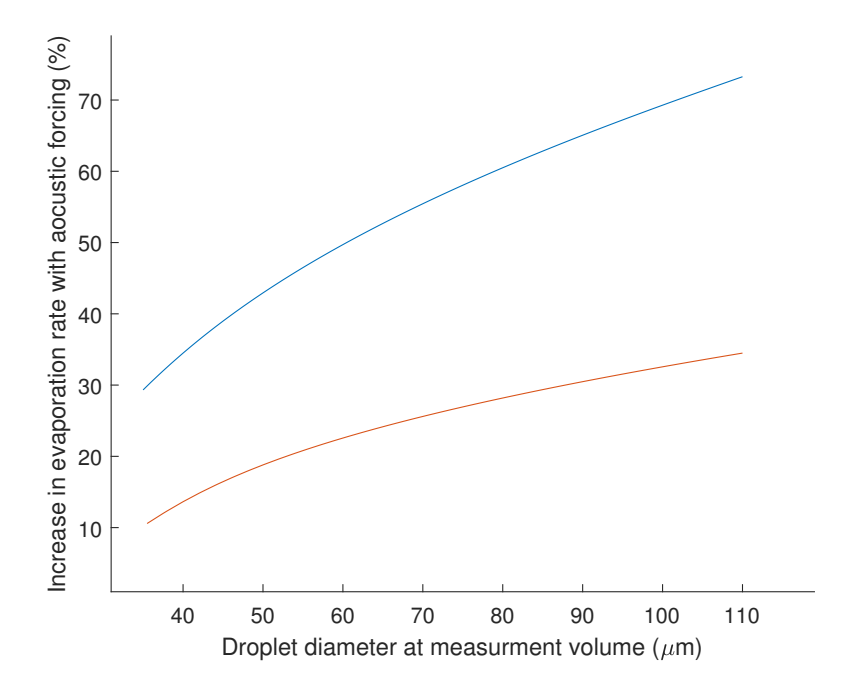


Figure 5.15: Modelled methanol droplet evaporation rate enhancement (%), due to the convection associated with a flow forced at 100 Hz, an amplitude of 0.48 m/s for air flow temperatures of 338 K (Blue) and 486 K (Red).

the evaporation rates of droplets within a spray. However, no significant variations between an acoustically forced flow field and a non-acoustically forced flow field could be identified when using PIT. This likely being a result of the droplet diameter measurement error associated with out of plane droplet motion being. Further as has been previously discussed, the effects of droplet history on droplet evaporation likely have considerable influence in both acoustically forced and unforced cases, as has been noted in the previous chapter. To account for such variations a large data set would have to be captured. The considerable amount of data reduction required and uncertainty in evaporation rate measurement mean that in it's current form PIT is not suitable for observing the enhancement of droplet evaporation through acoustic forcing.

Using the same optical setup as that used for PIT measurements, the camera image capture frequency was reduced to 300 frames per second, enabling the characterisation of the spray in use through the means of a slow speed IDS measurement

system (PIT was not in use for these tests).

All tests were performed using an acoustic forcing frequency of 100 Hz. Three forcing acoustic velocity amplitudes, 0.16, 0.33 and 0.48 m/s were compared with an unforced case at air temperatures 338 K, 369 K, 402 K and 486 K. The chosen temperatures relating to approximately 1×, 1.5×, 2× and 3.2× the boiling point of methanol. For each test condition 1,000 images were captured. The outcomes of this testing show how variations in temperature and acoustic velocity amplitude effect the mass flow rate and size distribution of droplets transiting the measurement volume, as well as spatial variations in mean droplet diameter. These measurements provide indications as to how temperature and acoustic velocity amplitude impact methanol droplet diameter reduction over a fixed distance (140 mm between nozzle and measurement volume) within the spray, they do not provide direct measurement of individual droplet evaporation rates.

When observing measurements, the effects of acoustic velocity amplitude on droplet mean axial velocity must be considered, with mean axial velocities reduced by approximately 25% when acoustic velocity amplitude is increased from 0.0 m/s to 0.48 m/s at 100 Hz frequency, figure 5.13. A reduction in droplet mean velocity within the measurement volume with increasing acoustic velocity amplitude infers an increased duration of travel for droplets transiting the 140 mm between the nozzle tip and measurement volume. The increased duration of travel will effect the measured mass flow rate and droplet diameter distribution of droplets transiting the measurement volume.

5.8.1 Spray geometry and droplet concentration

Contrary to the findings of Kumara Gurubaran and Sujith (2008), spray geometry showed no noticeable change in cone angle or spray radial direction with increasing forcing amplitude. Further, droplet radial velocity were not seen to significantly vary with increasing forcing amplitudes. It should be noted that in this experiment, the introduction of coaxial flow through an annular ring, figure 4.2, may act to impede the expansion of spray cone angle as was noted by Potdar et al. (2018).

Droplet concentrations within the measurement volume were seen to signifi-

cantly decrease with increasing forcing amplitudes and temperatures, Figure 5.16 (a). The reduction in droplet concentration with increasing temperature and forcing amplitude is likely due to increased evaporation rather than a redirection of droplets away from the measurement volume.

5.8.2 Mass flux of droplets

Figure 5.16 (b) shows the mean mass flow rate of droplets through the measurement volume. As would be expected for the unforced cases a decrease in mean mass flow rate is observed with increasing air temperature. However, for the lower temperature conditions (338 K and 369 K) it can be seen that mean mass flow rate increases with increased acoustic amplitude. Figure 5.16 (a) shows that at the low temperature conditions despite the number of droplets transiting the measurement volume reducing, there is an increase in mean mass flow rate. Thus it is evident that at the low temperature conditions the droplet size profile is changing such that despite the number of smaller droplets (D \leq 70 μ m) decreasing, there is an increase in the number of higher diameter droplets transiting the measurement volume, figure 5.17 (a) and (b). Though slight, the increase in the number of larger droplets has a significant effect on the total mass flux, figure 5.18. More observations are required to fully explain the observed phenomena though it is theorised that potentially there is an interaction between the acoustic forcing and ultrasonic atomisation process, resulting in a a greater proportion of larger droplets being produced, though there has been no specific research performed on this phenomena.

Using the lowest temperature condition (338 K) as a reference, the relative change in mass flow rate with increasing temperature and forcing amplitude can be more easily observed, figure 5.16 (c). A clear reduction in relative mass flow rate is seen with increasing forcing amplitude for the three temperature conditions, though at 369 K and 402 K forcing effects are only apparent at acoustic velocity amplitudes of 0.33 and 0.48 m/s respectively. At the highest temperature condition (486 K) there is an almost linear relation between the increasing forcing amplitude and relative reduction in mass flow rate. Increasing forcing amplitude is seen to offer significant levels of mass flow reduction in comparison to air flow temperature

increase.

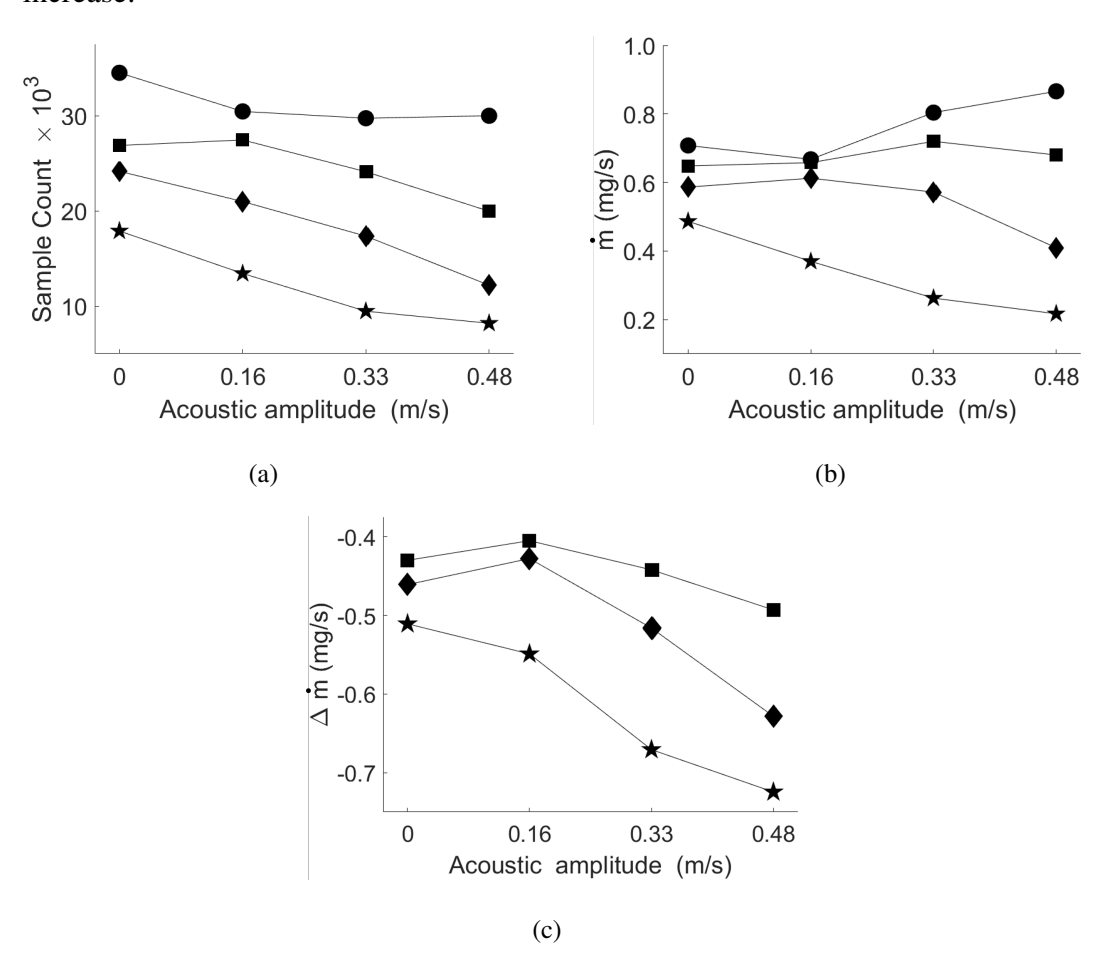
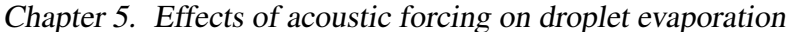


Figure 5.16: (a) Methanol droplet sample size with acoustic forcing amplitude,(b) Mass flow rate, \dot{m} , of measured methanol droplets through measurement volume with acoustic forcing amplitude, (c) Mass flow rate reduction relative to 338 K conditions ($\Delta \dot{m} = \dot{m}_T - \dot{m}_{338K}$) at 100 Hz and temperature, 338 K (\bullet), 369 K (\blacksquare), 402 K (\blacklozenge), 486 K (\star)

5.8.3 Mean droplet diameter

For all conditions tested, no significant trend between mean droplet diameter and radial displacement from the spray centreline was observed, as is shown in figure 5.19. It is apparent however, that mean droplet diameter across the full width of the measurement region increased with both increasing temperature and increasing forcing amplitude, with the exception of the 486 K air flow temperature condition, where little signification change is seen. Though counter intuitive it is well established that in cases of increased evaporation, mean droplet diameter measurements will



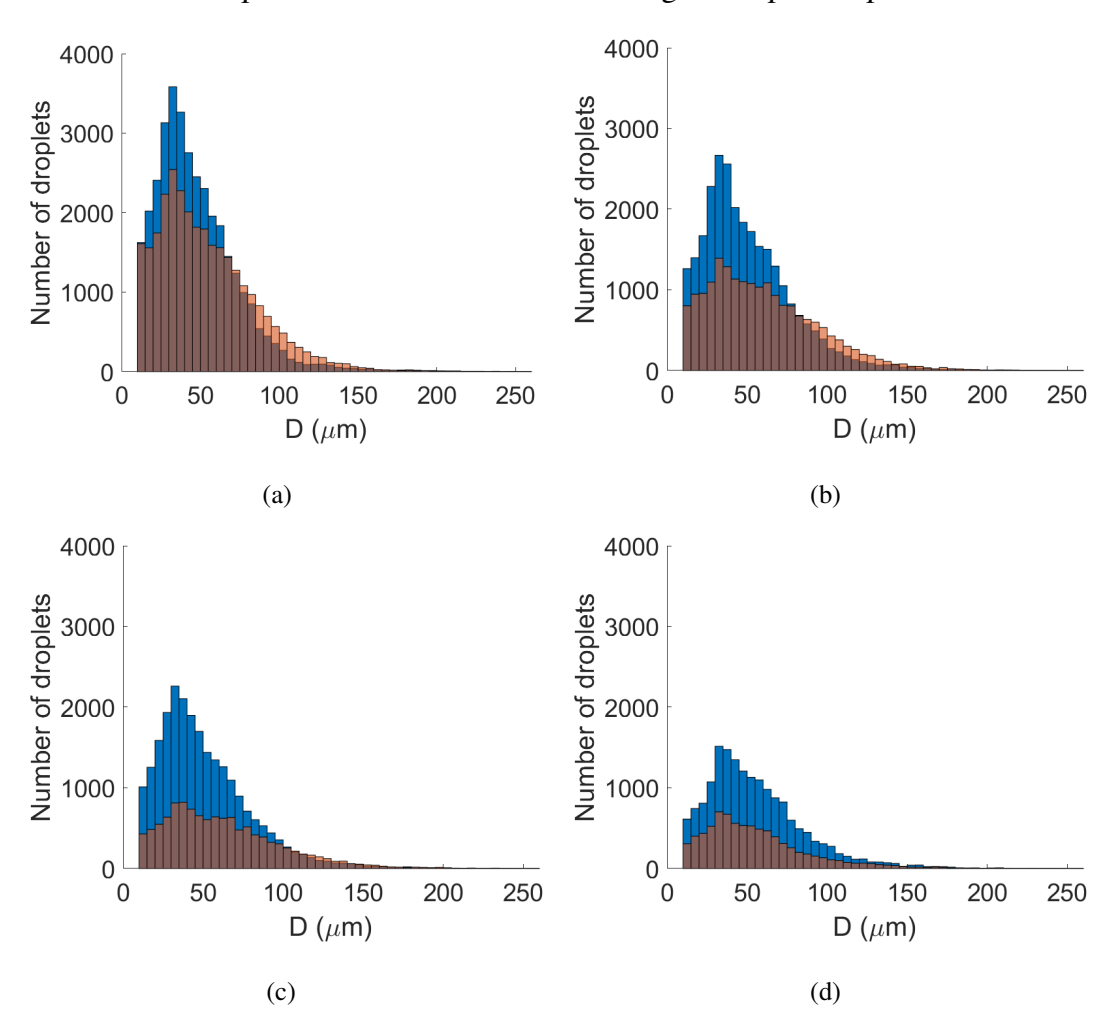


Figure 5.17: Droplet diameter histogram for an unforced (Blue) and forced (Red), (100 Hz 0.48 m/s) conditions where air flow temperature is (a) 338 K, (b) 369 K, (c) 402 K, (d) 486 K.

increase, as seen in works by Gong et al. (1992) when observing the effects of ambient air temperatures of diesel fuel sprays. This reasoning behind this phenomena can more easily be seen when the equation representing the D^2 law is rearranged to express the droplet diameter as a function of time,

$$D = \sqrt{D_0^2 - \kappa t} \tag{5.16}$$

for a given time interval the relative reduction in droplet diameter for a larger droplet will be less than that of a smaller droplet. In conditions conducive with high level of droplet evaporation, a large proportion of smaller droplets will reduce in size

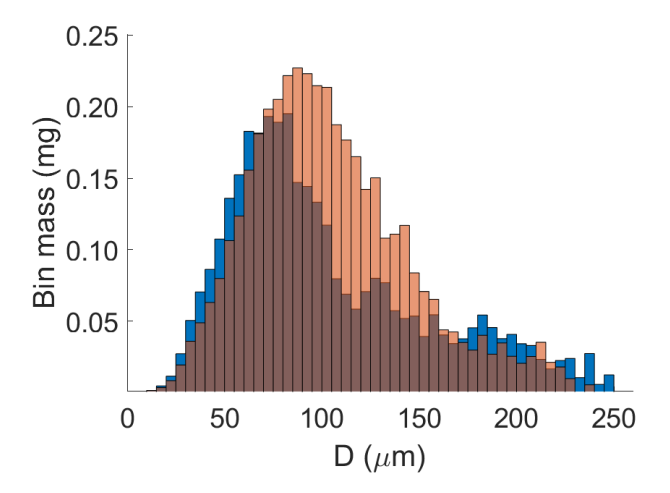


Figure 5.18: Mass contribution of droplets for an unforced (Blue) and forced (Red) (100 Hz 0.48 m/s) conditions where air flow temperature is 338 K.

such that they completely evaporate or decrease below the minimum measurable diameter, thus the mean droplet diameter increases. As can be seen in figure 5.17, in all cases increasing temperature and forcing amplitude reduces the number of of smaller droplets, whilst the proportion of larger droplets does not decrease as significantly¹, indicating an increase in the degree of evaporation.

When observing the effects of acoustic velocity amplitude on mean droplet diameter, the observed increase in larger droplets transiting the measurement volume must also be considered. This phenomena will further increase the measured mean droplet diameter, though to a much lesser extent relative to the greater decrease in number of smaller droplets (D \leq 70 μ m).

With increasing axial displacement from the atomiser nozzle, mean droplet diameters were seen to increase for all conditions tested, figure 5.20, further, with increasing forcing amplitude mean droplet diameters were consistently higher at the measured axial positions, this not being as apparent at the 486 K air flow temperature. The mean droplet diameter increased over the approximate 20 mm distance from the top of measurement volume to the bottom with increasing forcing amplitude for almost all cases, table 5.4. In the previous chapter discussing the

¹For the 338 K and 369 K conditions the increase in number of larger droplets present is likely due to the interaction between acoustic oscillations and atomisation process as mentioned previously

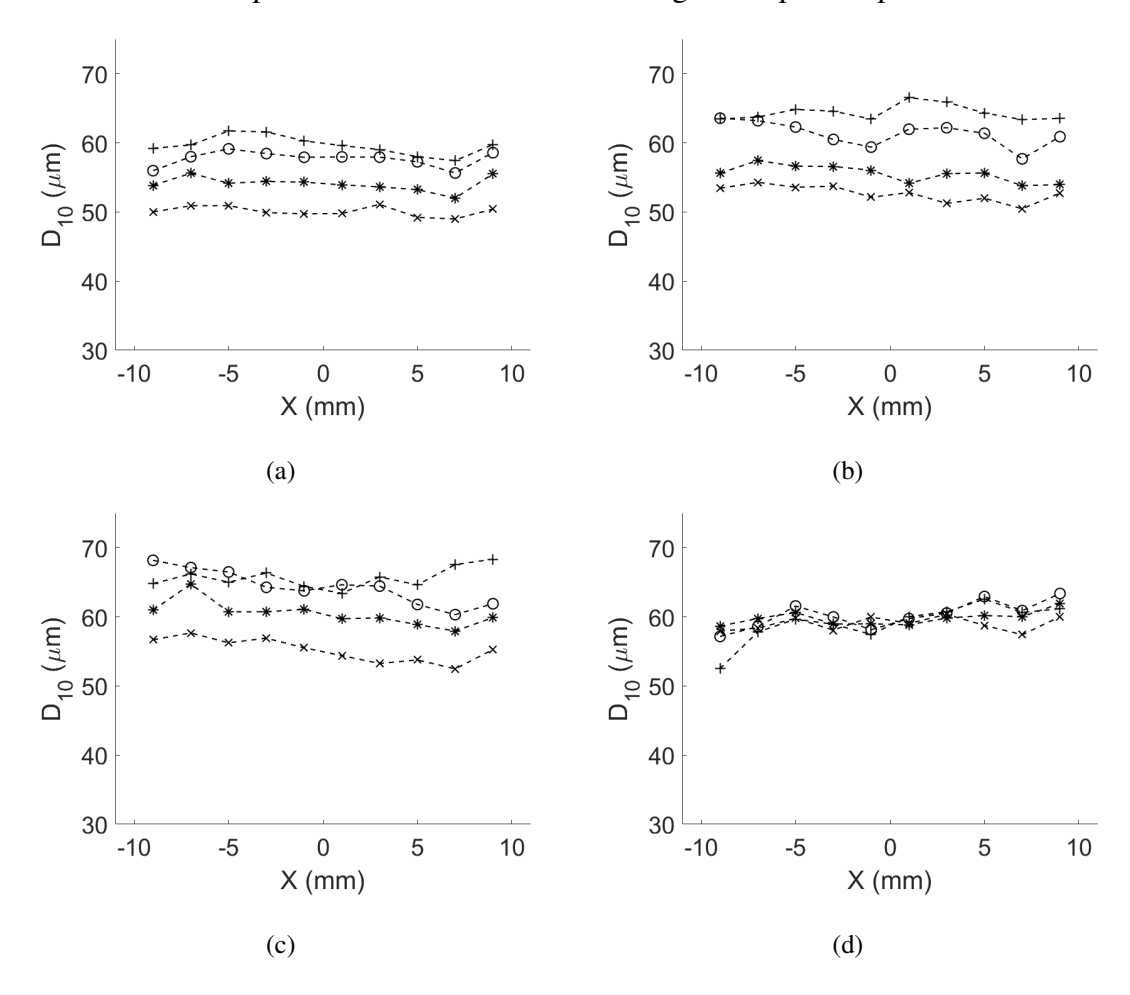


Figure 5.19: Mean droplet diameter, D_{10} , with radial displacement, X, at air flow temperatures (a) 338 K, (b) 369 K, (c) 402 K and (d) 486 K at a forcing frequency of 100 Hz and acoustic velocity amplitudes of, 0.0 m/s (×), 0.16 m/s (*), 0.33 m/s (\bigcirc) and 0.48 m/s (+).

PIT tracking of individual droplets², droplets transiting the measurement volume, with no acoustic forcing at air flow temperatures of 495 K, were seen to experience significant levels of evaporation. Droplets between 50 and 70 μ m were recorded to reduce in diameter by as much as 9 μ m in 25 ms, 25 ms being the approximate measurement volume transit time for a droplet travelling at 0.9 m/s, figure 4.9. Given these levels of diameter reduction in smaller droplets, it would be expected in similar conditions such as the unforced test case at 486 K in this study, that the mean droplet would increase, as is seen in figure 5.20. Thus, it is likely that the increase in between the mean droplet diameter at the top and bottom of the mea-

²No changes were made to the experimental setup apart from those discussed in section 4.3

surement volume is due to the additional evaporation of droplets. Considering this it is evident that increasing the forcing amplitude considerably increases the mean droplet diameter change, implying an increase in the rate of droplet evaporation with increasing acoustic velocity amplitude. When increasing air flow temperature, the effect of acoustic forcing on the proportional increase in mean droplet diameter between the top and bottom of the measurement volume is seen to reduce. Inferring the impact of acoustic velocity amplitude on droplet evaporation rate has decreased, this agreeing with model expectation previously described.

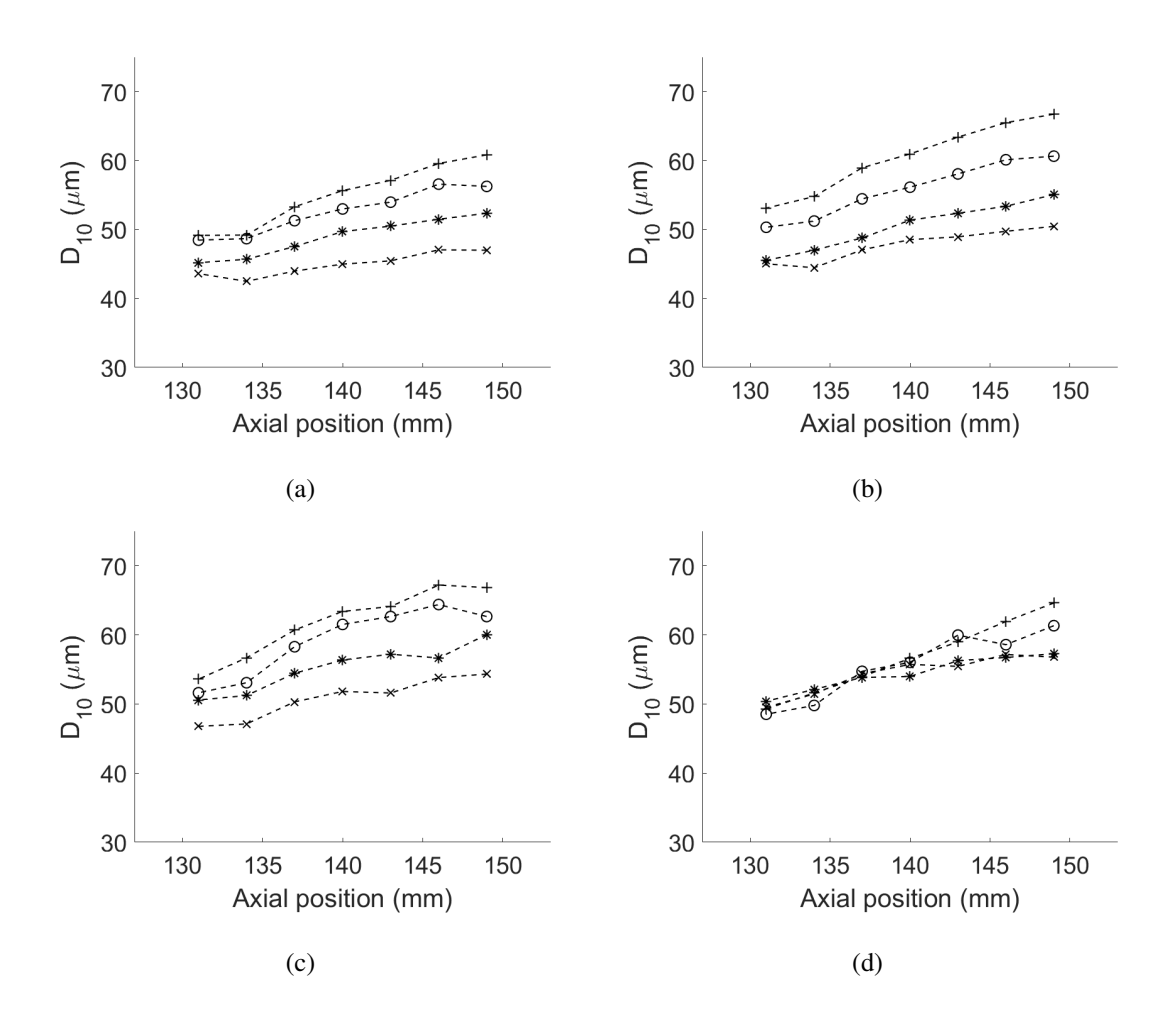


Figure 5.20: Mean droplet diameter, D_{10} , with axial position, at air flow temperatures (a) 338 K, (b) 369 K, (c) 402 K and (d) 486 K at a forcing frequency of 100 Hz and acoustic velocity amplitudes of, 0.0 m/s (×), 0.16 m/s (*), 0.33 m/s (\bigcirc) and 0.48 m/s (+).

Table 5.4: Mean droplet diameter increase (ΔD_{10}) with axial displacement from measurement volume top to bottom (≈ 20 mm).

Forcing Velocity	ΔD_{10} (μ m) at air flow temperatures					
Amplitude (m/s)	338 K	369 K	402 K	486 K		
0.00	3.4	5.4	7.6	7.3		
0.16	7.2	9.6	9.5	6.9		
0.33	7.8	10.3	11.0	12.8		
0.48	11.7	13.6	13.3	15.3		

5.9 Conclusion

In conclusion the Planar Interferometric Tracking (PIT) processor was applied to a spray produced by an ultrasonic atomiser, injecting droplets into a co-axial air flow at various air flow temperatures and acoustic field strengths. Droplets were observed transiting $16 \times 20 \times 2$ mm measurement volume located along the axial centreline of the spray, 140 mm downstream of the nozzle tip.

At all three forcing frequencies of 100 Hz, 257 hz and 400 Hz, relating to the 1^{st} , 3^{rd} and 5^{th} harmonics of the of the 920 mm long, square section pipe used, acoustic velocity amplitudes at the measurement volume position were estimated using a two microphone method, using data acquired from two dynamic pressure transducers. PIT results showed a clear link between the diameter and axial velocity amplitude of droplets tracked over multiple frames. By defining an entrainment factor, the ratio of droplet and acoustic velocity amplitudes, data was successfully normalised for acoustic velocity amplitude enabling the effect of forcing frequency to be observed. Data shows that entrainment factor reduced with increasing forcing frequency, with the entrainment factor of a 20 μ m reducing by approximately a third when forcing frequency is increased from 100 to 400 Hz. Additionally, for all forcing frequencies tested droplet entrainment factor was seen to be linearly proportional to the inverse of droplet surface area. Good agreement was found when comparing the experimental data to a model put forward by Hjelmfelt and Mockros

(1966), relating droplet Stokes number (defined as $\sqrt{\frac{v}{\omega D^2}}$) to droplet entrainment factor. In this study no significant link between phase delay of droplet oscillation and droplet diameter was seen. In all cases increasing forcing amplitude was seen to reduce the mean droplet velocity recorded at the measurement volume. Thus for these experiments any observed increases in droplet evaporation can be related to a combination of increased relative velocity between droplet and air flow, this being a function of droplet surface area, increasing heat and mass transfer through convection, and for a fixed droplet axial displacement, an increase in droplet residence time within the air flow.

Applying the measured droplet axial velocity amplitude response to a simple droplet evaporation model, it is apparent that at lower temperatures both convection effects and increased residence time have significant contributions to the enhancement in droplet mass reduction, particularly for larger droplets. At high air flow temperatures (486 K) convection effects have little influence on droplet mass reduction enhancement in comparison to the estimated increase in droplet residence time.

Using the same experimental setup a standard Interferometric Droplet Sizing (IDS) methodology was used to observe the effects of acoustic forcing on droplet mass flow and mean droplet diameters, at 100 Hz and acoustic velocity amplitudes varying from 0.00 to 0.48 m/s. Droplet mass flow through the measurement volume was seen to decrease with increasing temperature in unforced conditions, as would be expected with increased levels of evaporation. Increasing forcing amplitude at the lower air flow temperature conditions (338 and 369 K) was seen to increase mass flow. Further observations showed despite a significant reduction in the number of droplets less than 70 μ m in diameter more larger droplets were seen to transit the measurement volume at the higher forcing amplitudes, possibly due to the acoustic forcing in some manner effecting the atomisation process, though further work is needed to characterise this interaction. Observing the relative reduction in mass flow with respect to the lowest temperature condition, a reduction was seen with increasing forcing amplitude. Mean droplet diameters were seen to increase

174 Chapter 5. Effects of acoustic forcing on droplet evaporation

with both increasing temperature and increasing forcing amplitude. No variation in mean droplet diameter with radial displacement from the spray centreline was seen, though for all tests mean droplet diameter was seen to increase with increased axial displacement from the nozzle tip. The increase in mean droplet with the 20 mm axial displacement from the top of the measurement region to the bottom was seen to increase with increasing forcing amplitude in all test cases, suggesting an increase in evaporation.

Chapter 6

Characterisation of droplet flows produced during expiration

6.1 Chapter outline

During the course of this work, the global outbreak of COVID-19 refocused many research facilities to help improve the understanding of the spread of respiratory diseases. This chapter focusses on the work performed during the COVID-19 pandemic.

At the outbreak of the pandemic the information relevant to the spread of aerosolised viral droplets was relatively sparse. What was known indicated that the rate of droplet evaporation plays a critical role in the survivability of viral cell containing droplets and thus the likelihood of disease transmission (Mao et al., 2020). The rate of droplet evaporation can and has been modelled and experimentally observed Lieber et al. (2021). However, information relating to other key parameters such as the size, velocity and number of droplets emitted during expiration and vocalisation, all relevant to the rate of droplet spread and evaporation was sparse. One of the main reasons for the limited amount of information was the potential for variability between people and ways in which the aerosolised viral particles were formed (breathing, talking, singing, shouting etc.). To perform more detailed and experimentation relating to the travel and evaporation of human produced aerosols it was first imperative to have a more informed understanding of the 'plume' characteristics of droplets produced from the nose and mouth.

This chapter focusses on work carried out shortly after the outbreak of COVID-19 when our research group become involved in the CONFESS study (COvid aNd FacE maSkS). This study was designed as a cross-sectional study to assess the safety of group singing in religious worship during the COVID-19 pandemic, though also provided an opportunity to measure the number and velocity of droplets emitted by a variety of individuals using planar laser imaging.

6.2 Introduction to Covid Studies

During the outbreak of SARS CoV-2 (COVID-19) it became evident that airborne transmission is the dominant pathway for the disease spread (Stadnytskyi et al., 2021). Both Public Health England (PHE) and Centers for Disease Control and

Prevention (CDC) in the United States have recommended social distancing, wearing face coverings and avoiding large gatherings to reduce viral transmission risk. Early instances of large scale gatherings during the COVID-19 outbreak such as the Shincheonji Church of Jesus in South Korea and the Sri Petaling mass gathering in Malaysia, highlighted the magnitude by which such events could spread the disease. These two specific events accounting for over 60% and 35% of cases in their respective countries at their peaks (Che Mat et al., 2020; Kim et al., 2020). A common feature for these two specific events and that of the Skagit County choir cluster is the activity of group singing or chanting (Hamner, 2020).

During the COVID-19 pandemic various government run health organisation, including PHE, specifically restricted indoor communal singing. Though certain events, such as those mentioned previously, displayed the spread of COVID-19 at events where indoor communal singing had occurred, very little research has been performed to ascertain the significance of singing over other expiratory events such as talking, coughing and sneezing. All such expiratory events will generate a plume of muco-salivary particulates, originating from the oral cavity and pharynx to microscopic aerosols from the small airways of the lungs (Asadi et al., 2019; Gregson et al., 2021; Johnson et al., 2011).

The expiration of respirable aerosols (normally defined as droplets with diameters <5–10 μ m) are of particular importance to the spread of COVID-19 (Anderson et al., 2020). Whilst larger droplets (diameters <100 μ m will fall and settle onto nearby surfaces respirable aerosols can remain suspended for significant periods of time (often designated as airborne transmission). Droplets existing between these two ranges (those with diameters between 10 μ m and 100 μ m) are also considered to be of concern as when subject to evaporation, can become aerodynamically similar to respirable aerosols, (Anderson et al., 2020; Prather et al., 2020; Walker et al., 2021). Most expiratory droplets are less than 1 μ m in diameter, but speech and singing can produce additional droplets approximately 3.5-5 μ m in diameter (Gregson et al., 2021; Johnson et al., 2011; Morawska et al., 2009).

Several factors make singing higher risk for transmission of SARS CoV-2 and

other airborne viruses compared to normal speech. These include higher frequencies, continuous voicing, heavier breathing and more articulated consonants (Alsved et al., 2020). Mitigation factors have been studied to make singing safer. Echternach et al. (2020) investigated dispersion dynamics of aerosols in 10 professional singers and recommended up to 2.5 m social distance to persons in front and 1.5 m to the side to reduce aerosol droplet spread. Even with social distancing, poor ventilation could lead to a high risk of viral infection after as little as 8 minutes of contact (Yang et al., 2020).

The use of face masks can successfully block shedding of coronavirus and other seasonal viruses where the droplet particles are more than 5 μm in diameter (Leung et al., 2020). Thus, quantifying droplet generation and reducing transmission in the 1–5 μm range is likely to be of high importance. Loud singing with a face mask reduced the number of aerosol droplets to a level similar to normal talking, although this was not statistically significant (Alsved et al., 2020). Single use surgical face masks can capture coarse and fine respiratory aerosol droplets of sizes as small as 1–5 μm (Leung et al., 2020) and it is possible to make reusable face masks with similar efficacy, although the number of layers within a mask also can influence the number of droplets penetrating through the mask and subsequently breaking down into smaller sized droplets (Robinson et al., 2021; Sharma et al., 2021).

Currently the sizes, concentration and velocities of expired droplets are reasonably well researched, particularly for events such as coughing and sneezing, though an increasing number of groups a focusing on other forms of expiration activities. Much of the focus in studies predating the outbreak of COVID-19 focused on airflow velocities produced when coughing without a mask, (Chao et al., 2009; VanSciver et al., 2011). A common finding amongst these studies was a large variation in cough velocities between participants with VanSciver et al. (2011), reporting a maximum velocity variation between 1.5 and 28.8 m/s for a sample group of 29 volunteers.

Aerodynamic particle sizing (APS) techniques have been used by multiple re-

search groups to determine droplet numbers produced during a variety of verbal and non-verbal activities with and without masks (Alsved et al., 2020; Asadi et al., 2019), studies noting a significant decrease in median particle emission rates with the use of surgical masks, Alsved et al. (2020) reporting a 72% reduction for loud singing, and noting an 80% reduction across a variety of tasks. As with flow field velocities produced through expiration, these studies have found considerable individual variation in the numbers of droplets produced, noting one individual when cough produced a particle emission rate two orders of magnitude greater than the average from a sample of 10 participants.

Other studies, have reviewed the performance of masks in reducing flow field velocities produced from the mouth and nose created through emulation and live participants (Kähler and Hain, 2020; Verma et al., 2020; Viola et al., 2021). All have shown significant reduction in the distance of frontal through flow and air velocities with mask use. Directly relating the reduction flow field velocities to a reduction in emitted droplet velocities, accounting for the mask filtration effects, on in vivo participants was beyond the scope of these studies.

This study is focused on the measurement of both the spatial density and velocity of expired droplets formed during by 20 volunteer participants with and without the use of a type IIR face covering to provide judgement on frontal filtration effectiveness. To asses whether mask filtration is effected by the form of expiration various verbal and non-verbal tasks will be performed. The key questions this study seeks to answer are:

- To understand the differences in droplet transmission (droplet concentrations and velocities) across different vocal and non-vocal tasks.
- To examine inter-person variability.
- To explore the difference in the amount of droplets produced for singing compared to speaking and exhaling when wearing a face mask.
- To observe how II R face coverings effect emitted droplet concentrations and velocities.

• To explore the concept of 'Super Emitters' by observing whether any individual transmitted considerably more droplets for individual tasks.

To achieve these goals laser planar illuminated high-speed imaging was employed. From the captured images an inhouse blob detection programme was applied to determine the position and spatial concentration of illuminated droplets, as has similarly been performed by Alsved et al. (2020). High-speed imaging allowed for a sufficient temporal resolution to allow the observation of the time evolution of expired droplets. The droplet velocities for select tasks and participants were measured using Particle Tracking Velocimetry (PTV) and Particle Imaging Velocimetry (PIV).

6.3 Methodology

In this study laser Mie scattering was employed to characterise droplets expired by volunteer participants. Experiments took place in a laser safe facility in the UCL Mechanical Engineering laboratories. High capacity air extraction was enabled within the experiment room along with a comprehensive cleaning protocol to ensure participant safety. In total 20 individual volunteers were invited to attend experiments, the group of individuals chosen representing a wide range of demographics including age, sex and ethnicity. All volunteers were given brief instructions giving an outline of activities, though these instructions where provided such that they influence the volunteer performance as little as possible, ensuring a realistic outlook of individual behaviour is observed. As well as exhalation a three verbal tasks were chosen, these being the word Hello, Snake and the singing of a constant note. The two words were selected based on the recommendation of Dr Ruth Epstein, Consultant voice specialist at the London Ear, Nose and Throat clinic, as they included a combination of voiceless fricatives such as /h/ and /s/, consonants produced by airflow through a channel formed by the lips, tongue, teeth and/or palate, as well as the voiced consonants /p/ and /b/, produced with the vibration of the vocal cords. Finally, to make observations over longer durations, select participants was asked to sing the first verse of the song 'Happy Birthday'.

6.3.1 Laser and Camera setup

Planar laser imaging makes use of a high intensity laser and optics to produce a thin illumination sheet, approximating 2-dimensional plane. Solid particles and liquid droplets interacting with the laser sheet scatter light in accordance with Mie theory. Placing a camera with the lens axis perpendicular to the laser plane, allows scattered light from particles and droplets to be observed. In these experiments the laser sheet was positioned in front of the mouth, allowing for the capture of light scattered by expired droplets generated during the performance of aforementioned tasks.

A Coherent MX SLM (1 W 514 nm) continuous laser with TSI LASER-PULSETM light arm and sheet optic was selected for illumination, producing a sheet approximately 0.5 mm in thickness, with an output power of 1 W. To allow the laser sheet to bisect the face of the participant without being directed at the face and eyes, the laser arm outlet was placed beneath the face, at approximately knee height and directed vertically upwards, Figure. 6.1 (a). Phantom VEO 710 (1280 × 800 pixels) with NIKKOR 50 mm lenses were aligned with the laser and focused on the laser sheet. Two cameras were employed to reduce the attendance time for volunteers, removing the need to transfer images from the cameras internal RAM during attendance. Due to spatial constraints the two cameras were both mounted on the left side of the face, Figure. 6.1 (b). As such both cameras were fitted with Scheimpflug adapters to facilitate off axis imaging. The imaging windows measured approximately 170 mm × 110 mm when dewarped.

6.3.2 Experimental Rig

Participants were placed in a laser-safe enclosure to fully protect them from laser irradiation. In order to image a plane vertically bisecting the face of participants, a region 300 mm in height was exposed through an adjustable curtain, Figure. 6.2. The curtain positioning was further optimised to minimise the region of exposure. Participants wore laser safety goggles, preventing light inadvertently entering the eye. The laser sheet was aligned such that it could not come into contact with the participant, resulting in small region, typically 25-30 mm in width, of un-illuminated space between the participant's mouth and laser sheet, seen in Figure. 6.1 (b). To ac-

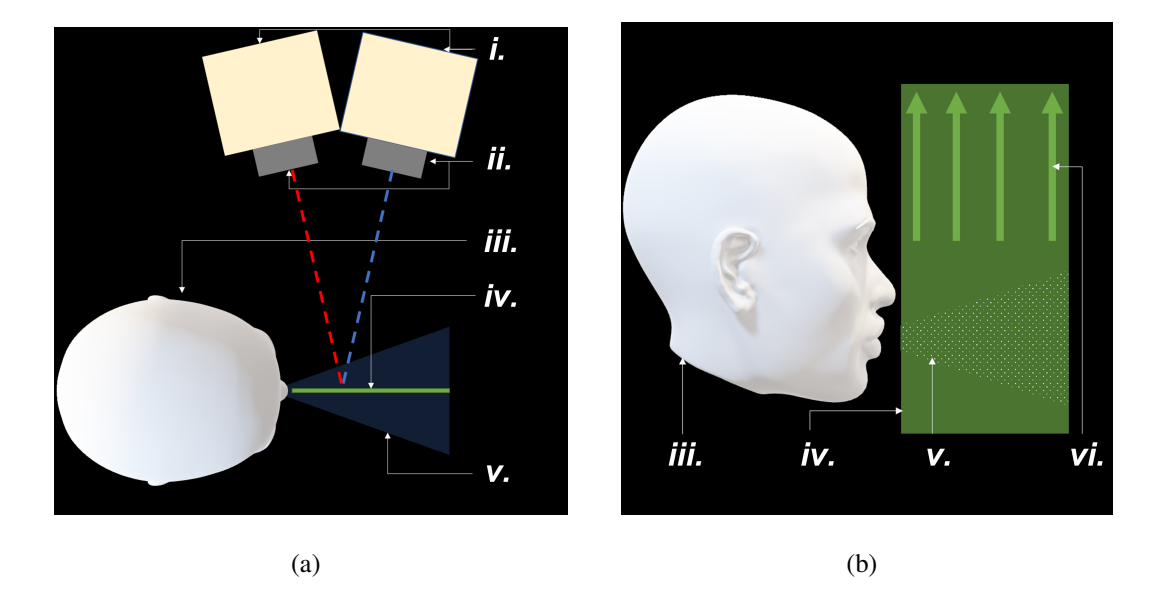


Figure 6.1: a) Top view showing laser sheet and camera alignment, b) Side view of laser sheet alignment, with *i*.), high speed camera, *ii*. 50 mm lens with Scheimpflug adapter, *iii*. participant, *iv*. laser sheet, *v*. spray produced by participant and *vi*. laser direction.

commodate for various participants of different statures the laser and cameras were set upon a support frame allowing for the vertical and horizontal traverse of the camera/laser setup and curtain opening, shown in Figure. 6.2. The camera, camera lenses, and laser remained in the same positions relative to the support frame for the entirety of testing.

Participants were aligned with the laser plane as shown in Figure. 6.1 (a) and (b), and then asked to complete tasks. Head position was maintained through the use frontal, lateral and rear beams, forming a box about the head. In the interests of participant comfort the head 'restraint' allowed for a small range of motion. A sound level meter was placed approximately 300 mm in front of the participant's mouth recording the maximum loudness of the verbal tasks. Cameras were triggered after a short countdown cueing the participant to begin the task. A sufficient number of frames were collected pre and post trigger to ensure the entire task was captured. In all tests the participants mouth was present within the imaging window as a point of reference so that droplet positions relative to greatest extent of the top lip from the face could be determined.

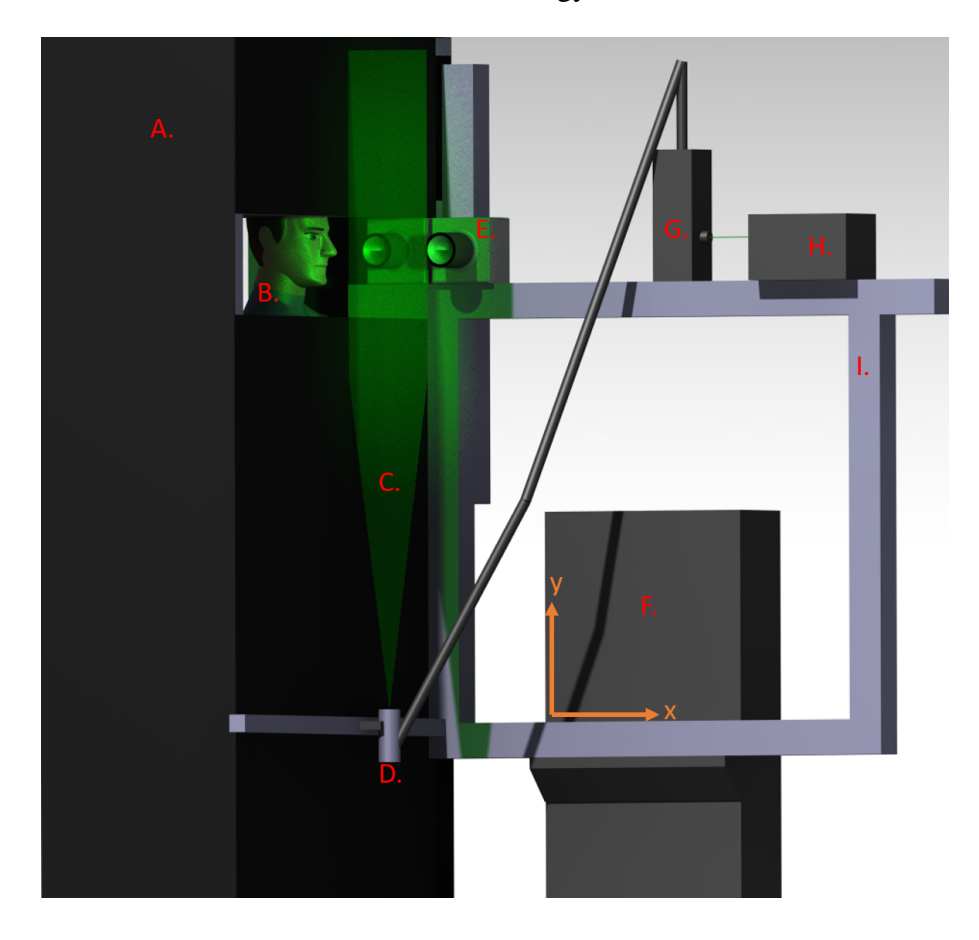


Figure 6.2: Laser safety booth and laser/camera traverse.

6.3.3 Validation of droplet detection

In two phase flow experimentation higher powered pulsed lasers are typical used to provide illumination, enabling shorter exposure times, beneficial in applications such as PIV. Available high frequency pulsed lasers in the visible frequency range had minimum outputs of $\approx 10 \text{W}$ at the expected experimental frequency ranges. Though the design of the laser safety structure prevented contact between participants and the laser sheet, in the unlikely event that contact was made the high power density output was deemed unsafe. As such a lower power continuous laser was used. A preliminary test to ensure the laser was able to illuminate the 0.3-4 um droplets typically produced in expiration was performed (Alsved et al., 2020; Asadi et al., 2019). Droplets produced by an Omron NE-C28P compressor nebuliser (stated to produce a distribution of droplets with a Mass Median Aerodynamic Diameter of approximately 3 μ m) were imaged using the outlined camera setup.

With the cameras set to an exposure time of 0.332 ms, at a laser output power of 1 W, large numbers of individual droplets produced by the nebuliser were clearly visible on images, thus providing confidence that droplets produced in expiration would be observed.

6.4 Image Analysis

For all tests the participants mouth was in frame, taking the average image for eack task performed, the approximate position of the mouth and nose could be determined through observation. The top lip position was then used as a datum (X_{mouth}) in all subsequent processing. In tasks involving the use of a mask, the greatest extent of the mask was assumed to be the tip of the nose. Using the difference between lip and nose positions $(X_{nose}-X_{mouth})$ from non-mask wearing tasks the mouth datum position could be estimated for each participant.

To account for differing facial structures, specifically the distance between the tip of the nose and the top lip $(X_{nose}-X_{mouth})$, the processing region was reduced to focus on a region beginning 35 mm from the mouth datum. This ensured the processing region began at the same relative position from the mouth datum in all tasks for all participants. In preliminary testing it was observed that the droplet density dropped significantly at approximately 60 mm from the mouth. At such low droplet concentrations, the signal to noise ratio in this region was significantly lower. As such the imaging window was terminated 60 mm from the mouth datum. These two factors resulted in the processing region for droplet velocity and number counting being defined between 35 mm and 60 mm from the mouth and having a height of approximately 100 mm.

To determine the number and position of illuminated droplets a bespoke imaging processing algorithm, based on blob detection, was developed in Matlab. An intensity threshold is applied to captured images forming a binary image. From this, the size, in pixels, positions and intensities of connected pixels (blobs) is determined, with blobs in this case representing droplets. The intensity threshold was determined by observing signal noise intensity in images with no droplets present.

To reduce the occurrence of camera sensor artifacts or non-droplet reflections from being erroneously recorded as droplets, the mean image was subtracted from each image set, removing any static objects. A minimum bob size of 3 pixels was used to remove additional signal noise.

Additionally, an open source particle tracking software, TracTrac (Heyman, 2019) for Matlab, was the primary method for determination of droplet velocities. PTV methods are typically used in low density particle flows with images captured at high frame rates. In general, PTV methods require a measurement known as the particle spacing displacement ratio, p, to be greater than 1 (Qian et al., 1991).

$$p = \sqrt{\frac{s}{N}} / v dt \tag{6.1}$$

Where S is the image surface, N is the number of droplets, v is mean droplet velocity magnitude and dt is the time between image capture. In these situations, particle motion between frames is sufficiently smaller than the average spacing between particles. In this study a frame rate of 3000 frames per second was selected at which the condition of p>1 was being met. TracTrac was set to use a 2 x 2-pixel median box filter for noise reduction. PTV blob detection method used within TracTrac was set to Difference of Gaussian with a blob scale of 1.2.

For the singing 'Happy Birthday' task the frame rate had to be reduced by a third to ensure a larger section of the song was captured with the exposure time maintained. Image sets recorded for this task were not used in velocity analysis.

In addition to PTV, a PIV system was deployed as a validation to the PTV software. PIV is a technique commonly used to determine 2-dimensional velocity vectors in multiphase flows. The basic principle is that of measuring the distance travelled by particles, in this case droplets, between two captured images. Knowing the time gap between the captured images, the particle velocity can be determined. In this study, two Phantom VEO 710 recorded images at 3,000 frames per second (0.33 ms between frames) and the PIV processor used a recursive Nyquist grid with an initial spot size of 32 x 32 pixels reducing to 16 x 16 pixels for the second pass. A fast Fourier transform (FFT) correlated spot pairs and a Gaussian peak to noise

6.5 Data Analysis

The key focus of this study is on the performance of face coverings over a variety of tasks. The main measure of performance of a face covering is the level of reduction in the number of droplets transiting through the mask in comparison to those emitted from the mouth when not using a mask. To provide this information a method for representing data determined through blob analysis as a meaningful representation of the amount of droplets produced was required. The number of droplets counted within a single image gives a measure of droplet density within the imaging region at that point in time. Capturing images at higher frequencies allows a detailed view of the development of droplet densities over time. To represent data that allows for comparison in the relative differences between participants and tasks two methods were chosen. The maximum instantaneous droplet density, the maximum thirty frame moving mean number of droplets divided by the measurement volume. The time averaged droplet density, that is the sum of droplet densities over the length of the task, divided by the time over which it occurred. To make this second measure meaningful the differences in droplet production time responses needed to be considered. Figure 10 shows typical droplet density time evolution for the four shorter from tasks. When saying 'Hello' droplet densities typically show a single, sharp, dominant peak response linked to the opening 'H' sound. Whereas singing a note for most participants showed a double peak with the second peak plateauing for a period of time. As such to define the time averaged droplet density only the active portions of each task were analysed. A threshold droplet density was defined through analysis of image background noise, any frames containing a droplet density higher than the threshold value were included in the time averaged measurement.

To determine droplet velocities both PTV and PIV techniques were deployed as previously outlined. Before applying PTV or PIV techniques to image sets, insignificant sections of image sets were removed, these being images where no droplets

are present, typically the periods before and after an event has taken place. The significant event for each task performed by a participant was defined as the longest sequence of images containing significant numbers of droplets determined through blob analysis. The image sets for each task per participant were then separated and analysed using both PTV and PIV. Image sets from tasks that did not have a continuous sequence of images with significant numbers of droplets longer than 200 images were not further analysed for droplet velocities.

6.6 Error and Uncertainty

Asadi et al. (2019) reported cases of mask material shedding resulting in the potential inflation of droplet number measurements with mask use. Particles were detected by and APS system during jaw movement and manual rubbing. Particle diameters produced during manual rubbing spiked at 6 μ m though presence was detected down to the 0.3 to 2 μ m range. In preliminary testing volunteers wearing masks performed various mouth and head movements without exhaling. No significant ejections of particles were observed from masks, particle densities within the imaging window did not exceed that of standard background values. The specific reasoning for this difference is unknown. From preliminary testing with both Nebuliser, there is very high confidence that the presence of a significant number of particles in the range of 6 μ m in diameter would have been clearly visible on captured images. One potentially relevant difference between the two studies methodology is the APS units use of a 5 $\frac{l}{min}$ suction, directing droplets and particles towards the measurement unit, this may have had a role in the increased measurement of material shedding.

Despite the controls in place for ensuring minimal head movement, head motion was still present. As such there is an uncertainty attached with the relative droplet positions from the mouth, typical head motions resulted in mouth movements of approximately 10 mm from the datum position, over the complete duration of the task. In addition, the direction of droplet flow from the mouth showed considerable variation between participants, though typically droplets exited the mouth

at a downward angle as also noted by Viola et al. (2021), Figure 6.3. In addition, in complex mouth movements such as saying 'Snake', the flow direction of droplets varied as the word was formed. Determining the variation in the central spray axis positioning in order to provide consistent axial and radial velocity components of droplets was beyond the scope of this study, with the droplet velocity magnitudes used to represent droplet velocities.

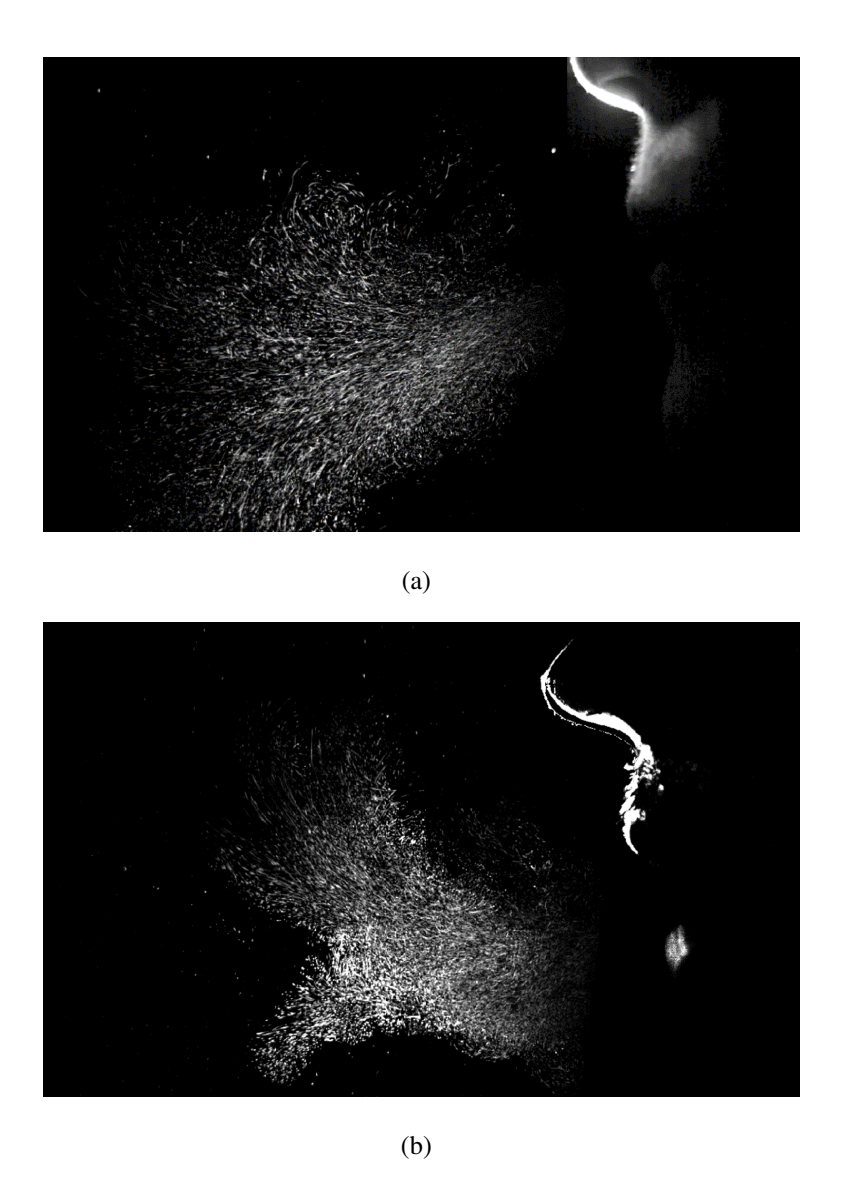


Figure 6.3: Composite image for all frames captured during: a) exhalation, b) singing a note from two different participants.

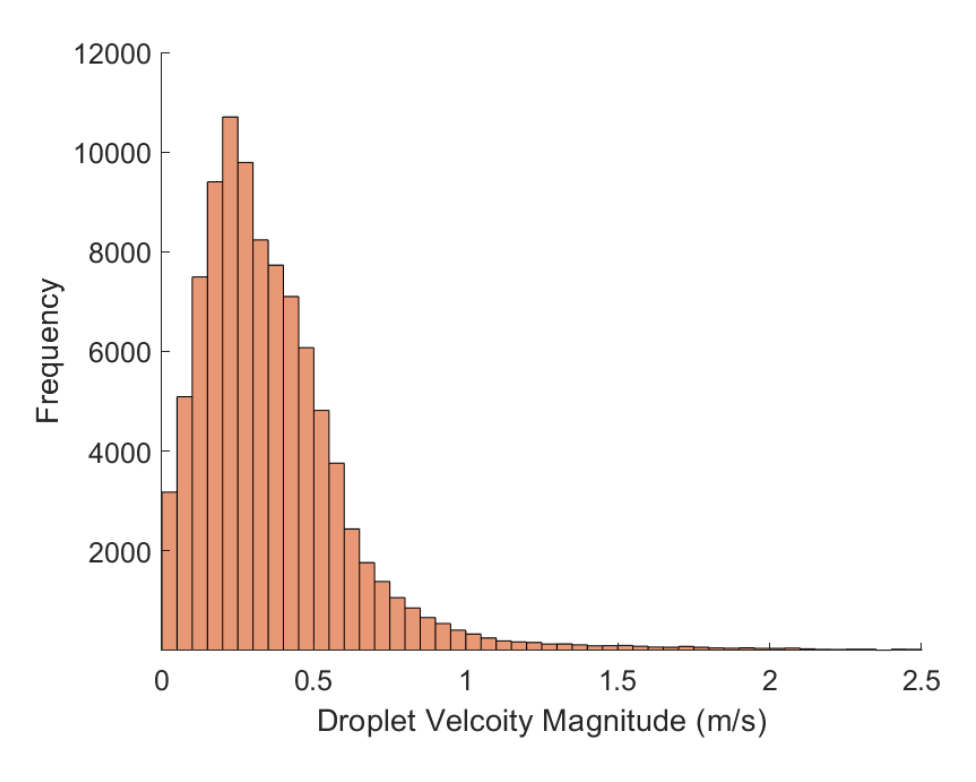


Figure 6.4: Histogram of individual droplet velocities determined through PTV for a participant singing a note.

6.7 Results and discussion

Figure 6.4 shows an example droplet velocity magnitude distribution for a verbal event. The velocity distribution does not follow a normal distribution, being better modelled as a lognormal or Rayleigh distribution, though goodness of fit for either distributions varied significantly across participants and tasks, as such distribution fitting was not further investigated.

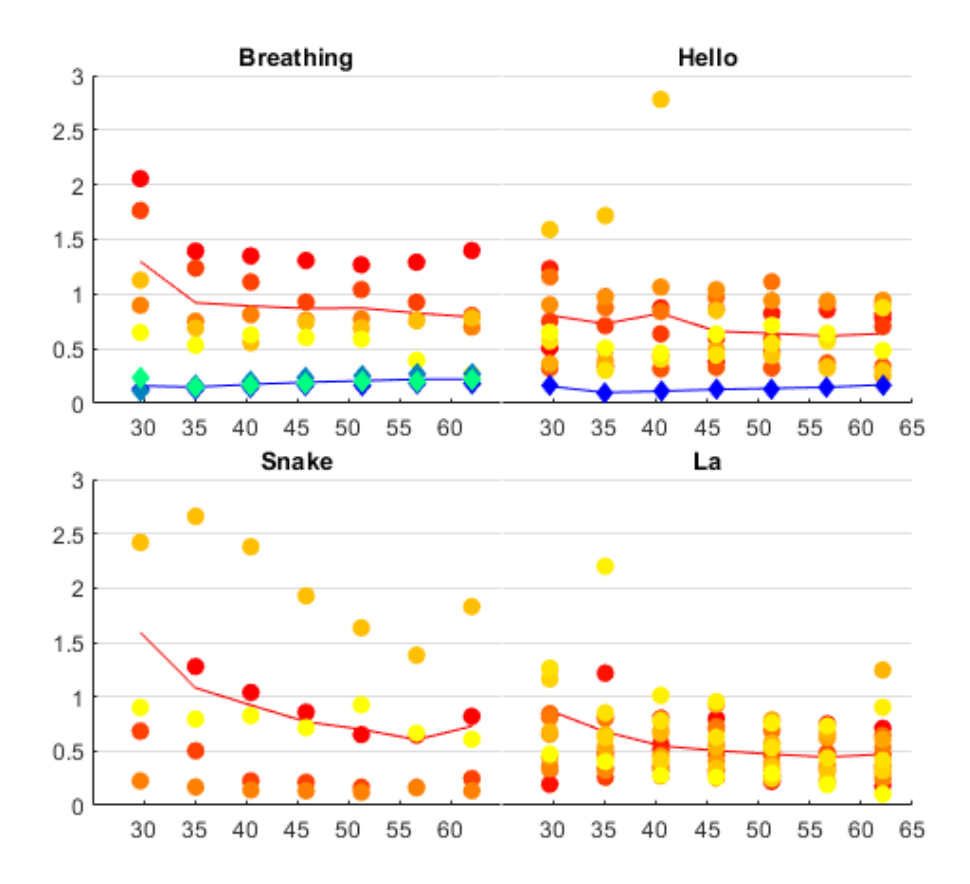


Figure 6.5: Variation in mean droplet velocity magnitude with distance from the mouth. Individual participant data displayed by markers, with overall means shown by lines. Unmasked tasks shown as yellow/red, masked (where applicable) shown by blue/green.

Figure 6.5 shows the mean droplet velocity magnitude with distance from the mouth for each participant and the general average for all participants for each task. Average droplet velocity magnitudes for all participants show similar values across tasks, typically ranging between 0.2 and 1.5 m/s. Vocal airflow velocities measured by Giovanni et al. (2021) using vaporised glycol to seed airflow from the mouth found similar air flow velocities with average velocities ranging from 0.28 to 1.8 m/s for two participants across a variety of vocal tasks. Chao et al. (2009) found an average air velocity of 3.1m/s between 0 and 45 mm from the mouth for two participants counting from 1 to 100 using a PIV measurement system. Droplet velocities reduce with displacement from the mouth in all cases, reducing by 50 to 25% depending on task and participant over the 30 mm region.

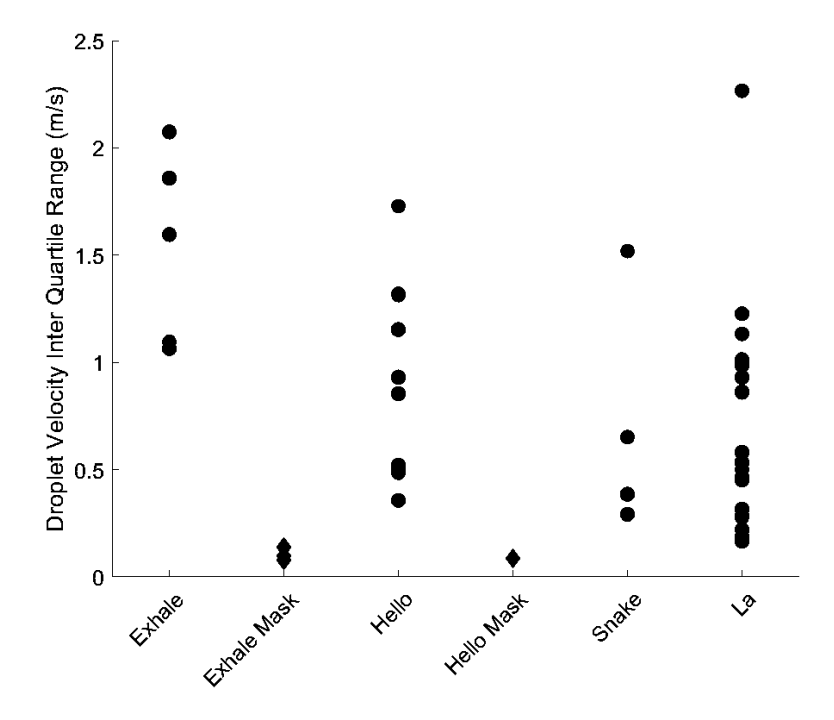


Figure 6.6: Droplet velocity magnitude inter-quartile range for tasks, markers showing individual participant ranges.

Droplet velocity interquartile ranges vary similarly across all tasks with a majority of participants producing ranges of 0.2 to 1.5 m/s, Figure 6.6.

Figure 6.7 shows PIV and PTV results for two tasks each with and without masks. The results from both techniques are in good agreement. While instances of mask frontal leakage were noted in a small number of participants for all tasks, in the tasks Exhaling and saying Hello four cases of prolonged droplet leakage occurred and were analysed. Figure 6.5 and Figure 6.6 both show the significance of the performance of masks in reducing droplet velocities in the events of droplet leakage through the mask. The mean droplet velocities for both tasks are reduced by 75% and the variation in droplet velocity is reduced significantly, leaked droplets having a velocity IQR of no greater than 0.2 m/s.

The effects of the droplet velocity reduction with mask use can be seen in the position of droplets from blob analysis, Figure 6.8. Droplets are not travelling as far from the mouth within the time of recording as compared with the same tasks performed without a mask. Giovanni et al. (2021) found the airflow velocities when exhaling to be higher than when vocalising. Whilst no significant increase in general

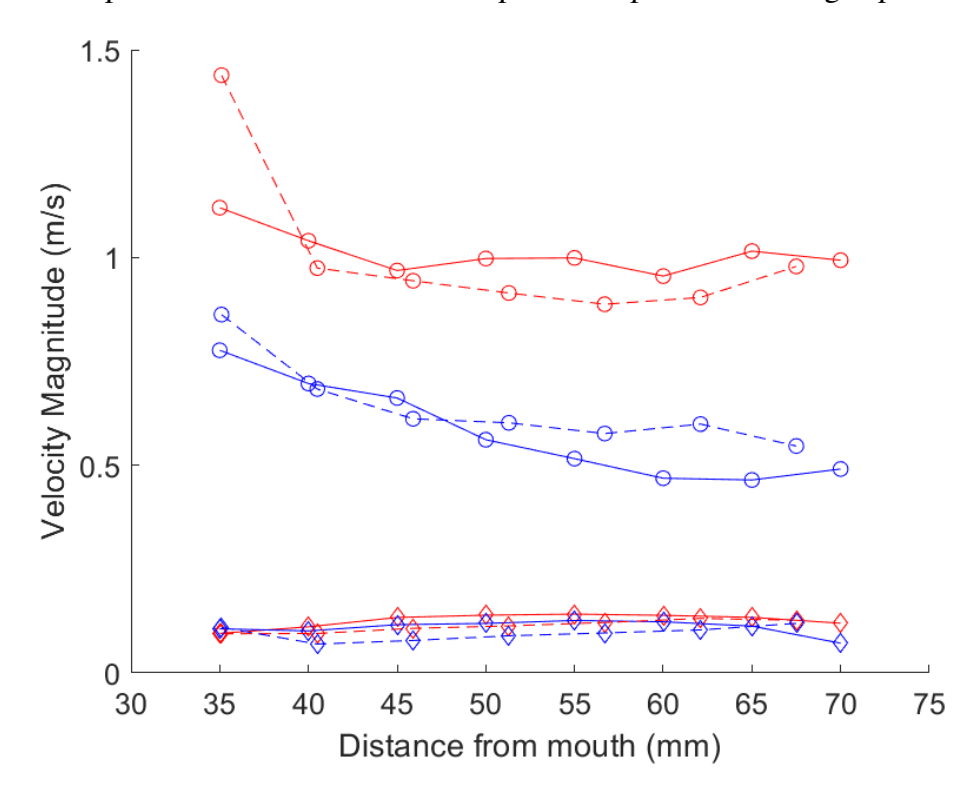


Figure 6.7: Comparison of PIV and PTV mean velocity magnitudes with variation in distance from the mouth, for the same participant exhaling (Red) and saying 'Hello' (Blue) with and without a mask.

average droplet magnitude, it can be seen in figure 6.5 that exhaling was the only tasks where all participants produced droplets with average velocity magnitudes higher than 0.5m/s. The inter-quartile range for all participants when exhaling is also consistently high, figure 6.6, in comparison to other tasks, suggesting a larger proportion of higher velocity droplets. The higher droplet velocity when exhaling versus vocalising could explain the increased occurrence of frontal mask leakage observed in the exhaling task.

6.7.1 Time evolution

Figure 6.9 shows the active duration of each task for each participant. In all cases the total recording time was 2140 ms. For most participants the length of time where droplets are present is significantly less than the amount of time taken to perform the task, with the two spoken words, 'Hello' and 'Snake' taking approximately 500 ms to say. For both spoken words droplet densities rapidly increased with the opening

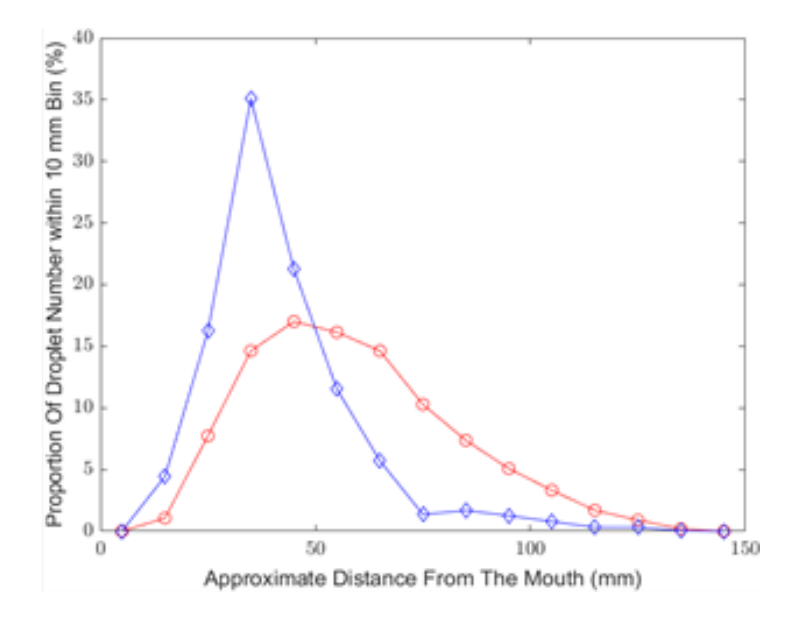


Figure 6.8: Variation in proportion of droplet number with distance from mouth, for unmasked and masked exhalation.

sound of either word, 'H' and 'S', as seen in Figure 6.10, with subsequent mouth movements and sounds generating fewer droplets, though in some cases a lesser secondary spike was observed, associated with the 'LL' and 'K' sounds in 'Hello' and 'Snake' respectively.

Though both exhaling and singing a note tasks where longer in duration than the recording time, there is a clear difference in the amount of time where droplets were present. Exhaling shows similar active droplet presence time to spoken words, despite the tasks longer duration. Again, looking at the droplet density time evolution a similar initial spike and then reduction over a relatively short period of time, suggesting most droplets are generated in the initial moments of the activity. Singing a note shows longer active droplet presence for most participants, with the droplet density time evolution typically showing two peaks with the second having a plateau. The increase in droplet presence time cannot be explained completely by a reduction in droplet velocity for this task, Figure 6.5, with droplet velocity magnitudes similar to other tasks.

Figure 6.11 exemplifies the effect of mask wearing on the time evolution of droplet densities in cases of significant mask leakage. The response peak is ex-



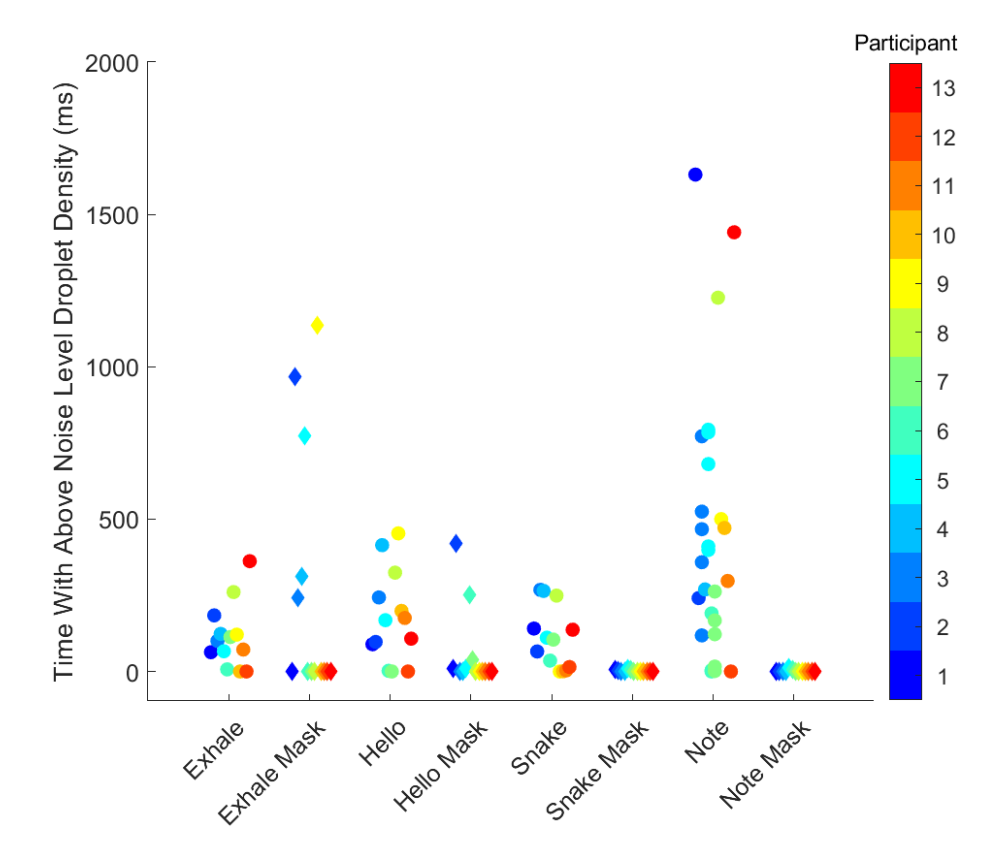


Figure 6.9: Time with above noise level droplet densities for each task and participant

tended and flattened with mask use. For all cases of significant droplet leakage the duration of droplet presence is extended significantly, in the case shown in Figure 6.11, being more than doubled from approximately 150 ms to over 400 ms. In all cases the peak droplet density is considerably reduced, typically by 40-50%. In addition to peak droplet density, the rate of increase in droplet density is also significantly higher in the case of no mask use. Data for no mask exhalation displayed in Figure 11 shows peak droplet density is achieved 50 ms after the initial droplet emission. In contrast peak droplet density occurs 150 ms from initial emission. This is despite the higher potential accumulation of droplets within the measurement volume for masked tasks due to droplet velocities approximately 10 times lower, Figure 6.5. Thus, it can be determined that mask use is both reducing the droplet velocity and total number of droplets transiting the measurement volume.



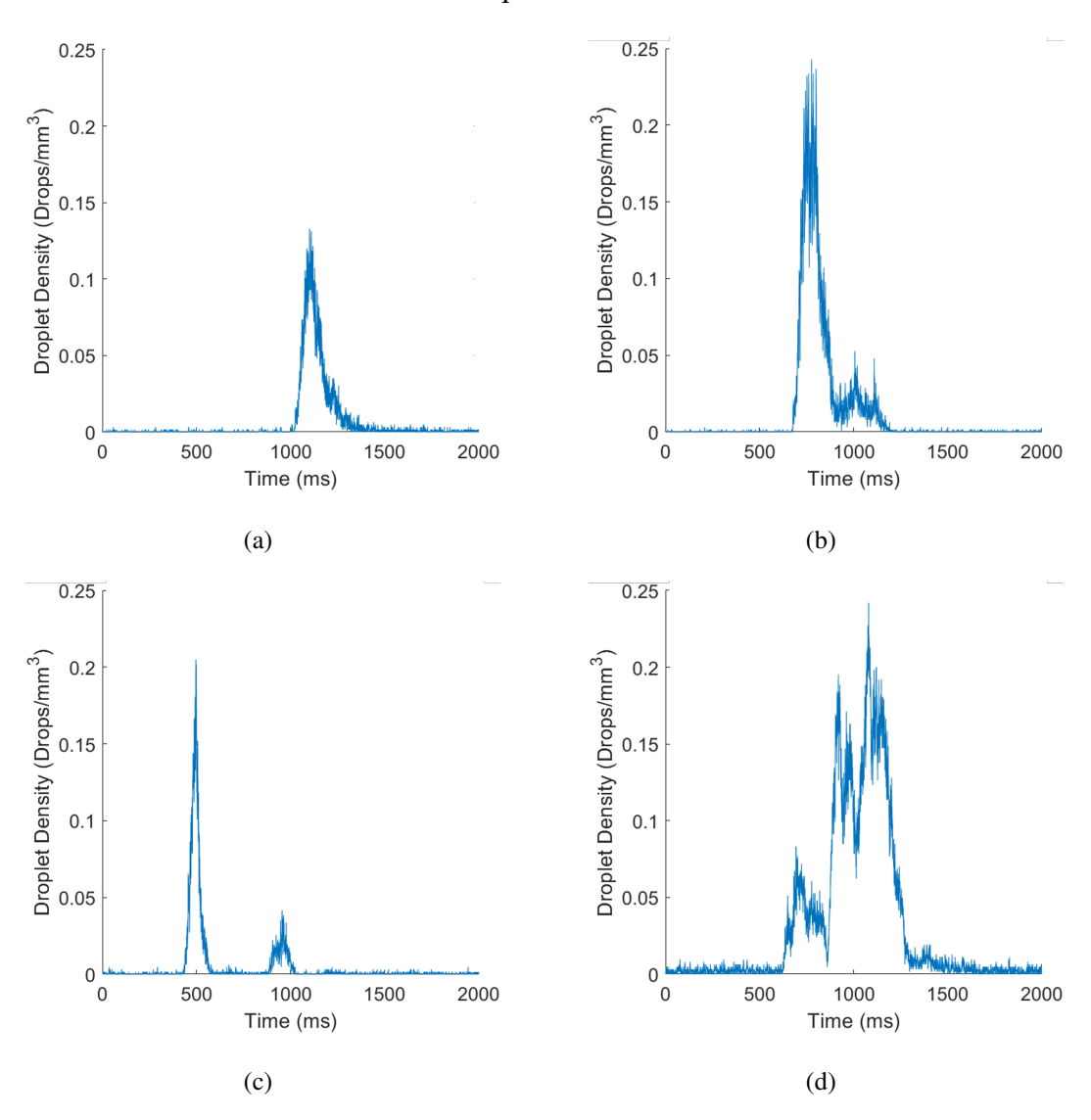


Figure 6.10: Example droplet density time evolution for: a) Exhale, b) 'Hello', c) 'Snake' and d) singing a note.

6.8 Droplet number

Figure 6.12 a) and b) show the two measures of droplet density for each task and participant. There is a significant variation in the droplet densities produced between participants, in all non-mask events time averaged droplet densities within the measurement region typically vary between 0 and ≈0.2 droplets per mm3. Findings from Asadi et al. (2019) have shown significant individual variation in the number of droplets being produced. The tasks 'Hello' and singing a note show the highest median time averaged and instantaneous maximum droplet densities respec-

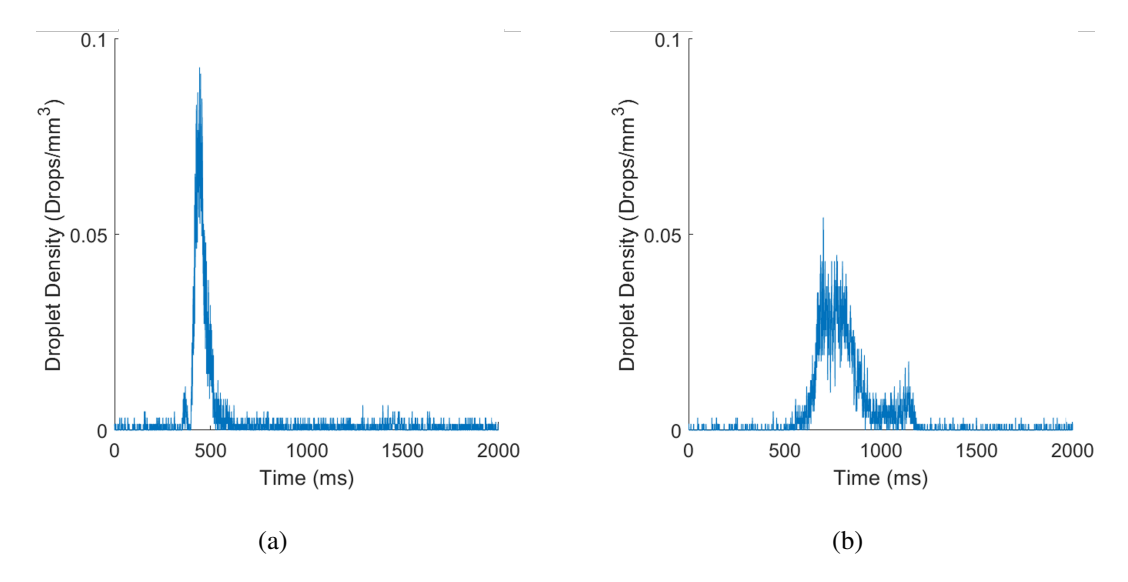


Figure 6.11: Droplet density time evolution for a single participant performing: a) Exhale and b) Exhale with mask.

tively. Asadi et al. (2019) reported an order of magnitude increase in the number of droplets measured on vocalised tasks, this study finds the increase in droplet concentrations with vocalisation to be lesser for the 'Hello' and singing a note tasks (\approx 80% increase), and in the case of saying 'Snake' both measures of droplet densities are lower than that of exhaling. It is evident that singing a note had the largest number of participants producing higher densities of droplets followed by saying hello and exhaling with the task of saying snake having the least number of high droplet density events. In all cases the number of droplets produced when wearing masks is significantly reduced, with few cases of significant mask frontal leakage.

Figure 6.13 (a) shows the percentage reduction in time averaged droplet density with mask use for each task. A majority of participants showed a near 100% reduction in droplets with mask use, even in the longer form task of singing the first two verses of 'Happy Birthday', similar results were reported by Alsved et al. (2020) for with mask use in loud singing. In cases of mask leakage, the percentage reduction is lessened though still significant with all participants showing at least a 40% reduction. The maximum instantaneous droplet density reduction, Figure 6.13 (b), show most participants having a 90% reduction for all tasks. The difference in values between the time averaged and instantaneous droplet densities could

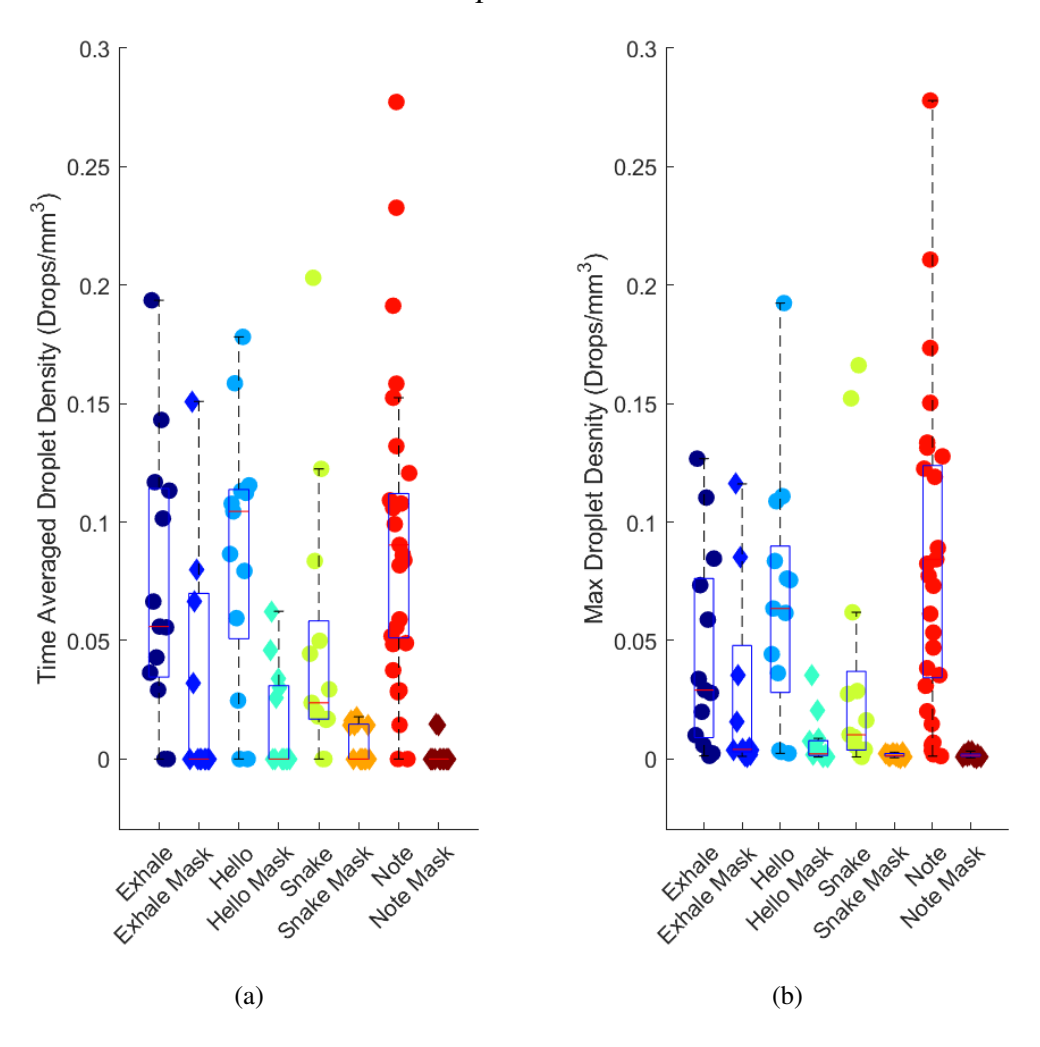


Figure 6.12: a) Time averaged droplet density and b) Instantaneous maximum droplet density for all tasks and participant. Unfilled markers highlighting data points where fewer than 200 frames contained above noise level droplet densities.

suggest that prolonged leakage through masks is relatively uncommon though momentary instances of frontal leakage, containing relatively few droplets may occur more often.

Figure 6.14 shows the time averaged droplet density versus the mean velocity magnitude for a selection of tasks and participants. Though not directly shown, by analysing Figure 6.14 comparisons between participants production of droplets can be inferred. Should all participants have produced the same or very similar number of droplets per unit volume of exhaled breath, data in Figure 6.14 would likely have shown a strong link between mean droplet velocity magnitude and time

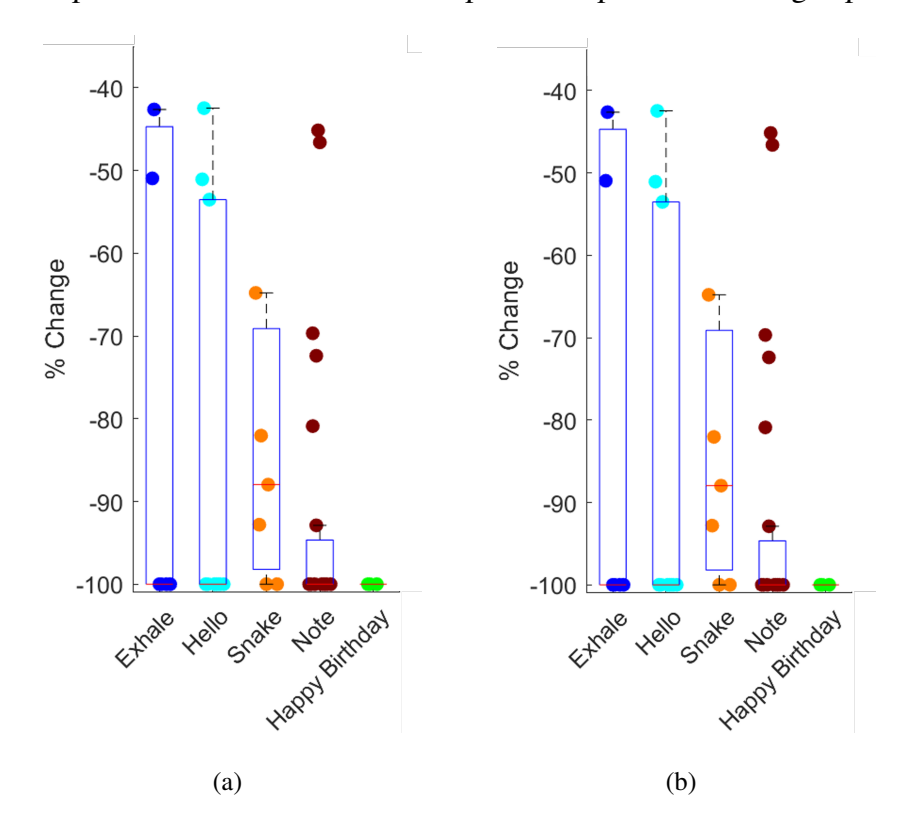


Figure 6.13: Percentage reduction in (a) time averaged droplet density and (b) instantaneous maximum droplet density for all tasks with mask use.

averaged droplet density. As at higher velocities the rate of dispersion of droplets is increased thus densities reduced. However, there is no significant link between these two parameters, suggesting the production of droplets varies between participants.

6.9 Droplet evaporation

To assess the degree of droplet diameter reduction due to evaporation a series of experiments using the PIT measurement technique in the same facilities shown in section 4.3 were performed. In these tests, saline (NaCl 9 g/l in distilled water, shown to be a good analogue for saliva (Basu et al., 2020; Vejerano and Marr, 2018; Zhang, 2011)) droplets were produced by the ultrasonic atomiser, with a coaxial flow of air at an outlet temperature of 36° C, replicating approximate temperature of exhaled air. The flow rate of air was set such that the mean droplet velocity at 100 mm from the nozzle outlet registered at approximately 1 m/s, matching the

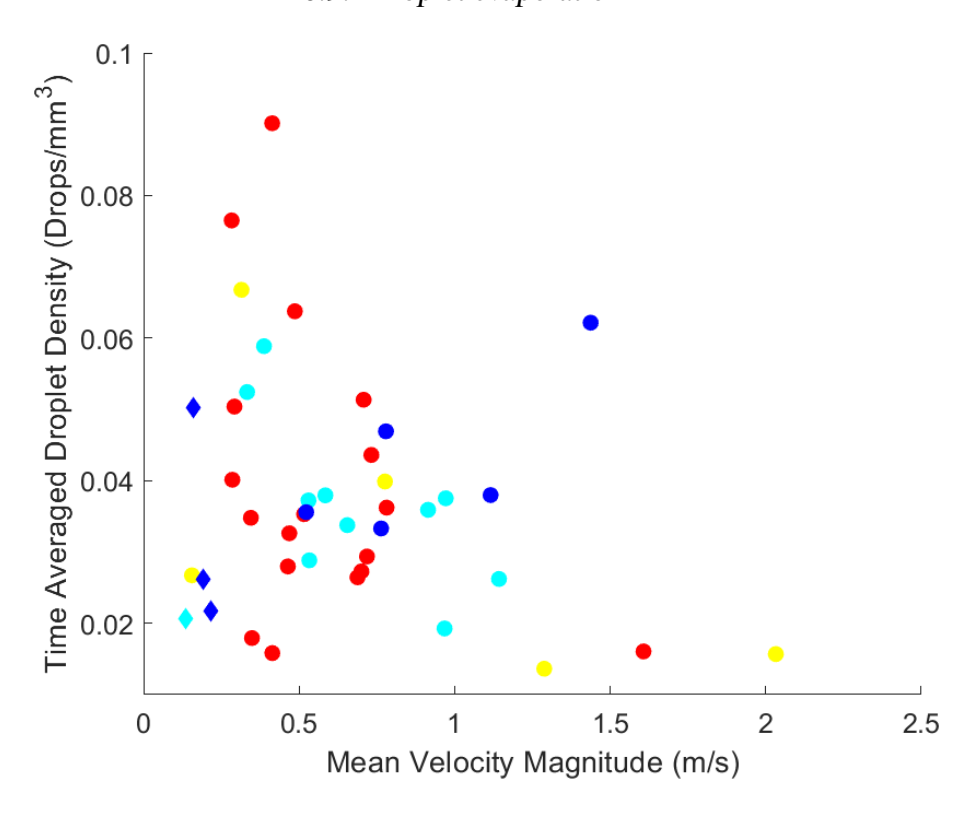


Figure 6.14: Mean velocity magnitude for entire processing window against time averaged droplet density.

mean droplet velocity of droplets entrained in an exhaled breath, figure 6.5. As the PIT technique in use is not capable of making reliable measurement of droplet below $10~\mu m$ in diameter the focus of these experiments was only on larger droplets, with the ultrasonic atomiser producing a mean droplet diameter of approximately $45~\mu m$ at 100~mm from the nozzle tip. Research regarding the size distribution of droplets produced by humans has shown a large proportion of droplets produced are below $5~\mu m$ in diameter, though a number of papers have shown that droplets of approximately $50~\mu m$ can be present in high concentrations Chao et al. (2009); Xie et al. (2009), thus the measurement of droplet evaporation within this size range in realistic flow conditions has meaningful value. The volumetric concentration of droplets at 100~mm from the nozzle tip was observed to be $0.15\pm0.05~drops/mm^3$, this being representative of peak droplet concentrations recorded when exhaling, figure 6.10.

Using a software controlled traverse the measurement volume, initially located

100 mm axially downstream of the nozzle tip along the spry centreline, was moved vertically downwards to 500 mm from the nozzle tip, thus the two measurement points were 400 mm apart. The velocity of droplets entrained within the coaxial annular air jet are seen to reduce between the two measurement locations, this being expected given the jet expansion. Mean axial droplet velocities are seen to reduce from 0.82 m/s to 0.23 m/s, additionally the standard deviation is seen to reduce from 0.58 m/s to 0.14 m/s suggesting the flow field is becoming more uniform.

Comparing the mean droplet diameter and droplet size distribution at these two points the degree of evaporation could be assessed. Figure 6.15 (a) and (b) shows the droplet diameter size distributions of measured saline droplets at the two measurement positions, whilst the total number of droplets measured at the lower positions is significantly reduced, the distributions at both measurement positions are very similar as seen in the normalised histogram, figure 6.15 (c), with the mean droplet diameter recorded at upper and lower positions being 45.4 μ m and 44.8 μ m respectively. Thus, it can be determined that there is no significant evaporation of droplets in the diameter range 10-100 μ m over the 400 mm of travel, in room conditions.

The cause of the reduced presence of droplets within the lower measurement region is likely due to the expansion of the spray, resulting in a larger proportion of droplets being present outside of the measurement volume, this being visually confirmed. Thus, in these tests no significant droplet diameter reduction due to evaporation was seen across the range of droplet sizes (15-80 μ m) during the 400 mm transit at comparable velocities, volumetric droplet concentrations and ambient temperatures as those recorded to be produced during actual exhalation.

6.10 Conclusion

This study made use of planar laser illuminated high speed imaging to determine droplet densities and velocities for 20 volunteer participants gently exhaling, saying 'Hello' and 'Snake', singing a note and singing the first two verses of 'Happy Birthday' with and without an IIR surgical mask. Both time averaged and maximum

instantaneous droplet densities were determined using an inhouse blob detection algorithm. PIV and PTV systems were implemented to measure expired droplet velocity magnitudes across a 25 mm region beginning at 30 mm from the mouth.

Observing the droplet density time evolution for the performed tasks has shown that droplet generation and dispersion does not necessarily occur for the entire duration of verbal or non-verbal expiration. In the case of exhalation and spoken words a majority of droplets are generated during the first instances, resulting in a pulse of droplets. Along with this it is evident that certain mouth movements and or sounds impact the amount of droplets being produced, producing subsequent pulses in droplet production though typically at of lower magnitudes. In comparison when singing a long note, droplet presence within the measurement volume was prolonged, suggesting a period continuous droplet production.

Time averaged droplet concentrations varied between 0-0.09 drops/mm³ with peak concentrations varying between 0-0.28 drops/mm³. The tasks singing a note and saying 'Hello' resulted in a higher proportion of participants producing larger droplet concentrations in comparison to exhaling and saying 'Snake' indicating the form of expiration does impact the production of droplets. Across all tasks performed individual variation was considerable with some participants producing little to no observed droplets while a small number of participants were seen to produce double or triple the group median.

All tasks showed similar mean velocity magnitude variations between participants, approximately 0.2-1.5 m/s. In a small number of cases, primarily when performing the exhale and 'Hello' tasks, significant frontal mask leakage was noted. In these cases, droplet velocities were significantly reduced in comparison to the same tasks performed without a mask. Leaked droplets had mean velocity magnitudes of less than 0.1 m/s across the analysis window, approximately a factor of ten reduction in comparison to the inter-participant median for the same tasks performed with a mask. Significant leakage occurred in only a small number of cases, with the use of a face mask for a majority of participants reduced maximum droplet concentrations by over 90% and time averaged droplet concentrations by over 98%. Even

202 Chapter 6. Characterisation of droplet flows produced during expiration in events of mask leakage, masks still proved to provide significant droplet density reductions, with the lowest observed droplet density reduction being greater than 40%.

An additional experiment using a spray of a saliva analogue, produced by an ultrasonic atomiser, observed that at similar droplet velocities, volumetric concentrations and ambient temperatures to those measured in actual exhalation, no significant evaporation of droplets of diameters ranging from approximately 10-100 μ m occurs during a 400 mm transit.

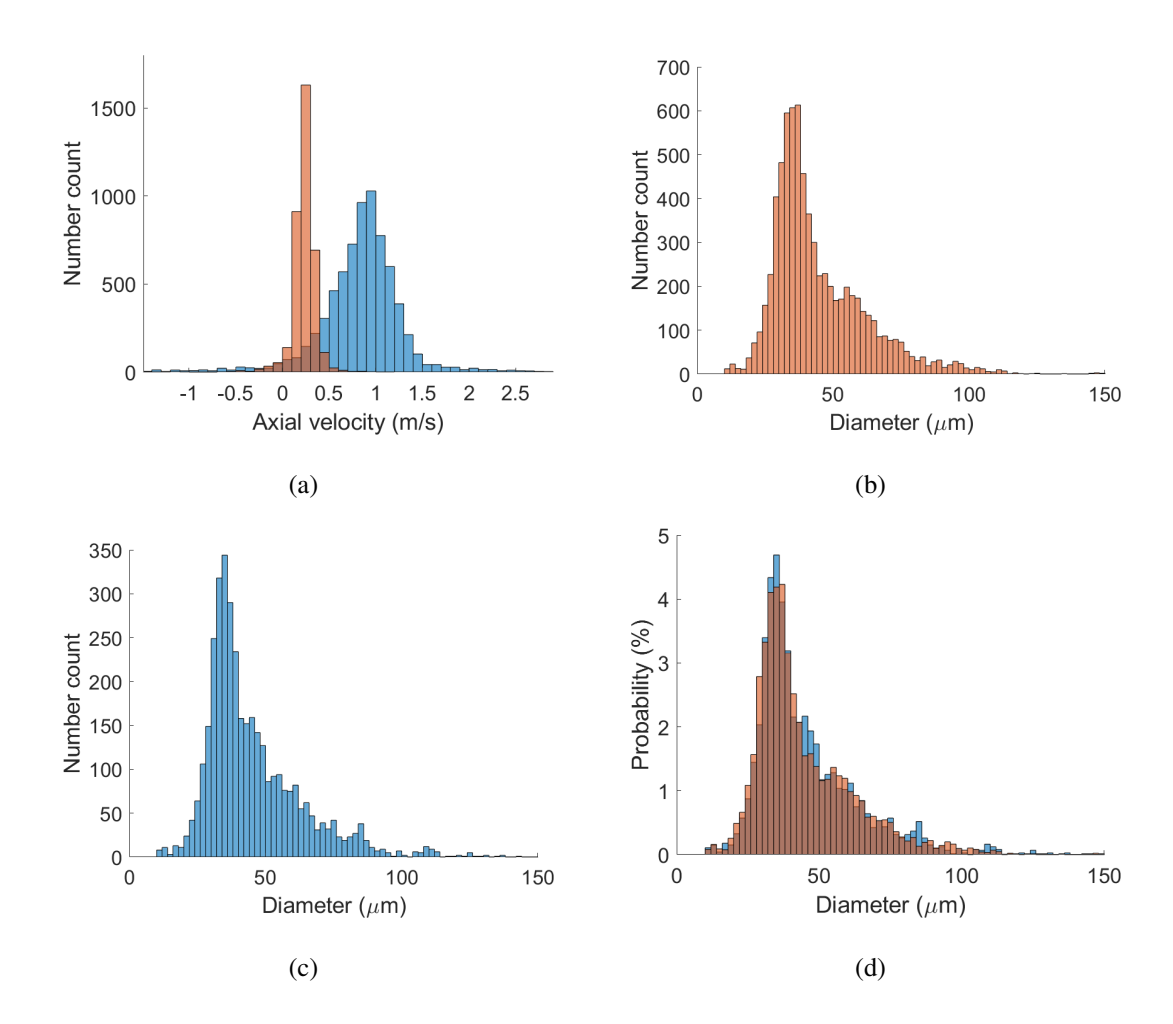


Figure 6.15: (a) Axial velocity distributions for measurement volume located at 100 mm downstream of nozzle tip (Red) and 500 mm downstream of nozzle tip (Blue). Droplet size distributions for measurement volume located at (b) 100 mm downstream of nozzle tip, (c) 500 mm downstream of nozzle tip and (d) overlay of normalised distributions for both measurement positions.

Chapter 7

Summary of conclusions and future work

7.1 Engineering impact

The current mechanistic understanding of droplet heat and mass transfer is somewhat limited to idealised situations of single droplet evaporation. It is known that localised interactions between droplets as well as the relative motion between droplets and flow field in conditions more realistic to spray scenarios play a significant role in determining the heat and mass transfer. However, due to the complexity of turbulent multiphase flows, performing direct measurements of key parameters relevant to droplet evaporation is very limited. The implications of this complexity barrier are far reaching, not least holding back our ability to accurately experimentally and computationally model real world scenarios containing droplet flows, whether is be the evaporation of; human produced aerosols relating to the spread of infectious diseases, inhaled medication in pharmaceutical drug delivery or fuel droplets in energy generation.

The use of a variety of planar optical diagnostic techniques presented in this work have shown the usefulness of it as a tool in determining the spatio-temporal evolution of key droplet parameters such as droplet; diameter, position, spatial concentration and velocity. The purposes of this work have ranged from the building of fundamental understanding of droplet characteristics in a variety of applications including transient aerosols produced during human expiration, and the injection renewable ethanol-gasoline fuel blends. To further our mechanistic understanding of droplet evaporation in complex spray systems a new planar Lagrangian tracking processor was developed, enabling the measurement of individual droplet diameter and position evolution over time. This processor was used to measure the evaporation rates of methanol droplets in a heated air flow, allowing the observation of diameter reduction of droplets within a spray. This method was then further applied to observe the effects of acoustic forcing on droplet-gas slip velocity with respect to forcing frequency, amplitude and droplet diameter.

The measurement methods generated as part of this thesis can be used to improve understanding of droplet evaporation by monitoring parameters relevant to droplet mass and heat transfer as well as direct measurement of droplet evaporation within these complex multiphase flows. Thus, enabling the effects of turbulent/acoustic flow fields and inter-droplet interactions to be accounted for in scenarios relevant to applications stretching from industrial spray atomisation to human produced aerosols.

7.2 Chapter conclusions

7.2.1 IDS characterisation of ethanol-gasoline fuel sprays.

With the increasing use of a variety of bio-derived fuel blends in automotive combustion, the impact that changing liquid fuel properties has on fuel spray evaporation is of key importance to fuel blend selection and fuel injector design. In this chapter the effects of increasing ethanol content in an ethanol-gasoline fuel blend sprays produced by an automotive Port Fuel Injection (PFI) atomiser were assessed through the monitoring of two characteristics known to effect by droplet evaporation and combustion dynamics. These being the spatial distribution of droplet volumetric concentration and mean droplet diameter.

To achieve these measurements a commercially available planar IDS technique, TSI's Global Sizing Velocimetry (GSV), was employed to measure both the size and position of ethanol-gasoline droplets within a $10 \times 12 \times 0.25$ mm measurement volume. As a planar measurement method, a large proportion of the spray is able to be captured within the measurement volume in comparison to point measurement methods such as Phase Doppler Anemometry (PDA), reducing the time taken to characterise the radial and axial variations in droplet diameter and concentration. To ensure the accuracy of GSV measurements in comparison to PDA, a series of validations tests were performed using a mono-disperse droplet generator. Results showing GSV measurements to be within $1.6~\mu m$ of the expected droplet diameter with a maximum standard deviation of $1.6~\mu m$. Due to relatively high droplet concentrations along the spray centreline (>3000 drops/cm³), the measurement volume was centred 50 mm downstream of the spray nozzle and radially displaced 20 mm from the spray centreline, this highlighting a limiting factor inherent to planar IDS measurement methods in comparison to PDA.

Ten different ethanol-gasoline fuel blends ranging from pure ethanol to pure gasoline were tested to asses the effects of ethanol content on spray properties. When varying the ethanol content within the ethanol-gasoline fuel blend two key trends were noted in droplet measurements taken with the measurement volume:

- The mean droplet diameter was seen to increase with increasing ethanol content, as has been noted in previous studies. Both the arithmetic mean and Sauter mean diameter was seen to increase by approximately 13% from pure gasoline to pure ethanol. The relation between ethanol content and increasing mean droplet diameter was observed to be approximately linear between blends containing 30% ethanol and pure ethanol.
- For blends containing an ethanol content of less than 30% a reduction in image quality was seen to compromise mean droplet diameter measurements as a result of an increase in erroneous droplet diameter measurements. The cause of which could be due to the increase in colouration and opacity of liquid fuel with increasing gasoline content, resulting in a higher degree of off-axis attenuation, though further work is required to understand the factors involved.
- For all fuel blends tested, droplet volumetric concentration decreased with radial distance from the spray centreline. As ethanol content increased the distribution of droplets within the measurement volume became more evenly radially distributed.
- When analysing the droplet volumetric concentrations it became apparent that the GSV technique was not recognising all interference patterns present in the captured images, typically 30-50% going unrecognised. As such it was not possible to use GSV for the reliable measurement of absolute droplet volumetric concentration, limiting the study to the observation of proportional change in analysed droplet volumetric concentration.

7.2.2 Development of Planar Interferometric Tracking (PIT) processor.

Using high speed imaging and a further processing element, a multi-frame Lagrangian Planar Interferometric Tracking (PIT) method is developed, capable of recording the position, velocity and diameter of individual droplets present within a polydisperse spray. Such measurement methods have seen very limited use despite the apparent benefits such a system offers, especially when applied to the characterisation of droplet evaporation in sprays.

Using TSI's GSV to provide droplet diameter and position of droplets within individual images of a water spray produced by an ultrasonic atomiser, a processor was developed to identify individual droplets across multiple frames, recording droplet diameter and position variation over time. As the GSV processor had the tendency to incorrectly size or not recognise interference patterns, this processor was capable of re-assessing interference patterns, based upon expected droplet positions as determined through velocity vector extrapolation. The use of the PIT processor increased the number of valid interference pattern measurement by 35.2% for a test case of 771 captured images (11,100 additional droplet measurements). With the re-measurement capability the PIT was seen to be capable of measuring droplets across prolonged duration's, the longest recorded droplet being observed in 182 images over a 26 ms period.

The PIT processor provided insight into the significance of a source of measurement error (inherent in all IDS methods) when performing the Lagrangian tracking of droplet diameters. Due to droplet out of plane velocities, the actual defocus displacement of a droplet varies over time. As such when tracking droplet diameter over time, droplets in non-evaporating conditions were seen to either increase or decrease in diameter. Measured 'apparent' droplet diameter change was seen to closely follow predicted trends based upon droplet direction and laser sheet thickness. The magnitude of this apparent diameter change was seen to be significant, for a laser sheet of approximately 1.5 mm in thickness droplet surface areas were observed to increase/decrease by over 10%. Without being able to determine

droplet out of plane direction this measurement error, creates a considerable source of uncertainty in the measurement of droplet diameter change due to evaporation. A number of potential methods for determining droplet out of plane direction are mentioned within the future work section of this chapter, though methods attempted within this study were not seen to be sufficiently reliable.

7.2.3 PIT measurement of droplet diameter in evaporating spray.

The formation of methanol from waste biomass, offers a method of bio-derived renewable fuel production without any potential conflicts with food production. To develop new and existing energy production facilities a proper understanding of the key characteristics of methanol fuel sprays needs to be developed, with droplet evaporation being of particular importance. Though methanol and other short chain alcohol fuels typically have lower boiling points than traditional fossil fuel hydrocarbons, they posses a greater latent heat of vaporisation.

Applying the newly developed PIT processor, droplet diameter reduction over time due to evaporation was observed for individual methanol droplets in a dedicated optical test facility. Methanol droplets ranging from 20 to 200 μ m (D10 of 62.4 μ m) produced by an ultrasonic atomiser entered a heated annular coaxial air flow (approximately 485 K at a flow rate of 100 slpm) and were measured in a 16 \times 20 \times 1.2 mm measurement volume located 140 mm downstream of the nozzle tip along the spray centre-line. A single droplet evaporation model (Lefebvre and McDonell, 2017), was adapted for use with methanol and used to estimate droplet evaporation rate at the given conditions. The steady state evaporation rate being estimated as approximately 43.3 μ m 2 /ms, ensuring appreciable droplet diameter variation should be detected at the given conditions. By comparing modelled droplet evaporation and that determined through PIT measurement a number of observations were made:

• On initial inspection the PIT measured evaporation rates showed considerable deviation from that estimated from the model, some droplets even displaying

an increase in droplet diameter over time. This non-physical phenomena was confirmed to be due to variations in the actual droplet defocus due to droplet out of plane velocity, as has been previously mentioned.

- Observing only droplets with a higher measured rate of change of proportional droplet surface area, $\frac{d}{dt}\left(\frac{D^2}{D_0^2}\right)$ and longer residence times within the measurement volume, the agreement between modelled and measured droplet evaporation could be compared for droplets effected by measurement error to a lesser extent. For such droplets the average evaporation rate was observed to be 41.7 μ m²/ms, within 4% of that predicted by the model. However, considerable variance was noted, with droplets seen to vary by \pm 50% from the model prediction.
- A small number of droplets were observed to traverse the entire height of the measurement volume (20 mm). Thus, as these droplets had a very low out of plane velocity component and high residence time within the measurement volume, they are very weakly affected by the outlined erroneous temporal change in droplet diameter. For the droplets fitting this criteria a considerable improvement in agreement between modelled and estimated droplet evaporation rates was seen, with the evaporation rates for all such droplets being within 25% of the model estimate. This finding confirming that as the expected measurement error resulting from change in actual defocus reduces, agreement between model and measurement increases. Given the inherent differences between idealised conditions on which this and other single droplet evaporation models assume and the actual conditions present within a complex spray environment, complete agreement would not be expected. Indeed, the differences between measurement and model potentially highlight the uncertainty associated with applying single droplet evaporation models to droplets within a spray.

Though developments could be made to further improve the use of PIT (these being listed in the future work section of this chapter), the PIT processor in its current iteration was shown to allow the direct observation of diameter change due to evaporation of individual droplets within a spray. This tool shows great potential in allowing the improvement in the understanding of mechanisms involved within droplet evaporation in sprays, this being of particular importance in the development of liquid renewable fuel systems.

7.2.4 Impact of droplet slip velocity of evaporation and characterisation of slip velocity-diameter relation through the use of PIT.

The presence of a velocity differential between droplets and gas present within a spray has been shown to enhance droplet evaporation due to convection. In the presence of turbulent and acoustic flow fields, the variations in flow velocity at a given point within the flow are such that even smaller droplets, as are typically used in many industrial applications will not remain fully entrained within the flow, resulting in the existence of a 'slip' velocity between droplet and gas phase. Velocity differentials between gas and droplet have been shown to enhance evaporation rates through the convective transfer of heat and mass.

The PIT processor was used to monitor the temporal velocity evolution of individual water droplets (ranging from 20-140 μ m) in a 120 slpm, room temperature annular coaxial air flow. From this the entrainment of droplets as a function of droplet diameter, acoustic velocity amplitude and frequency could be monitored in a $16 \times 20 \times 2$ mm measurement volume located 140 mm downstream of the nozzle tip along the spray centre-line. Tests were performed at three acoustic frequencies (100 Hz, 257 Hz and 400 Hz) relating to the 1^{st} , 3^{rd} and 5^{th} harmonics of the 920 mm long square pipe section used in the test rig. Five acoustic velocity amplitudes were tested at each forcing frequency, these varying from 0.16 to 3.47 m/s. The results emerging from the observation of droplet velocity response to acoustic flow field variation are as follows:

• For all test cases a clear relation between droplet diameter and axial velocity amplitude was observed. Droplet axial velocity amplitudes were seen to be

considerably lower than acoustic velocity amplitudes (determined using a two microphone method), implying no droplets within the measurable size range ($i20 \mu m$) were fully entrained within the flow at any of the test conditions

- Defining an entrainment factor as the ratio of droplet and acoustic axial velocity amplitudes was seen to effectively normalise data with respect to axial acoustic velocity amplitude. For all tested forcing frequencies entrainment factor was seen to linearly increase with inverse droplet surface area.
- Increasing forcing frequency was seen to reduce the entrainment factor of droplets, with the entrainment factor of a 20 μ m reducing by a third as forcing frequency increased from 100 to 400 Hz.
- Very good agreement was noted when comparing a model relating droplet stokes number and entrainment factor put forward by Hjelmfelt and Mockros (1966) to experimental data. Though the model predicted increasing phase delay between droplet and acoustic velocity oscillations with increasing droplet diameter was not noted in these experiments, with no evident trend in droplet velocity phase delay noted.
- For all tested forcing frequencies, increasing forcing amplitude reduced droplet mean axial velocity within the measurement volume, at 100 Hz mean droplet velocity reduced by approximately 50% when acoustic velocity amplitudes increased from 0 m/s to 0.71 m/s.
- The enhancement of spray droplet evaporation over a given displacement in
 the acoustic flow field tested is effected by both the increase in convection
 with increasing axial slip velocity resulting from an increase in acoustic amplitude and frequency, as well as an increase in droplet residence time due
 to a decrease in droplet mean axial velocity with increase acoustic velocity
 amplitude.
- The observed relations between droplet diameter and slip velocity were used within a single droplet evaporation model containing a factor that accounts for

convective heat and mass transfer as put forward by Lefebvre and McDonell (2017). The model estimating a considerable enhancement of droplet evaporation rate due to the presence of an acoustic flow field. Modelled droplet evaporation rate was seen to increase with droplet diameter, this being due to the decreased entrainment of such droplets. In alignment with trends expected from Damkoholer vaporisation number, the proportional evaporation rate enhancement due to the presence of an acoustic flow field was observed to decrease with increasing air flow temperatures.

Measurements of the same ultrasonic atomiser producing a methanol spray at various air flow temperatures (338 to 486 K) and acoustic velocity amplitudes (0.00 to 0.48 m/s) at a frequency of 100 HZ, were performed using a standard low frame rate IDS measurement method (TSI's GSV). The relative change in mean droplet diameter across the measurement window was then used to observe the effects of increasing acoustic velocity amplitude and air flow temperature on methanol spray evaporation.

- Droplet mass flux was seen to decrease with increasing air flow temperature, reducing by approximately 30% as air flow temperatures increased from 338 to 486 K, consistent with increased evaporation at higher temperatures. Additionally with increasing temperature mean droplet diameter was seen to increase due to a reduction in the number of smaller droplets being present within the measurement volume as is typical of increasing evaporation in polydisperse sprays.
- At the lower air flow temperatures of 338 K and 369 K, increasing acoustic velocity amplitude was seen to increase the number of larger droplets transiting the measurement volume, resulting in an increased droplet mass flow rate, despite a reduction in the total number of droplets measured. Given the spray geometry and droplet velocity profiles the reasons for this phenomena are unknown. However, as air flow temperature increased (402 K and 486 K), increasing acoustic velocity amplitude was seen to reduce the mass flow of droplets through the measurement volume.

For both acoustically forced and unforced conditions the Mean droplet diameter increased over the 20 mm axial displacement from the top of the measurement region to the bottom with increasing forcing amplitude in all test cases, suggesting an increase in evaporation.

7.2.5 Optical characterisation of human produced droplet flows.

The exhalation of aerosols is a key mechanism in the spread of infectious respiratory diseases. Characterising the droplets expelled from the mouth and nose in expiration is key in developing public guidelines to mitigate the spread of disease. Little is known about the degree of variation in aerosol production between individuals, and how dependant droplet production is on the form of expiration, be it breathing, talking or shouting.

The use of face coverings has been used globally as a method to inhibit the emission of contagions. However, little is known about the efficacy of common face coverings across all forms of expiration. By inviting 20 volunteers, the interperson and individual variation in droplet concentrations produced across various expiration tasks (breathing, talking and singing) was observed using planar laser illuminated high speed imaging. In addition, the effectiveness of face coverings, in reducing the concentration, duration and velocity of produced droplets was observed. The key findings of this study are:

- Droplet generation during expiration tasks showed that a majority of droplets
 are expelled in the first instances. For spoken words certain sounds were seen
 to correlate with secondary and tertiary increases in the number of droplets
 present within the measurement region. This would suggest certain motions
 relating to specific sounds influence the production and emission of droplets.
 When singing a long note, higher droplet concentrations were seen to be
 maintained for a greater period of time in comparison to the other verbal and
 non-verbal tasks performed for a large proportion of participants
- Of the verbal and non-verbal tasks performed, average droplet concentrations produced varied from 0-0.09 droplets per mm³, with peak droplet concentra-

tions ranging from 0-0.28 droplets per mm³. Inter-person variation was seen to be very large, some participants observed to produce little to no droplets across the full range of tasks, whilst other produced double or triple the cohort median.

- Only a few instances of frontal mask leakage were noted during testing, particularly when exhaling and saying 'Hello'. In such cases mask use was shown to reduce both time averaged and maximum droplet concentrations by a minimum of 40%. However, in a majority of cases mask use reduced droplet concentrations within the measurement volume by over 90%.
- Significant inter-person variation was seen to in mean droplet velocities, these
 varying between 0.2 and 1.5 m/s for all expiration tasks. In rare instances of
 frontal mask leakage, droplet velocities were seen to reduce to less than 0.1
 m/s in all cases.

7.3 Future Work

The development of the PIT processor put forward in this thesis has shown considerable promise in a number of useful applications, including the actual measurement of multiple individual droplet diameter reduction due to evaporation over time in a spray as well as the determination of slip velocity in an unsteady flow field with respect to droplet diameter. Whilst the PIT processor in its current configuration has been shown to be measurement method, a few improvements would greatly improve its capability. The improvements outlined are predominantly targeted at the reduction of an error in the droplet diameter measurement associated with the variation in droplet defocus during its traversal of the illumination plane. Additionally, a number of improvements can be made to the optical equipment and setup allowing for improved droplet size and position measurements. The suggested improvements are:

Development of a method for determining droplet out of plane direction.
 In conditions where droplet diameter change due to legitimate reasons could

be considered to be negligible, a method for correcting droplet diameter measurement errors resulting droplet defocus variation with droplet out of plane motion have been put forward in this thesis. However, when significant evaporation is expected, this method is not valid thus a method for determining the out of plane direction of motion for individual droplets is required. One such method was attempted using similar principles to those discussed by Damaschke et al. (2002, 2005) and Kawaguchi et al. (2010), where it is observed that the total length of an oscillation pattern is dependant only on the defocus distance of a droplet, thus an increase or decrease over the duration of tracking can be used to determine the out of plane direction. However, given the optical equipment and setup used, droplet oscillation pattern length could not be determined to a sufficient resolution such that an appreciable change in length could be detected above length measurement error, largely resulting from image noise, similar issues being defined by Sugimoto et al. (2006).

The use of high speed camera with a smaller pixel size would improve spatial resolution, making changes in oscillation pattern length measurements more apparent. Similar results could be achieved by using a lens setup providing a higher magnification, however this would compromise on measurement volume size. A more robust method for accurately determining the 3-component droplet velocities is through the use of a stereoscopic IDS technique, such as that outline by Sugimoto et al. (2006). As well as enabling the correction of droplet diameter change over time, a stereoscopic PIT measurement method would allow a droplet to be tracked across 3-D space. The only potential drawback to such a method would be the increased complexity and requirement of an additional high speed camera.

2. 3-component velocity measurement in non-evaporating conditions. As mentioned in conditions where no significant droplet diameter change is expected (i.e. no droplet evaporation) droplet diameter measurements were seen to increase or decrease due to changes in the defocus distance as droplets traversed the laser sheet thickness. The apparent ratio of initial to finial mea-

sured 'droplet surface area' change was observed to increase/decrease approximately linearly with time, with droplet 'surface areas' increasing or decreasing by approximately 10% for a laser sheet 1 mm in thickness. The gradient of this linear diameter change is directly related to rate of change of droplet defocus, from which the droplet out of plane velocity, in theory, can easily be determined. Verification of the out of plane velocity component from such a method could be carried by the simultaneous use of a stereoscopic IDS measurement technique.

3. Evaporation model validation and research. Either in its current state or with the methods for droplet diameter measurement correction mentioned, applying PIT to a greater variety of ambient conditions, flow fields and liquid properties would allow the direct observation of how such parameters effect the evaporation of droplets within spray. This can be used to both verify and associated levels of uncertainty to existing droplet evaporation models, or to develop new models based on experimental data produced by PIT. One specific parameter that PIT has seen to be very capable of accurately observing is the slip velocity between droplets and gas flow present within an acoustically forced flow. With the measurement technique improvements outlined, it may well be possible to directly compare individual droplet slip velocity and droplet size reduction due to evaporation within a spray.

The outcomes of the work outlined in Chapter 6 provide the building blocks for further research regarding the human production of aerosols and the spread of infectious disease. With key parameters now more thoroughly understood, experimental and model-based work can ensue. Being able to place values on the velocity, concentration and inter-person variation of droplets produced during expiration as well as the influence of face coverings enables more controlled lab-based experimentation to be pursued. Using the data gathered in Chapter 6 it is possible to create a mechanical analogue for an expiring human, emitting droplets of the correct size, velocity, and quantities. This analogue could be used to observe the effects of environmental conditions and mitigation methods on the propagation of droplets through space. Indeed the data gathered as part of the work represented in Chapter 6 has been used by Salmonsmith et al. (2023) to create an analogue for an expiring human enabling the effectiveness of air purification in reducing the presence of aerosols in a hospital setting to be assessed.

Bibliography

- B. Abramzon and W. A. Sirignano. Droplet vaporization model for spray combustion calculations. *International journal of heat and mass transfer*, 32(9):1605–1618, 1989.
- H.-E. Albrecht, N. Damaschke, M. Borys, and C. Tropea. *Laser Doppler and phase Doppler measurement techniques*. Springer Science & Business Media, 2013.
- P. Aleiferis, M. Behringer, D. OudeNijeweme, and P. Freeland. Spray imaging and droplet sizing of spark-eroded and laser-drilled injectors with gasoline-butanol and gasoline-ethanol blends. 2015.
- M. Alsved, A. Matamis, R. Bohlin, M. Richter, P.-E. Bengtsson, C.-J. Fraenkel,
 P. Medstrand, and J. Löndahl. Exhaled respiratory particles during singing and talking. *Aerosol Science and Technology*, 54(11):1245–1248, 2020.
- E. L. Anderson, P. Turnham, J. R. Griffin, and C. C. Clarke. Consideration of the aerosol transmission for covid-19 and public health. *Risk Analysis*, 40(5):902–907, 2020.
- A. Arce, A. Blanco, A. Soto, and I. Vidal. Phase equilibria of water+ methanol+ hexyl acetate mixtures. *Fluid phase equilibria*, 128(1-2):261–270, 1997.
- S. Asadi, A. S. Wexler, C. D. Cappa, S. Barreda, N. M. Bouvier, and W. D. Ristenpart. Aerosol emission and superemission during human speech increase with voice loudness. *Scientific reports*, 9(1):1–10, 2019.
- M. Baird, M. Senior, and R. Thompson. Terminal velocities of spherical particles

- in a vertically oscillating liquid. *Chemical Engineering Science*, 22(4):551–558, 1967.
- R. Balachandran, B. Ayoola, C. Kaminski, A. Dowling, and E. Mastorakos. Experimental investigation of the nonlinear response of turbulent premixed flames to imposed inlet velocity oscillations. *Combustion and Flame*, 143(1-2):37–55, 2005.
- R. Balachandran, S. Chakravarthy, and R. Sujith. Characterization of an acoustically self-excited combustor for spray evaporation. *Journal of propulsion and power*, 24(6):1382–1389, 2008.
- E. Bänsch and M. Götz. Numerical study of droplet evaporation in an acoustic levitator. *Physics of Fluids*, 30(3):037103, 2018.
- S. Basu, P. Kabi, S. Chaudhuri, and A. Saha. Insights on drying and precipitation dynamics of respiratory droplets from the perspective of covid-19. *Physics of Fluids*, 32(12):123317, 2020.
- A. Burdukov and V. Nakoryakov. On mass transfer in an acoustic field. *Journal of Applied Mechanics and Technical Physics*, 6(2):51–55, 1965.
- A. J. Butcher, P. G. Aleiferis, and D. Richardson. Development of a real-size optical injector nozzle for studies of cavitation, spray formation and flash-boiling at conditions relevant to direct-injection spark-ignition engines. *International Journal of Engine Research*, 14(6):557–577, 2013.
- R. Calabria and P. Massoli. Experimental study of droplets in evaporating regime by 2d scattering analysis. In *10th International Symposium on Applications of laser techniques*, 2000.
- C. Y. H. Chao, M. P. Wan, L. Morawska, G. R. Johnson, Z. Ristovski, M. Hargreaves, K. Mengersen, S. Corbett, Y. Li, X. Xie, et al. Characterization of expiration air jets and droplet size distributions immediately at the mouth opening. *Journal of aerosol science*, 40(2):122–133, 2009.

- G. Charalampous and Y. Hardalupas. Numerical evaluation of droplet sizing based on the ratio of fluorescent and scattered light intensities (lif/mie technique). *Applied optics*, 50(9):1197–1209, 2011.
- C. Chauveau, M. Birouk, F. Halter, and I. Gökalp. An analysis of the droplet support fiber effect on the evaporation process. *International Journal of Heat and Mass Transfer*, 128:885–891, 2019.
- N. F. Che Mat, H. A. Edinur, M. K. A. Abdul Razab, and S. Safuan. A single mass gathering resulted in massive transmission of covid-19 infections in malaysia with further international spread. *Journal of Travel Medicine*, 27(3):059, 2020.
- W. A. Chishty, U. Vandsburger, W. R. Saunders, and W. T. Baumann. Interaction between thermoacoustic oscillations and spray combustion. In *Engineering Turbulence Modelling and Experiments 6*, pages 865–874. Elsevier, 2005.
- H. Chiu and T. Liu. Group combustion of liquid droplets. *Combustion Science and Technology*, 17(3-4):127–142, 1977.
- H. Chiu, H. Kim, and E. Croke. Internal group combustion of liquid droplets. In *Symposium (international) on combustion*, volume 19, pages 971–980. Elsevier, 1982.
- R. Clift, J. R. Grace, and M. E. Weber. Bubbles, drops, and particles. pages 306–314, 2005.
- E. Cossali and Y. Hardalupas. Comparison between laser diffraction and phase doppler velocimeter techniques in high turbidity, small diameter sprays. *Experiments in fluids*, 13(6):414–422, 1992.
- I. M. Cotabarren, D. Bertín, M. Razuc, M. V. Ramírez-Rigo, and J. Piña. Modelling of the spray drying process for particle design. *Chemical Engineering Research* and Design, 132:1091–1104, 2018.
- D. Dabiri. Cross-correlation digital particle image velocimetry—a review. Department of Aeronautics & Astronautics, University of

- Washington, Seattle, WA, Review Paper. https://www. aa. washington. edu/sites/aa/files/faculty/dabiri/pubs/piV. Review. Paper. final. pdf, 2006.
- N. Damaschke, H. Nobach, and C. Tropea. Optical limits of particle concentration for multi-dimensional particle sizing techniques in fluid mechanics. *Experiments in fluids*, 32(2):143–152, 2002.
- N. Damaschke, H. Nobach, T. I. Nonn, N. Semidetnov, and C. Tropea. Multi-dimensional particle sizing techniques. *Experiments in fluids*, 39(2):336–350, 2005.
- E. Dan Hirleman. History of development of the phase-doppler particle-sizing velocimeter. *Particle & particle systems characterization*, 13(2):59–67, 1996.
- A. M. Danis, I. Namer, and N. P. Cernansky. Droplet size and equivalence ratio effects on spark ignition of monodisperse n-heptane and methanol sprays. *Combustion and flame*, 74(3):285–294, 1988.
- H. Davies, M. Talibi, M. Hyde, and R. Balachandran. Investigating ethanol-gasoline spray characteristics using an interferometric drop sizing technique. In *Turbo Expo: Power for Land, Sea, and Air*, volume 58677, page V006T05A023. American Society of Mechanical Engineers, 2019.
- H. Davies, M. Talibi, A. Ducci, N. Parsania, and R. Balachandran. Planar interferometric tracking of droplets in evaporating conditions. *Experiments in Fluids*, 63 (10):167, 2022.
- S. Dehaeck and J. Van Beeck. Multifrequency interferometric particle imaging for gas bubble sizing. *Experiments in fluids*, 45(5):823, 2008.
- V. Deprédurand, G. Castanet, and F. Lemoine. Heat and mass transfer in evaporating droplets in interaction: Influence of the fuel. *International journal of heat and mass transfer*, 53(17-18):3495–3502, 2010.

- J.-W. Ding, G.-X. Li, and Y.-S. Yu. The instability and droplet size distribution of liquid-liquid coaxial swirling spray: An experimental investigation. *Experimental Thermal and Fluid Science*, 82:166–173, 2017.
- V. Dorfner, J. Domnick, F. Durst, and R. Kohler. Viscosity and surface tension effects in pressure swirl atomization. *Atomization and Sprays*, 5(3), 1995.
- H. Duan, F. Romay, B. Liu, and A. Naqwi. Flow-focusing monodisperse aerosol generator for calibration of spray diagnostics instruments. In 18th International Symposium on the Application of Laser and Imaging Techniques to Fluid Mechanics, Lisbon, Portugal, 2016.
- R. Dubey, M. McQuay, and J. Carvalho Jr. An experimental and theoretical investigation on the effects of acoustics on spray combustion. In *Symposium (International) on Combustion*, volume 27, pages 2017–2023. Elsevier, 1998.
- F. Durst and M. Zaré. Laser doppler measurements in two-phase flows. In *The accuracy of flow measurements by laser Doppler methods*, pages 403–429, 1976.
- M. Echternach, S. Gantner, G. Peters, C. Westphalen, T. Benthaus, B. Jakubaß, L. Kuranova, M. Döllinger, and S. Kniesburges. Impulse dispersion of aerosols during singing and speaking: a potential covid-19 transmission pathway. *American journal of respiratory and critical care medicine*, 202(11):1584–1587, 2020.
- C. Ejim, B. Fleck, and A. Amirfazli. Analytical study for atomization of biodiesels and their blends in a typical injector: surface tension and viscosity effects. *Fuel*, 86(10-11):1534–1544, 2007.
- S. Elghobashi. Direct numerical simulation of turbulent flows laden with droplets or bubbles. *Annual Review of Fluid Mechanics*, 51:217–244, 2019.
- A. Faghri and Y. Zhang. *Transport phenomena in multiphase systems*. Elsevier, 2006.

- R. Fajgenbaum and R. G. dos Santos. Influence of fuel temperature on atomization parameters in a pressure-swirl atomizer from a port fuel injector by shadowgraphy technique. *Journal of the Brazilian Society of Mechanical Sciences and Engineering*, 38(7):1877–1892, 2016.
- W. M. Farmer. Measurement of particle size, number density, and velocity using a laser interferometer. *Applied Optics*, 11(11):2603–2612, 1972.
- Z. Feng, C. Zhan, C. Tang, K. Yang, and Z. Huang. Experimental investigation on spray and atomization characteristics of diesel/gasoline/ethanol blends in high pressure common rail injection system. *Energy*, 112:549–561, 2016.
- A. Ferrante and S. Elghobashi. On the physical mechanisms of two-way coupling in particle-laden isotropic turbulence. *Physics of fluids*, 15(2):315–329, 2003.
- J. R. Fessler, J. D. Kulick, and J. K. Eaton. Preferential concentration of heavy particles in a turbulent channel flow. *Physics of Fluids*, 6(11):3742–3749, 1994.
- J. Gao, D. Jiang, and Z. Huang. Spray properties of alternative fuels: A comparative analysis of ethanol–gasoline blends and gasoline. *Fuel*, 86(10-11):1645–1650, 2007.
- A. Giovanni, T. Radulesco, G. Bouchet, A. Mattei, J. Révis, E. Bogdanski, and J. Michel. Transmission of droplet-conveyed infectious agents such as sars-cov-2 by speech and vocal exercises during speech therapy: preliminary experiment concerning airflow velocity. *European Archives of Oto-Rhino-Laryngology*, 278 (5):1687–1692, 2021.
- A. Glover, S. Skippon, and R. Boyle. Interferometric laser imaging for droplet sizing: a method for droplet-size measurement in sparse spray systems. *Applied Optics*, 34(36):8409–8421, 1995.
- I. Gökalp, C. Chauveau, O. Simon, and X. Chesneau. Mass transfer from liquid fuel droplets in turbulent flow. *Combustion and flame*, 89(3-4):286–298, 1992.

- Y.-y. Gong, L.-h. You, and X.-m. Liang. An investigation on droplet size distribution and evaporation of diesel fuel sprays at high injection pressure by using laser diagnostic technique. *SAE transactions*, pages 162–174, 1992.
- S. Gorman and J. F. Widmann. Investigation of multiphase particle image velocimetry using monte carlo simulations. *Atomization and Sprays*, 14(6), 2004.
- F. K. Gregson, N. A. Watson, C. M. Orton, A. E. Haddrell, L. P. McCarthy, T. J. Finnie, N. Gent, G. C. Donaldson, P. L. Shah, J. D. Calder, et al. Comparing aerosol concentrations and particle size distributions generated by singing, speaking and breathing. *Aerosol Science and Technology*, 55(6):681–691, 2021.
- L. Hamner. High sars-cov-2 attack rate following exposure at a choir practice—skagit county, washington, march 2020. *MMWR. Morbidity and mortality weekly report*, 69, 2020.
- Y. Hardalupas, S. Sahu, A. M. Taylor, and K. Zarogoulidis. Simultaneous planar measurement of droplet velocity and size with gas phase velocities in a spray by combined ilids and piv techniques. *Experiments in fluids*, 49(2):417–434, 2010.
- Y. Hardalupas, A. Taylor, and K. Zarogoulidis. Detection and evaluation of droplet and bubble fringe patterns in images of planar interferometric measurement techniques using the wavelet transform. In *International Conference on Optical Particle Characterization (OPC 2014)*, volume 9232, pages 65–70. SPIE, 2014.
- K. H. Hesselbacher, K. Anders, and A. Frohn. Experimental investigation of gaussian beam effects on the accuracy of a droplet sizing method. *Applied optics*, 30 (33):4930–4935, 1991.
- J. Heyman. Tractrac: A fast multi-object tracking algorithm for motion estimation. *Computers & Geosciences*, 128:11–18, 2019.
- A. Hjelmfelt and L. Mockros. Motion of discrete particles in a turbulent fluid. *Applied Scientific Research*, 16(1):149–161, 1966.

- K. M. A. Ho, H. Davies, R. Epstein, P. Bassett, Á. Hogan, Y. Kabir, J. Rubin, G. Y. Shin, J. P. Reid, R. Torii, et al. Spatiotemporal droplet dispersion measurements demonstrate face masks reduce risks from singing. *Scientific reports*, 11(1):1–11, 2021.
- G. Houghton. Particle trajectories and terminal velocities in vertically oscillating fluids. *The Canadian Journal of Chemical Engineering*, 44(2):90–95, 1966.
- G. Hubbard, V. Denny, and A. Mills. Droplet evaporation: effects of transients and variable properties. *International journal of heat and mass transfer*, 18(9): 1003–1008, 1975.
- B. P. Husted, P. Petersson, I. Lund, and G. Holmstedt. Comparison of piv and pda droplet velocity measurement techniques on two high-pressure water mist nozzles. *Fire safety journal*, 44(8):1030–1045, 2009.
- G. Johnson, L. Morawska, Z. Ristovski, M. Hargreaves, K. Mengersen, C. H. Chao, M. Wan, Y. Li, X. Xie, D. Katoshevski, et al. Modality of human expired aerosol size distributions. *Journal of Aerosol Science*, 42(12):839–851, 2011.
- C. J. Kähler and R. Hain. Fundamental protective mechanisms of face masks against droplet infections. *Journal of aerosol science*, 148:105617, 2020.
- K. Kannaiyan and R. Sadr. Experimental investigation of spray characteristics of alternative aviation fuels. *Energy Conversion and Management*, 88:1060–1069, 2014.
- S. Kawaguchi, Satoh. High-speed ilids measurement of evaporating droplet, 2012.
- T. Kawaguchi, Y. Akasaka, and M. Maeda. Size measurements of droplets and bubbles by advanced interferometric laser imaging technique. *Measurement Science and Technology*, 13(3):308, 2002.
- T. Kawaguchi, I. Satoh, and T. Saito. Dynamic ilids measurement by means of high-speed nd: Ylf laser. In *Proc. 23rd Annual Conf. on Liquid Atomization and Spray Systems, ILASS-Europe, 2010*, 2010.

- R. D. Keane and R. J. Adrian. Theory of cross-correlation analysis of piv images. *Applied scientific research*, 49(3):191–215, 1992.
- T. Khasanshin and T. Zykova. Specific heat of saturated monatomic alcohols. *Journal of engineering physics*, 56(6):698–700, 1989.
- A. F. Kheiralla, M. Elawad, M. Y. Hassan, M. Hussen, and H. I. Osman. Effect of ethanol/gasoline blends on fuel properties characteristics of spark ignition engines. 2011.
- L. Khuong, H. Masjuki, N. Zulkifli, E. N. Mohamad, M. Kalam, A. Alabdulkarem, A. Arslan, M. Mosarof, A. Syahir, and M. Jamshaid. Effect of gasoline–bioethanol blends on the properties and lubrication characteristics of commercial engine oil. *RSC advances*, 7(25):15005–15019, 2017.
- S. Kim, Y. D. Jeong, J. H. Byun, G. Cho, A. Park, J. H. Jung, Y. Roh, S. Choi, I. M. Muhammad, and I. H. Jung. Evaluation of covid-19 epidemic outbreak caused by temporal contact-increase in south korea. *International Journal of Infectious Diseases*, 96:454–457, 2020.
- W. Kim, H. Kim, and W. Yoon. Experiments on atomization characteristics of the flash swirl spray. In 50th AIAA Aerospace Sciences Meeting including the New Horizons Forum and Aerospace Exposition, page 176, 2012.
- S. Kirschke, P. Bousquet, P. Ciais, M. Saunois, J. G. Canadell, E. J. Dlugokencky, P. Bergamaschi, D. Bergmann, D. R. Blake, L. Bruhwiler, et al. Three decades of global methane sources and sinks. *Nature geoscience*, 6(10):813–823, 2013.
- N. Ko and W. Chan. Similarity in the initial region of annular jets: three configurations. *Journal of Fluid Mechanics*, 84(4):641–656, 1978.
- N. Ko and W. Chan. The inner regions of annular jets. *Journal of Fluid Mechanics*, 93(3):549–584, 1979.

- T. Kobayashi, T. Kawaguchi, and M. Maeda. Measurement of spray flow by an improved interferometric laser imaging droplet sizing (ilids) system. In *10th International Symposium on Applications of laser techniques*, 2000.
- G. König, K. Anders, and A. Frohn. A new light-scattering technique to measure the diameter of periodically generated moving droplets. *Journal of aerosol science*, 17(2):157–167, 1986.
- R. Kumara Gurubaran and R. P. Sujith. An experimental investigation of non-evaporative sprays in axial acoustic fields. In *46th AIAA Aerospace Sciences Meeting and Exhibit*, page 1046, 2008.
- M. Labowsky. The effects of nearest neighbor interactions on the evaporation rate of cloud particles. *Chemical Engineering Science*, 31(9):803–813, 1976.
- J. R. Lakowicz. *Principles of fluorescence spectroscopy*. Springer Science & Business Media, 2013.
- A. H. Lefebvre and V. G. McDonell. *Atomization and sprays*. CRC press, 2017.
- N. H. Leung, D. K. Chu, E. Y. Shiu, K.-H. Chan, J. J. McDevitt, B. J. Hau, H.-L. Yen, Y. Li, D. K. Ip, J. Peiris, et al. Respiratory virus shedding in exhaled breath and efficacy of face masks. *Nature medicine*, 26(5):676–680, 2020.
- T. Li, K. Nishida, and H. Hiroyasu. Droplet size distribution and evaporation characteristics of fuel spray by a swirl type atomizer. *Fuel*, 90(7):2367–2376, 2011.
- C. Lieber, S. Melekidis, R. Koch, and H.-J. Bauer. Insights into the evaporation characteristics of saliva droplets and aerosols: Levitation experiments and numerical modeling. *Journal of aerosol science*, 154:105760, 2021.
- G. Lupo, A. Gruber, L. Brandt, and C. Duwig. Direct numerical simulation of spray droplet evaporation in hot turbulent channel flow. *International Journal of Heat and Mass Transfer*, 160:120184, 2020.

- V. Majer and V. Svoboda. Enthalpies of vaporization of organic compounds: a critical review and data compilation. 1986.
- N. Mao, C. An, L. Guo, M. Wang, L. Guo, S. Guo, and E. Long. Transmission risk of infectious droplets in physical spreading process at different times: a review. *Building and Environment*, 185:107307, 2020.
- Y. Maruyama and K. Hasegawa. Evaporation and drying kinetics of water-nacl droplets via acoustic levitation. *RSC Advances*, 10(4):1870–1877, 2020.
- K. Matsuura, K. Zarogoulidis, Y. Hardalupas, A. M. Taylor, T. Kawaguchi, D. Sugimoto, and K. Hishida. Simultaneous planar measurement of size and three-component velocity of droplets in an aero-engine airblast fuel spray by stereoscopic interferometric laser imaging technique. In 10th International Conference on Liquid Atomization and Spray Systems, ICLASS 2006, 2006.
- J. Maybank, K. Yoshida, and R. Grover. Spray drift from agricultural pesticide applications. *Journal of the Air Pollution Control Association*, 28(10):1009–1014, 1978.
- M. McQuay and R. Dubey. The interaction of well-characterized, longitudinal acoustic waves with a nonreacting spray. *Atomization and Sprays*, 8(4), 1998.
- H. G. Merkus. *Particle size measurements: fundamentals, practice, quality*, volume 17. Springer Science & Business Media, 2009.
- L. Morawska, G. Johnson, Z. Ristovski, M. Hargreaves, K. Mengersen, S. Corbett,
 C. Y. H. Chao, Y. Li, and D. Katoshevski. Size distribution and sites of origin of droplets expelled from the human respiratory tract during expiratory activities.
 Journal of aerosol science, 40(3):256–269, 2009.
- Y. Moriyoshi, R. Uchida, M. Takagi, and M. Kubota. Numerical and experimental analyses of mixture formation process using a fan-shaped di gasoline spray: Examinations on effects of crosswind and wall impingement. Technical report, SAE Technical Paper, 2009.

- A. Naqwi, F. Durst, and X. Liu. Extended phase-doppler system for characterization of multiphase flows. *Particle & Particle Systems Characterization*, 8(1-4):16–22, 1991.
- H. Oh, C. Bae, and K. Min. Spray and combustion characteristics of ethanol blended gasoline in a spray guided disi engine under lean stratified operation. *SAE International Journal of Engines*, 3(2):213–222, 2010.
- M. Orme. Experiments on droplet collisions, bounce, coalescence and disruption. *Progress in Energy and Combustion Science*, 23(1):65–79, 1997.
- G. Pan, J. Shakal, W. Lai, R. Calabria, and P. Massoli. Spray features investigated by gsv: A new planar laser technique. In *Tenth International Conference on Liquid Atomization and Spray Systems (ICLASS), Kyoto, Japan, Aug*, 2006.
- G. Parant, L. Zimmer, A. Renaud, and F. Richecoeur. Adaptation of the ptv method for droplets evaporating in vicinity of a flame. 2021.
- S. H. Park, H. J. Kim, H. K. Suh, and C. S. Lee. Atomization and spray characteristics of bioethanol and bioethanol blended gasoline fuel injected through a direct injection gasoline injector. *International Journal of Heat and Fluid Flow*, 30(6):1183 1192, 2009. ISSN 0142-727X. doi: https://doi.org/10.1016/j.ijheatfluidflow.2009.07.002. URL http://www.sciencedirect.com/science/article/pii/S0142727X09001167.
- S. Pierson, S. Richardson, P. Rubini, M. Jermy, and D. Greenhalgh. Laser characterization of a port fuel injector to provide boundary data for computational fluid dynamics. In *IMechE Conference Transactions*, volume 8, pages 167–178. Citeseer, 2000.
- U. Potdar, O. Pawar, R. Sikka, and S. Kumar. Experimental investigations on the stabilization of lifted kerosene spray flames with coflow air. *Combustion Science* and Technology, 190(10):1689–1709, 2018.

- A. K. Prasad. Stereoscopic particle image velocimetry. *Experiments in fluids*, 29 (2):103–116, 2000.
- K. A. Prather, L. C. Marr, R. T. Schooley, M. A. McDiarmid, M. E. Wilson, and D. K. Milton. Airborne transmission of sars-cov-2. *Science*, 370(6514):303–304, 2020.
- H. Qian, M. P. Sheetz, and E. L. Elson. Single particle tracking. analysis of diffusion and flow in two-dimensional systems. *Biophysical journal*, 60(4):910–921, 1991.
- R. Ragucci, A. Cavaliere, and P. Massoli. Drop sizing by laser light scattring exploiting intensity angular oscillation in the mie regime. *Particle & Particle Systems Characterization*, 7(1-4):221–225, 1990.
- J. F. Robinson, I. Rios de Anda, F. J. Moore, J. P. Reid, R. P. Sear, and C. P. Royall. Efficacy of face coverings in reducing transmission of covid-19: Calculations based on models of droplet capture. *Physics of fluids*, 33(4):043112, 2021.
- S. Sahu, Y. Hardalupas, and A. Taylor. Application of combined ilids and plif techniques to study droplet and vapour phase interaction in an evaporative and non-reacting spray. In 17th International Symposium on Applications of Laser Techniques to Fluid Mechanics, 2014a.
- S. Sahu, Y. Hardalupas, and A. M. Taylor. Simultaneous droplet and vapour-phase measurements in an evaporative spray by combined ilids and plif techniques. *Experiments in fluids*, 55(2):1–21, 2014b.
- S. Sahu, Y. Hardalupas, and A. Taylor. Interaction of droplet dispersion and evaporation in a polydispersed spray. *Journal of Fluid Mechanics*, 846:37–81, 2018a.
- S. Sahu et al. Analysis of droplet clustering in air-assist sprays using voronoi tessellations. *Physics of Fluids*, 30(12):123305, 2018b.
- J. Salmonsmith, A. Ducci, R. Balachandran, L. Guo, R. Torii, C. Houlihan, R. Epstein, J. Rubin, M. K. Tiwari, and L. B. Lovat. Use of portable air purifiers to

- reduce aerosols in hospital settings and cut down the clinical backlog. *Epidemiology & Infection*, 151:e21, 2023.
- D. Santos, A. C. Maurício, V. Sencadas, J. D. Santos, M. H. Fernandes, and P. S. Gomes. Spray drying: an overview. *Biomaterials-Physics and Chemistry-New Edition*, pages 9–35, 2018.
- S. S. Sazhin. Advanced models of fuel droplet heating and evaporation. *Progress in energy and combustion science*, 32(2):162–214, 2006.
- T. Scheimpflug. Improved method and apparatus for the systematic alteration or distortion of plane pictures and images by means of lenses and mirrors for photography and for other purposes. *GB patent*, 1196, 1904.
- J. Serras-Pereira, P. Aleiferis, D. Richardson, and S. Wallace. Characteristics of ethanol, butanol, iso-octane and gasoline sprays and combustion from a multihole injector in a disi engine. SAE International Journal of Fuels and Lubricants, 1(1):893–909, 2009.
- S. Sharma, R. Pinto, A. Saha, S. Chaudhuri, and S. Basu. On secondary atomization and blockage of surrogate cough droplets in single-and multilayer face masks. *Science advances*, 7(10):eabf0452, 2021.
- S. Skippon and Y. Tagaki. Ilids measurements of the evaporation of fuel droplets during the intake and compression strokes in a firing lean burn engine. *SAE transactions*, pages 1111–1126, 1996.
- D. B. Spalding. Combustion of liquid fuels. *Nature*, 165(4187):160–160, 1950.
- V. Stadnytskyi, P. Anfinrud, and A. Bax. Breathing, speaking, coughing or sneezing: What drives transmission of sars-cov-2? *Journal of Internal Medicine*, 290(5): 1010–1027, 2021.
- C. Steger. A comprehensive and versatile camera model for cameras with tilt lenses. *International Journal of Computer Vision*, 123(2):121–159, 2017.

- P. Strizhak, R. Volkov, G. Castanet, F. Lemoine, O. Rybdylova, and S. Sazhin. Heating and evaporation of suspended water droplets: Experimental studies and modelling. *International Journal of Heat and Mass Transfer*, 127:92–106, 2018.
- E. Strömsöe, H. Rönne, and A. Lydersen. Heat capacity of alcohol vapors at atmospheric pressure. *Journal of Chemical and Engineering Data*, 15(286-290):18, 1970.
- D. Sugimoto, K. Zarogoulidis, T. Kawaguchi, K. Matsuura, Y. Hardalupas, A. Taylor, and K. Hishida. Extension of the compressed interferometric particle sizing technique for three component velocity measurements. In *13th international symposium on applications of laser techniques to fluid mechanics Lisbon, Portugal*, pages 26–29, 2006.
- R. Sujith. An experimental investigation of interaction of sprays with acoustic fields. *Experiments in Fluids*, 38(5):576–587, 2005.
- R. Sujith, G. Waldherr, J. Jagoda, and B. Zinn. An experimental investigation of the behavior of droplets in axial acoustic fields. 1997.
- R. Sujith, G. Waldherr, J. Jagoda, and B. Zinn. A theoretical investigation of the behavior of droplets in axial acoustic fields. 1999.
- R. Sujith, G. Waldherr, J. Jagoda, and B. Zinn. Experimental investigation of the evaporation of droplets in axial acoustic fields. *Journal of Propulsion and Power*, 16(2):278–285, 2000.
- W. J. Tango, J. K. Link, and R. N. Zare. Spectroscopy of k2 using laser-induced fluorescence. *The Journal of Chemical Physics*, 49(10):4264–4268, 1968.
- H. Tennekes, J. L. Lumley, J. L. Lumley, et al. *A first course in turbulence*. MIT press, 1972.
- R. Thimothée, C. Chauveau, F. Halter, and I. Gökalp. Experimental investigation of the passage of fuel droplets through a spherical two-phase flame. *Proceedings* of the Combustion Institute, 36(2):2549–2557, 2017.

- P. Thybo, L. Hovgaard, S. K. Andersen, and J. S. Lindeløv. Droplet size measurements for spray dryer scale-up. *Pharmaceutical development and technology*, 13 (2):93–104, 2008.
- Y. Touloukian, P. Liley, and S. Saxena. Thermal conductivity: Nonmetallic liquids and gases, ifi, 1970.
- M. VanSciver, S. Miller, and J. Hertzberg. Particle image velocimetry of human cough. *Aerosol Science and Technology*, 45(3):415–422, 2011.
- E. P. Vejerano and L. C. Marr. Physico-chemical characteristics of evaporating respiratory fluid droplets. *Journal of The Royal Society Interface*, 15(139): 20170939, 2018.
- S. Verma, M. Dhanak, and J. Frankenfield. Visualizing the effectiveness of face masks in obstructing respiratory jets. *Physics of Fluids*, 32(6):061708, 2020.
- I. M. Viola, B. Peterson, G. Pisetta, G. Pavar, H. Akhtar, F. Menoloascina, E. Mangano, K. E. Dunn, R. Gabl, A. Nila, et al. Face coverings, aerosol dispersion and mitigation of virus transmission risk. *IEEE Open Journal of Engineering in Medicine and Biology*, 2:26–35, 2021.
- H. Vogel and A. Weiss. Transport properties of liquids. iv. self-diffusion, viscosity, and density of irregular liquid mixtures: Crown ether/alcohol. *Berichte der Bunsengesellschaft für physikalische Chemie*, 86(7):615–620, 1982.
- R. S. Volkov, G. V. Kuznetsov, and P. A. Strizhak. Influence of droplet concentration on evaporation in a high-temperature gas. *International Journal of Heat and Mass Transfer*, 96:20–28, 2016.
- J. S. Walker, J. Archer, F. K. Gregson, S. E. Michel, B. R. Bzdek, and J. P. Reid. Accurate representations of the microphysical processes occurring during the transport of exhaled aerosols and droplets. ACS Central Science, 7(1):200–209, 2021.

- F. Wang, J. Wu, and Z. Liu. Surface tensions of mixtures of diesel oil or gasoline and dimethoxymethane, dimethyl carbonate, or ethanol. *Energy & fuels*, 20(6): 2471–2474, 2006.
- J. Westerweel. Digital particle image velocimetry: theory and application. 1993.
- F. M. White and J. Majdalani. *Viscous fluid flow*, volume 3. McGraw-Hill New York, 2006.
- J. F. Widmann, D. T. Sheppard, and R. M. Lueptow. Non-intrusive measurements in fire sprinkler sprays. *Fire Technology*, 37(4):297–315, 2001.
- J.-S. Wu, K.-H. Hsu, P.-M. Kuo, and H.-J. Sheen. Evaporation model of a single hydrocarbon fuel droplet due to ambient turbulence at intermediate reynolds numbers. *International journal of heat and mass transfer*, 46(24):4741–4745, 2003.
- X. Xie, Y. Li, H. Sun, and L. Liu. Exhaled droplets due to talking and coughing. *Journal of the Royal Society Interface*, 6(suppl_6):S703–S714, 2009.
- F. Yang, A. A. Pahlavan, S. Mendez, M. Abkarian, and H. A. Stone. Towards improved social distancing guidelines: Space and time dependence of virus transmission from speech-driven aerosol transport between two individuals. *Physical Review Fluids*, 5(12):122501, 2020.
- J.-R. Yang and S.-C. Wong. An experimental and theoretical study of the effects of heat conduction through the support fiber on the evaporation of a droplet in a weakly convective flow. *International journal of heat and mass transfer*, 45(23): 4589–4598, 2002.
- A. Yarin, G. Brenn, O. Kastner, D. Rensink, and C. Tropea. Evaporation of acoustically levitated droplets. *Journal of Fluid Mechanics*, 399:151–204, 1999.
- C. Yeh. A fluorescense/scattering imaging technique for instantaneous 2-d measurement of particle size distribution in a transient spray. In *The Third International Congress on Optical Particle Sizing*, 1993.

- G. Yvon-Durocher, A. P. Allen, D. Bastviken, R. Conrad, C. Gudasz, A. St-Pierre, N. Thanh-Duc, and P. A. Del Giorgio. Methane fluxes show consistent temperature dependence across microbial to ecosystem scales. *Nature*, 507(7493): 488–491, 2014.
- T. Zhang. Study on surface tension and evaporation rate of human saliva, saline, and water droplets. West Virginia University, 2011.
- L. Zimmer and Y. Ikeda. Planar droplet sizing for the characterization of droplet clusters in an industrial gun-type burner. *Particle & Particle Systems Characterization: Measurement and Description of Particle Properties and Behavior in Powders and Other Disperse Systems*, 20(3):199–208, 2003.

List of publications

Journal

- H. Davies, M. Talibi, A. Ducci, N. Parsania, and R. Balachandran. Planar interferometric tracking of droplets in evaporating conditions. *Experiments* in Fluids, 63(10):167, 2022
- 2. K. M. A. Ho, H. Davies, R. Epstein, P. Bassett, Á. Hogan, Y. Kabir, J. Rubin, G. Y. Shin, J. P. Reid, R. Torii, et al. Spatiotemporal droplet dispersion measurements demonstrate face masks reduce risks from singing. *Scientific reports*, 11(1):1–11, 2021

Conference Proceedings

1. H. Davies, M. Talibi, M. Hyde, and R. Balachandran. Investigating ethanol-gasoline spray characteristics using an interferometric drop sizing technique. In *Turbo Expo: Power for Land, Sea, and Air*, volume 58677, page V006T05A023. American Society of Mechanical Engineers, 2019